

Behaviour of materials at high strain rates: numerical modelling

14th Technical Meeting, 2002
Sevilla, Spain

Numerical Modelling of the Dynamic Fracture Process in Ductile Metals

D C Barton

School of Mechanical Engineering

University of Leeds

Leeds LS2 9JT, UK

ABSTRACT

Numerical schemes for simulating high strain rate, large deformation events usually require some form of fracture or failure algorithm to fully describe the material response. This paper firstly reviews several of the more commonly available ductile failure models for metals, including an explicit void nucleation and growth model known as the Tvergaard-Needleman-Gurson (TNG) model and a new path dependent model attributed to Goldthorpe. The need for precise validation tests is explained and the advantages of the interrupted notched tensile test outlined together with some typical results and the description of a new technique for interrupted testing at high strain rates. The Goldthorpe model is demonstrated to be robust and accurate in predicting tensile failure across a range of conditions whereas the TNG model appears less generally applicable. The paper concludes by outlining the development of fracture algorithms to take account of the complexities of real material behaviour such as interactions between different modes of failure and directional anisotropy.

INTRODUCTION

High strain rate events such as ballistic impacts, vehicle crashes and high rate materials processing normally involve some form of material degradation or failure. One very common type of failure is ductile fracture arising from the nucleation, growth and coalescence of microscopic voids in the materials under a tensile stress field. Various numerical algorithms have been proposed over the years which purport to model this process of ductile tensile failure. Several of the more commonly available and widely used models are reviewed in the section that follows. Included in this review is the most popular model which explicitly calculates a void volume fraction as the state variable controlling ductile failure and alternative models which use the concept of a damage number for the same purpose.

Whatever forms the fracture algorithm takes, it must be validated by means of precise and meaningful comparisons with experimental results which should ideally cover a range of loading and strain rate conditions. The paper therefore briefly reviews some of the more important test techniques before proceeding to concentrate on one in particular, the notched tensile test, that offers the opportunity of interrupting the failure process to provide a more accurate basis for comparison with numerical results. A new extension of this test to truly high strain rate loading conditions is described and some typical results presented. The paper concludes by discussing the relative merits of the different fracture models considered and recommending how these models should be enhanced to take account of some of the complexities of real material behaviour.

NUMERICAL MODELS OF DUCTILE FAILURE

THE JOHNSON-COOK MODEL

Based on the pioneering work of Hancock and Mackenzie [1] and their own tests on various metals [2], Johnson and Cook proposed a strain-based ductile failure model in which a strain to failure ϵ_f at each point in space and time within a numerical scheme is calculated as a function of the stress triaxiality parameter σ_m/σ_y (where σ_m is the mean stress and σ_y is the current material flow stress), the non-dimensional strain rate $\dot{\epsilon}^*$ and the homologous temperature T^* :

$$\epsilon_f = \left[C_1 + C_2 \exp \left(C_3 \frac{\sigma_m}{\sigma_y} \right) \right] \left[1 + C_4 \ln \dot{\epsilon}^* \right] \left[1 + C_5 T^* \right] \quad (1)$$

where $C_1 - C_5$ are constants to be determined from experimental data.

At each time step, a cumulative damage parameter is calculated for each element:

$$D = \sum \frac{\Delta \epsilon}{\epsilon_f}$$

where $\Delta \epsilon$ is the current increment of plastic strain.

When D reaches a certain predetermined value (usually unity), the element is assumed to have failed. In most Lagrangian numerical schemes, this involves simply setting the stresses in that element to zero, or removing it completely from the mesh using an element erosion algorithm.

Although the mechanics of void growth in a ductile matrix as determined by the analyses of McClintock [3] or Rice and Tracey [4] is recognized in the relation between failure strain and stress triaxiality in equation (1), there is no strong theoretical basis for the remaining terms in $\dot{\epsilon}^*$ and T^* . Hence this ductile exhaustion model is at best semi-empirical. However it is path dependent in the sense that the value of D depends on the history of loading (and not simply on the current state) and the scheme has been shown to be numerically robust and accurate over certain limited ranges of conditions.

THE TVERGAARD-NEEDLEMAN-GURSON (TNG) MODEL

From their studies of void nucleation and growth from second phase particles under notched tensile test conditions, Tvergaard and Needleman [5] proposed a failure model which explicitly calculates the void volume fraction as an independent parameter to indicate damage. The total rate of increase of void volume fraction \dot{f} is considered to be the sum of the rates due to nucleation of new voids \dot{f}_n and due to growth of existing voids \dot{f}_g :

$$\dot{f} = \dot{f}_g + \dot{f}_n \quad (2)$$

Assuming the matrix material to be incompressible, the void growth rate is given simply by:

$$\dot{f}_g = (1 - f) \dot{\eta} \quad (3)$$

where $\dot{\eta}$ is the volumetric plastic strain rate.

Following the work of Chu and Needleman [6], either a stress or strain based nucleation criterion is used. The latter gives the nucleation rate as:

$$\dot{f} = A \dot{\epsilon} \quad (4)$$

where $\dot{\epsilon}$ is the effective plastic strain rate and A is given by:

$$A = \frac{f_N}{S_N \sqrt{2\pi}} \exp \left[-\frac{1}{2} \left(\frac{\epsilon - \epsilon_N}{S_N} \right)^2 \right] \quad (5)$$

The terms f_N and S_N are the volume fraction and standard deviation of void nucleating particles, ϵ is the local plastic strain and ϵ_N is the mean strain at which voids nucleate (usually assumed constant).

The above void nucleation and growth model is usually combined with the Gurson yield surface which in its modified form as suggested by Tvergaard [7], gives the yield function as:

$$\phi = \left(\frac{\sigma_e}{\sigma_y} \right)^2 + 2q_1 f \cosh \left[\frac{3}{2} \frac{\sigma_m}{\sigma_y} \right] - \left(1 + q_1^2 f^2 \right) \quad (6)$$

where σ_e is the von Mises equivalent stress and $q_1 = 1.5$ is a parameter introduced to take account of the effect of neighbouring voids rather than the single void considered by Gurson.

There can be convergence problems in implementing such a model in an explicit finite element code since the Gurson yield surface shrinks very rapidly when voids start to grow. The problem to be addressed is that of updating the known stresses and other state variables associated with the converged state at time t_n into their corresponding values which should lie on or very near the new yield surface at time t_{n+1} . At Leeds, the stress update algorithm due to Ortiz and Popov [8] and Ortiz and Simo [9] has been adapted in order to implement the above failure model in the explicit Lagrangian code DYNA2D. This has been shown to be numerically robust provided a sensible limit is placed on the void volume fraction when the material is assumed to have failed.

GOLDTHORPE PATH DEPENDENT MODEL

This model developed by Goldthorpe [10] uses the general principles of path dependency and void growth to calculate a new damage parameter S which depends on the value of hydrostatic tension integrated with respect to strain over the loading path:

$$S = 0.67 \int_0^{\epsilon} \exp \left[\frac{3}{2} \frac{\sigma_m}{\sigma_y} - 0.04 \left(\frac{\sigma_m}{\sigma_y} \right)^{-1.5} \right] d\epsilon \quad (7)$$

The first term in the exponent refers to the standard Rice and Tracey [4] equation for the growth of spherical voids whilst the second term takes account of the results of Budiansky et al. [11] for very low values of σ_m/σ_y . Failure is assumed to occur when the damage parameter reaches a certain critical value which can be determined from a simple uniaxial tension test where the hydrostatic tension can be identified at all points along the strain path.

This model is relatively straightforward to implement in a Lagrangian finite element code. At Leeds, this has been achieved by simply modifying the standard Johnson-Cook failure subroutine in DYNA2D. As with this latter an element in which the critical damage parameter is reached is simply removed from the mesh using an element erosion algorithm. This is considered a reasonable approach provided the mesh density is sufficiently fine; the small amount of mass lost when the element is removed may then be representative of the mass lost in reality due to fragmentation of the material.

EXPERIMENTAL VALIDATION

When implemented in a numerical solver, a dynamic ductile fracture model should be robust, stable and not overly sensitive to numerical parameters such as the mesh density or time step. Furthermore, it should ideally be applicable over a range of conditions which may be quite different from the conditions under which the parameters of the model were derived. These requirements suggest that fracture models should be validated by comparison with experimental results from different types of dynamics test which may expose the limitations of each type of model. Tests which are commonly used for validation purposes include:

- (i) the plate impact spall test in which failure occurs under very high stress triaxiality but low strain condition
- (ii) the Taylor test (ideally under symmetrical impact conditions) in which stress wave interactions cause regions of tensile plastic strain and localised failure to occur near the axis of the specimen
- (iii) the explosive cylinder test in which denotation of an explosive inside a thick wall cylinder causes a conical fracture surface to develop at one end of the cylinder
- (iv) the dynamic notched tensile test in which a range of stress triaxiality conditions can be produced at the centre of a tensile specimen by pre-machining notches of different profile radius.

Tests (i) and (ii) are well known and have been widely used to validate numerical models of material constitutive behaviour. Indeed test (i), the plate impact test, offers the possibility of using very accurate instrumentation (e.g. VISAR) to precisely determine the response of the plate material during the test. The explosive cylinder test is less well known but has recently been used to compare the predictions of the TNG and Goldthorpe fracture models as implemented in the Lagrangian code DYNA2D [12]. An iron specimen sectioned after the test is shown in Fig. 1(a) in which the conically shaped fracture region is clearly visible. The Goldthorpe model results shown in Fig. 1(b) are in good agreement with both the position and extent of the fractured region. This was particularly encouraging because the critical damage parameter for the iron ($S_c = 2.2$) had been derived from simple uniaxial tensile tests which give a very much lower level of stress triaxiality than in the cylinder test. In contrast Fig. 1(c) shows that the TNG model grossly overpredicts the extent of the failure zone despite the fact that the coefficients for this version of the model were derived from plate impact spall tests which produce similar values of stress triaxiality parameter (around 400).

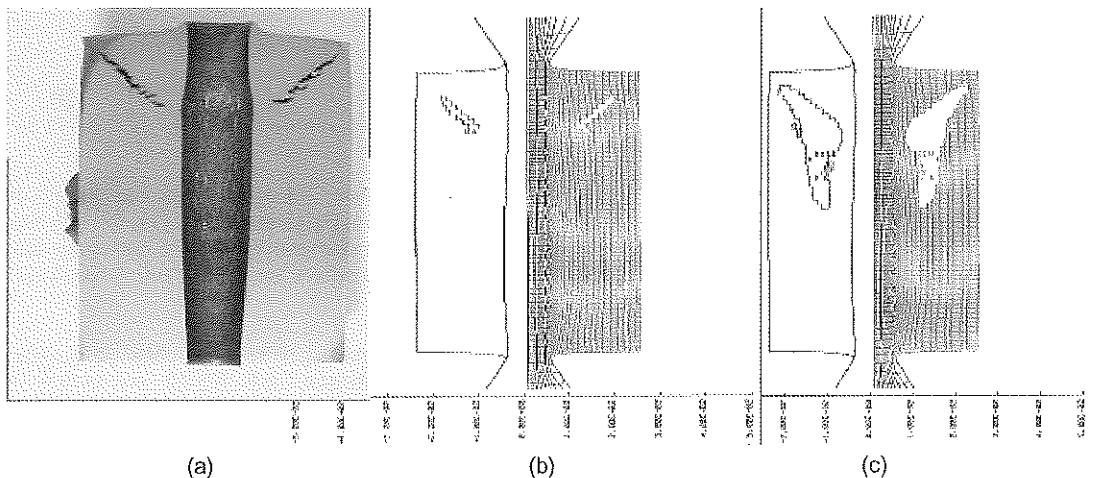


Figure 1. Explosive cylinder test results for iron (a) experiment, (b) Goldthorpe model, (c) TNG model.

Test (iv), the notched tensile test, has been widely used to investigate the fracture characteristics of ductile metals e.g. [13]. It is relatively easy and cheap to perform and, with the aid of numerical simulations and an accurate constitutive relation, the conditions at the centre of the notch can be precisely determined as a function of the overall deformation of the specimen. The test can be carried out quasi-statically or dynamically at high strain rates using devices such as the tensile split Hopkinson bar or, in the case of the work at Leeds, the so-called "Flying Wedge". The latter device, shown schematically in Fig. 2, applies a symmetrical simultaneous loading to each end of the specimen causing it to fail in a very short time duration.

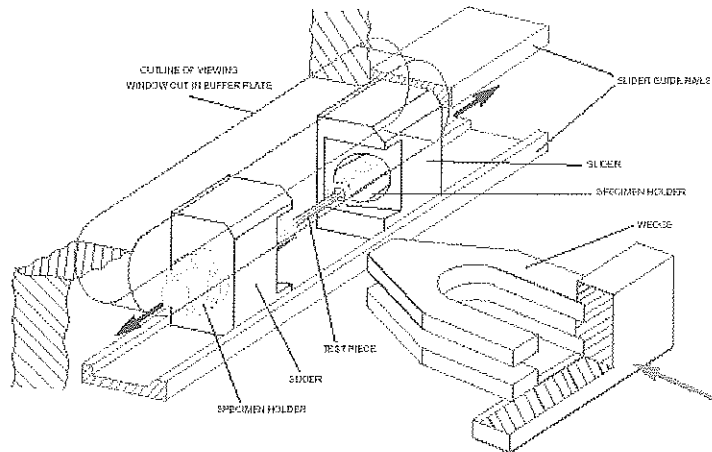


Figure 2. The 'Flying Wedge' dynamic tensile test apparatus

By varying the impacting wedge semi-angles and its velocity, it is possible to produce strain rates in the specimens ranging from around 10^2 s^{-1} upto in excess of 10^4 s^{-1} (locally, for small specimens). Furthermore, facilities to heat (using an induction furnace) or cool (using liquid nitrogen) the specimen are available to enable testing to be carried out over a range of temperatures as well as strain rates. Usually finite element analyses of the different notch profile radii are conducted using meshes such as shown in Fig. 3 to give predictions of the stress triaxiality and local deformation conditions at the centre of the notch.

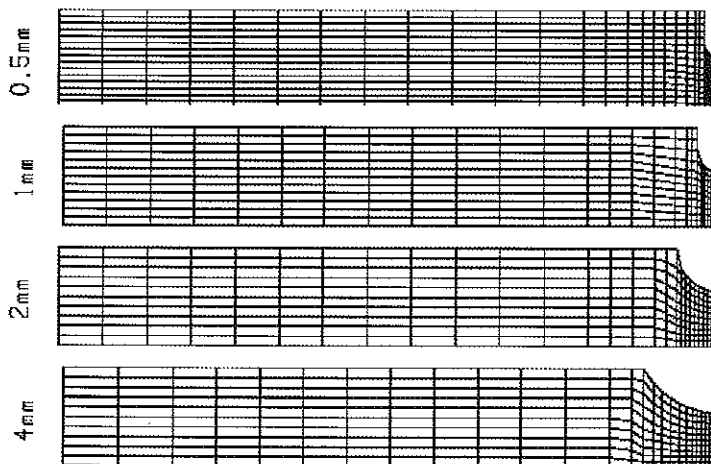


Figure 3. Typical finite element meshes for different notch profile radius tensile specimens

INTERRUPTED TENSILE TESTS

As discussed above, ductile failure is a progressive process and, in validating a fracture model, it is highly desirable to be able to isolate and identify the various stages of the process. Unfortunately tests (i) – (iii) mentioned above, along with most other tests involving high impact velocities or energies, are not very amenable to this kind of study as it is quite difficult to interrupt or control the amount of damage occurring in the specimen. Test (iv), the notched tensile test, offers possibilities in this regard as in theory the test can be interrupted at different levels of deformation to allow examination of the specimen before final and complete fracture. In so doing, another serious disadvantage of the simple tensile test can be overcome, namely that conventional comparisons are made between measured and predicted strains after the specimen has been broken. For ductile materials, there may be significant additional radial strain between the coalescence of voids to form microcracks at the centre of the neck/notch and the final separation of the specimen. This is due to the resistance of a ductile material to crack propagation and the reducing triaxial tension as the crack propagates towards the outside of the specimen. By interrupting the test at different levels of deformation, it should be possible by microscopy of sectioned specimens to delineate the different stages of the ductile fracture process and thereby provide a more accurate basis for the validation of fracture models (and indeed for optimising the parameters of such models).

It is relatively straightforward to interrupt a quasi-static tensile test at predetermined levels of deformation prior to fracture. A programme of such testing has recently been carried out at Leeds on a number of different metals including OFHC copper, AQ80 pure iron and a rolled homogeneous armour (RHA) steel. Of these, copper was the most ductile and the test programme demonstrated that the onset of failure in terms of the first visible appearance of voids and their coalescence to form microcracks occurred at strains much less than the final fracture strain. Furthermore, the different stages of the failure process were found to follow the same trend with respect to stress triaxiality as the strain at final failure (see Fig. 4).

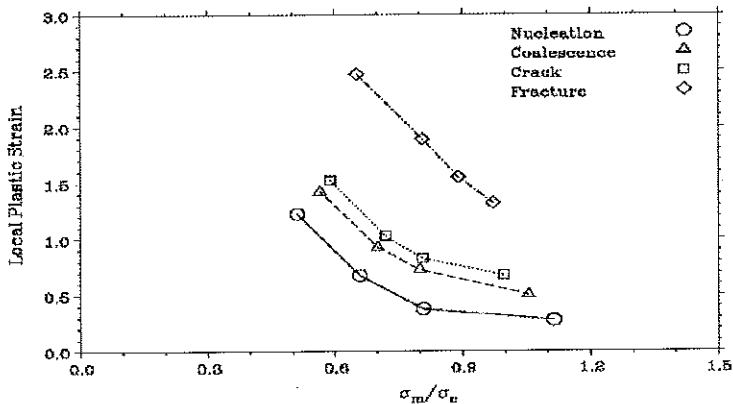


Figure 4. Results of interrupted tensile testing for OFHC copper

These results were used to establish a stress triaxiality dependent criterion for void nucleation for this high purity copper which takes the usual form:

$$\epsilon_N = C_1 + C_2 \exp \left(C_3 \frac{\sigma_m}{\sigma_y} \right) \quad (8)$$

where best fit constants $C_1 = 0.09$, $C_2 = 19.98$ and $C_3 = -5.54$ were determined from the experimental results. This criterion was coded into the Leeds version of the TNG fracture model and is considered an important enhancement of the standard model in that the model can now take account of the low strains to nucleate voids under conditions of high stress triaxiality (e.g. as in the plate impact test) rather than resorting to a stress controlled criterion as has previously been required.

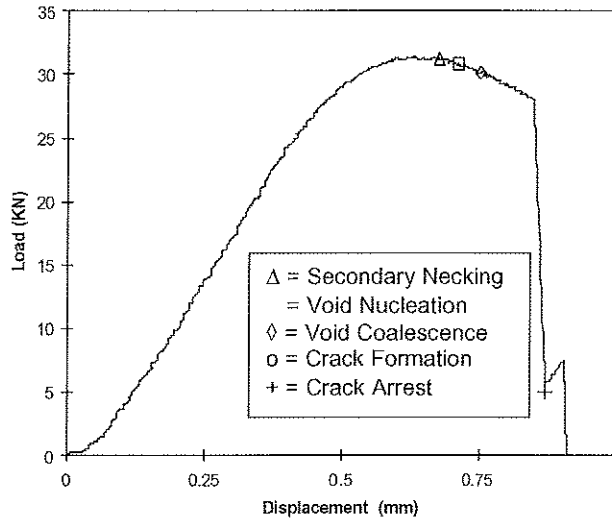


Figure 5. Interrupted test results for 1mm notch radius RHA specimen

Although much less ductile than OFHC copper and the AQ80 iron, the RHA was shown to suffer internal damage in the form of microscopically visible voiding at strains much lower than the final failure strain [14]. Furthermore, for the 1 mm notch profile geometry in particular, the main crack was seen to be temporarily arrested before eventually propagating to the outside of the specimen as indicated in the typical load-displacement curve shown in Fig. 5.

As for copper it is therefore not valid to compare the predictions of a numerical fracture model for this material with experiment on the basis of the final separation strain. Instead a programme of interrupted tensile tests was used to identify a mean strain to cause void nucleation and these results compared with the DYNA2D predictions of strain to first element failure for the different fracture models described above. It can be seen from the comparative results shown in Table 1 that the Goldthorpe model using a critical damage parameter $S_c = 2.2$ indicated by uniaxial tests on plain specimens accurately predicts the magnitude of the nucleation strains with just a relatively minor overprediction for the smaller notch radii specimens. The TNG model, used in this comparison with a constant nucleation strain equal to 0.1, does not give such good agreement. Moreover, if the nucleation strain were made a function of stress triaxiality as indicated in eqn. (8), the correlation would be even poorer. The Johnson-Cook fracture model results are in good agreement with experimental strains to final fracture as expected since these experimental strains were used to derive the parameters of the model.

Table 1: Experimental and predicted failure strains for Rolled Homogeneous Armour

Notch Profile Radius (mm)	Mean Experimental Strains		Numerically Predicted Strains		
	Final Fracture	Void Nucleation	Goldthorpe model ($S_c = 2.2$)	TNG model (nucleation strain = 0.1)	Johnson-Cook model
4	0.825	0.697	0.702	0.858	0.817
2	0.597	0.499	0.498	0.596	0.602
1	0.517	0.354	0.397	0.376	0.510
0.5	0.352	0.331	0.360	0.225	0.362

DYNAMIC INTERRUPTED TESTING

The experimental results described above were all obtained from quasi-static tests using a servo-hydraulic machine. It is relatively straightforward to stop such tests at a pre-determined level of deformation to allow specimens to be sectioned and examined microscopically. However it is much more challenging to conduct the same kind of interrupted testing on a truly dynamic high strain rate test facility. The Flying Wedge, for example, operates with many times more kinetic energy than that required to simply fracture the specimen and it is impractical to consider stopping the wedge itself mid-test after a controlled amount of specimen deformation has recurred. Instead a novel technique was developed which makes of a double-notched specimen design and a special split fixture which is clamped around the notch of primary interest as indicated in Fig. 6.

The principle behind this arrangement is that only a certain amount of axial deformation, controlled by the use of shims, of the primary notch is allowed before the square shoulders on either side of the notch come into contact with the internal shoulders on the fixture. Further deformation and fracture then occurs in the secondary notch which is of slightly larger root diameter, leaving the primary notch intact for subsequent sectioning and microscopic examination. As indicated by the broken specimen in Fig. 6, this technique has been demonstrated to work successfully at high loading rates on the Flying Wedge for mild steel and, more recently, titanium alloy specimens. The technique will shortly be used to conduct the first programme of high strain rate interrupted tensile testing on the titanium and the results compared with those from the corresponding quasi-static tests.

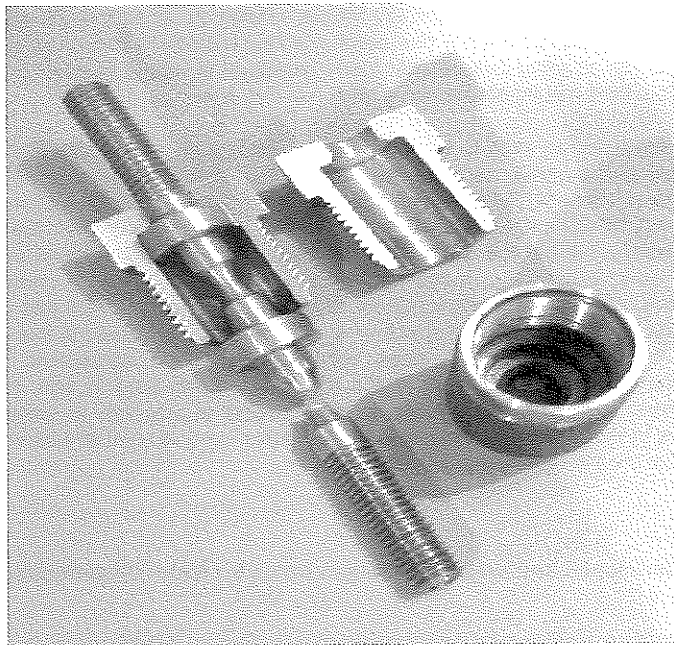


Figure 6. Double-notched specimen and split clamp for interrupted testing at high strain rates

FURTHER DISCUSSION AND FUTURE DIRECTIONS

Of the various fracture models reviewed and investigated in this paper, the Goldthorpe path dependent model appears the most promising for the following reasons:

- it is based on sound theoretical background concerning the growth of a spherical void in a plastically deforming material
- the single critical damage parameter required can be determined from simple uniaxial tensile tests.
- it has been shown to be numerically robust and to give accurate predictions of the onset of ductile failure in a number of tests for stress triaxiality conditions ranging from moderate (notched tensile test) to very high (plate impact test, explosive cylinder test).

In contrast, the TNG model, although physically based, can be difficult to implement numerically due to the rapidly shrinking Gurson yield surface as voids start to grow. There are a number of parameter values that must be measured or assumed and there are two potential void nucleation criteria, one based on stress and the other on strain.

Work reported in this paper has in fact indicated that the strain to nucleate voids for a nearly pure metal such as OFHC copper should be a function of stress triaxiality rather than a constant value as assumed in the standard Tvergaard – Needleman model. Despite this modification, the TNG model has not been found to be particularly accurate in predicting the onset of failure in the notched tensile test. Furthermore, when applied to simulations of much more intensively dynamic events such as the plate impact or explosive cylinder test, the TNG model tended to grossly overestimate the extent of the fracture zone.

The simple Johnson-Cook fracture model is basically a semi-empirical fit to experimental data generated by tensile tests over a range of stress triaxiality, strain rate and temperature conditions. As such it should work well in numerical situations of the tests from which the data was derived. What is less clear is how well the model can be extrapolated to more extreme conditions. However, the model is path dependent in the sense that the contribution to the damage parameter is calculated at each step dependent on the local conditions and it can be readily implemented in a numerical hydrocode to give robust solutions.

Despite the good results obtained so far, one criticism of the current Goldthorpe model is that there is no direct link between the damage accumulation in the specimen (as measured by the damage parameter) and the constitutive or deformation model for the material. Thus the usual von Mises plasticity relations (with the accompanying assumption of zero volumetric strain) will continue to apply up to the point of fracture. In reality, the onset of damage in the form of microvoiding will cause an increase in volumetric strain and a corresponding reduction in the stress-carrying capacity of the material (which is what the TNG model aims to represent by means of an explicit void volume fraction and the Gurson yield surface). Thus there is a requirement to link the deformation and damage models by some feedback mechanism to allow for calculation of volumetric strain and its effect on the stress-strain response of the material.

Also the current Goldthorpe model is based on growth equations for a simple spherical void. No account is taken of the potential interactions between neighbouring voids or that voids may grow to become non-spherical (oblate). These aspects are currently being investigated by the model's originators at QinetiQ using a combined analytical/numerical unit cell approach. Also under consideration is how to account for mixed mode failure where for example tensile failure is accompanied by shear. An interim approach is to add a shear strain (ϵ_s) term multiplied by a material dependent constant A to the evolution of the tensile damage parameter S:

$$S = 0.67 \int_0^{\epsilon} \exp \left[\frac{3}{2} \frac{\sigma_m}{\sigma_y} - 0.04 \left(\frac{\sigma_m}{\sigma_y} \right)^{-1.5} \right] d\epsilon + A\epsilon_s \quad (9)$$

What is required to investigate the validity of this simple approach is a test which produces a significant amount of both tensile and shear damage. Similarly, transitions between ductile and brittle modes of fracture need to be considered. For example, it has been demonstrated by means of dynamic notched tensile tests that, under certain combinations of stress triaxiality and strain rate, a normally ductile metal will fail in an almost completely brittle manner [13]. None of the fracture models discussed in this paper would currently be able to predict this transition without modification.

Finally, there are issues of anisotropy to consider. Some form of directional anisotropy due to the effects of texture, crystallographic/molecular orientation or mechanical processing is present, to varying degrees, in most materials. This is reflected not only in a direction-dependent deformation response but also in different strains to failure for loading in different directions. For example, recent tensile tests on plain (unnotched) titanium alloy specimens aligned both longitudinal and transversely with respect to the processing direction have indicated large differences in strains to failure, as shown at notch radius = 0 in Fig. 7. This is despite the fact that no significant difference in the material deformation response in the two directions could be determined. When notches are introduced to increase the level of stress triaxiality in the specimen, the failure strains for the two directions of loading converge so that, for a notch profile radius of 1 mm or less, there is no discernable difference, Fig. 7.

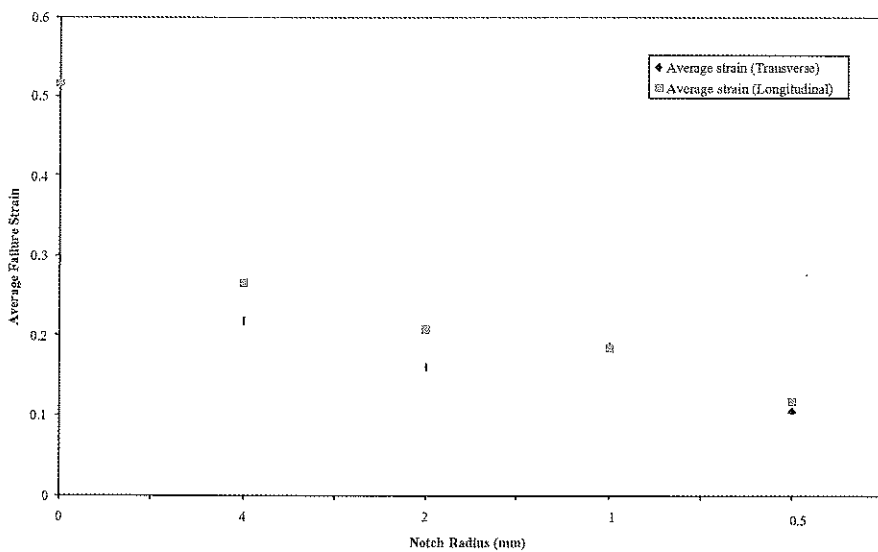


Figure 7. Average failure strain vs. specimen geometry for titanium alloy in transverse and longitudinal directions

Clearly uniaxial tests on this material would indicate different critical damage parameters or different strains to cause void nucleation in the two directions. What is not clear is how these parameters could then be incorporated in a numerical fracture model which takes account of this anisotropy under multi-axial loading conditions. One possibility would be to make use of an equivalent failure surface, such as illustrated for 2D loading conditions in Fig. 8. At present, only the points where the surface intersects the principal strain axes are known. Careful interpretation of multi-axial test data is required to determine the shape of the surface between these points.

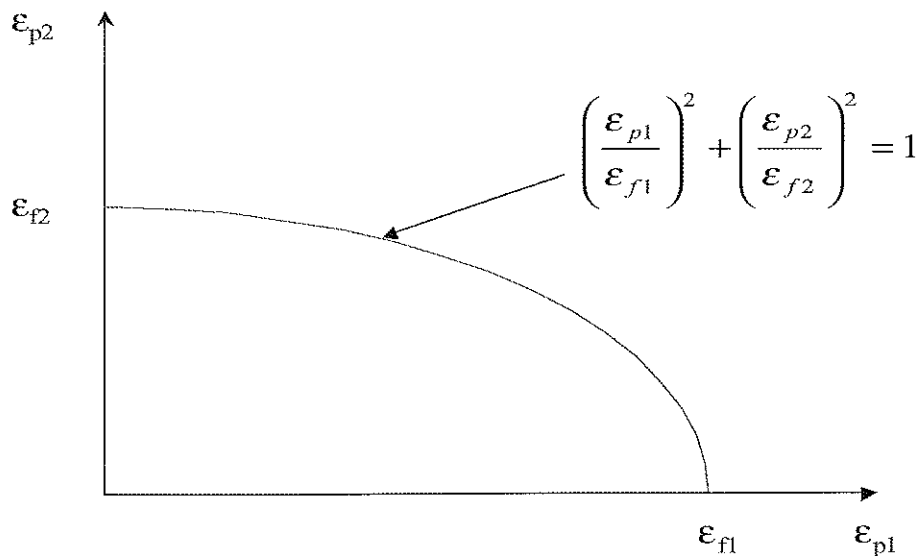


Figure 8. Potential anisotropic failure surface in 2D strain space

CONCLUSION

Three different approaches to modelling ductile failure have been reviewed and their implementation within Lagrangian hydrocodes briefly discussed. Interrupted testing of notched tensile specimens provides a precise means of validating such models since it allows the different stages in the ductile failure process to be defined. Results confirmed that the onset of voiding is a strong function of the stress triaxiality at the centre of the notch which contradicts the usual assumption in the Tvergaard-Needleman-Gurson strain-controlled model that voids nucleate at a constant strain. The TNG model gives rather poor agreement with results from interrupted tensile tests and other high rate experiments even when a stress triaxiality nucleation strain is specified. On the other hand, results from the Goldthorpe path dependent model appear promising across a range of different test conditions. However issues remain to be resolved with respect to how this model interacts with the material deformation response and also how it accounts for mixed modes of failure and material anisotropy.

ACKNOWLEDGMENTS

The author would like to thank Mr P Church, Mr A Andrews and their colleagues at QinetiQ for their support and the many useful discussions over the years. Acknowledgment is also due to researchers who have been supported by QinetiQ at Leeds, namely Dr S Mirza, Ms C Cameron and Dr A Mir, who between them have generated most of the experimental results reported in this paper.

REFERENCES

1. Hancock J.W. and Mackenzie A.C., *J. Mech. Phys. Solids*. 24(1976) 147-169.
2. Johnson G.R. and Cook W.H., *Eng. Fract. Mech.* 21(1985) 31-48.
3. McClintock F.A., *J. Appl. Mech.* 35(1968) 363-371.
4. Rice J.R. and Tracey D.M., *J. Mech. Phys. Solids*. 17(1969) 201-217.
5. Tvergaard V. and Needleman A., *J. Mech. Phys. Solids*. 32(1984) 461-490.
6. Chu C.C. and Needleman A., *J. Engng. Mat. Tech.* 102(1980) 249-256.
7. Tvergaard V., *Int. J. Fract.* 17(1981) 389-397.
8. Ortiz M. and Popov E.P., *Int. J. Num. Meth. Engg.* 21(1985) 1561-1576.
9. Ortiz M. and Simo J.C., *Int. J. Num. Meth. Engg.* 23(1986) 353-366.
10. Goldthorpe B.D., *J. de Physique III*, C3 (1997) 705-710.
11. Buidiansky B., Hutchinson J.N. and Slutsky S., *Mechanics of Solids*, Pergamon, (1980).
12. Church P.D., Macmahon J., Softley P. and Cameron C., *J. de Physique III*, C3 (2000) 292-297.
13. Mirza M.S., Barton D.C. and Church P.D., *J. Mat. Sci.* 31(1996) 453-461.
14. Cameron C., Barton D. C., Andrews T.D. and Church P.D., *J. de Physique III*, C3 (2000) 209-214.

Propagation of adiabatic shear bands: dimensional analysis.

A.S. Bonnet, P. Lipinski, A. Molinari

Laboratoire de Physique et Mécanique des Matériaux, U.M.R. CNRS 7554, ISGMP, Ecole Nat. d'Ingenieurs de Metz, Université de Metz, Ile du Saulcy, 57045 Metz Cedex 01, France

ABSTRACT

Numerical simulations are carried out in order to study the dynamic propagation of adiabatic shear bands inside a layer of finite length and finite thickness submitted to shear loading. After a period of transient response, a steady state is attained in which the bands propagate with a constant velocity. A special attention is accorded to the dependence of the stationary shear band speed upon a set of physical parameters. The evolution of the shear band speed is firstly determined as a function of the applied velocity. Then, a dimensional analysis provides a general law describing the role of all parameters on the propagation process.

INTRODUCTION

The use of very high strain rates in the actual forming processes frequently leads to the formation of adiabatic shear bands. This mechanism of formation is now well known as it has been studied by many authors during the last decades (e.g. Clifton (1980), Bai (1982), Wright and Batra (1985), Molinari and Clifton (1987), Giovanoia (1988), Molinari (1988)). However the phenomenon of propagation of these bands still needs to be explained. Experimental works have been carried out in order to reproduce the localization process and to observe the propagation of adiabatic shear bands. Thus, Marchand and Duffy (1988) managed to evaluate the speed of propagation of a shear band in a thin-walled HY 100 steel tube twisted at a strain rate of 1600s^{-1} . They measured a speed of propagation of 520m/s in the case where only one tip of the band is supposed to propagate and 260m/s in the case of a two-directional propagation. Numerical simulations were also conducted by Batra and Zhang (1994) to reproduce the experiments of Marchand and Duffy. Several values of strain rates were considered. They obtained a shear band propagating in both directions along the tube circumference and with a non-stationary speed. A strong dependence of the speed of propagation on the nominal strain rate was also observed. The experimental and numerical work of Zhou et al. (1996) also provided very interesting information. They study the propagation of an adiabatic shear band in impacted prenotched plates made of C300 steel. A strong dependence of shear band speed on impact velocity, at lower impact velocities, and a tendency to saturate at higher impact velocities were observed. An analytical model, neglecting heat conduction, was also developed by Mercier and Molinari (1998) for a shear band propagating into an infinite layer of finite thickness submitted to shear loading. This model allowed to characterize the influence of strain hardening, strain-rate sensitivity, thermal softening and elastic shear modulus on the shear band speed and on the length of the process zone. The shear band velocity reported for a CRS 1018 steel was about 1200m/s.

In this paper, numerical simulations are carried out to model the propagation of an adiabatic shear band in a layer of finite length and finite thickness submitted to simple shear. The results of the simulations enable to obtain the evolution of the shear band propagation speed as a function of the applied velocity. A dimensional analysis is then realized to establish a general law describing the evolution of the shear band speed as a function of each problem's parameter.

MODELLING.

We assume the material to be elastic thermo-viscoplastic. The elastic law takes the following form:

$$\sigma_{ij}^* = C_{ijkl} d_{kl}^e \quad (1)$$

where C_{ijkl} are the elastic moduli and d_{kl}^e is the elastic strain rate. The additive decomposition of the total strain rate d into elastic and plastic parts is supposed:

$$d = d^p + d^e \quad (2)$$

In (1), $\sigma_{ij}^* = \dot{\sigma}_{ij} - \omega_{jk} \sigma_{ki} - \omega_{ik} \sigma_{kj}$ denotes the Jaumann rate of the stress tensor, with ω_{jk} being the antisymmetric part of the velocity gradient.

The constitutive law used to calculate the plastic part of the deformation is the one from Molinari & Clifton (1987):

$$\sigma_e = K(\bar{\epsilon}^p + \epsilon_0^p)^n T^{-v} (D_{eq}^p + D_0^p)^m \quad (3)$$

where σ_e and D_{eq}^p state for the effective stress and the effective plastic strain rate, respectively given by

$$\sigma_e = \left(\frac{3}{2} s_{ij} s_{ij}\right)^{1/2}, D_{eq}^p = \left(\frac{2}{3} d_{ij}^p d_{ij}^p\right)^{1/2} \quad (4)$$

s_{ij} corresponds to the deviatoric stress tensor and d_{ij}^p is given by the J_2 flow theory :

$$d_{ij}^p = \frac{3}{2} \frac{D_{eq}^p}{\sigma_e} s_{ij} \quad (5)$$

The cumulated plastic strain is defined by :

$$\bar{\epsilon}^p(t) = \int_0^t D_{eq}^p(t') dt' \quad (6)$$

The flow stress level is scaled by K , ϵ_0^p is a plastic prestrain, n is the strain hardening exponent ($n > 0$), T is the absolute temperature, v ($v > 0$) and m ($m > 0$) are respectively the thermal softening and the strain rate sensitivity exponents.

The values of this constitutive law's parameters are reported in table 1 for a CRS 1018 steel.

At high strain rates ($\geq 10^3 s^{-1}$ - $10^4 s^{-1}$ for steels), a strong increase of the strain rate sensitivity is observed. This phenomenon is not accounted for by the law (3). However, by changing the value of m in this law, the influence of the strain rate sensitivity on shear band propagation will be analysed.

Considering our problem as two-dimensional, the energy equation providing the evolution law for the temperature has the form:

$$\rho C_p \dot{T} - k \left(\frac{\partial^2 T}{\partial x^2} + \frac{\partial^2 T}{\partial y^2} \right) = \beta \sigma \dot{\epsilon}^p \quad (7)$$

where C_p is the heat capacity, ρ is the mass density, k is the heat conductivity and β is the Taylor-Quinney coefficient which defines the fraction of plastic work converted into heat ; usually β is taken constant and equal to 0.9.

Table 1. Material parameters of C.R.S. 1018 steel

Parameter	K	m	n	v	C_p	k	ρ	ϵ_0^p	D_0^p	μ
C.R.S. 1018	6300×10^6 Pa	0.019	0.015	0.38	500 $J/(kg K)^{-1}$	50 W /m K	7800 $kg m^{-3}$	0.057	10^{-3}	80 GPa

A specimen of finite length $L=200mm$ and finite height $2h=2.5mm$ is considered, see Figure 1. Boundary conditions $v_x=\pm V$ and $v_y=0$ are prescribed at the frontiers $y=\pm h$. The displacements are imposed to be the same at $x=0$ and $x=L$ in order to better approach the tubular specimen of Marchand and Duffy. A geometrical defect is introduced in the middle of the specimen, at the left edge, to initiate the band. This defect is materialized by a reduction of thickness of 20% with respect to the rest of the specimen. Adiabatic thermal conditions are also assumed on the specimen boundaries. Finally, an initial velocity field is introduced to correspond to the field existing in Marchand and Duffy's specimen when the shear band initiates. This velocity field varies linearly from $v_x=-V$ on $y=-h$ to $v_x=+V$ on $y=h$.

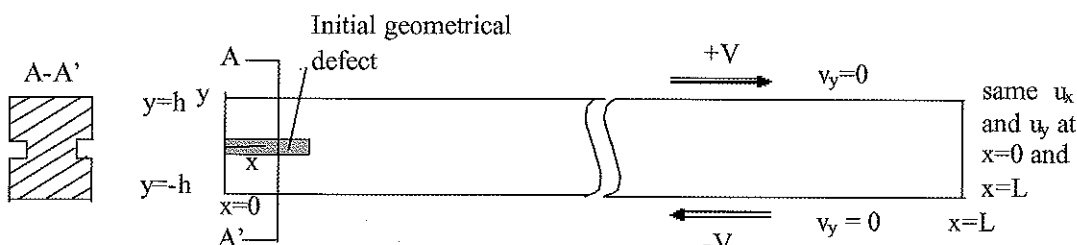


Figure 1. Schematic view of a finite layer of steel, length $L=200mm$, width $2h=2.5mm$. Constant velocities $v_x=\pm V$ and $v_y=0$ are applied at the boundaries $y=\pm h$. Periodic boundary conditions are taken at the extremities $x=0$ and $x=L$. An initial geometrical defect is introduced (thickness $e_{def}<e$).

The FE ABAQUS/Explicit code (2000) is used to perform the numerical simulations. The two-dimensional aspect of the problem is represented by the 'plane strain' CPE4RT elements.

INFLUENCE OF LOADING CONDITIONS ON THE SHEAR BAND SPEED

To study the influence of loading conditions on the shear band propagation speed, the following range of nominal strain rates is considered: from $\dot{\gamma}=400$ to $2.4 \times 10^5 s^{-1}$ (corresponding to velocities V varying from 0.5 to 300m/s as $\dot{\gamma} = V/h$). The shear band speed C is evaluated by following the equivalent plastic strain isolines with time. After a transient, a steady state is attained in which two shear bands emanating from the boundaries $x=0$ and $x=L$ propagate with a constant velocity.

Figure 2 shows the influence of the applied velocity V on the shear band propagation speed C . Three distinct stages can be seen on this figure. The first one (stage I) is characterized by the quasi-linear dependence of C upon V . In stage II, the slope of the curve strongly decreases indicating that the shear band speed seems to saturate with the applied velocity. The particular velocity value V^* separating stages I and II has been introduced by Lebouvier et al. (2000) and can be determined by the energy balance of the whole layer. The stage III finally shows a very slight evolution of C with V . These results are in good agreement with those reported by Zhou et al. (1996) for impact tests.

Focussing our attention on the lowest values of V , we can observe the existence of a critical velocity V_c , below which no shear band propagation is obtained. This last observation matches with the results of Zhou et al. (1996). Indeed, this minimum value had already been reported by these authors for impacted plates.

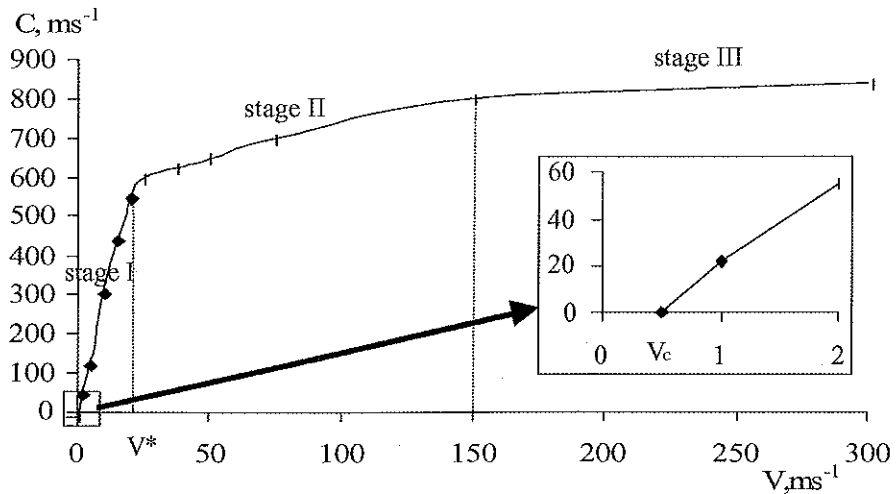


Figure 2. Effects of the applied velocity V on the stationary shear band speed C . A CRS 1018 steel is considered. The enlarged box shows the existence of a critical velocity V_c below which no propagation is observed. Note the presence of three stages.

DIMENSIONAL ANALYSIS

In this section, a dimensional analysis is made in order to understand the whole adiabatic shear band propagation phenomenon. A review of all the parameters which are able to influence the process is firstly made.

According to Equation (7), the thermal behaviour of the material is represented by the following parameters : the specific heat C_p , the heat conductivity k and the mass density ρ . The influence of the thermal expansion is neglected here.

As the elastic behaviour is assumed to be linear and isotropic, the elastic tensor is defined by two material constants only : the elastic shear modulus μ and the Poisson's coefficient ν_p . The influence of the elastic shear modulus on the shear band propagation is analysed in this section.

The fraction of plastic energy converted into heat is characterized, according to Equation (7), by the Taylor-Quinney coefficient β . Several authors (Lipinski et al. (1990)) have shown that the value of β could vary as a function of the plastic strain. Therefore, the role of this parameter on the shear band propagation is also studied .

According to equation (3), the constants describing the thermo-viscoplastic behaviour of the material are: strain hardening n , strain rate sensitivity m , thermal softening v , stress level K .

Finally, the parameters related to the geometry of the specimen and to the initial and boundary conditions are the following ones: half-width of the sheared layer h , length of the layer L , defect thickness e_{def} , initial temperature T_0 , applied velocity V .

The dimensional analysis is made in order to present and analyse the numerical results in a rational way. A special attention is accorded to the dependence of the shear band speed (C) with respect to all the parameters cited above.

Using the Vashy-Buckingham theorem, the dimensional analysis provides the following relationship :

$$\frac{C}{V} = F \left(\frac{K}{\mu}, \frac{\rho V^2}{\mu}, \frac{\rho C_p T_0}{\mu}, \frac{k T_0}{V \mu h}, \frac{h}{L}, \frac{h}{e_{def}}, m, n, \beta, \nu \right) \quad (8)$$

where F can be specified for stages I and III but is hard to be determined for the transient stage II.

STAGE I.

To determine function F, a large number of numerical simulations are performed. Indeed, it is necessary to vary each non-dimensional parameter while keeping the others constant.

The following relationship is finally found for equation (8).

$$\frac{C}{V - V_c} \approx \frac{C}{V} = \alpha \left(\frac{K}{\mu} \right)^{0.97} \left(\frac{\mu}{\rho C_p T_0} \right)^{0.98} \beta^{1.01} \frac{1}{m^{1.08}} (-An + B) \quad (9)$$

when assuming that $C/(V - V_c) \approx C/V$ for $V \gg V_c$. We obtain $A \approx 257$ and $B \approx 38,2$; α depends on the thermal softening exponent ν . Because of the precision related to the shear band speed estimation, the exponents can be fairly approximated by 1. Thus (9) becomes

$$\frac{C}{V} = \alpha \left(\frac{K}{\mu} \right) \left(\frac{\mu}{\rho C_p T_0} \right) \frac{\beta}{m} (-An + B) = \alpha \frac{K \beta}{\rho C_p T_0 m} (-An + B) \quad (10)$$

Figure 3 shows, for instance, the evolution of the parameter C/V as a function of respectively K/μ , $\rho C_p T_0/\mu$ and n .

The relationship (10) has been established for the range of values reported below. No extrapolation can be made beyond this range.

$$\begin{array}{ll} 3.15 \times 10^3 \leq K \leq 12.6 \times 10^3 \text{ MPa}, & 0.005 \leq m \leq 0.05, \\ 0.45 \leq \beta \leq 1, & 40 \times 10^3 \leq \mu \leq 160 \times 10^3 \text{ MPa}, \\ 0 \leq n \leq 0.12, & 0 \leq k \leq 500 \text{ W/mK}, \\ 1950 \leq \rho \leq 15600 \text{ kg.m}^{-3}, & 1.25 \leq e/e_{def} \leq 2, \\ 125 \leq C_p \leq 1000 \text{ J/kgK}, & V_c < V < V^* \\ 75 \text{ K} \leq T_0 \leq 600 \text{ K}, & \end{array}$$

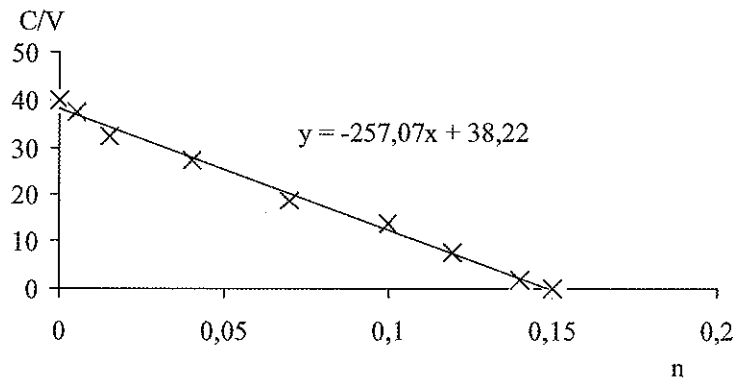
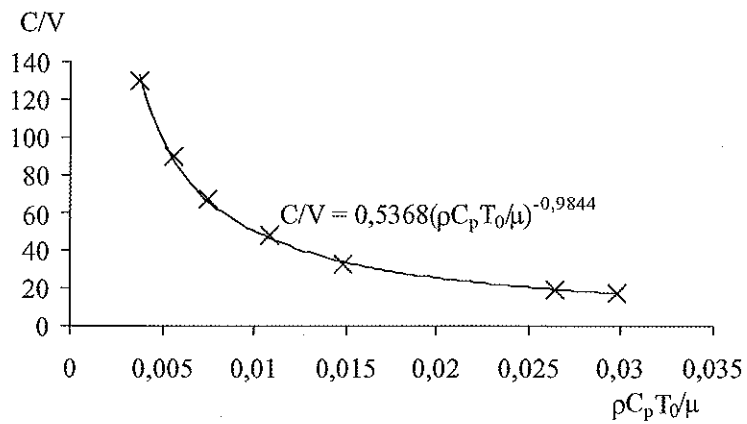
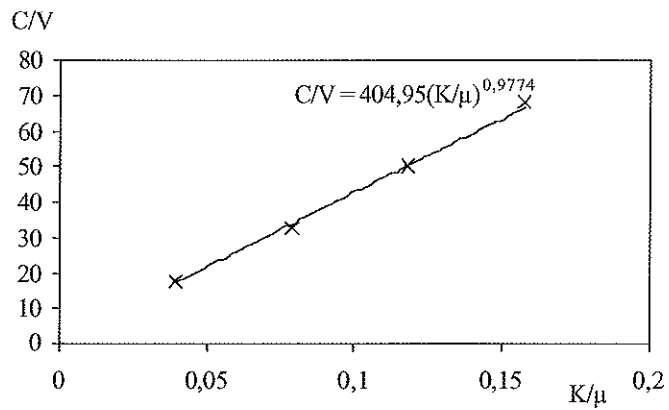


Figure 3. Evolution of the shear band speed C normalized by the applied velocity V as a function of :

- a) K/μ
- b) $\rho C_p T_0/\mu$
- c) n

for fixed values of the other non dimensional parameters. All calculations refer to stage I.

The parameters involved in the problem are K/μ , $\rho V^2/\mu$, $\rho C_p T_0/\mu$, $kT_0/V\mu h$, h/L , e/e_{de} , m , n , β and ν .

The simplest way to understand the influence of the above parameters on shear band velocity is to analyse the terms appearing in the energy balance.

Influence of the stress level K .

K is included in two terms of the balance equation via the shear stress τ : the elastic energy which is proportional to $\tau^2/2\mu$ (with τ corresponding to the value of the shear stress far ahead the tip of the band) and the external rate of work τV . As C/V depends linearly on K and does not depend on μ , according to relationship (10), it can be deduced that the shear band propagation is controlled by the external work in stage I. Moreover, it can be noted that an increase of K leads to an increase of C/V . This last remark can be explained by the fact that K controls not only the amount of energy injected into the system but also the stress drop due to thermal softening. Consequently, an increase of K leads to an increase of the injected energy (higher stress level) and to a stronger release of this energy via the stress drop.

Influence of inertia effects.

Inertia can be physically characterized by the kinetic energy term ρV^2 and by all terms related to elastic wave propagation. We postulate here that elastic shear waves, propagating with the velocity $C_2 = \sqrt{\mu/\rho}$, are of most interest. In expression (10), none of these terms appears. It can thus be deduced that the elastic wave speed does not play any role on the shear band propagation in this stage and also that the kinetic effects can be neglected for this range of velocities V ($V_c \leq V \leq V^*$).

Influence of heat generation

Heat generation is associated to two distinct terms of the dimensional analysis: $\rho C_p T_0/\mu$ and β . According to relationship (10), an increase of C_p (or a decrease of β) leads to a diminution of the shear band speed C . Indeed, the two dimensional parameters are strongly related to the shear band speed, as they determine, via equation (7), the magnitude of the stress drop due to the thermal softening. Thus, increasing C_p (or reducing β) leads to a diminution of \dot{T} for a given value of D_{c0}^p . As a consequence, the stress drop due to thermal softening is weaker and C decreases. A similar behaviour is obtained for the parameter T_0 as it controls the initial stress level. A lower initial temperature leads to an increase of the initial stress and thus to a stronger thermal softening. Consequently C increases.

Influence of the strain rate sensitivity

The stabilizing effect of strain rate sensitivity on strain localization is well known. In the area of the propagation of adiabatic shear bands, it manifests itself by a significant decrease of the shear band speed when m increases. The evolution law of C/V upon m given by (10) is valid for the range of values of m considered ($0.005 \leq m \leq 0.05$). Beyond this range, the existence of a critical value ($m=0.12$) from which no localization can take place, is observed. This last remark is in agreement with the instability criterion established by Molinari and Clifton (1987) for a one-dimensional process under velocity controlled boundary conditions: $m(1-\nu)+n+\nu < 0$. It is worth noting that the critical value provided by this criterion ($m=0.26$) does not correspond to the one obtained with our calculations as this criterion cannot be strictly applied to the 2D problem of shear band propagation. However, it gives indications concerning the influence of material parameters on the instability process.

Influence of strain hardening

As strain rate sensitivity, strain hardening n is also stabilizing for the shear band propagation. The diminution of C when n increases is illustrated in Figure 3c. The existence of a critical value of n beyond which no localization can take place confirms once again the instability criterion of Molinari and Clifton (1987), although the values reported are quite different ($n=0.15$ according to our simulations and $n=0.353$ with the criterion).

Influence of the elastic shear modulus μ

According to relationship (10), the combination of all dimensional terms makes the ratio C/V independent of the elastic shear modulus μ . From the physics of the problem, μ is included into two different terms : the elastic energy $\tau^2/2\mu$ and the elastic shear wave speed $\sqrt{\mu/\rho}$. As there is no way to combine these quantities to be compatible with the expression (10), it can be concluded that elastic energy and elastic shear wave speed have no significant influence on the shear band propagation in stage I. As a consequence, the fact that the external work controls the shear band propagation in stage I is confirmed.

Influence of the heat conductivity k

One can deduce from (10) that there is no important effect of k on C for the proposed range of applied velocities in stage I. However, heat conductivity can play a significant role on C in the vicinity of V_c , (see figure 8 of Bonnet-Lebouvier et al., 2002).

Influence of the geometrical defect

The magnitude of the geometrical defect e_{def} directly influences the time to localization. The more pronounced the defect, the earlier localization takes place. However, once the steady-state is attained, the initial value of the defect has no effect on the shear band speed.

Influence of the specimen dimensions L and h

The geometrical parameters L and h do not appear in relationship (10). Therefore, it can be concluded that they do not influence the shear band propagation in stage I, for the range of values considered here. However this is only verified when the specimen length L is sufficient to allow the shear band speed to reach a stationary value and when h is large enough with respect to the shear band width w .

STAGE III.

For stage III, the numerical simulations lead to the following expression for equation (8):

$$\frac{C}{V} = \eta \left(\frac{K}{\mu} \right)^{0.92} \left(\frac{\mu}{\rho V^2} \right)^{0.44} \left(\frac{\mu}{\rho C_p T_0} \right)^{0.45} \left(\frac{1}{m} \right)^{0.49} \beta^{0.52} (-A'n + B') \quad (11)$$

which is approximated by :

$$C = \eta C_2 \sqrt{\frac{K^2 \beta}{\mu \rho C_p T_0 m}} (-A'n + B') \quad (12)$$

where $C_2 = \sqrt{\mu/\rho}$. The values $A' = 34.6$ and $B' = 5.8$ are obtained ; η depends on v . The evolution of the parameter C/V as a function of, for instance, K/μ , $\rho V^2/\mu$, $\rho C_p T_0/\mu$ is reported in Figure 4. The analysis was driven for the following values of parameters :

$$\begin{array}{ll} 3.15 \times 10^3 \leq K \leq 12.6 \times 10^3 \text{ MPa,} & 0.01 \leq m \leq 0.12, \\ 0.3 \leq \beta \leq 1, & 40 \times 10^3 \leq \mu \leq 160 \times 10^3 \text{ MPa,} \\ 0.005 \leq n \leq 0.15, & 0 \leq k \leq 500 \text{ W/mK,} \\ 3900 \leq \rho \leq 31200 \text{ kg.m}^{-3}, & 1.25 \leq e/e_{def} \leq 2, \\ 250 \leq C_p \leq 2000 \text{ J/kgK,} & V > V^* \\ 150 \leq T_0 \leq 1200 \text{ K,} & \end{array}$$

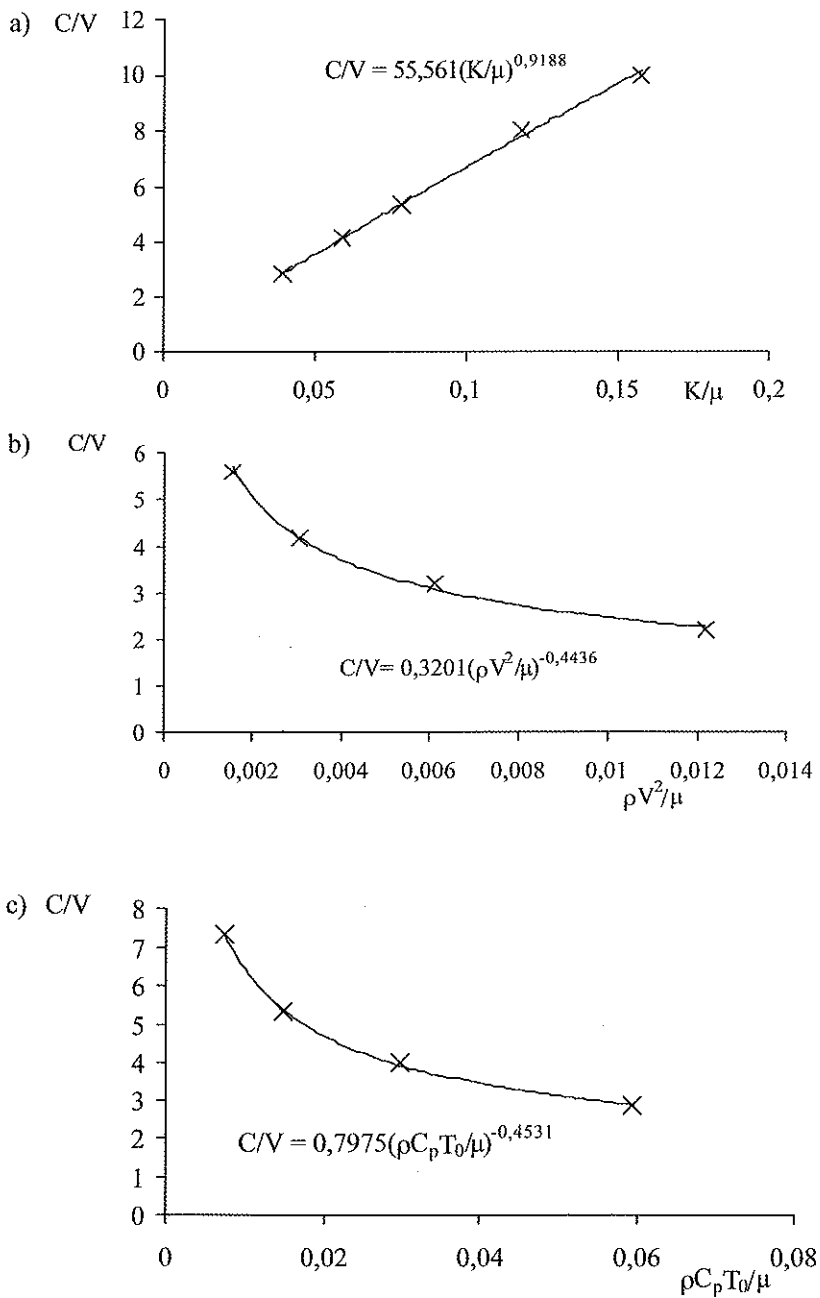


Figure 4. Evolution of shear band speed C normalized by the applied velocity V as a function of :

- a) K/μ
- b) $\rho V^2/\mu$
- c) $\rho C_p T_0/\mu$

for fixed values of the other non dimensional parameters. All calculations refer to stage III.

The parameters involved in the problem are K/μ , $\rho V^2/\mu$, $\rho C_p T_0/\mu$, $kT_0/V\mu h$, h/L , c/ϵ_{def} , m , n , β and v .

Influence of the stress level K .

According to (10), the shear band speed is independent on the applied velocity V . Consequently, the external work does not govern the shear band propagation in this stage. Moreover, K appears through the term K^2/μ which scales with an elastic energy. We can thus assume that the shear band propagation is controlled by the elastic energy release. An increase of K leads to an increase of the elastic energy release and thus to a higher shear band speed.

Influence of the elastic shear modulus μ

The elastic shear modulus is included into the elastic wave speed $\sqrt{\mu/\rho}$ and into the elastic energy term $\tau^2/2\mu$. On the one hand, as wave propagation is responsible for the elastic energy transport to the shear band tip, an increase of μ should intensify the energy flux to the band tip and should lead to an increase of C . But on the other hand, increasing μ reduces the level of the stored elastic energy in the vicinity of the band tip and should produce a decrease of C . Because of this competition between two opposite effects, a variation of μ seems to have no influence on the shear band speed.

Influence of inertia effects

Inertia appears in (12) through $\sqrt{\mu/\rho}$ indicating that wave propagation has a significant role to play in the propagation phenomenon in stage III. Moreover, the shear band speed C becomes a fraction of the elastic shear wave speed, confirming the model developed by Freund et al. (1985) about the propagation of adiabatic shear bands inside a slab submitted to a mode III loading.

Finally, the parameters $\rho C_p T_0 / \beta$, m , n , k , ϵ_{def} , L and h have the same influence on the shear band propagation in stage III as in stage I.

CONCLUSION

The mechanism of propagation of adiabatic shear bands has been studied in the configuration of Marchand and Duffy's experiments. A layer of finite length L and of finite width $2h$ was submitted to simple shear via constant velocities applied at the upper and lower edges. The evolution of the shear band speed C as a function of the applied velocity V was found to be composed of three distinct stages : the first one (stage I) in which C increases in a quasi-linear manner with V , a second one (stage II) where a tendency towards an asymptotic value is obtained and a third one (stage III) where C remains approximately constant.

Then, a dimensional analysis has provided a general law characterizing the role of all parameters on the shear band speed and allowing to better understand the whole propagation process. It has also shown that stage I is governed by the external work coming from the boundaries and that stage III is controlled by the elastic energy release.

REFERENCES

- Abaqus Manuals, 2000, Version 6.1, Hibbit, Karlson & Sorensen, Inc. Providence, U.S.A.
- Bai, Y.L., 1982. Thermo-plastic instability in simple shear. *Journal of Mechanics and Physics of Solids* 30 (4), 195-207.
- Batra, R.C., Zhang, X., 1994. On the propagation of a shear band in a steel tube. *ASME Journal of Engineering Materials and Technology* 116; 155-161.
- Bonnet-Lebouvier, A.S, Molinari, A., Lipinski, P., 2002. Analysis of the dynamic propagation of adiabatic shear bands. *International Journal of Solids and Structures* 39, 16, 4249-4269.
- Clifton, R.J., Duffy, J., Hartley, K.A., Shawki, T.G., 1984. On critical conditions for shear band formation at high strain rates. *Scripta Metal.*, 18, 443-448.

- Freund, L., Wu, F., Hawley, R., 1985. Initiation and propagation of shear band in antiplane shear deformation. In Proc. of the Considere Memorial Symposium, 125-143. Presse de l'Ecole Nationale des Ponts et Chaussées.
- Giovanola, J.H., 1988a. Adiabatic shear banding under pure shear loading. Part I : Direct observation of strain localization and energy dissipation measurements, *Mechanics of Materials* 7, 59-71.
- Giovanola, J.H., 1988b. Adiabatic shear banding under pure shear loading. Part II : Fractographic and metallographic observations, *Mechanics of Materials* 7, 73-87.
- Lebouvier, A. S., Lipinski, P., Molinari, A., 2000. Numerical simulations of the propagation of an adiabatic shear band. *Journal de Physique IV*, vol 10, 9.
- Lipinski, P., Krier, J., Berveiller, M., 1990. Elastoplasticité des métaux en grandes déformations : comportement global et évolution de la texture interne. *Revue Phys. Appl.* 25, 361-388.
- Marchand, A., Duffy, J., 1988. An experimental study of the formation process of adiabatic shear band in a structural steel. *Journal of Mechanics and Physics of Solids* 36, 251-283.
- Mercier, S., Molinari, A., 1998. Steady-state shear band propagation under dynamic conditions. *Journal of Mechanics and Physics of Solids* 46 (8), 1463-1495.
- Molinari, A., 1988. Shear band analysis. In : *Nonlinear Phenomena in Materials Science, Vol. 3 of Solid State Phenomena*, pp 447-468, Trans. Tech. Publ.
- Molinari, A., Clifton, R.J., 1987. Analytical characterization of shear localization in thermoviscoplastic materials. *ASME Journal of Applied Mechanics* 54, 806-812.
- Wright, T.W., Batra, R.C., 1985. The initiation and growth of adiabatic shear bands. *International Journal of Plasticity* 1, 205-212.
- Zhou, M., Ravichandran, G., Rosakis, A.J., 1996a. Dynamically propagating shear band in impact-loaded prenotched plates II - Numerical simulations. *Journal of Mechanics and Physics of Solids* 44, 1007-1032.
- Zhou, M., Rosakis, A.J., Ravichandran, G., 1996b. Dynamically propagating shear band in impact-loaded prenotched plates I – Experimental investigations of temperature signatures and propagation speed. *Journal of Mechanics and Physics of Solids* 44, 981-1006.

On the influence of strain rate and stress triaxiality on strength and ductility of a structural steel: experiments and numerical simulations

Tore Børvik and Odd Sture Hopperstad

SIMLab/Department of Structural Engineering, Norwegian University of Science and Technology,
N-7491 Trondheim, Norway

ABSTRACT

Notched axisymmetric specimens of the structural steel Weldox 460 E have been tested at high strain rates in a Split Hopkinson Tension Bar. The aim was to study the combined effects of strain rate and stress triaxiality on the material's behaviour. Force and elongation of the specimens were measured by strain gauges. In addition, the notch deformation was obtained using a digital high-speed camera system and the true strain against time at minimum cross-section was estimated. Non-linear finite element analyses of the experimental tests were then carried out, and the numerical results are discussed and compared against the experimental observations.

INTRODUCTION

Computer simulations of the mechanical response of engineering structures under impact loading require constitutive relationships accounting for large strains, high strain rates and thermal softening (Harding 1). In many cases, it is also important to model the failure of the structure, and damage and fracture may have to be included in the structural model (Lemaitre 2). Constitutive relations for metallic materials at high strain rates vary from purely empirical, based on available experimental data, to theoretical relationships, based on the micro-mechanical processes assumed to govern the macroscopic behaviour of the material (Harding 1). Typically the constitutive relation defines the equivalent stress in terms of equivalent (or accumulated) plastic strain, equivalent plastic strain rate and temperature (Johnson and Cook 3; Zerilli and Armstrong 4; Khan and Liang 5). The material parameters introduced in the constitutive equations are usually identified based on test data obtained from tension or torsion tests for wide ranges of strain rate and temperature. While the strength of metallic materials depends on strain, strain rate and temperature, many experimental investigations show that the ductility depends markedly on the triaxiality of the stress state (Hancock and Mackenzie 6; Mackenzie et al. 7; Hancock and Brown 8). The stress triaxiality is defined by a dimensionless parameter, given as the mean stress divided by the equivalent stress. Computational fracture models have been proposed that includes the influence of stress triaxiality (Beremin group 9) and the effects of stress triaxiality, strain rate and temperature (Johnson and Cook 10). The influence of the stress triaxiality in these models is based on the void growth equation proposed by Rice and Tracey (11). It is common to fit the material parameters of the computational fracture models to data obtained from tensile tests with notched axisymmetric specimens. Different stress triaxiality levels are obtained by varying the notch radius of the specimens.

This paper gives a summary of two journal articles recently published in the European Journal of Mechanics – A/Solids (Hopperstad et al. 12, Børvik et al. 13). The aim of the study was to investigate the influence of stress triaxiality and strain rate on the behaviour of a structural steel and to obtain experimental data that may be used to validate constitutive relations and fracture criteria. To this end smooth axisymmetric specimens and notched axisymmetric specimens with three different notch radii

of Weldox 460 E steel have been tested in tension at two different strain rates. The tests were performed in a Split Hopkinson Tension Bar, using a digital high-speed camera system to record the local deformation in the notch. Experimental procedures, visual observations and test results are presented and discussed in the first part of the paper. In the last part, the material constants in the constitutive relation and fracture model of Johnson and Cook (3,10) are defined from existing data for Weldox 460 E steel (Børvik et al. 14). Computer simulations are then performed to validate the constitutive relation and fracture model, and to study in detail the material behaviour during high-rate tension tests of smooth and notched specimens.

EXPERIMENTAL PROGRAMME

The specimens were made from a 12 mm thick plate of Weldox 460 E steel and tested in the as-received condition. Weldox 460 E is a thermo-mechanically rolled ferritic structural steel offering high strength combined with a high degree of ductility. All specimens were taken parallel to the rolling direction of the steel plate. A previous study by Børvik et al. (14) gave no indications of planar anisotropy, while a slight normal anisotropy was found. The test specimens were made of material from the same delivery that was used in previous material and projectile impact tests reported by Børvik et al. (14,15,16). The geometry and dimensions of the notched specimens are given in Figure 1. Tests were performed for three different notch root radii R_0 equal to 0.4 mm, 0.8 mm and 2 mm. Two levels of loading rate were applied, defined by a pre-loading force N_0 of the loading device equal to 20 kN and 40 kN. For each of the six combinations, four parallel tests were performed. A test identification system is adopted herein where e.g. R0.8-20-4 has the following meaning: R0.8 – notch radius $R_0 = 0.8$ mm; 20 – pre-loading force $N_0 = 20$ kN; 4 – parallel test No. 4.

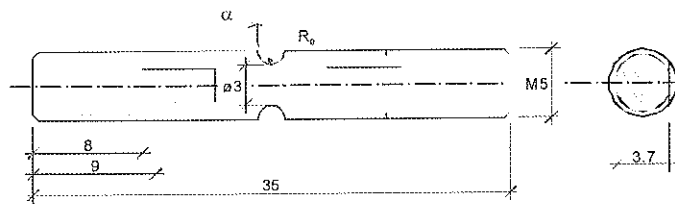


Figure 1: Geometry and dimensions (in mm) of notched test specimens for high rate tests in the Split Hopkinson Tension Bar (Note: For manufacturing reasons, the side faces of the notch were inclined at an angle $\alpha = 17.5^\circ$ to the normal of the specimen axis for specimens with $R_0 = 0.4$ and 0.8 mm, while for $R = 2.0$ mm the side faces were normal to the specimen axis, i.e. $\alpha = 0$).

The tensile tests of the notched specimens were performed in a Split Hopkinson Tension Bar (Albertini and Montagnani 17) at the European Commission Joint Research Centre in Ispra, Italy. A sketch of the Split Hopkinson Tension Bar is shown in Figure 2. The test apparatus consists of two half-bars called the input bar A-B-C and the output bar DE, and the specimen C-D is inserted between these two bars. Elastic energy is stored in a pre-stressed loading device A-B, which is the solid continuation of the input bar. By rupturing the brittle intermediate piece B, a tension wave with a rise-time of about 50 ns is transmitted along the input bar and loads the specimen to fracture. The strain rate is changed by varying the pre-loading force N_0 of the loading device and thus the stored elastic energy. Three strain gauges are placed on the input and output bars, at locations 1, 2 and 3 in Figure 2. The strain gauges are used to measure the elastic deformations versus time in the half-bars caused by the incident, reflected and transmitted pulses. These measurements are subsequently used to calculate the elongation, force and rate of elongation of the specimen, using one-dimensional elastic wave theory (Lindholm and Yeakley 18).

In some of the parallel tests, a digital high-speed camera system was used to obtain optical recordings of the notch deformation. The purpose of the set-up for optical measurements was to capture images of the specimen during deformation and to derive a diameter reduction curve as a function of time. In order to measure the diameter accurately, it is important to have a sharp edge between the background and the specimen. A shadow photography technique was therefore chosen. In order to

give diffuse light, a flashlight was placed behind a translucent screen. A digital Ultramac FS501 image converter camera, capable of framing rates from 2.000 to 20.000.000 frames per second, was used to photograph the specimen. The camera was focused on the edge of the specimen, and the event was triggered by the strain gauge at location 1 on the input bar of the Split Hopkinson Tension Bar (see Figure 2). Hence, the images could be directly correlated to the actual force applied to the specimen at given times. The camera was operated in a 15-image mode, and calibration images were taken of the specimen prior to every test. For each test, the specimen diameter was calculated for the pre-test calibration images and the test images. The calculated diameter from the test image was then divided by the diameter of the corresponding calibration image to achieve a relative diameter. This procedure was found to reduce the influence of aberrations in the digital images introduced by the high-speed camera system.

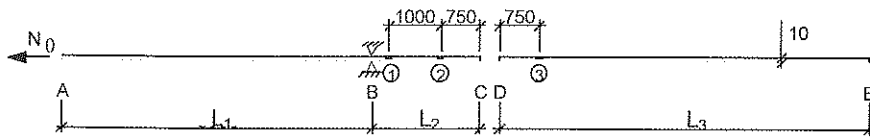


Figure 2: Sketch of the Split Hopkinson Tension Bar. The diameter of the input bar A-B-C and the output bar DE is 10 mm, and the specimen C-D is inserted between these two bars. The strain gauges on the input bar are at location 1 and 2, while the strain gauge on the output bar is at location 3. The pre-loading force N_0 is applied to the left extremity of the input bar A, while the bar is fixed in the longitudinal direction with a brittle intermediate piece at B. By rupturing the brittle intermediate piece, a tensile wave is transmitted along the input bar and loads the specimen to failure.

EXPERIMENTAL RESULTS

The notched-specimen tensile tests are considered as tests on structural components, since the stress and strain fields within the specimens are non-uniform. The results are therefore obtained as force vs. elongation curves, where the elongation refers to the specimen elongation as measured from the strain gauges located on the input and output bars. The ductility is measured by the true strain to fracture (or the fracture strain), which is calculated as

$$\epsilon_f = \ln(A_0/A_f) \quad (1)$$

where A is the current minimum cross-section area of the specimen; A_0 is measured before testing and A_f after fracture (Dieter 19). All the fracture areas were measured in a microscope to improve the accuracy of the measurements. The mean values of the fracture strains, calculated according to Eq. (1), for each combination of notch radius and pre-loading force are plotted against the initial stress triaxiality in the centre of the notch in Figure 3. The initial stress triaxiality was calculated according to Bridgman's analysis (Bridgman 20) as

$$(\sigma_m/\sigma_{eq})_0 = 1/3 + \ln(1 + a_0/2R_0) \quad (2)$$

where a_0 is the original radius of the specimen in the centre of the notch and R_0 is the initial notch radius. Hancock and Mackenzie (6), Mackenzie et al. (7) and Hancock and Brown (8) have discussed the application of Bridgman's analysis to notched specimens. More recently, Alves and Jones (21) examined this issue, and pointed out that use of Bridgman's analysis for notched specimens may involve significant errors. Figure 3 also includes data obtained by Børvik et al. (14) from quasi-static tests on smooth and notched specimens and high-rate tests on smooth specimens. The following observations are made based on the results presented in Figure 3. First, considerable scatter in the measurements of the fracture strain was found. Second, the fracture strain decreases with increasing stress triaxiality $(\sigma_m/\sigma_{eq})_0$. Third, no significant effect of pre-loading (or strain rate) on the fracture strain can be ascertained for the notched specimens, while a significant reduction in fracture strain with increased strain rate is indicated for smooth specimens. The reason for this difference in behaviour between smooth and notched specimens is not obvious. Note that the initial stress triaxiality

parameter is, in general, not equal to the true stress triaxiality in the centre of the notch. During the test, the stress triaxiality varies owing to the strong deformation of the notched part of the specimen (see e.g. Alves and Jones 21). The main trends observed from the force-elongation curves are as follows: the force increases with decreasing notch radius and increasing pre-load, the elongation to fracture increases with increasing notch radius, while the pre-load seems to have no significant effect on the elongation to fracture for notched specimens.

Based on the optical measurements of the current diameter $d = 2a$ in the centre of the notch, it is possible to reconstruct the true strain vs. time curves for the notched specimens. The true strain ϵ in the centre of the notch (i.e. at the minimum cross-section) is calculated as (Dieter 19)

$$\epsilon = \ln(A_0/A) = 2\ln(d_0/d) \quad (3)$$

where it is assumed that the strain is constant across the minimum cross-section, and that the cross-section shape remains unaltered by the deformation. The latter assumption does not hold completely, due to an ovalisation of the cross-section in some of the specimens due to normal anisotropy. The first assumption is reasonably accurate for a relatively large notch radius R_0 , while the strain may vary considerably over the cross-section when R_0 becomes small (Hancock and Brown 8, Alves and Jones 21). Indeed, it is not certain that the fracture process initiates in the central region of the notch (i.e. at the minimum cross-section on the axis of the specimen) when the notch radius decreases, but rather at the surface in the notch root. It follows that the true strain ϵ should be considered as an average strain measure for the notched specimens.

For the tests in which optical measurements of the diameter reduction were obtained, the fracture diameter d_f was measured in the microscope in the plane that was monitored with the digital high-speed camera system. The fracture strain was then calculated as $\epsilon_f = 2\ln(d_0/d_f)$. Comparing the fracture strains based on the area and diameter reductions at fracture, respectively, it was realised that there may be relatively large errors involved in the high-speed camera measurements of the strain. Measurements from the quasi-static tests on smooth and notched specimens performed by Børvik et al. (14) indicate that from diffuse necking to fracture the cross-section gradually develops an oval shape. It follows that the error induced by defining the true strain as $2\ln(d_0/d)$ instead of $\ln(A_0/A)$ increases with increasing strain. Better results could have been obtained by using mirrors to get measurements of the diameter in two orthogonal planes.

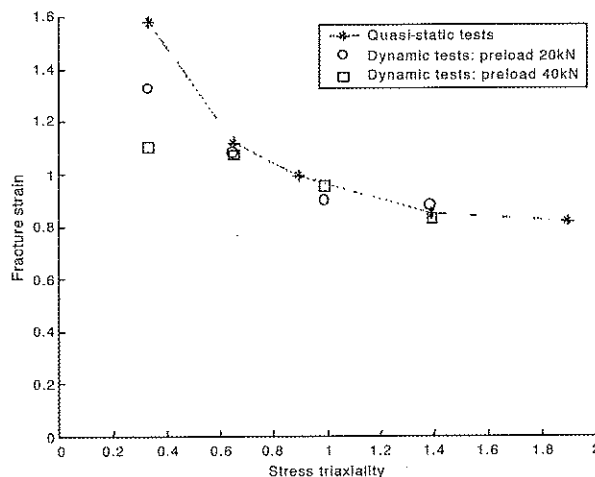
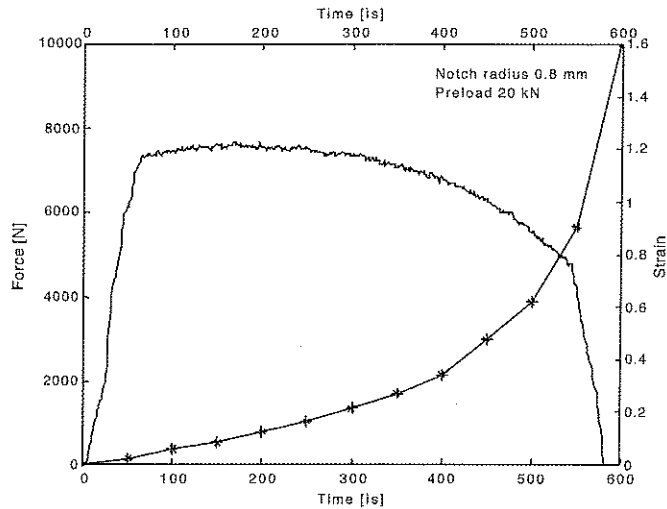
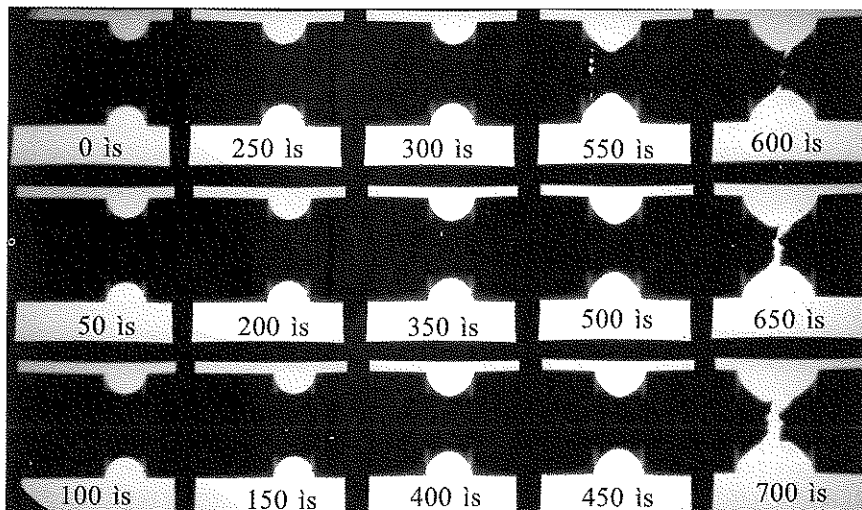


Figure 3: Mean values of fracture strain vs. stress triaxiality (based on initial geometry). Note: Quasi-static test results for smooth and notched specimens and Split Hopkinson Tension Bar tests for smooth specimens from Børvik et al. (14) are included.

Typical diagrams of force F and true strain ϵ against time and high-speed camera images of the notch deformation for one representative test with pre-load force 20 kN are shown Figure 4. In the figure, the first image is just before the incidence pulse reaches the specimen, while the fixed interval between the photographs is 50 is for this particular test. Similar images were obtained for a pre-load force equal to 40 kN. There is good agreement between the points of time of sudden loss of load bearing capacity, due to coalescence of voids (Hancock and Mackenzie 6), and the marked increase of strain which indicates incipient failure. Some of the final strain measurements that are included in the strain-time plots are obtained when macro-cracks have appeared in the specimen, while others are obtained after separation of the specimen parts. This can be seen clearly by studying the presented images that show the geometry of the notched part changes significantly during the deformation process. The notch geometry changes from the original U-shape into something more like a V-shape close to fracture. This indicates that there is a reduction of the notch profile radius R with strain, i.e. as the radius a of the minimum cross-section decreases.



(a) Force and true strain against time



(b) Notch deformation against time ($\Delta t = 50 \mu s$)

Figure 4: Measured force, true strain and notch deformation against time (Test # R0.8-20-5).

NUMERICAL SIMULATIONS

In the present section, non-linear finite element analyses of dynamic tensile tests with smooth and notched axisymmetric specimens are performed, and the results are compared with the experimental data presented above. Previous analyses on axisymmetric notched bars pulled in tension have been carried out by e.g. Hancock and Brown (8), Alves and Jones (21), Needleman and Tvergaard (22) and Mirza et al. (23). The aim of the simulations is to evaluate the constitutive relation and fracture criterion for Weldox 460 steel in cases where strain rate, temperature and stress triaxiality changes during plastic deformation. A parametric study is also carried out to investigate different aspects concerning the identification of fracture criteria under dynamic loading conditions. Since ductile fracture is strongly influenced by the stress state, the influence of adiabatic heating and inertia on the stress triaxiality in the smooth and notched tensile specimens is studied. In addition, the use of Bridgman's analysis (20) to estimate the stress triaxiality in axisymmetric notched specimens and the determination of the fracture criterion based on experimental data are discussed.

The explicit finite element code LS-DYNA (24) was used in all simulations, where both smooth (Børvik et al. 14) and notched (Hopperstad et al. 12) axisymmetric specimens with geometry as shown in Figure 1 were analysed. The notched specimens have initial notch root radius R_0 equal to 0.4, 0.8 and 2.0 mm, while the initial minimum radius a_0 was 1.5 mm in all tests. According to Eq. (2), this gives an initial stress triaxiality in the centre of the notch equal to $1/3$ (smooth), 0.652 ($R_0 = 2.0$ mm), 0.995 ($R_0 = 0.8$ mm) and 1.389 ($R_0 = 0.4$ mm). The specimens were modelled using four-node axisymmetric elements with one-point integration and stiffness-based hourglass control. The specimens were modelled using 20 elements across the radius, giving an element size in the critical gauge region of approximately 0.075×0.075 mm². This element size resulted in 3400 elements (3591 nodes) for the smooth specimens, while 4560 elements (4809 nodes) were used for the notched specimens.

Finite element solutions for problems involving strain localisation and failure tend to be sensitive to the mesh size (see Børvik et al. 14). Introductory simulations of a typical test were therefore performed to evaluate the influence of mesh density. It was found that there is only a slight change in the force-elongation curve when the number of elements across the radius of the specimen is increased from 20 to 40. Further, it was noted that the peak force was almost unaffected by the mesh density, while the elongation to failure was significantly increased when the element mesh became too coarse. Based on these observations, it was decided to run all simulations with 20 elements across the radius. It was also found experimentally that the mechanical behaviour of the notched specimens changed only slightly when the preload of the modified Hopkinson bar apparatus was increased from 20 kN to 40 kN. Thus, only tests with a preload of 20 kN were considered in the dynamic simulations.

The loading was defined by prescribing the elongation at one end of the specimen against time, using the measured elongation-time curves from typical experiments, while the other end was fixed. Severe oscillations occurred in some of the numerical force-time curves, while this was not the case for the experimental curves. The reason seems to be that only the specimen, without the bars, is modelled in the numerical simulations and it follows that the calculated force is disturbed by an elastic wave that propagates along the specimen length and reflects from the specimen ends. The wavelength of the oscillations agrees well with the time it takes for the elastic wave to travel twice from one side of the specimen to the other. In order to reduce the force oscillations, the force signals from the numerical simulations were filtered using a cosine filter with a cut-off frequency of 10000 Hz.

A coupled computational model of viscoplasticity and ductile damage for penetration and impact related problems has been formulated and implemented in LS-DYNA by Børvik et al. (14). The model is based on the work by Johnson-Cook (3,10) and Lemaitre (2), and includes linear thermoelasticity, the von Mises yield criterion, the associated flow rule, isotropic strain hardening, strain-rate hardening, softening due to adiabatic heating, softening due to isotropic damage evolution and a fracture criterion. In this study, the uncoupled version of this model was used in all simulations, i.e. damage has no influence on the strength. Material constants for Weldox 460 E steel are given in Børvik et al. (14,13). It is important at this stage to keep in mind that the experimental results given above have not been used in the identification of the constitutive model and the fracture criterion, and that the material constants are solely based on quasi-static and dynamic tensile test data for Weldox 460 E.

Computed force and true strain against time for R0.8-20-5 are compared with the corresponding experimental results in Figure 5a). The true strain from the numerical simulation is calculated based on

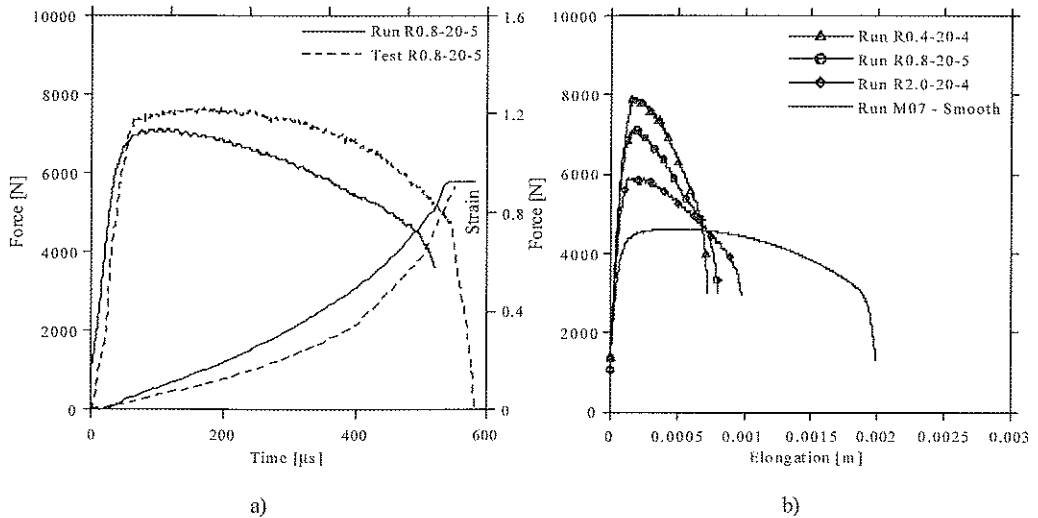


Figure 5: a) Comparison between calculated and measured force and true strain against time for dynamic tension tests with preload 20 kN (Test R0.8-20-5). b) Force-elongation curves from numerical simulations of dynamic tension tests with preload 20 kN.

the diameter reduction in the notched area, i.e. $\varepsilon = 2\ln(d_0/d)$, where d_0 and d are the initial and current diameters of the specimen at minimum cross-section, respectively. In the experiments, the current value of d was based on high-speed camera measurements, which implies that only discrete values were obtained. In the comparison, it should be kept in mind that some distortion of the cross-section appeared in the experiments, i.e. the section developed an oval shape with plastic straining, while axisymmetric deformation is postulated in the simulations, and that the scatter in the experimental results was quite large. The comparison indicates that the finite element model is capable of describing both the force-time curves and true strain-time curves with reasonable accuracy, taking the complexity of the problem into consideration. The main difference seems to be that the numerical model overestimates the material softening compared with the experiments. The figure also reveals that the time to fracture obtained in the simulations is in reasonable agreement with the experimental value. Figure 5b) presents a comparison between the force-elongation curves for smooth and notched specimens from the numerical simulations with preload 20 kN. It is found that the overall agreement between the experimental and numerical results is good. The main trend that the force increases with decreasing notch radius, while the elongation to fracture increases (especially for smooth specimens) with increasing notch radius, seems to be captured in the simulations. However, due to the filtering of the numerical force-time curves, the high peak force observed in some of the tests is smoothed out.

In Figure 6, the deformed geometry of the specimen obtained in the numerical simulations is plotted as white contours on top of the high-speed camera images from the corresponding experimental test (R0.8-20-5). It is seen that the numerical predictions are in good agreement with the experimental behaviour. The numerical simulations are able to describe the geometrical change in the notch, i.e. that the original U-shape of the notch changes into something more like a V-shape close to fracture. Also the fracturing of the specimens is well predicted.

The computed fracture strains are given in Figure 7, where they are compared to average experimental values from tests with preload 20 kN. In the figure, experimental failure strains from quasi-static tension tests (Børvik et al. 14) are given for comparison. The dotted line between the quasi-static data points indicate the failure locus used in the calibration of the failure strain, while the solid vertical lines give the experimental spread in the fracture strains for dynamic tests with preload 20 kN. It is seen that the agreement between experimental and numerical fracture strains is good for notched specimens, and well within the experimental scatter. However, for the smooth specimen the numerical simulation underestimates the experimentally obtained fracture strain. The reason for this seems to be that the initial stress triaxiality was used in the calibration of the fracture strain.

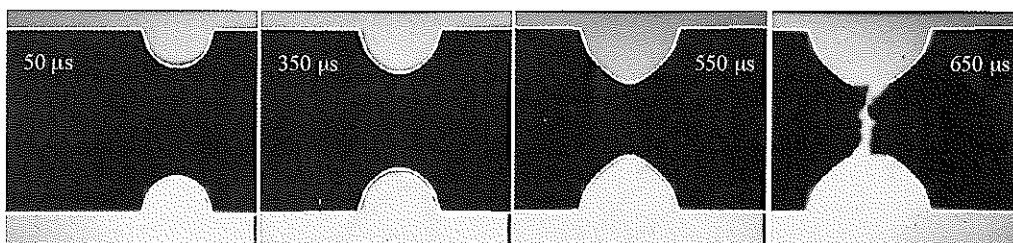


Figure 6: Typical high-speed camera images from a test (Test R0.8-20-5) compared to contours from the numerical simulations showing notch deformation against time.

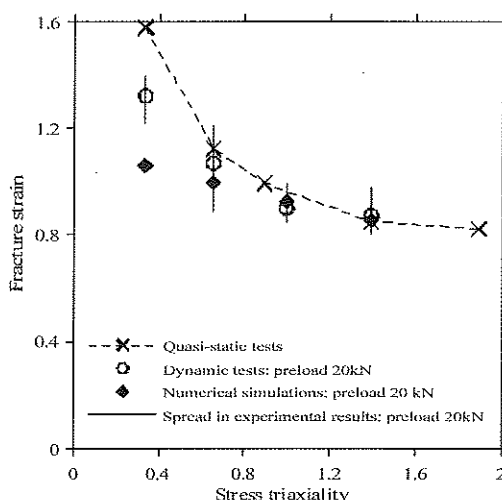


Figure 7: Mean values of fracture strain versus stress triaxiality using Bridgman's analysis (20) on the initial geometry.

In the calibration of the fracture criterion, Bridgman's analysis (20) was used to determine the initial stress triaxiality in the notched specimens. It was assumed that the fracture initiates in the centre of the notch due to the higher stress triaxiality there (e.g. Hancock and Brown (8), Mackenzie et al. (7)), and that the stress triaxiality in the centre of the notch is approximately constant during plastic deformation (Mackenzie et al. 7). In addition, the increase in stress triaxiality in the smooth specimen after necking was neglected. The failure locus was then determined from the measured data. However, it has been found that there are large differences in stress triaxiality in the centre of the neck/notch predicted by numerical simulations and Bridgman's analysis, and that there are significant variations in the stress triaxiality with plastic strain also for the notched specimens. It was also found that the difference in stress triaxiality between quasi-static and dynamic analyses is small, even though the latter includes strain rate effects, inertia and thermal softening due to adiabatic heating.

It is now possible to construct a more accurate failure locus for Weldox 460 E steel based on the measured fracture strain and the computed stress triaxiality in the centre of the neck/ notch. Figure 8 presents the experimental fracture strains ϵ_f plotted against the computed stress triaxiality $\sigma^* = (\sigma_m/\sigma_{eq})$ both for quasi-static and dynamic loading. The experimental data for the quasi-static tests and for the smooth specimen at high rates of strain is from Børvik et al. (14). The failure locus based on the stress triaxiality from Bridgman's analysis on the initial specimen geometry is plotted for comparison. The figure clearly shows that the adopted calibration procedure for the failure criterion, i.e. the use of Bridgman's analysis to estimate the stress triaxiality in the centre of the notch and the assumption of constant stress triaxiality, tends to give very conservative estimates on the ductility of the material.

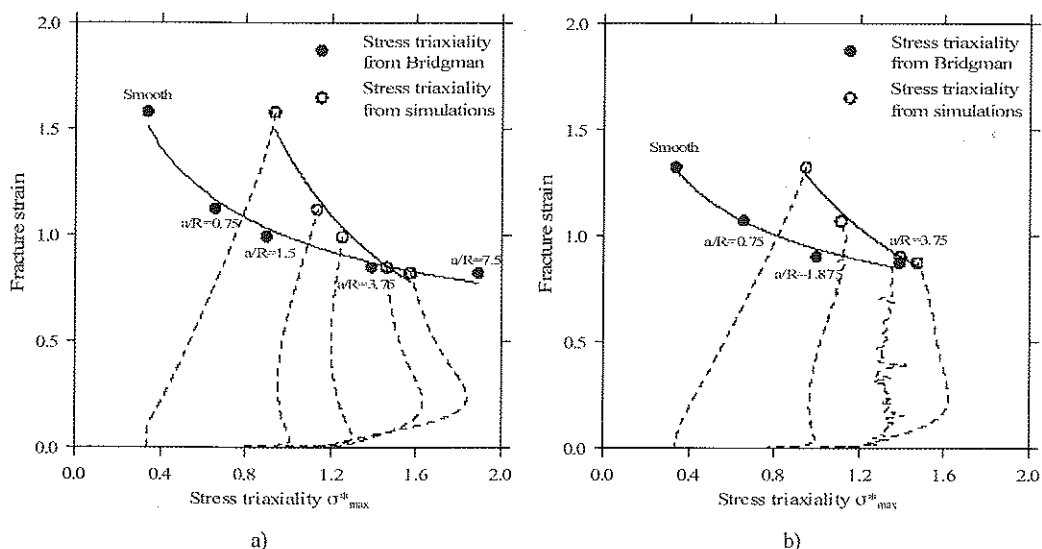


Figure 8: Fracture strain versus stress triaxiality for a) quasi-static and b) dynamic loading conditions. The filled circles indicate the results based on Bridgman's analysis on initial geometry, while the hollow circles give the results based on numerical simulations.

This tendency is particularly strong for low stress triaxiality, which explains the strong underestimation of the fracture strain for the smooth specimen, while the predicted fracture strains for the notched specimen are acceptable. A parametric study was then carried out in order to study this in more detail. This study revealed that the stress triaxiality is nearly insensitive to strain rate and inertia, while the effect of temperature on the stress triaxiality is somewhat stronger but not very significant. This indicates that the variation in failure strain obtained in tests with varying temperature and strain rates is caused mainly by the temperature and strain rate variation and not by variations in the stress triaxiality. A more detailed description of the parametric study is given in Børvik et al. (13). It should finally be mentioned that even though there are some discrepancy between the numerical and experimental results using the procedure given above (see Figure 5a)), the constitutive model given in (14) has been used successfully in numerical simulations of projectile penetration and perforation of Weldox 460 E steel plates (14,16,25). This illustrates that even though the model fails to describe the local material behaviour in detail, it might give good estimates of the global structural response.

ACKNOWLEDGMENTS

The authors would like to acknowledge the Norwegian Defence Estate Agency, Research and Development Section, for their generous support of this study.

REFERENCES

1. J. Harding, "The development of constitutive relationships for material behaviour at high rates of strain", *Inst. Phys. Conf. Ser. No 102, Session 5*, 189-202, 1989.
2. J. Lemaitre, "A course on damage mechanics", Springer-Verlag, 1992.
3. G.R. Johnson and W.H. Cook, "A constitutive model and data for metals subjected to large strains, high strain rates and high temperatures", In: *Proceedings of the 7th International Symposium on Ballistics, The Hague Netherlands*, 541-547, 1983.
4. F.J. Zerilli and R.W. Armstrong, "Dislocation-mechanics-based constitutive relations for material dynamics calculations", *Journal of Applied Physics*, 61 (5), 1816-1825, 1987.
5. A.S. Khan and R. Liang, "Behaviors of three BCC metal over a wide range of strain rates and temperatures: experiments and modeling", *International Journal of Plasticity*, 15, 1089-1109, 1999.

6. J.W. Hancock and A.C. Mackenzie, "On the mechanisms of ductile failure in high-strength steels subjected to multi-axial stress-states", *Journal of the Mechanics and Physics of Solids*, 24, 147-169, 1976.
7. A.C. Mackenzie, J.W. Hancock and D.K. Brown, "On the influence of state of stress on ductile failure initiation in high strength steels", *Engineering Fracture Mechanics*, 9, 167-188, 1977.
8. J.W. Hancock and D.K. Brown, "On the role of strain and stress state in ductile failure", *Journal of the Mechanics and Physics of Solids*, 31, 1-24, 1983.
9. F.M. Beremin, "Experimental and numerical study of the different stages in ductile rupture: Application to crack initiation and stable crack growth", in S. Nemat-Nasser (ed.) *Three-Dimensional Constitutive Relations and Ductile Fracture*, North-Holland Publishing Company, 185-205, 1981.
10. G.R. Johnson and W.H. Cook, "Fracture characteristics of three metals subjected to various strains, strain rates, temperatures, and pressures", *Engineering Fracture Mechanics*, 21 (1), 31-48, 1985.
11. J.R. Rice and D.M. Tracey, "On the ductile enlargement of voids in triaxial stress fields", *Journal of the Mechanics and Physics of Solids*, 17, 210-217, 1969.
12. O.S. Hopperstad, T. Børvik, M. Langseth, K. Labibes and C. Albertini, "On the Influence of Stress Triaxiality and Strain Rate on the Behaviour of Structural Steel. Part I. Experiments", in press, *European Journal of Mechanics – A/Solids*, 2002.
13. T. Børvik, O.S. Hopperstad and T. Berstad, "On the Influence of Stress Triaxiality and Strain Rate on the Behaviour of Structural Steel. Part II. Numerical Simulations", in press, *European Journal of Mechanics – A/Solids*, 2002.
14. T. Børvik, O.S. Hopperstad, T. Berstad and M. Langseth, "A computational model of viscoplasticity and ductile damage for impact and penetration", *European Journal of Mechanics A/Solids*, 20, 685-712, 2001.
15. T. Børvik, J.R. Leinum, J.K. Solberg, O.S. Hopperstad and M. Langseth, "Observations on Shear plug formation in Weldox 460 E steel plates impacted by blunt-nosed projectiles", *International Journal of Impact Engineering*, 25, 553-572, 2001.
16. T. Børvik, M. Langseth, O.S. Hopperstad, K.A. Malo, "Ballistic penetration of steel plates", *International Journal of Impact Engineering*, 22, 855-886, 1999.
17. C. Albertini and M. Montagnani, "Testing techniques based on the split Hopkinson bar", *Inst. Phys. Conf. Ser. No 21*, 1974.
18. U.S. Lindholm and L.M. Yeakley, "High strain-rate testing: tension and compression", *Experimental mechanics*, 8, 1-9, 1968.
19. G. E. Dieter, "Mechanical Metallurgy", McGraw Hill, 1988.
20. P.W. Bridgman, "Studies in large plastic flow and fracture", McGraw-Hill, New York, 1952.
21. M. Alves and N. Jones, "Influence of hydrostatic stress on failure of axisymmetric notched specimens", *Journal of the Mechanics and Physics of Solids*, 47, 643-667, 1999.
22. A. Needleman and V. Tvergaard, "An analysis of ductile rupture in notched bars", *Journal of the Mechanics and Physics of Solids*, 32 (6), 461-490, 1984.
23. M.S. Mirza, D.C. Barton and P. Church, "The effect of stress triaxiality and strain-rate on the fracture characteristics of ductile materials", *Journal of Materials Science*, 31, 453-461, 1996.
24. LS-DYNA, "LS-DYNA Keyword User's Manual", Version 960, Volume I and II, 2001.
25. T. Børvik, O.S. Hopperstad, T. Berstad and M. Langseth, Numerical Simulation of Plugging Failure in Ballistic Penetration, *International Journal of Solids and Structures*, 38 (34-35), 6241-6264, 2001.

Behavior of soda-lime glasses impacted by a soft bullet: experimental and numerical investigations

X. Brajer,^{1,3} F. Hild¹

¹LMT-Cachan, ENS de Cachan / CNRS-UMR 8535 / Université Paris 6
61 avenue du president Wilson F-94235 CACHAN Cedex, France

S. Roux²

²SVI, UMR CNRS / Saint-Gobain, 39 quai Lucien Lefranc, F-93303 Aubervilliers Cedex, France

R. Gy³

³Saint-Gobain Recherche, 39 quai Lucien Lefranc, F-93303 Aubervilliers Cedex, France

ABSTRACT

This work presents an anisotropic damage model and its non-local extension to deal with fragmentation induced by impact loadings. Discrete cracks are described via non-local damage parameters under the hypothesis of a cylindrical divergent wave. The damage model is based on quasi-static properties of flaw distributions and enables us to reproduce cracking patterns obtained in edge-on-impact tests. Different regimes such as single or multiple fragmentation appear and can be explained by this approach. Moreover, the damage front speed found experimentally is related to these fragmentation regimes and is reproduced numerically.

INTRODUCTION

The use of brittle materials in armors requires studies on their response to impact [1,2]. For example, glass can be used against ballistic threats (e.g., in windshields). Furthermore, multi-layered armor materials are used (with polycarbonate, PC, as back layer and polyurethane, PU, between glass plies) to optimize the ballistic performance. The use of PU and PC is essential to maintain the fragments when glass is impacted, especially for the back layer that ensures the structural integrity and absorbs part of the impact energy.

The work presented herein aims at modeling the fragmentation of soda-lime glasses impacted by a 44 Magnum bullet. Edge-on-impact (EOI) configurations [3,4] allow for the visualization of cracking during the experiment by using a high-speed camera or thereafter when a sarcophagus configuration is utilized. Different cracking patterns are observed. The present work intends describing numerically the cracking features observed experimentally. Some phenomenological models exist for glass (e.g., [5]) but the relationship with the microstructure is remote. Based upon a dynamic fragmentation analysis, an anisotropic damage model is introduced. The latter uses characteristic parameters that depend on material properties (i.e., distribution of surface flaws in glass [4]) and loading conditions. 3D-FE simulations are performed and analyzed with respect to experimental observations. A non-local extension accounts for macrocrack propagation in a finite element mesh. These developments are implemented in a simplified explicit code to model cylindrical divergent waves describing edge-on-impacts. The transition between multiple fragmentation close to the impact zone and single fragmentation far from impact is studied with the non-local version of the model. Last, a sensitivity analysis is performed to study the mesh-dependence of the results.

EXPERIMENTAL RESULTS

Bullets are fired by a gun and impact a glass target of surface $100 \times 100 \text{ mm}^2$ and of thicknesses varying between 8 and 15 mm. The projectile speed is measured by two optical cells one meter apart. An "open" configuration is used, enabling for in-situ observations by utilizing a high-speed camera. The interframe time can be as low as $0.2 \mu\text{s}$. When the bullet reaches the second cell, flashlights are triggered. When the bullet impacts the target, it activates the camera to take pictures. According to the European standard EN1063 [6], one of the threats for armors is a "soft" bullet (*i.e.*, magnum 44) further referred to as "BR4", traveling at a moderate speed of 430m/s. "BR4" bullets have a soft core made of lead and an envelope of brass wire.

Typical results obtained by using the high-speed camera are shown in Fig. 1. When the bullet impacts the glass sample and induces cracking a few microseconds thereafter, dark zones appear on pictures. They correspond to damaged zones and glass is no longer transparent. One can observe the damage zone propagating in the sample and the crack front is faithfully identified by this type of inspection and consequently propagation velocities can be determined with a good accuracy. After impact, fragments of the impacted sample are scattered and the BR4 core (made of lead) is fully sublimated.

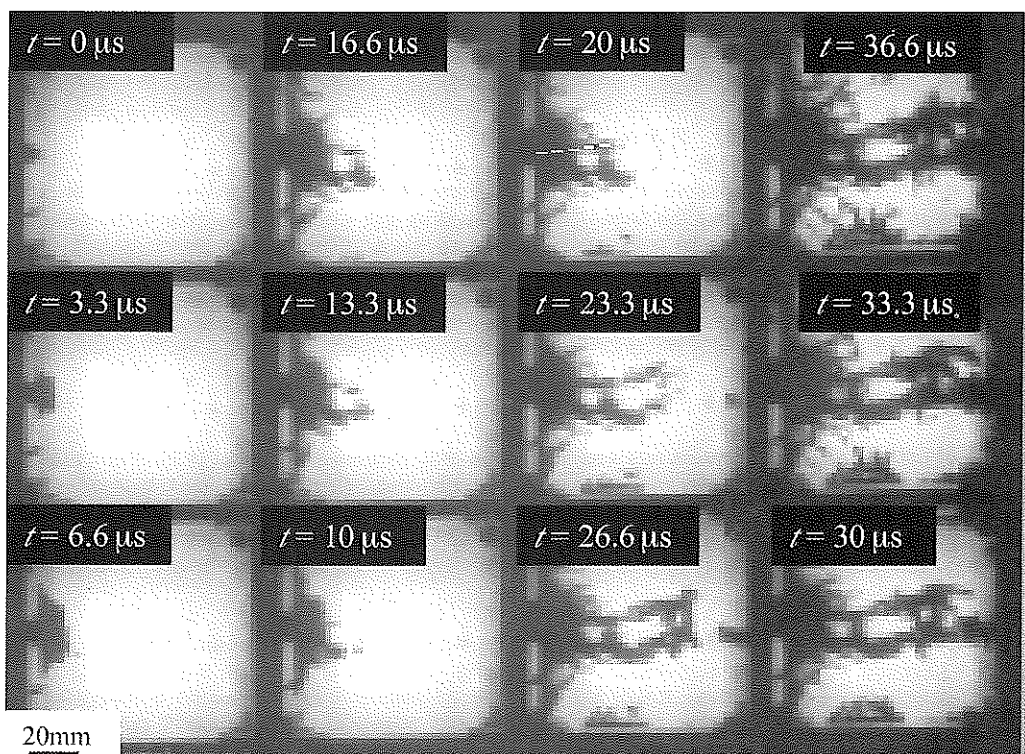


Fig. 1: Sequence of pictures of the impact of a 44 Magnum bullet (velocity = 430 m/s) on a $100 \times 100 \times 8 \text{ mm}^3$ soda-lime target. The dark zones correspond to the damaged zones. The dotted line shows the main crack used in Fig. 8 for comparison between predicted and experimental results.

A "sarcophagus" configuration [7] that maintains fragments together on a soda-lime target of size $100 \times 100 \times 10 \text{ mm}^3$ is also used (Fig. 2). After impact, a hyper-fluid resin infiltrates the cracks and maintains the fragments together to observe the impacted sample. The projectile does not penetrate the target. There are different zones that characterize the interaction between the projectile and the target. A first zone in the vicinity of the impact is totally comminuted. A second area displays a high

density of radial and orthoradial cracks. A third zone appears in which long radial cracks propagate. These zones correspond to different cracking features in brittle materials [5,7]:

- multiple fragmentation in the first zone with mainly closed cracks (glass is totally comminuted; the size of thinner fragments can be estimated to a few micrometers), this fragmentation is caused by high shear stresses just under the contact zone;
- multiple fragmentation under mode I loading in the second zone, due to high tensile stresses induced by the radial motion of the initial compressive wave;
- single fragmentation in the third zone (consisting only in radial macrocracks).

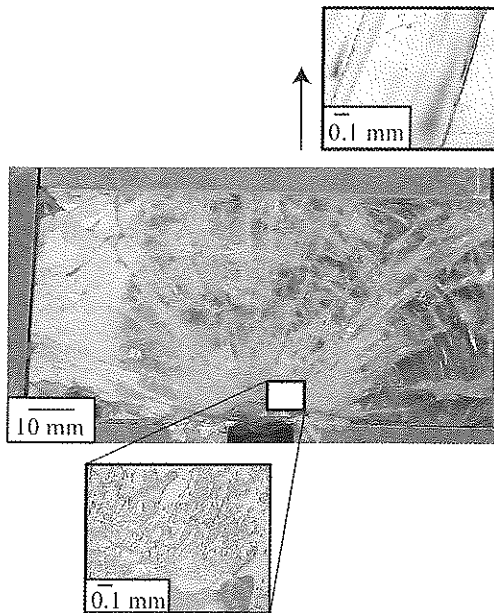


Fig. 2: Cracking pattern of impacted soda-lime glass (44 Magnum bullet, $V = 330$ m/s) obtained with a sarcophagus configuration. Near the impact, the material is fully comminuted. Far from impact, long cracks are observed.

AN ANISOTROPIC DAMAGE MODEL

When a bullet impacts a glass target, a compressive stress wave propagates ahead of the impacted area, with the speed of longitudinal acoustic waves [8]. The radial displacement also induces hoop tensile stresses that nucleate defects inducing microcracking. The latter can be described by an anisotropic damage model [9]. The level of stress and stress rate determine the type of fragmentation, namely single or multiple fragmentation.

A so-called multi-scale model [10] is used to determine the transition between the single / multiple fragmentation regimes. This fragmentation model accounts for quasi-static and dynamic loading conditions. It is assumed that the flaw population leading to damage (described by Weibull parameters [11]) and failure is identical when the material is subjected to quasi-static and dynamic loading conditions. The Weibull parameters used for soda-lime glasses are either surface [12] or bulk [13] parameters. With a Weibull model, the defect density λ_f is modeled as a power law function so that the cumulative failure probability P_f is written as

$$P_F = 1 - \exp\left[-Z_{eff}\lambda_t(\sigma_F)\right] \text{ with } \lambda_t(\sigma_F) = \lambda_0\left(\frac{\sigma_F}{S_0}\right)^m \quad (1)$$

where σ_F is the failure stress, Z_{eff} the effective surface or volume, m the Weibull modulus and S_0^m / λ_0 the Weibull scale parameter. Under dynamic loading conditions, a crack shields other defects that would nucleate because of the dynamic growth of a domain of measure Z_0 where stresses are relaxed to zero. The cracking pattern then results from a competition between obscuration (or shielding) phenomena and the loading rate (Fig. 3). The density of flaw λ_t can be divided into two parts, namely λ_b the crack density and λ_{obsc} the obscured flaw density. The probability of obscuration can be expressed as an extension of the classical Weibull law [9]

$$P_o = 1 - \exp\left(-\hat{Z}\lambda_t(\sigma)\right) \text{ with } \hat{Z}\lambda_t(\sigma) = \int_0^T Z_o(T-t)\frac{d\lambda_t}{dt} dt = Z_o * \dot{\lambda}_t \quad (2)$$

where \hat{Z} is the measure of the mean obscuration zone, $*$ the convolution product, and Z_o the size of the obscuration zone, which is dependent on the crack propagation velocity kC_0 , a shape factor S and the space dimension n . $Z_o(t) = S(kC_0 t)^n H(t)$, where $H(\cdot)$ is the Heaviside step function. If the loading rate is small enough, \hat{Z} becomes equal to the entire representative volume or surface, and yields the Weibull failure probability (1).

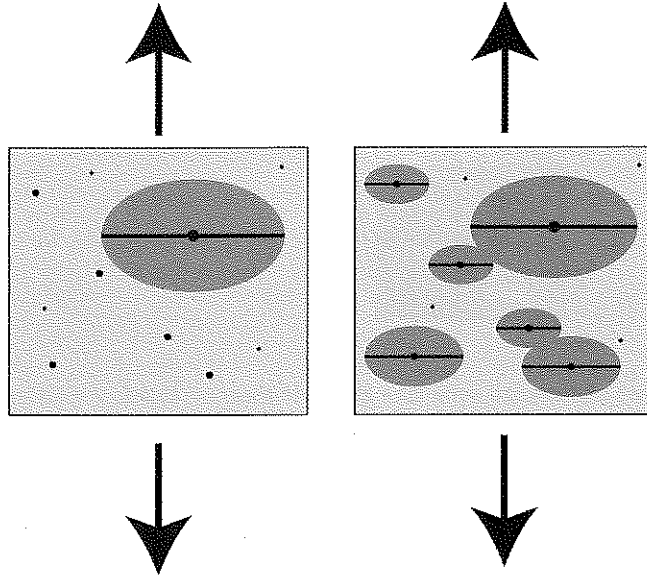


Fig. 3: Schematic of a representative element in tension. The dots depict defects that are potential cracking sites. Left) The tensile stress rate is low; one single crack is nucleated, leading to the entire obscuration of the element. Right) The tensile stress rate is high; there is a competition between the increase of stress and the obscuration of the element. Several cracks are nucleated.

The kinetics of the obscuration probability can be derived from Eq. (2). When $n = 3$

$$-\frac{d^3}{dt^3} \ln(1 - P_o) = (\hat{Z}\dot{\lambda}_t) = \ddot{Z}_o * \lambda_t = 6S(kC_0)^3 \lambda_t \quad (3)$$

By averaging over a representative zone, the macroscopic principal stress Σ_i is equal to $\sigma_i(1 - D_i)$, where σ_i is the local stress. The damage variable D_i is equal to P_0 associated to a given cracking normal, and the kinetic law of each damage variable D_i in a 3D situation can be derived from Eq. (3)

$$\frac{d^2}{dt^2} \left(\frac{1}{1 - D_i} \frac{dD_i}{dt} \right) = 6S(kC_0)^3 \hat{\lambda}_i(\sigma_i) \quad \text{when } \sigma_i > 0 \quad \text{and} \quad \frac{d\sigma_i}{dt} > 0 \quad (4)$$

where the modified defect density $\hat{\lambda}_i$, associated to the Weibull model is expressed as [10]

$$V_{FE} \hat{\lambda}_i(\sigma_i) = \begin{cases} 0 & \text{if } \sigma_i < \sigma_F \\ \max \left[V_{FE} \lambda_0 \left(\frac{\sigma_i}{S_0} \right)^m, 1 \right] & \text{otherwise} \end{cases} \quad (5)$$

where V_{FE} is the volume of the considered finite element. The value σ_F is a stress obtained by random selection of a real P_F lying between 0 and 1 and by applying Eq. (1) when $V_{FE} = Z_{off}$. Equation (5) expresses the average number of broken defects within a volume V_{FE} which is equal to 0, 1 or greater than 1. The integration of Eqs. (3) and (4) usually assumes zero initial conditions. The compliance tensor \underline{S} is written in the principal frame

$$\underline{S} = \frac{1}{E} \begin{bmatrix} \frac{1}{1 - D_1} & -\nu & -\nu \\ -\nu & \frac{1}{1 - D_2} & -\nu \\ -\nu & -\nu & \frac{1}{1 - D_3} \end{bmatrix} \quad (6)$$

where E is the Young's modulus of the undamaged material and ν the corresponding Poisson's ratio. Two different fragmentation regimes can be obtained for brittle materials (Fig. 4):

- For high stress rates, multiple fragmentation occurs and the behavior becomes more and more deterministic (and size effects disappear);
- For low stress rates, the weakest link hypothesis applies and the strength is scattered.

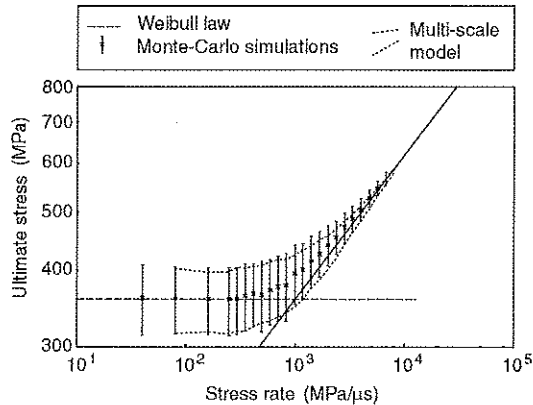


Fig.4: Ultimate strength vs. stress rate for a SiC-100 ceramic. The dots and error bar represent results obtained by Monte Carlo simulations (500 realizations / point) and their standard deviation [9].

The transition between single and multiple fragmentation can be estimated by the intersection between the weakest link solution (under quasi-static loading conditions, see dashed horizontal line of Fig. 4) and the multiple fragmentation solution (see solid line of Fig. 4). The ultimate stress reached in tension is a function of the stress rate as it is observed experimentally not only for glass but also for rocks, concrete and ceramics [14].

NUMERICAL SIMULATIONS WITH A MULTI-SCALE DAMAGE MODEL

Materials of the bullets are assumed to behave elasto-plastically. Glass is supposed to be elasto-plastic ($E = 70$ GPa, $\nu = 0.22$) with an HEL (Hugoniot elastic limit) evaluated at 10 GPa. The FE mesh accounts for a surface layer of thickness $200 \mu\text{m}$ endowed with Weibull parameters $m = 4$, $S_0 = 50$ MPa, $S_{eff} = 50 \text{ cm}^2$ [12], whereas the bulk of the tile is characterized by intrinsic flaws with Weibull parameters $m = 30$, $\sigma_0 = 3$ GPa, $V_{eff} = 10^{-3} \text{ mm}^3$ [13]. As a consequence, damage is mainly nucleated on external surfaces of the samples. Figure 5 shows that multiple fragmentation appears in the first half of the target and along the side. This 3D computation is expected to describe accurately the initial stage of bullet impact. In the sequel, we will make use of a contact force history determined from this computation to address later stages of damage developments. This simulation does not account for the propagation of long cracks but only for crack nucleation illustrated in Fig. 5. This limitation can be overcome by the introduction of the following non-local approach where crack extension will be allowed to extend beyond single finite elements.

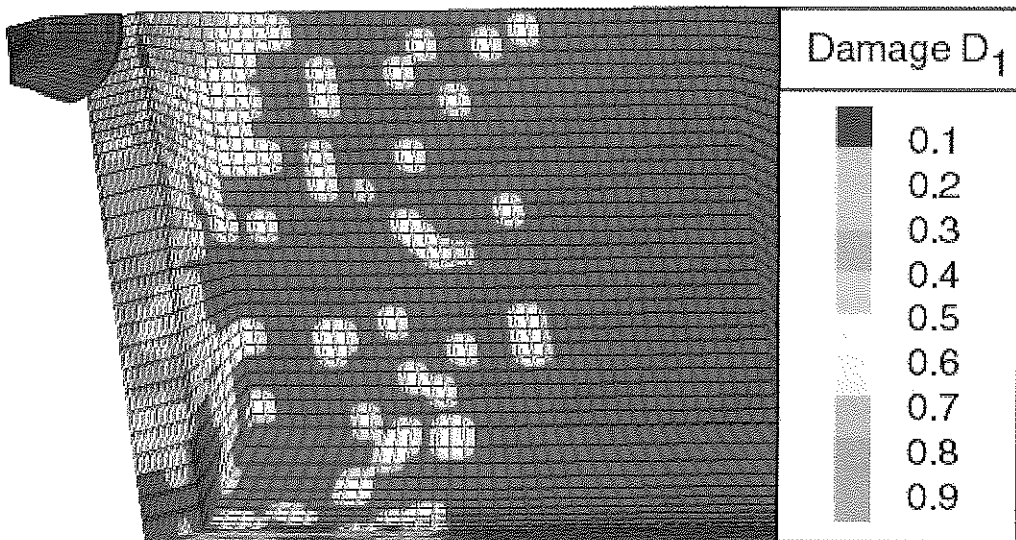


Fig. 5: FE simulations of one quarter of an EOI configuration. The damage variable D_1 associated with the first principal stress shows the location of flaw nucleations.

A NON-LOCAL APPROACH

Let now consider the propagation of long cracks. For the sake of simplicity, it is performed in a cylindrical divergent wave configuration. The stress state is two-dimensional (i.e., radial and hoop stresses) and the displacement is only radial. New damage parameters Δ_1 are introduced so that the macroscopic principal stress Σ_1 is now equal to $\sigma_1(1 - D_1)(1 - \Delta_1)$, where σ_1 is the local stress. Fracture propagation is described by the occultation zone that grows at a constant speed $kC_0 = 1500 \text{ m/s}$ [4]. Again, the damage variables Δ_1 are equal to the ratio between the occultation volume and the total volume in one element (Fig. 6) associated to the three cracking directions. The kinetics of Δ_1 is obtained by direct derivation of $S(kC_0(T-t))^3 / V_{FE}$ (when $n = 3$)

$$\frac{d^2}{dt^2} \left(\frac{d\Delta_1}{dt} \right) = 6\tilde{\lambda}_1(\sigma_1) S(kC_0)^3 \quad (6)$$

where $\bar{\lambda}_i$ is equal to $1/V_{FE}$, which means that a *single* mesocrack propagates in the element. One can note that this kinetics is identical to that used in the case of multiple fragmentation (4) except for the factor $1/(1-D_i)$ which accounts for overlappings of obscuration zones. All elements where $\Delta_i \neq 0$ are listed and they numerically correspond to a crack of length a equal to the length of all elements traversed by the latter. In practice, the local damage variables start to grow, i.e., $D_i \neq 0$ (Fig. 6a). When D_i reaches a critical value D_c corresponding to coalescence in the considered element, Δ_i starts to grow towards the neighboring element (Fig. 6b). The size of the crack is followed by computing the size of the obscuration zone. Two cases can occur:

- the stress at the tip of the crack is high enough to let it propagate (i.e., $\sigma_i(1-D_i)\sqrt{a} > K_c$, where K_c denotes the toughness of the material) and the element begins to crack and the kinetics of Δ_i is given by Eq. (6);
- the stresses are not high enough; no propagation occurs in the neighborhood of the initially damaged element.

This process is repeated as the stress wave invades the material. The macrocrack propagation can therefore be the result of a series of “mesoscopic” coalescences when the damage variables D_i are high enough ($D_i \geq D_c$). These multiple events induce a velocity of the crack front that can be greater than kC_0 . A multiple fragmentation regime is observed. Conversely, the propagation conditions can be satisfied (i.e., $\sigma_i(1-D_i)\sqrt{a} > K_c$) even though the local values of D_i are less than D_c . A single fragmentation regime is observed.

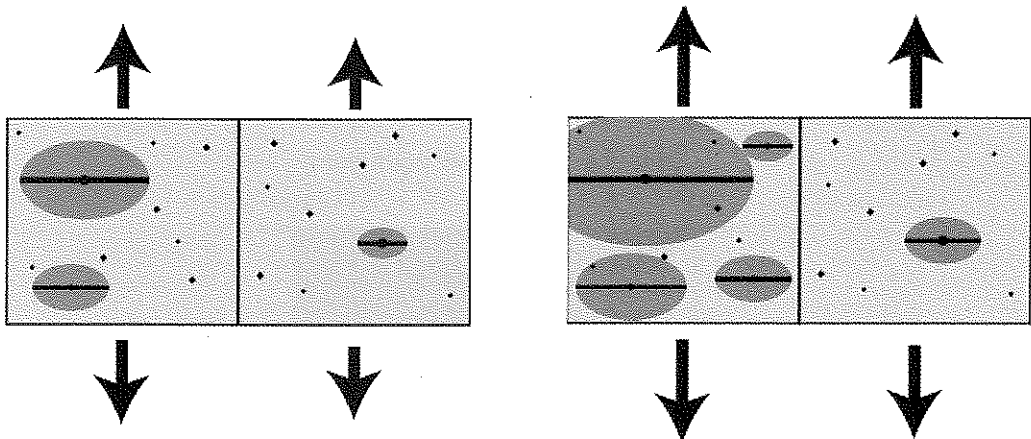


Fig. 6: Schematic of a propagation of a long crack via the non-local damage model. The first step (left) corresponds to distributed damage modeled by local variables D_i . The second step (right) corresponds to coalescence in one element described by non-local damage variables Δ_i .

NUMERICAL SIMULATIONS WITH THE NON-LOCAL DAMAGE MODEL

The previous 3D simulations help us in determining a contact force between the 44 Magnum bullet and the surface of the target (Fig. 7). During the first microseconds after impact, the initial shock wave propagates followed by the collapse of the projectile so that the contact force increases. The following simulations use an in-house FE code simulating the propagation of a cylindrical divergent wave [15]. The projectile impact is described via a pressure induced by the contact force determined by the 3D FE simulations.

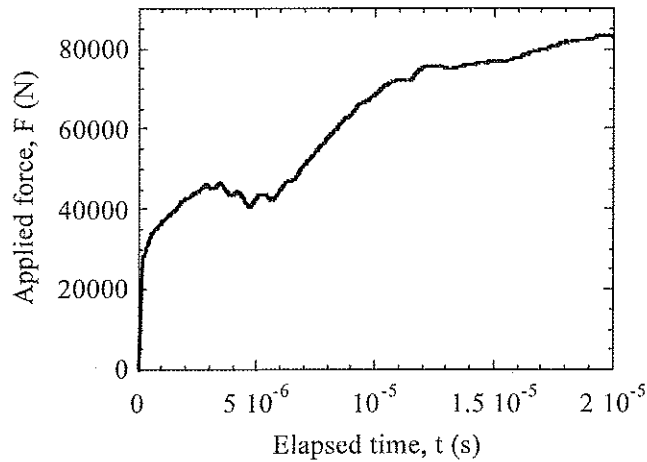


Fig. 7: Contact force vs. time for an impact of a 44 Magnum bullet on a soda-lime target determined by a 3D FE simulation.

Figure 8 shows the results obtained by using the damage variable Δ_I . In the first part of the interaction, the stress level induced by the compressive wave are high enough to nucleate several defects in each finite element and the damage front velocity is related to the speed at which the induced tensile (hoop) stress develops. The zigzagged profile corresponds to the multiple coalescences. Later, as observed in post-mortem analyses of impacted samples, long cracks begin to propagate at a *constant* speed $kC_0 \approx 1500\text{m/s}$ with no further nucleation. This transition could not have been assessed by using a local damage model alone.

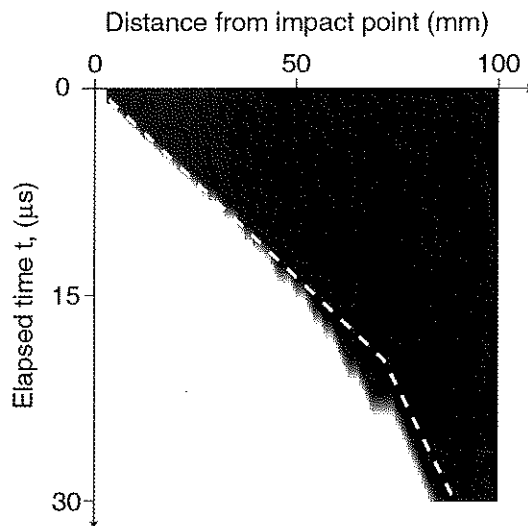


Fig. 8: Space-time diagram of the damage variable Δ_I obtained by using the non-local model. The white zone corresponds to a damage Δ_I greater than 0.85. It is compared with an experimental crack front velocity evaluated from Fig. 1 (dotted line).

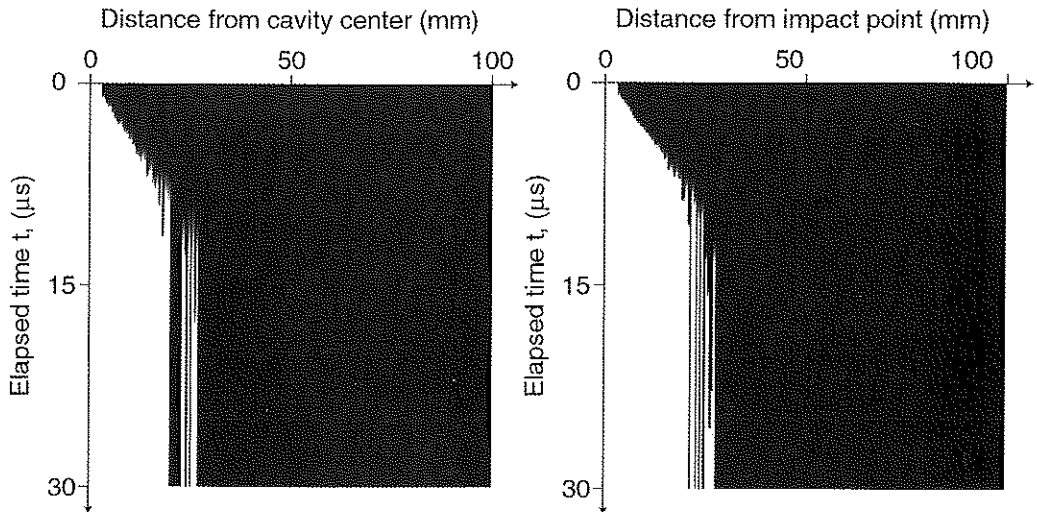


Fig. 9: Comparison of the space-time diagrams of the damage variable Δ_f for two different meshes. Left) 4 elements per mm. Right) 16 elements per mm.

Moreover, the model is quasi mesh-independent except for the scatter induced by the multi-scale damage model. This result is obtained when a cavity is subjected to a pressure step of -6 GPa (Fig. 9). Two different mesh densities are used and the space-time diagrams are virtually identical.

CONCLUSION

Edge-on-impact tests have been performed on soda-lime glass by using a soft bullet. These experiments allow for a visualization of the cracking pattern by using a high-speed camera or a sarcophagus configuration. Fragmentation of impacted soda-lime glass is mainly caused by the growth of cracks nucleated on the surface of glass. Far from the impact surface, propagation of long cracks is always observed.

Numerically, the zone of multiple fragmentation is reproduced with the help of a local anisotropic damage model based on a fragmentation analysis. Since the population of defects is the key parameter that governs the cracking pattern, Weibull parameters representative of the surface and the bulk have been used. Since the propagation of long cracks is a non-local phenomenon for classical FE simulation, the zone obscured by one macrocrack is used to follow its propagation. This is achieved through a non-local damage model coupled with the previous one.

1D simulations prove that the different zones observed in edge-on-impact tests can be reproduced by the present approach. A local approach only gives the initiation sites and is not able to capture the macrocrack formation. The different regimes of damage front velocities observed experimentally are found in the simulations under the hypothesis of a cylindrical divergent wave.

REFERENCES

1. J. Cagnoux, *Déformation et ruine d'un verre Pyrex soumis à un choc intense : Étude expérimentale et modélisation du comportement*, Thèse d'état, University of Poitiers, France (1985).
2. den Reijer, *Impact on ceramic faced armour*, Ph.D. dissertation, Technische Universiteit Delft, the Netherlands (1991).
3. U. Hornemann, J.F. Kalthoff, H. Rothenhäusler, H. Senf and S. Winkler, *Experimental Investigation of Wave and Fracture Propagation in Glass-Slabs Loaded by Steel Cylinders at High Impact Velocities*, EMI report **E 4/84**, Weil am Rhein, Germany (1984). See also: E. Strassburger and H. Senf, *Experimental Investigation of Wave and Fracture Phenomena in Impacted Ceramics and Glasses*, ARL report **ARL-CR-214** (1994).

4. X. Brajer, P. Forquin, R. Gy and F. Hild, *The role of Surface and Volume Defects in the Fracture of Glass under Quasi-Static and Dynamic loading*, J. Non-Cryst. Solids, accepted (2002).
5. G.R. Johnson and T.J. Holmquist, *An Improved Computational Constitutive Model for Brittle Materials*, High Pres. Sci. Tech. **2** (1992) 981-984.
6. NF EN1063 standard: *Verre dans la construction. Vitrage de sécurité. Mise à essai et classification de la résistance à l'attaque par balle*.
7. C. Denoual, *Approche probabiliste du comportement à l'impact du carbure de silicium : application aux blindages moyens*, PhD thesis, ENS de Cachan, France (1998). See also: C. Denoual, C. E. Cottenot and F. Hild, *Analysis of the Degradation Mechanisms in an Impacted Ceramic*, in: S. C. Schmidt, D. P. Dandekar and J. W. Forbes, eds., Proc. Shock Compression of Condensed Matter, (AIP Press, New York (USA), 1998), 427-430.
8. K.F. Graff, *Wave Motion in Elastic Solids*, (Clarendon Press, Oxford (UK), 1975).
9. C. Denoual and F. Hild, *A Damage Model for the Dynamic Fragmentation of Brittle Solids*, Comput. Meth. Appl. Mech. Eng. **183** (2000) 247-258.
10. C. Denoual and F. Hild, *Dynamic Fragmentation of Brittle Solids: A Multi-Scale Model*, Eur. J. Mech. A/Solids **21** (2002) 105-120.
11. W. Weibull, *A Statistical Theory of the Strength of Materials*, Roy. Swed. Inst. Eng. Res. **151** (1939).
12. D.R. Oakley, *An Empirical Study of the Effect of Stressed Area on the Strength of Float Glass Surfaces*, J. Non-Cryst. Solids **196** (1996) 134-138.
13. R. Gy and C. Guillemet, *Characterization of a mode of rupture of glass at 610°C*, in L.D. Pye, W.C. La Course and H.J. Stevens, eds., *The Physics of Non-Crystalline Solids*, (Taylor & Francis, London (UK), 1992).
14. F. Hild, C. Denoual, P. Forquin and X. Brajer, *On the Probabilistic-Deterministic Transition involved in a Fragmentation Process of Brittle Materials*, Comput. & Struct., accepted (2002).
15. C. Denoual, C. E. Cottenot and F. Hild, *On the Identification of Damage during Impact of a Ceramic by a Hard Projectile*, Proc. 16th International Conference on BALLISTICS, (APDS, Arlington, VA (USA), 1996), 541-550.

Modelling Dynamic Material Response: The Impact of Numerical Schemes

P Church, I Cullis

Modelling & Explosive Application, QinetiQ, Mod Fort Halstead, Sevenoaks, Kent TN14 7BP, United Kingdom

ABSTRACT

The simulation of dynamic material response requires accurate numerical schemes, constitutive and fractures models. These models need to be integrated within the numerical scheme in a self consistent fashion to accurately represent the observed material behaviour, particularly with regard to meso-macro scale behaviour. This paper addresses the issues associated with Lagrange and Eulerian numerical schemes, which need to be understood and correctly formulated in order to develop a predictive simulation capability. These issues are illustrated by a range of validation tests, which identify the importance of the effect of the numerical scheme. Future approaches being developed within QinetiQ are then described to address some of these fundamental issues.

INTRODUCTION

Accurate constitutive models and the onset of fracture, its growth and post failure behaviour limit most computational methods for engineering materials that experience large stresses and strains. Simple empirical fracture models have existed for a number of years and have been successfully applied in high velocity impact calculations. The most significant problem is that different criteria apply under different loading conditions and great care must be exercised when attempting to model material fracture. Any fracture algorithm must ultimately be capable of recognizing not only the loading condition but also changes in loading condition. The other important consideration is the recognition of the importance of the micro-mechanical basis for a proper treatment of brittle, ductile and shear failure. Without this a comprehensive treatment of fracture with a single universally applicable model will not be possible. Our research over the past 15 years has been aimed at achieving this goal.

The challenge for the numerical methods and material algorithms is the range of fracture features that are observed experimentally. These include:

Static fracture characterized by one fracture or crack, which propagates to separate the material. Fragments form from the branching of the original crack.

Dynamic fracture characterized by rapid nucleation of micro-voids or micro-cracks at a large number of locations, which then grow and coalesce to form one or more continuous fracture surfaces.

Damage growth that leads to failure characterized by a function of the applied stress history. There is no instantaneous jump from undamaged to a fully separated material. As the level of damage increases the material is weakened, its stiffness is locally reduced with associated changes in stress wave propagation.

MATERIAL & FRACTURE MODELS

Work in QinetiQ over the past 15 years has demonstrated that the simulation of fracture processes cannot be isolated to the definition of a fracture model. The fracture process is greatly influenced by the deformation model, which dictates the stress system and degree of localization within the material [1]. For a metal these are primarily a function of strain, strain rate and temperature and our research

has developed advanced validated constitutive and fracture models capable of reproducing this behaviour [2]. The localization and the state of stress then drive the failure process leading to fracture of the material. Our most significant advance in this area has been the development of computationally efficient algorithms capable of reproducing observed path dependent behaviour, both for deformation and ductile fracture, due to Goldthorpe [3,4].

In particular the use of a generalized path dependent approach adapted to ductile fracture is novel and reduces the damage evolution to a physically based integral form. This interim approach expresses the void growth as a function of stress triaxiality and strain increment and is defined as follows:

$$S_c = 0.67 \int_0^{\epsilon} \exp[1.5 \sigma_n - 0.04 \sigma_n^{-1.5}] d\epsilon \quad (1)$$

where S_c = critical damage threshold

σ_n = Pressure/Yield (P/Y)

ϵ = effective plastic strain

The S_c value is determined from a quasi-static tension test and has been validated against tensile tests performed by Bridgeman under hydrostatic pressure [4]. The model is an interim approach since it assumes the voids grow independently in a rigid plastic material. In reality the voids will interact and the local work-hardening behaviour of the material surrounding the voids will affect their growth.

CURRENT CAPABILITIES

The choice of numerical method can only be made when all the physical phenomena of interest possible in a physical problem have been considered. Each method has its advantages and disadvantages and the merit of one method over the other is not always obvious. In our research in the study of detonics and penetration mechanics we are interested in very large fluid distortions and inter-penetration of material. For these problems an Euler scheme is the preferred numerical method. Our research into the development of material constitutive and fracture algorithms and the response of structures and systems to dynamic and quasi-static loading conditions, however, requires a Lagrange method. We therefore have to ensure that our material and fracture algorithms are robust, producing equivalent results when used in either numerical method, thus ensuring that the model formulation is consistent with the numerical integration scheme. If this is not the case then the hydrocode can produce inconsistent predictions, or become unstable, resulting in a false interpretation of the physics of the event

LAGRANGE

Numerics: In a Lagrangian scheme such as that used in DYNA, the numerical mesh is mapped to the material boundaries and distorts as the material deforms. The mesh consists of elements with nodes at each vertex and the mass within each element remains constant. The computational cycle commences using the initial conditions to calculate the acceleration at each node using Newton's second law. This relies on a lumped mass within the element being apportioned to each node through various averaging techniques, such as those attributed to Wilkins [5]. The accelerations are then used to calculate the velocities and displacements at each node using simple integration. This allows the calculation of the strain components and hence the stresses and the pressures, which are stored at the centre of the element. This is achieved through a definition of an equation of state defined in P,V,E space and a constitutive model describing the stress state within the element. These can be linked to a failure model if the fracture behaviour of the material is being investigated. Lagrangian methods are very powerful in addressing dynamic material behaviour since the numerical scheme is extremely robust and stable and material interfaces are precisely defined.

Whilst this is true for low element distortions, it has been demonstrated by Benson, Hallquist [6] that significant element aspect ratios and distortions reduce the accuracy in the basic calculations of strain and hence stress. There are two main reasons for this; firstly for aspect ratios exceeding about 3:1 the

transmission of certain wavelengths or frequencies is diminished, resulting in erroneous shock wave profiles. For this reason it is usually best to use square mesh elements in order to preserve shock wave profiles. Secondly when the elements become distorted in shape the techniques required for lumping nodal masses becomes flawed due to the averaging techniques, which have increasing errors as the distortion becomes more pronounced. This latter aspect has been addressed by numerous researchers and resulted in a variety of more accurate averaging methods, such as the area Galerkin technique [7] and many others. However, it is fair to say that the best methodology usually depends on the nature of the problem.

These limitations are quite severe since it is very difficult to design an optimum mesh for a given scenario. This is illustrated with an Explosively Formed Projectile (EFP) simulation where the mesh in the liner is orientated laterally with respect to the axis of symmetry at the start of the simulation but then changes its orientation to an axial alignment during the calculation. Therefore one must compromise between capturing the general deformation process that produces the projectile and computing inaccurate wave propagation and state variable information due to the elongated elements.

This technique is adequate for capturing the shape information of the projectile, but is prone to inaccuracy if investigating local strain or temperature within the projectile is of interest.

The numerical accuracy of the elements also implies that to achieve sensible results the mesh resolution must be fine enough to resolve all the necessary physics within the equation of state and the constitutive model. This is important if one is attempting to resolve a deformation gradient, otherwise an incorrect stress state will be predicted. This has important knock-on effects if we then wish to predict the likelihood and form of any fracture that might result.

The two main obstacles to accurate predictions within a Lagrange scheme are the contact algorithm describing how material interfaces are treated and the method used to determine post failure treatment of an element.

Contact Algorithms: There have been numerous significant improvements to the contact or sideline treatment within Lagrangian hydrocodes [8] and it is outside the scope of the paper to describe these in any great detail. Suffice it to say that these developments have vastly increased the scope of calculations now routinely conducted using Lagrangian hydrocodes, including crash worthiness, structural modelling, metal forming, machining problems, airbag inflation etc. Indeed some of these problems required special contact algorithm development simply to allow the simulation to run.

However, in terms of simulating material and fracture behaviour, the sideline treatment can have a significant influence on the prediction, particularly in those cases where friction is important. This is illustrated in a simple compression Hopkinson bar test, where the omission of friction at the interface results in the specimen compressing evenly, such that the cylindrical shape is preserved under uniaxial stress. The Hopkinson bar test tries to achieve this condition using advanced lubricants between the bars and the specimen. However the inclusion of friction in the simulation results in a distorted specimen, since the shear stresses induced by friction (Figure 1) produces a complex triaxial state of stress. The interpretation of any material test involving loading by compression or impact, therefore, can be greatly influenced by the presence of friction, which will exist, even with lubrication. This presents significant difficulties since the friction law and the static and dynamic friction coefficients can be difficult to determine. Thus for validation purposes there is always the difficulty of whether the constitutive model is inadequate or the sideline treatment results in an inaccurate representation of the friction. A valuable use of simulations, therefore, is to understand the sensitivity of the friction coefficient on the constitutive response.

Erosion Algorithms: One of the main difficulties in the treatment of fracture in a Lagrangian numerical scheme is the method used to describe the element behaviour after they have been deemed to fail. A simple approach is to set all the stresses and moduli to zero, such that the element can recompress, but cannot support tension. This can work surprisingly well in a number of scenarios, such as spall under uniaxial strain conditions. The main problem with this technique is that, the failed elements become much more susceptible to hourglass modes, due to the strength discontinuities, which can then affect the rest of the adjacent unfailed mesh, resulting in unstable solutions. In addition the fracture process can be driven by the formulation of the numerical treatment, rather than through any physics. An example of this behaviour is the propagation of cracks at velocities in excess of the

Rayleigh wavespeed. Many experimental studies have demonstrated that cracks cannot propagate at these higher velocities.

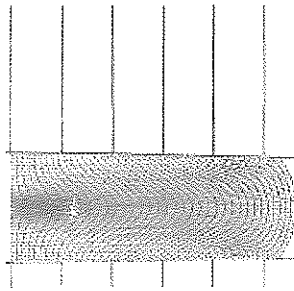


Fig 1 – DYNA Simulation of Hopkinson bar compression test with friction between bars and specimen

An extreme solution to this problem is to simply delete or erode the elements. This is completely artificial and results in the loss of mass, momentum and energy, which in a coarse mesh can be significant. However, eroding the elements does have some advantages. Modern sideline algorithms (e.g. automatic contact) can cope with the opening of internal free surfaces and their subsequent reclosure. If the numerical scheme can also cope with the free surface, without inducing significant hourglass modes, then a stable solution can result, although this depends on the class of problem being investigated. In addition, eroding the elements creates a definite break in the material, such that waves cannot propagate across the ensuing gap. For applications involving spall, this is quite important when validating a fracture model against a VISAR trace in a plate impact test. Careful analysis is required to determine whether the numerical treatment or constitutive and fracture model is the problem in not obtaining good agreement between experiment and simulation. An example of the significant improvement that can be obtained by using the Goldthorpe Path Dependent Fracture Model in DYNA2D to predict a plate impact spall VISAR trace is given in Figure 2. Also shown in the figure is the comparison with a simple semi-empirical P/Y against failure strain fracture algorithm and the results for cAst Euler.

The real issue concerning the use of erosion algorithms is the mesh resolution used in the simulation around the point of fracture. If the mesh becomes finer, then the mass of material being deleted becomes much smaller and in the limit insignificant. Experimental investigations have demonstrated that even for 'clean' spall fractures, some mass of the material is lost (i.e. broken off). This has been demonstrated by Shockey [9], who used detailed mapping of the topology of post fracture spall surfaces and compared them with the unfractured material.

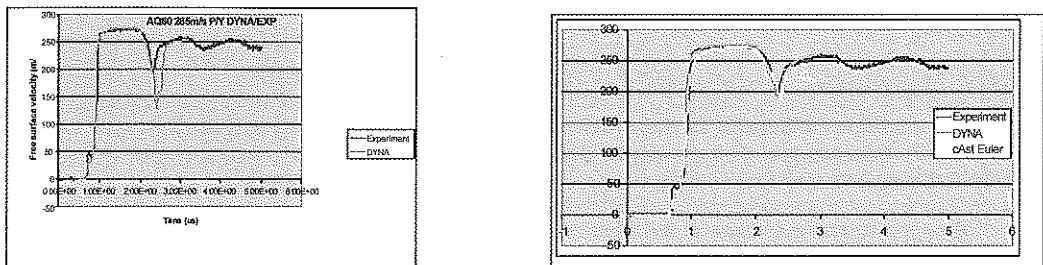


Fig 2: Plate Impact: Copper Flyer Armco Iron Target at 285m/s: Comparison of Numerical Schemes with Experiment: P/Y model (left), Path Dependent Failure Model (right)

The real issue concerning the use of erosion algorithms is the mesh resolution used in the simulation around the point of fracture. If the mesh becomes finer, then the mass of material being deleted

becomes much smaller and in the limit insignificant. For these reasons and for simplicity, the work in QinetiQ still uses the erosion technique for the post failure treatment of Lagrangian elements. However, great care is taken to ensure that the mesh resolution is sufficient to resolve the necessary physics gradients and to ensure that the loss of mass and momentum is minimized in the erosion process. An example of this is demonstrated in Figure 3 for a spigot intrusion through a steel plate. The constitutive model used was the modified Armstrong-Zerilli model and the fracture model was the Goldthorpe model described previously. The calculation is important since the width of the 'crack' is similar to the experimental observation and the mesh resolution is such that the crack velocity has converged at a value not inconsistent with experimental measurements of crack velocity in steel plates. This process has enabled the threshold spigot velocity, below which the spigot does not perforate the plate to be simulated much more accurately than with previous techniques. We consider this to be a vindication for our approach to pursue constitutive and fracture models, which are physically based deriving their coefficients from basic material tests.

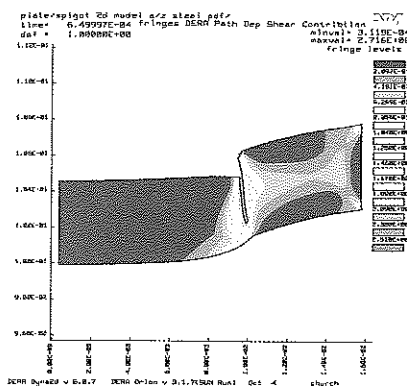


Fig. 3 – DYNA Simulation of Spigot Intrusion

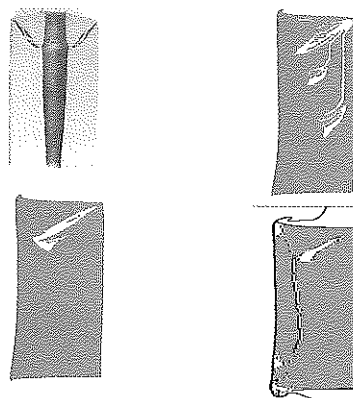


Fig. 4 – Copper fracture cylinder, experiment (top left), DYNA simulations (XM copper top right), Prestressed copper (DYNA bottom left, Euler bottom right)

Due to the attention to detail in the integration of the constitutive and failure algorithms within the Lagrangian numerical scheme, the simulations have identified important sensitivities and influences of material properties on the fracture process. This is illustrated with the copper fracture cylinder test [10], where the fracture predicted was grossly overestimated, unless one accounted for the initial pre-stressing within the copper (Figure 4). The results are also shown for cAst Euler.

The above discussion has shown how the formulation of the basic Lagrange numerical scheme, capable of simulating 'real problems' of interest, has to include a number of assumptions that can conflict with constitutive algorithms and the treatment of failure processes. Nevertheless Lagrange codes can make excellent predictions of the failure process.

EULER

Numerics: In an Eulerian scheme the numerical mesh is fixed in space and material moves through it. For infinitesimal displacements the definition of strain in an Euler or Lagrange frame of reference is the same. Under this assumption the Euler scheme can be represented by a Lagrange step followed by a remap of the flow field back to the original reference frame. This is the methodology adopted by all Euler hydrocodes. In our development of the cAst Euler capability we have adopted a staggered grid scheme with velocities defined at the cell corner nodes and all other variables at the cell centre. The resulting Lagrange step is solved using a finite difference scheme and involves similar steps to those described above for a Lagrange code such as DYNA. The Lagrange phase in cAst Euler is then as accurate as the basic Lagrange scheme in DYNA. In some respects, because the mesh is always square many of the problems with mesh distortion, described above do not occur. In addition the problems of slide line formulations are avoided.

However, the material transport or advection component of the formulation in any Euler code, is considerably more complicated than the Lagrange step. In the case of the staggered grid we have the additional problem associated with the transport of momentum and the allocation of mass to each velocity vertex.

In principle the fact that an Euler code is always dealing with a rectilinear mesh that does not distort implies that flow field variables can be accurately defined. In practice, however, the advection step will always introduce dispersion and dissipation into the flow field, even though it conserves mass and momentum through the equations used. In implementing material constitutive and failure algorithms into an Euler code the influence of the advection step on algorithm performance is the critical factor.

The advection step in an Euler code can be considered as passively convecting material across the spatially fixed Eulerian cell boundaries. Thus the value of a flow field quantity, F , in cell (i,j) , is determined by the following equation:

$$F_{i,j}^{n+1} = F_{i,j}^n + \Delta F_{i,j}^{inflow} - \Delta F_{i,j}^{outflow} \quad (2)$$

This is a conservation equation even though there may be no physical conservation law for the flow field variable being advected, e.g. stress deviators. The effect of equation 1 is to average the properties of the material in the cell. This can be a particular problem when the property is damage, since the effect of the advection step is to continually dissipate/disperse the damage level as the material moves through the mesh. Clearly the amount of dissipation will be very dependent upon the mesh size used to define the problem.

All of the numerical schemes used in an advection step are dispersive and some also introduce severe dissipation, for example if the scheme is first order. In the case of mass and momentum advection kinetic energy is not necessarily conserved and can appear in other parts of the mesh. In addition low order schemes will fail to maintain gradients in density and energy, which can affect the formation and propagation of a shock wave or other material or flow field discontinuity. This is particularly important when we are trying to introduce fracture into our material description. Our group at Fort Halstead has studied these problems in some detail. We have found for prompt fracture processes a first order scheme can still provide useful solutions [11] provided we define the problem on a relatively finely resolved mesh. However for an accurate solution with minimum dispersion and dissipation we have to resort to a third order accurate numerical advection scheme. This has been implemented in cAst Euler. We have found that in addition to a more accurate solution we can also define problems on meshes with larger cell sizes.

In a higher order advection scheme the properties of the material, within the volume that is moving across a cell volume, are calculated using information from the upwind and downwind cells. This approach is quite flexible since the material property can be considered a function of a dependent variable, (distance, volume, or mass). Whilst the process is rigorous for conserved quantities such as mass and energy, it is less rigorous for non-conserved quantities such as plastic strain or work, stress deviators, damage and other material histories. Our approach has therefore been pragmatic in the selection of the appropriate dependent variable. For example plastic work has the dimensions of energy and therefore has mass as the dependent distribution variable.

As our understanding of material deformation theory has improved we have been able to develop algorithms capable of describing path dependent processes, including failure. The impact of the advection step on the material histories used in these algorithms, therefore, has to be accounted for in their numerical formulation. Indeed the progress achieved has been possible because the material and computational scientists have worked closely together.

Mixed cell: The other major difference between an Euler and Lagrange scheme is that in an Euler scheme a cell can contain more than one material. We therefore have to identify and track material interfaces to minimize material mixing. The interface-tracking algorithm developed in cAst Euler constructs the interfaces between materials in a mixed cell by utilizing information on the material volume fractions within the 8 (2D) and 26 (3D) neighbouring cells. It performs an excellent job

in maintaining interfaces and the shape of objects in uniform translation across the mesh as well as having the ability to track thin layers of materials within a cell.

The physics of the mixed cell presents other problems, since it requires cell average values to drive the Lagrange step. We thus have to define the algorithms that calculate the cell pressure to determine the acceleration and the way in which the cell divergence is apportioned between the materials in the cell. In cAst Euler we use a non-equilibrium in mixed cells by applying a constant divergence to each material and then volume weighting each material pressure. There is clearly a wide range of alternatives that could be applied to the mixed cell and other codes do employ them [12]. Whilst our approach avoids violating the Courant stability criterion it is not without its problems. When the compressibility of the materials within the cell are very different, for example a metal and a gas, the use of an average pressure will under/over compress the higher/lower compressible materials. In terms of the acceleration of the cell our experience has shown that the situation rapidly reduces to the correct free-surface conditions within a few cycles. However, the material energies and hence temperatures within the cell will also be incorrect. This is a similar problem to that encountered in a Lagrange scheme at material boundaries. Given the importance of temperature in modern constitutive and fracture algorithms this can have a significant effect on the response of a material. This is a universal problem whatever the numerical scheme employed. In part it derives from the fact that all hydrocodes use a P,V, E material description and not a P,V,E, T description. It is therefore important to understand that the mixed cell surface cells of an object within the mesh may well have very different constitutive properties compared to those cells internal to the object.

In terms of a mixed cell where the constituents all carry strength the usually mixed cell algorithms imply that surfaces cannot support lateral motion, i.e. the friction force is infinite. This obviously has a similar impact to the problems discussed above concerned with slidelines in a Lagrange framework.

Fracture representation: Within cAst Euler once a cell has been flagged as having failed in tension the material within it is relaxed back to ambient density. This creates a volume deficit within the cell, which is filled with either a gas or void. This process thus attempts to reproduce the nucleation of voids at the meso-scale. At the same time the stress deviators and strain are relaxed on the basis of the volume of void/gas introduced into the cell. Whilst this is an arbitrary approach, since there is no conservation law for stress or strain, it does work well for most situations. To avoid energy conservation errors the change in energy of the failed material is assigned to the inserted gas. Thus the process conserves mass momentum and energy and avoids the requirement in a Lagrange scheme of deleting a cell and its contents from the mesh.

Whilst this process has created an internal interface within the cell the velocity nodes on either side of this interface are still connected through the finite difference operators. This should be compared to a Lagrange scheme where we create a true free surface by deleting an element. The introduction of a surface separation algorithm, which confines further expansion to the void/gas inserted into the failed cell, is likely to improve the free surface condition at the fracture surface and provide a sharpened discontinuity in the stress field. This is currently being investigated. Its general implementation in 3D is however, not straightforward.

The process described assumes that the fracture surface extends beyond the cell under consideration into neighbouring cells. If, however, the failed cell is isolated within the material the interface algorithm cannot currently determine its motion within the flow field. The 'hole' in the material thus can get 'left behind'. For slowly developing failure processes or the development of cracks in moving objects this can prove a significant problem and research is underway to develop alternative strategies for the interface algorithm. The research also extends to the integration of the fracture model into the solution framework. For fracture criteria that are based upon a level of stress, strain or tri-axial state of stress (P/Y) - effective strain, the point within the solution step where failure is determined is arbitrary. In previous versions of cAst Euler this was performed at the start of a cycle. This minimized the impact on code performance due to the need to call the equations of state for cells that had failed. However when failure criteria are based upon increments of strain as in the Goldthorpe path dependent ductile fracture models, consistent time and space centred variables have to be used to determine whether a cell has failed. Currently we therefore check cells for failure in the half-timestep ($n+\frac{1}{2}$) calculation in the Lagrange step.

Clearly the relation of the failure algorithm in an Euler code to actual material behaviour is very dependent upon the numerical resolution employed. However for the general case the resolution is such that this representation of fracture can only be considered phenomenological. Its success is related to the introduction of a free surface, which alters the local state of stress and the wave propagation within the material. Provided the stress wave propagation induced by the fracture surface is accurate the predicted and observed global fracture behaviour will agree. This is most likely to occur in situations driven by strong discontinuities such as shock and rarefaction waves.

The simplest fracture system is spall since it can be considered a 1D prompt process. The ability of cAst Euler to reproduce the VISAR velocity time history of a plate impact experiment is shown in Figure 2. The level of agreement between the Euler prediction and experiment is very good for the PDF algorithms. The results are also in good agreement with the Lagrange code DYNA. The differences in the recovery velocity and subsequent spall signals reflect some of the issues discussed above, particularly the free surface condition at the spall plane. This is complicated due to the fact that the failure process manifests as a complex series of closely spaced free surfaces. The mesh resolution is fine enough to resolve the sensitivity of the VISAR system.

A very useful 2D test of a fracture algorithm in an Eulerian frame is the explosively loaded fracture cylinder discussed above. Once again it is a prompt fracture test, driven by the strong shock waves and release waves generated by the axial column of explosive. The ability of the Euler scheme to describe the process is illustrated in figure 4, where it can be directly compared with the Lagrange result. In this case the fracture model was a simple semi-empirical P/Y against failure strain fracture algorithm. Many materials, such as copper also show internal structure to the fracture surface in this test, which provides a challenge for both the scheme and that is a strong test of the fracture model and the code.

The above examples relate to a prompt failure process driven by a single mode of fracture. A situation where this does not apply is the plugging phenomenon observed when a projectile impacts a plate at relatively low ballistic velocities. The initiation of failure as the plate deforms is a ductile one driven by stress triaxiality i.e. a POY process. Simulations showed, however, that once the crack initiates the shear strain localizes and drives the failure process [13]. This change of failure mode can be accommodated within the existing P/Y algorithm by extending the fail - no fail boundary into the positive POY region and defining the effective strain in terms of the plastic strain, since the plastic strain includes the shear strain in its calculation. The ability of the algorithm in an Euler frame to reproduce the observed plug formed experimentally, including the change of propagation direction of the crack is shown in Figure 5



Fig 5 - cAst Euler simulation of plugging of 10mm thick RHA plate Impacted by aluminum sphere at 1200m/s

The extension of the POY model in this manner, although not based upon any rigorous theoretical approach, works very well for ductile materials. However, for more brittle materials, where the data does not extend to high levels of effective strain the approach is not as successful. Our research has demonstrated that we need a failure model that can describe the range of failure modes observed in a material that is soundly based on theory and characterized by simple experiments. As will be discussed below, whilst this is our long-term objective. We recognize, however, that a properly constructed phenomenological model can be as equally successful for a specific set of applications.

algorithm to represent the observed fracture behaviours of interest in the material. The final one is the mesh resolution employed in the simulation. In general the finer the resolution the better the predictive capability. If the model is attempting to reproduce meso-scale fracture processes that may be governed by different length scales, however, it must be recognized that extremely fine numerical meshes will be required. One way of achieving this in a simulation of a realistic structure is to employ adaptive meshing methods. Whilst this is potentially a promising option considerable research needs to be undertaken into the appropriate mesh adaptation criteria. The main advantage of using adaptive techniques is that the numerical scheme is consistent and the issue is more about boundary conditions between fine and coarse meshes and the general data structure between the meshes.

Another approach for linking the meso-scale to macro-scale response is to embed analytical damage models within the hydrocode. The methodology makes use of the ability of the analytical damage model to accurately track the progress of damage within the cell. In this way much more precisely defined failure criteria, which can account for void interaction, under well-defined stress states or boundary conditions can be applied. It is extremely difficult, however, to calculate evolving boundary conditions analytically. If an analytic solution can be obtained, however, the progression of damage information can be fed back into the hydrocode scheme, which then calculates the new stress-state. As hydrocodes have extreme difficulty in simulating the meso-scale this approach offers the best aspects of each approach in an efficient computational algorithm.

The difficulties of this approach should not be under-estimated, however, since the analytical solutions to describe void interaction are novel. There is therefore little or no reference within the literature, to benchmark the predictions. Thus we are employing selected detailed simulations of void growth and interaction under well-defined boundary conditions to validate the analytic predictions. The other significant difficulty is relating the analytic variables, such as radius of curvature of voids, into a tractable hydrocode variable such as stress, strain, strain rate etc. Once this is achieved the subroutine would be structured such that the hydrocode would predict the state of stress in the cell or element and a library of analytic solutions would be searched to determine whether the cell had failed. This approach also has a potential counter-intuitive culture shock since the mesh has to be large enough to ensure the analytic model is representative of the real material behaviour and contains enough voids. The aim in QinetiQ is to use this approach, together with adaptive Euler numerics.

Another potential benefit of the generic path dependent models being developed is that the model can be defined in terms of strain components. This allows the model to describe anisotropic behaviour in a continuum frame of reference using a physically based approach

CONCLUSION

1. This paper has reviewed the research at Fort Halstead over the past 15 years into the development of material constitutive and failure algorithms for use in Lagrange and Euler hydrocodes.
2. The careful integration of algorithms into the numerical scheme is crucial for the effective validation of constitutive and failure algorithms.
3. A future methodology for linking meso-scale to macro-scale within a continuum hydrocode framework has been proposed.

ACKNOWLEDGMENTS

The authors would like to acknowledge the contribution of Barry Goldthorpe, Peter Gould and Tony Andrews in the development of this work.

REFERENCES

- 1 Goldthorpe B, Church P 'The Effect of Algorithm Form on Deformation and Instability in Tension', J de Phys IV, 1997, 7, C3, p 753
- 2 Butler A, Church P, Goldthorpe B 'A Wide ranging Constitutive Model for bcc Steels', Jnl de Physique C8-471, 1994.
- 3 Goldthorpe B, Gould P A Path Dependent Constitutive Model for Gilding Copper, Jnl de Physique, Vol 10, Pr9, pp 39-44, DYMAT 2000, Krakow
- 4 Goldthorpe B 'A Path Dependent Model for Ductile Fracture', Jnl de Physique 7,C3-705, Aug 97.
- 5 Wilkins M 'Calculations of Elastic-Plastic Flow', LLnL Rept UCRL-7322, Rev I, 1969
- 6 Benson D, Hallquist J 'Sliding Interfaces with Contact-Impact in Large-Scale Lagrangian Computations', Comp Meths Appl Mech Eng, 51 pp 107-137, 1985
- 7 Goudreau G, Hallquist J 'Recent Developments in Large-Scale Finite Element Lagrangian Hydrocode Technology', J Comp Meths Appl Mech, Eng 30, 1982
- 8 Hallquist J DYN3D Users Manual
- 9 Shockey 'Understanding Dynamic Fracture Phenomenology with Fractography', Materials Applications of Shock Wave and High Strain Rate Phenomena, 1995, pp 151-162.
- 10 Church P, Macmahon I, Softely C, Cameron 'Simulation of Explosive Fracture Cylinder Test Using DYNA', Jnl de Physique, Vol 10, Pr9, pp391-396, DYMAT 2000, Krakow.
- 11 Nash M A, Cullis I G The Use of Fracture Models in the Theoretical Study of Explosive-Metal Interactions. 9th International Symposium on Ballistics, Shrivenham, May 1986, Vol: 2 p285-292
- 12 Benson D J A Mixture Theory for Contact in Multi-Material Eulerian Formulations. Comput. Methods Appl. Mech. Engrg. Vol:140 1997, p 59-86
- 13 Church P, Cornish R, Cullis I, Lynch N Simulation of Shear Plugging through Thin Plates Using the GRIM Eulerian Hydrocode. Metallurgical and Materials Transactions A: Volume 31A, p853-860. March 2000
- 14 Church P, Cullis I, Goldthorpe B, Rosenfeld D Development and Validation of a Dwell Model. 19th International Symposium on Ballistics, Interlaken, 7-11 May 2001. Vol. III pp 1053-1060
- 15 Johnson G 'Incorporation of an SPH module into the EPIC code for a Wide Range of High Velocity Impact', Vol 413, Allied Technologies Inc.
- 16 Fahrenthold E P, Horban B A A hybrid particle-finite element method for hypervelocity impact simulation. International Journal of Impact Engineering, 1999, Vol. 23: p 237-248.

CONTACT

P Church/I Cullis – Tel: (44) 01959 515138, fax (44) 01959 516050
Email: pdchurch@qinetiq.com, igcullis@qinetiq.com

© Copyright QinetiQ Ltd 2002

Numerical Analyses of the Shear Zone Formation in Impact Shear Tests

P. Chwalik, J.R. Klepaczko and A. Rusinek

Laboratory of Physics and Mechanics of Materials
Metz University, Ile du Saulcy, 57045 Metz cedex 01, France

ABSTRACT

In this paper a shear zone evolution is studied in Ti-6Al-4V alloy. Such process of deformation, leading to development of adiabatic shear band, is typical for fast and impact shearing. A very special experimental technique developed at LPMM-Metz has permitted for shear tests at a wide range of strain rates and also for development of an advanced constitutive relation valid for a large range of strain rates and temperatures (range of strain rate from 10^{-4} 1/s to about 10^5 1/s). Four different specimen geometries with different stress concentrators are tested and analyzed. After identification of all material constants for Ti-6Al-4V alloy in an advanced constitutive relation, such relation has been introduced into the finite element code ABAQUS Explicit. The constitutive relation accounts for strain hardening, rate sensitivity and thermal coupling. In this way a complete dynamic approach with elastic-plastic wave propagation, adiabatic shear band development and failure could be considered. In addition, the critical impact velocity in shear has been estimated for Ti-6Al-4V.

INTRODUCTION

The effects of different impact velocities, but also temperature coupling by adiabatic heating, and different stress concentrators are very important in a variety of applications in aviation and armament industries. Usually a shear mode of deformation dominates during impact loading and perforation. In order to study the processes of impact shearing the modified double shear tests was chosen to study Ti-6Al-4V alloy. This alloy shows a low strain hardening rate combined with a low thermal conductivity and relatively high rate sensitivity. This combination of mechanical and thermal characteristics leads to an easy triggering of adiabatic shear bands (ASB) in all Ti alloys.

EXPERIMENTAL TECHNIQUES OF SHEAR AT DIFFERENT STRAIN RATES

In order to study behavior of Ti-6Al-4V alloy a wide range of strain rates in shear was applied. The lower range of strain rates, from 10^{-4} 1/s to 10^2 1/s, was covered by application of a fast hydraulic machine. A special device to support and clamp of the modified double shear (MDS) specimens was used together with a high-precision displacement measurement system based on two LVDT gages, [1,2]. The higher range of the nominal strain rates in shear, from 10^3 1/s to near from 10^5 1/s was also covered. A new original experimental technique has been developed in LPMM – Metz to test materials in shear at high strain rates, [1]. This experiment is based on direct impact on the modified double shear (MDS) specimen geometry, so the same specimen geometry can be used within the whole spectrum of strain rates. The scheme of this technique is shown on Fig.1. The direct impact of a round projectile is applied to deform plastically up to failure the MDS specimen, [1]. The MDS specimen is supported by the Hopkinson tube instrumented with SR gages. The transmitted elastic wave measured by the SR gages, which is proportional to the force transmitted by the MDS specimen, can be measured by a digital oscilloscope. The projectiles of different lengths, from 100 mm to 400 mm, are made of maraging steel and have diameter of 10 mm. They are launched from an air gun with predetermined velocities V_0 , from 10 m/s up to over 100 m/s. The impact velocity is measured by the setup using three sources of light, fiber optic leads and three photodiodes which activate two time counters. The time intervals of dark signals from the photodiodes generated during the passage of

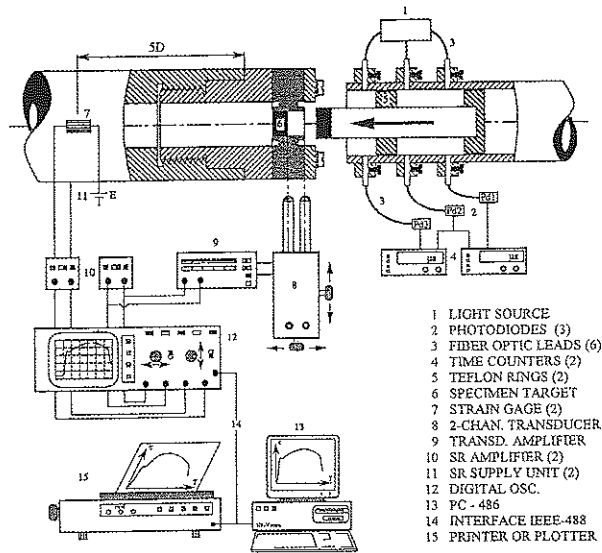


Figure 1. Scheme of experimental setup for impact shearing of the MDS specimen designed in LPMM

a projectile are recorded after amplification by the time counters. In this way the impact velocity at the contact point projectile-specimen can be precisely measured. Axial displacement $U_x(t)$ of the central part of the MDS specimen is measured as a function of time by an optical extensometer used as a displacement gage. Axial displacement of a black and white target attached to the middle part of the MDS specimen can be detected by this optical gauge, [1]. Axial force transmitted by the specimen can be determined as a function of time from the transmitted longitudinal wave $\varepsilon_t(t)$. All electric signals, that is the displacement $U_{ext}(t)$ of the black and white target and strain on the surface of the Hopkinson tube $\varepsilon_T(t)$, via signal conditioners, are recorded by a digital oscilloscope. All experimental results are stored in a PC hard disk and analyzed later. Relations (1), (2), (3) permit for determination, both as a function of time, of shear strain $\Gamma(t)$ and shear stress $\tau(t)$ in the MDS specimens. Elimination of time leads to determination of $\tau(\Gamma)$ at specific strain rate.

$$\Gamma(t) = \frac{1}{h} \left[U_{ext}(t) - C_0 \int_0^{t_m} \varepsilon_T(\xi) d\xi \right] \quad (1)$$

$$C_0 = \sqrt{\frac{E}{\rho}} \quad (2)$$

$$\tau(t) = \frac{\pi(D^2 - d^2)E_{tube}}{8ab} \varepsilon_T(t) \quad (3)$$

The final results of quasi-static and direct impact tests are shown in Fig 2 in the form of the maximum shear stress as a function of the logarithm of the nominal strain rate. Three specimen geometries with different stress concentrators have been tested. The main task of such tests was to evaluate an effect of stress concentrator on the failure triggering, mainly in adiabatic conditions of deformation. The all

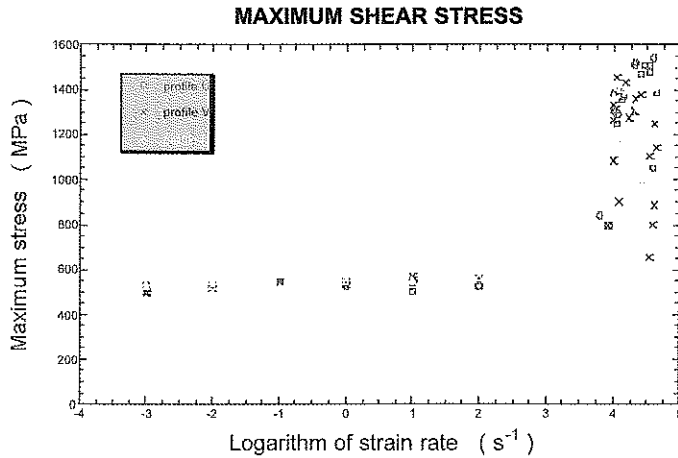


Figure 2. Experimental results for "U", "V" and "I" profiles: maximum shear stress vs. logarithm of strain rate

geometries applied in this study, that is with three notch shapes: "U", "V" and "I" are shown in Fig.4b, c and d. In Fig.4a the standard geometry is shown, [1]. Fig.2 shows that the maximum shear stress is practically the same for all three geometries ("U", "V" and "I"), moreover, at low strain rates the maximum stress is proportional to the logarithm of strain rate. At very high strain rates the maximum stress increases substantially then it stabilizes at the level ~1550 MPa and next drops rapidly. It means that at very high nominal strain rate the critical impact velocity in shear (CIV) was reached, [3,4]. Such behavior has been analyzed numerically for VAR 4340 steel and Ti-6Al-4V alloy, [5, 6]. The geometry has no influence on the maximum stress in quasi-static deformation, but become important at high strain rates. The energy up to the maximum force transmitted by the "U", "V" and "I" specimens is shown in Fig.3 versus the impact velocity. Behavior is similar as compared to numerical results for VAR 4340 steel, [5]. When the nominal strain rate increase, the energy to break the VAR 4340 steel diminishes, whereas for Ti-6Al-4V increases up to high values. Those large differences in adiabatic failure are fundamental and should be clarified in the future.

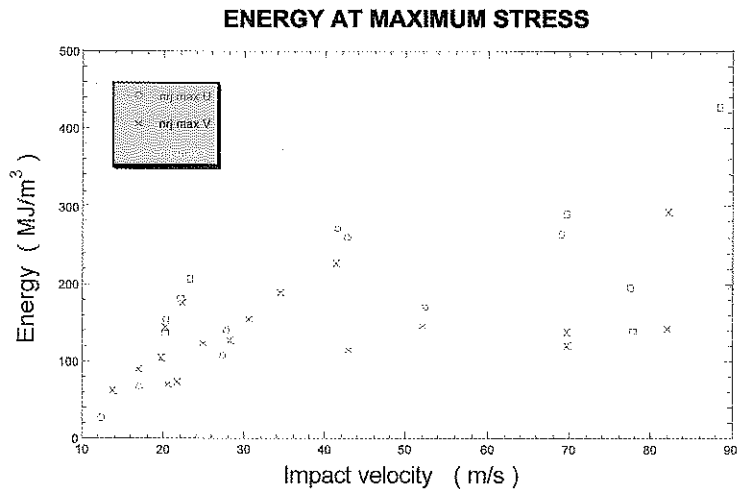


Figure 3. Experimental results for "U", "V" and "I" profiles: energy at maximum stress vs. impact velocity

CONSTITUTIVE RELATIONS FOR Ti-6Al-4V

After analysis of experimental data available in the open literature for Ti-6Al-4V alloy and the results obtained with the MDS technique (standard specimen geometry), the following explicit form of the constitutive relation has been developed [2, 5, 6, 7, 8]

$$\tau = \frac{\mu(T)}{\mu_0} \left[B \left(\frac{T}{T_0} \right)^v (\Gamma + \Gamma_p)^p + \left(1 + \frac{T}{D} \log \frac{\dot{\Gamma}_0}{\Gamma} \right)^{1/m} \right] \quad (4)$$

where B , μ_b , n , n , m are respectively, the modulus of plasticity, the shear modulus at $T=300K$, the temperature index, the strain hardening exponent and the logarithmic rate sensitivity, T_0 , Γ_0 , Γ and D are normalization constants. The temperature change of the shear modulus is given by, [5, 8]

$$\mu(T) = \mu_0 (1 - AT^* - CT^{*2}) \quad \text{and} \quad T^* = T - 300 \quad (5)$$

where A and C are constants, and $T^* = T - 300K$ is the modified temperature. In principle, this version of constitutive equations can be applied at RT and above. Since it is known that the rate of strain hardening in metals and alloys is temperature dependent and it diminishes with an increase of temperature, [9,10], the strain hardening exponent n was assumed as a linearly decreasing function of the homologous temperature [5, 6, 9,10]

$$n(T) = n_0 \left(1 - \frac{T}{T_m} \right) \quad (6)$$

where n_0 is the strain hardening exponent at $T=300K$, and T_m is the melting point. This modification was found essential for very high strain rates where adiabatic increase of temperature may be substantial. The total number of constants in relations (4), (5), (6) is 12 and they are determined by an optimization procedure, [2]. The main core of the constitutive equation is based on physical considerations, [10]. Since a large part of the plastic work is converted into heat the temperature of a deformed solid increases when plastic deformation advances. The principle of energy balance with the heat conduction leads to the standard relation, [11]

$$\beta \tau = \rho C_v \frac{\partial T}{\partial t} - \lambda \frac{\partial^2 T}{\partial y^2} \quad (7)$$

where y is the axis of heat conduction, β is coefficient of stored energy, ρ , C_v and λ are respectively the density, the specific heat and the heat conductivity. When the process is entirely adiabatic then $\lambda=0$ and the simplified relation (7) leads to the expression (8) giving the adiabatic increase of temperature

$$\Delta T = \frac{\beta}{\rho C_v} \int \tau d\Gamma \quad (8)$$

The material constants for Ti-6Al-4V are as follows: $\beta = 0.9$, $C_v = 543 \text{ J/(kg K)}$; $\rho = 4.51 \text{ g/cm}^3$. Recent studies on pure Ti but also on Ti-6Al-4V indicate that the conversion coefficient β increases as a function of strain rate, [12]. In order to take into account his effect relation (9) is introduced as follows

$$\beta = \beta_0 - \alpha \log \left(\frac{\dot{\Gamma}_0}{\Gamma} \right) \quad (9)$$

The formation of ASBs is due to localization of plastic deformation in the adiabatic conditions. If the local strain rate is very high, it leads to the trapping of plastic waves by adiabatic shearing. This phenomenon is called the Critical Impact Velocity (CIV) in shear, [3, 4,]. By analogy to the CIV in tension, [9, 13], it is possible to develop a model based on the criterion of the adiabatic instability, $(\partial\tau/\partial\Gamma)_A = 0$, [9]. According to the rate-independent theory of elastic-plastic wave propagation, an analytical model to calculate the CIV was developed by Klepaczko, [3, 4]. The following wave equation is applied to analyze the CIV in shear

$$\frac{\partial^2 U}{\partial t^2} = C_{2p}(\Gamma) \frac{\partial^2 U}{\partial y^2} \quad (10)$$

where U is the displacement along the x -axis (shear direction) and the wave propagation is along the y -axis (perpendicular). The solution by characteristics leads to expression for V_c by separating elastic and plastic parts.

$$V_c = \int_0^{\Gamma_e} C_{2e} d\Gamma + \int_{\Gamma_e}^{\Gamma_m} C_{2p}(\Gamma) d\Gamma \quad (11)$$

with

$$C_{2e} = \sqrt{\frac{\mu}{\rho}} \quad \text{and} \quad C_{2p} = \left(\frac{1}{\rho} \frac{d\tau}{d\Gamma} \right)_A^{1/2} \quad (12)$$

where Γ_e is the limit of elasticity, Γ_m represents the value of Γ corresponding to the stress maximum of the $\tau - \Gamma$ adiabatic curve (Fig.9), C_{2e} and C_{2p} are respectively elastic and plastic wave speeds in adiabatic conditions. Such procedure for determination of V_c was applied for Ti-6Al-4V using the constitutive relations (4), (5), (6). A more detailed discussion of this procedure but also the verification by FE method can be found elsewhere, in [5] for VAR 4340 steel, and in [6] for Ti-6Al-4V. In the case of Ti-6Al-4V the elastic term constitutes an important contribution to the final value of CIV, the second term is relatively low because of the low rate of strain hardening causes very low plastic wave speeds. The nominal strain rate chosen for the calculations was 10^4 1/s. Thus, the two terms found are $V_{ce} = 106.4$ m/s and $V_{cp} = 14.0$ m/s, giving the final value $V_c \approx 121$ m/s. This value is comparable with other values for the CIV in shear for other materials, for example ~ 110 m/s for VAR 4340 [5]. The CIV in shear can be treated as a new material constant, very important in estimation of fragmentation processes by ASBs

NUMERICAL ANALYSES BY FE METHOD

Development and evolution of ASB and failure in all four specimen geometries were analyzed by FE method. Numerical analyses were performed by the FE code ABAQUS Explicit. The method uses a central difference rule to integrate the equations of motion explicitly through time. At the beginning of the increment, the nodal accelerations determined from dynamic equilibrium are integrated giving nodal velocities. After second integration the nodal displacements complete the total spatial-temporal solution of our problem. In order to calculate numerically an evolution of the plastic zones and failure, it is necessary to introduce a local failure criterion. A simple approach has been adapted after [14]. It is assumed that the critical value of shear strain in adiabatic conditions generates failure. Value of the critical strain Γ_f in the criterion can be determined as proportional to the instability strain defined by $(\partial\tau/\partial\Gamma)_A = 0$ in the adiabatic conditions of deformation with the proportionality coefficient α ,

$$\Gamma_f(\dot{\Gamma}) = \alpha \Gamma_i(\dot{\Gamma}) \quad (13)$$

Value of α applied in the preliminary analysis was 10 with the first version of the material constants giving the minimum of the instability strain as 0.024. However, this value was two times lower than the corrected value. Recently values for the coefficient α were estimated by an inverse technique using FE code, [14]. It has been found that the order of α is about 29. Klepaczko proposed to set the value

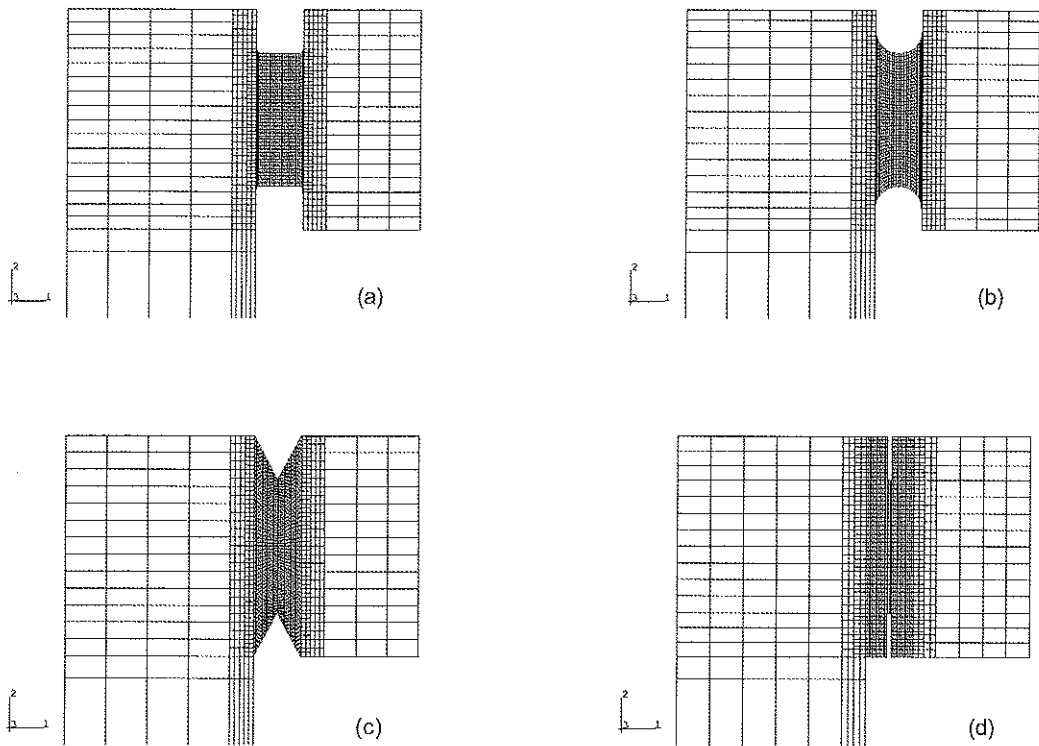


Figure 4. Four meshes used in FE calculations: (a)-MDS, (b)-profile "U", (c)-profile "V", (d)-profile "I"

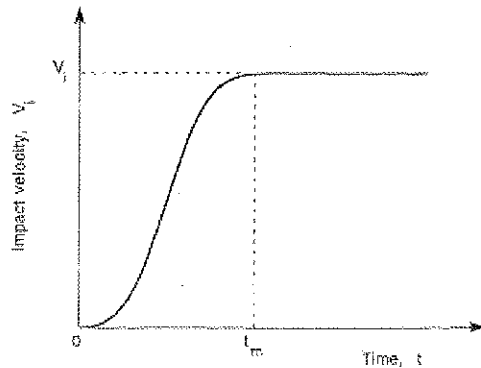


Figure 5. Schematic representation of the rise time function

of α to 30, [14]. The FE computations with corrected value of α are in progress. The double shear experiments were reproduced in FE simulations. Many aspects in FE analysis were optimized by Klosak, [5], for example the meshes density, boundary and initial conditions etc. All profiles, that is the standard, "U", "V" and "I" were meshed using plane stress elements CPS4R (four nodes, reduced integration). The mesh for all four geometries is shown in Fig.4a, b, c and d. Also, different contacts specimen-tube were tried, such analyses had lead to the choice of free contact surface between the

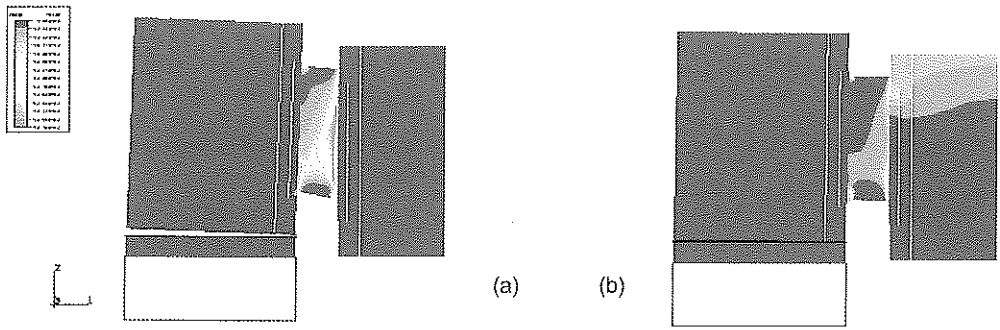


Figure 6. Evolution of deformation field as a function of impact velocity: (a)-20 m/s, (b)-100 m/s

specimen support and Hopkinson tube. The initial conditions in velocity were imposed in the form of the finite rise-time. Schematic representation of the rise time function is shown in Fig 5. The total rise time t_m is chosen according to the experimental observation and is equal to $0.2 \mu s$. At lower impact velocities, the localization of shear band is situated in the middle of the sheared zone, when the impact velocity increases (about to 100 m/s), a shift of the band is observed in the direction of the impact side of specimen as it is shown in Figs.6a and 6b for the standard geometry.

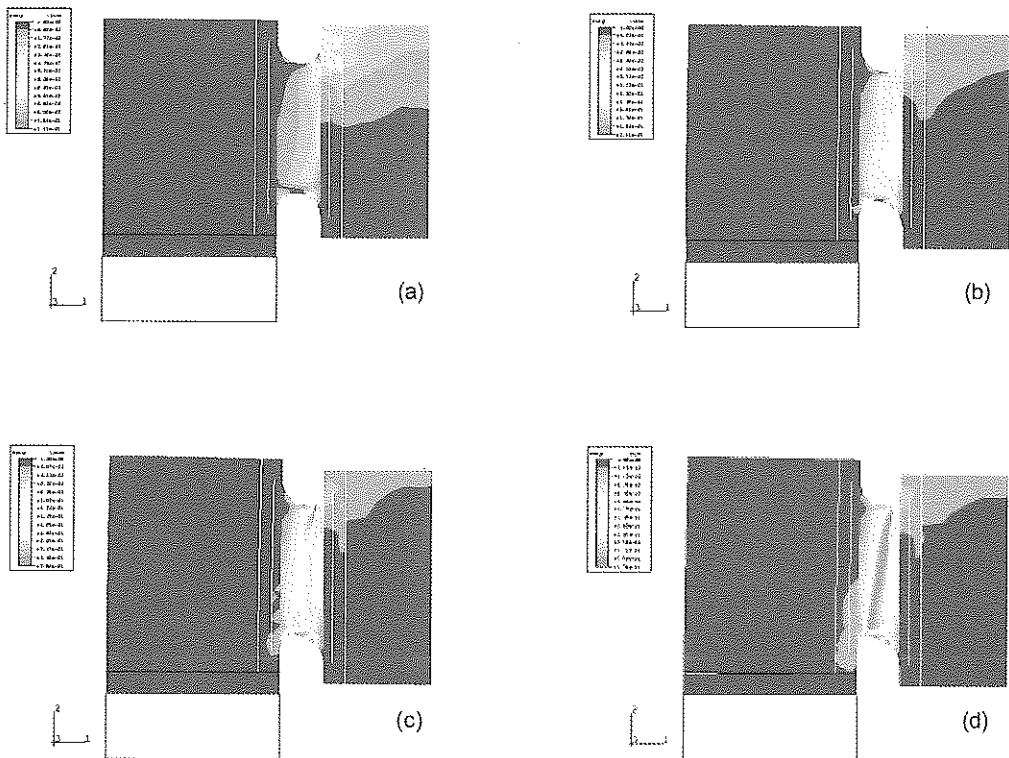


Figure 7. ASB formation for "U"-profile 80 m/s impact: (a) - $1.4 \mu s$, (b) - $3.6 \mu s$, (c) - $6.9 \mu s$, (d) - $9.1 \mu s$

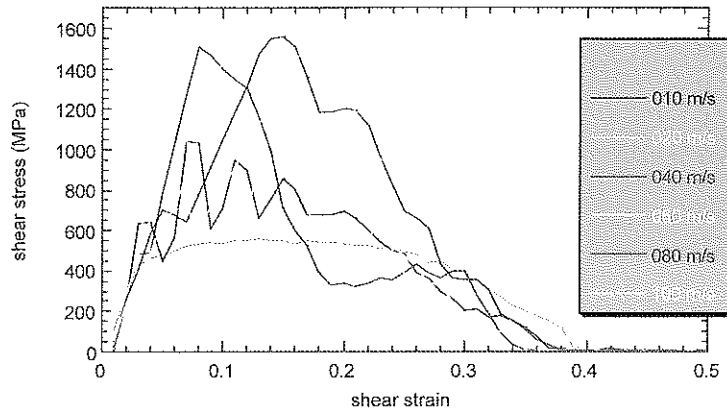


Figure 8. Numerical results for MDS specimen with local failure criterion, $\alpha=10$

This transition is caused by the superposition of plastic waves and adiabatic shear. This happens when the impact velocity is close to the CIV in shear. Since for the “U” geometry the stress concentration is the lowest the shift of the ASB into direction of the impact side is relatively small, Figs.7a, b, c, d. A very good levels of maximum shear stress were obtained by FE calculations. The reconstituted shear stress versus shear strain curves obtained by FE with value of $\alpha = 10$ in the criterion (13) are shown in Fig.8. An important level of vibration appears when the impact velocity is higher than 10m/s. After filtering the FE specimen response the maximum shear stress approaches theoretical predictions from the constitutive relations as it is shown in Fig.9 The solid lines are the prediction by the constitutive model and the points represent FE results (filtered results of Fig.8). The points obtained by the FE method show also presence of the CIV in shear. Concerning the CIV the analytical predictions are slightly superior to that found by FE, this may be caused by a small value of α assumed in FE calculations.

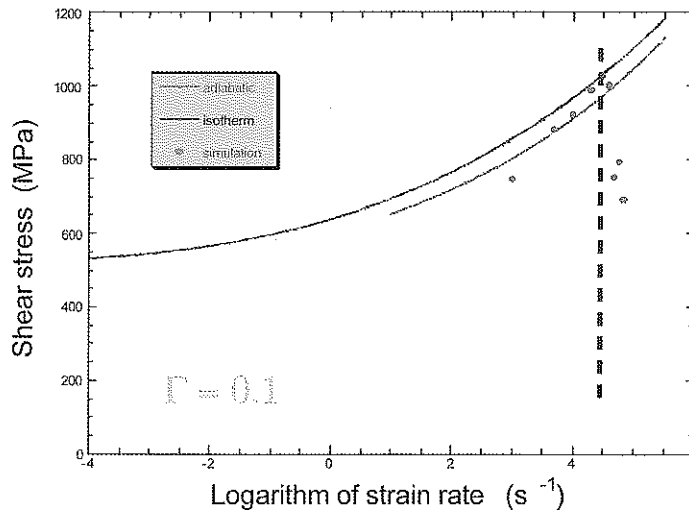


Figure 9. Shear stress vs. logarithm of strain rate at strain 0.1, comparison between model (isotherm and adiabatic conditions) prediction and numerically filtered results, dashed line indicates the beginning of CIV

CONCLUSION

The constitutive relation developed in LPMM gives a good possibility of implantation in finite element codes like ABAQUS Explicit. It permits to find a good agreement between experimental results, analytical prediction and FE simulations. This has been proven so far in many cases, for example of double shearing for Ti-6Al-4V and steels, [2,5,6,8]. In the case of Ti-6Al-4V experiments show similar behavior at low and medium strain rates for all four geometries of specimens used. But at the nominal strain rate higher than $2 \cdot 10^4$ 1/s the stress concentrators begin to dominate along with a very high rate sensitivity. The stress concentrators enhance the local strain rates. The local levels of strain rate may be much higher than the nominal values. The microscope observations have permitted to make important corrections [8] and to modify the local failure criterion.

The FE simulations of the MDS specimen backed by the Hopkinson tube seem to give a good reconstitution of dynamic response of the specimen for different impact velocity in the form of shear stress versus shear strain. It has permitted to estimate the CIV for these specimens by the FE code. The value of CIV ≈ 100 m/s obtained by these first simulations is comparable to the theoretical value of 121 m/s. However it is lower than 132 m/s for an infinite-length layer, [6]. The local failure criteria must be verified for different stress concentrators, and it is a subject of actual work. The phenomena of vibration must be understood to allow for a better comprehension and exploitation of numerical and experimental results. Concerning the temperature coupling, and more precisely a very high temperature gradients observed in the latest stages of failure, suggest that introduction of the heat flow into numerical calculations by FE codes instead of adiabatic approximation is needed.

ACKNOWLEDGEMENT

Part of the research results presented in this paper was sponsored by the US Army and in part by CNRS-France.

REFERENCES

1. J.R.Klepaczko, An experimental technique for shear testing at high and very high strain rates. The case of a mild steel, *Int. J. Impact Engng.* **15** (1994), 25.
2. A.Rusinek and J.R. Klepaczko, A double shear testing of a sheet steel at low and high strain rate in large deformation and a constitutive relation on the strain rate and temperature dependence of the flow stress, *Int. J. of Plasticity*, **17**, (2000), 87.
3. J.R.Klepaczko, Plastic shearing at high and very high strain rates, *Proc. Int. Conf. EURODMAT'94, J. de Physique IV, Coll. C8, 4* (1994), C8-35.
4. J.R.Klepaczko, On the critical impact velocity in plastic shearing, *Proc. Int. Conf. EXPLOMET'95, Elsevier Sci.*, (1995), 413.
5. J.R. Klepaczko and M. Klosak, Numerical study of the impact velocity in shear, *Eur. J. Mech. A/ Solids* **18** (1999), 93.
6. A.S. Bonnet-Lebouvier and J.R. Klepaczko, Numerical study of shear deformation in Ti-6Al-4V at medium and high strain rates, critical impact velocity in shear, *Int. J. Impact Engng* **27** (2001), 755.
7. A.Rusinek et J.R.Klepaczko, Comportement viscoplastique des tôles en traction et cisaillement, analyse de la vitesse d'impact critique, *Matériaux & Techniques*, **87** (1999), 41.
8. P.Chwalik, Numerical analysis and constitutive relation of TA6V, DEA Report, University of Metz, LPMM (2000).
9. J.R.Klepaczko, Generalized conditions for stability in tension test, *Int. J. Mech. Sci.* **10** (1968), 297.
10. J.R.Klepaczko, Thermally activated flow and strain rate history effects for some polycrystalline FCC metals, *Mat. Sci. and Engng*, **18**, (1987),143.
11. H.S.Carslaw and J.C.Jaeger, *Conduction of Heat in Solids*, Clarendon Press, Oxford, (1959).
12. J.Hodowany, G.Ravichandran, A.J.Rosakis and P.Rosakis, Partition of plastic work into heat and stored energy in metals, *Experimental Mechanics* **40** (1999), 1.
13. T.Kärman and P.E.Duvez, The propagation of plastic deformation in solids, *J. Appl. Phys.*, **21** (1950), 987.
14. J.R.Klepaczko, Effects of impact velocity and stress concentrators in Titanium on failure by adiabatic shearing, Final Technical Report, US Army, N68171-00-M-5964, Metz, (2001).

Development and Application of a Rankine Plasticity Model for Improved Prediction of Tensile Cracking in Ceramic and Concrete Materials under Impact

Richard A Clegg, Colin J Hayhurst, Iain Robertson
Century Dynamics Ltd, Dynamics House, Hurst Rd, Horsham, UK
email:richard.clegg@centurydynamics.co.uk

ABSTRACT

Brittle materials such as ceramics and concrete are commonly used in ballistic protection. The response of such materials to impact, perforation and penetration is complex and only limited physical instrumentation can be used in experiments. This paper demonstrates how a hydrocode, such as AUTODYN, can be used to aid in the understanding of the response of brittle materials to high pressure impact loading. While the penetration process is dominated by the material compressive thermodynamic and deviatoric response, the final damaged state of the material can be significantly influenced by the tensile behaviour. Modelling of the final damage state is important since this is often the only physical experimental information available and traditionally hydrocodes have had limited capabilities for modelling tensile behaviour. In this paper we present a unique implementation, in a hydrocode, of a tensile crack softening model for improved modelling of brittle materials in the tensile regime. Tensile failure initiation is based on principal stress while the post-failure tensile strength of the material is controlled through a damaging Rankine plasticity failure surface. The performance of the model is demonstrated through several simulations of impacts onto ceramic and concrete and the results compared with experiments.

INTRODUCTION

The numerical simulation of impacts on brittle materials, such as ceramics and concrete, requires the definition of appropriate material constitutive relations. These must be able to represent the evolving macro-mechanical material properties resulting from the detailed and complex micro-mechanical material behaviour. For ceramics the model presented by Johnson and Holmquist (JH2) [1] is commonly employed for this purpose. For concrete, the model by Riedel, Hiermaier and Thoma (RHT) [2] is commonly used in AUTODYN. A phenomenological rate dependant elasto-plastic approach is taken in both these models to represent the pressure dependent octahedral shear strength of the material in both intact and fully damaged states. Transition from the intact to damaged state is based on the accumulation of inelastic deviatoric shear strain.

While the brittle material penetration process is dominated by the material compressive thermodynamic and shear response, the final damaged state of the material can be significantly influenced by the tensile behaviour. Modelling of the final damaged state is important for predicting the multi-shot performance of materials/systems. Further, it is often the only physical information that is available experimentally. Here we describe the implementation, in a hydrocode, of an elasto-plastic tensile crack softening model for representing material fracture and damage due to principal tensile stresses. The tensile damage model can be combined with many existing brittle material models and therefore allows coupling of material damage caused by octahedral shear stress and volumetric tensile pressure.

An overview of the AUTODYN software [13],[15] is presented followed by a description of the implementation of the tensile crack softening model and how this is coupled with existing constitutive models for brittle materials.

Two example simulations are presented which combine the tensile crack softening model with the JH2 brittle damage model. The simulations are performed using the SPH (Smooth Particle Hydrodynamics) numerical technique and consist of a steel ball impact onto a block of Sintox-FA ceramic and a steel cylinder impacting edge on to a SiC ceramic target. Results are compared with experiments. A third example is presented to demonstrate the capability to couple the tensile crack softening model with the RHT concrete model. This example consists of a metallic kinetic energy penetrator impacting on a concrete structure.

AUTODYN

The AUTODYN-2D & 3D[13] transient non-linear dynamic software are based on explicit finite difference, finite volume and finite element techniques that use both grid based and meshfree numerical methods. The codes are commercially available and have been under continuous development since 1985. The software are based on classical continuum mechanics, which are used to describe the dynamics of a continuous media with a set of differential equations established through the application of the principles of conservation of mass, momentum and energy from a macroscopic point of view.

There are two fundamental descriptions of the spatial discretisation of a continuous media, which are the Lagrange and Euler formulations. The Eulerian description uses a grid which remains spatially fixed in time with the mass, momentum and energy flowing across cell boundaries, which avoids mesh tangling problems when modelling large material deformations. The Lagrangian description uses a set of grid points attached to the material that leads to a numerically efficient solution and has the advantage of precisely tracking material boundaries.

Based on these two spatial discretisation methods, AUTODYN has eight different numerical solvers. The Lagrange, Shell and Beam solvers are Lagrangian solvers where the grid deforms with the material it is attached to. Springs and dampers can be defined using special elements in the beam solver. The Arbitrary Lagrange Euler (ALE) solver is a grid-based hybrid between a Lagrange and Euler type solver. The Smoothed Particle Hydrodynamics (SPH) is a meshfree Lagrangian type solver. Finally three types of Euler solver are available: a structured mesh multi-material solver including material strength; a high resolution Euler-FCT solver optimised for efficient air blast simulations; a general purpose Euler-Godunov second order accurate multi-material solver again including material strength effects.

Selected solvers may be coupled in space and time so that the most appropriate solvers for each region in the analysis may be combined. Additionally Lagrangian type grids can interact with each other using AUTODYN's robust interaction logic. This automatically checks for any contact between grids and corrects for any penetration that may have occurred and can be used in conjunction with erosion and friction.

AUTODYN-3D includes capabilities for greatly increasing the efficiency of large 3D calculations by parallel processing across multiple solvers [15][16]. The Lagrange, ALE, Shell and Lagrange/Lagrange contact algorithms are currently parallelised and work continues on the remaining solvers. Parallel processing is available on a range of operating systems including MS Windows NT and 2000, Linux, and most Unix workstations. A parallel calculation can use a mixture of shared memory and distributed memory systems allowing efficient usage of available processing power.

A very wide range of material models are available in both AUTODYN-2D & 3D. The equations of state include the well known Linear, Polynomial, Shock, JWL, Slow-burn, and Ideal Gas as well as Orthotropic, Porous, Tillotson, PUFF and Sesame models. Strength models include Hydrodynamic, Elastic, Piecewise hardening, Brittle, Von Mises and Mohr-Coulomb models, the Johnson-Cook, Zerilli-Armstrong and Steinberg-Guinan models which include the effects of strain and strain rate hardening and thermal softening, the AMMHIS model for non-linear shock response of composites, the Johnson-Holmquist model for ceramics and glass and the RHT model for concrete. An extensive range of failure models are available, including bulk failure criteria such as hydro-tensile limit, bulk strain, directional failure based on principal stress and/or strain and material stress and/or strain, as well as special models such as cumulative damage and tensile crack softening.

The underlying data structures in AUTODYN are modular in nature thus facilitating easy customisation by users and developers alike. For example, the same material modelling routines are called by each solver hence once developed, a material model will work for all solvers (if appropriate).

BRITTLE MATERIAL MODELLING

JH2 MODEL

The brittle material model proposed by Johnson and Holmquist (JH2) [1] consists of a polynomial equation of state to represent the thermodynamic or shock compression response of the material coupled with rate dependant elasto-plastic constitutive relation with damage to represent the octahedral shear resistance of the intact and fractured material. The transition of the material strength from the intact to fractured curve is achieved through a scalar damage law in which damage is accumulated as a function of the effective deviatoric plastic strain.

The material model has mainly been applied to ceramic and glass materials. The input data for this model is usually derived from basic quasi-static measurements of elastic moduli and density followed by the calibration of numerical simulations to well characterised uniaxial and triaxial dynamic impact experiments.

RHT MODEL

The brittle material model presented by Riedel, Hiermaier and Thoma [2] has similar basic rate dependent elasto-plastic constitutive relations with damage as the JH2 model. The RHT model also includes additional features to enable the capture of additional phenomena observed in brittle materials. This includes strain hardening as well as pressure hardening, third invariant dependence of the failure surface, different strain rate effects in tension and compression, coupling with p-alpha type compaction equations of state. A typical set of failure surfaces for the RHT model are shown in Figure 1.

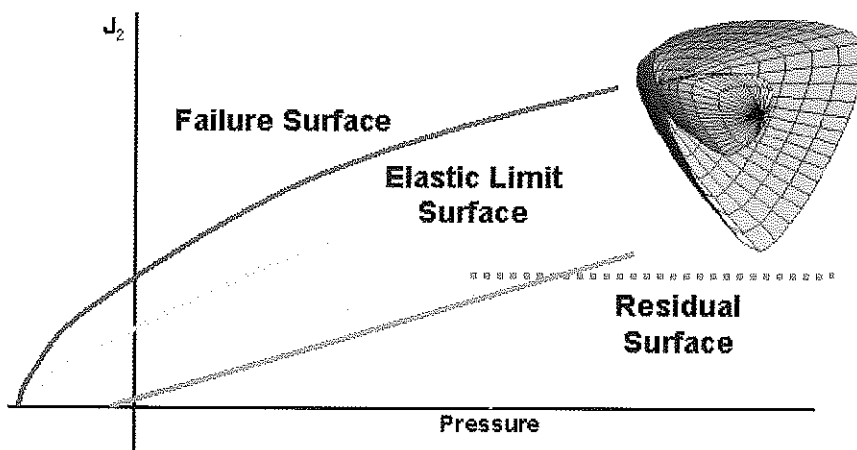


Figure 1. Typical Failure surface for the RHT concrete model

TENSILE FAILURE MODELLING

Both the JH2 and RHT constitutive models have a damage law that is formulated in such a way that material damage can only result from inelastic deviatoric straining of the material. This is most

representative of the material behaviour in the high pressure region which exists ahead of a projectile during the penetration process.

In other regions of the target the pressures are lower and principal tensile material stresses can be of the same order as the deviatoric stresses. Under these conditions, it is postulated that the maximum principal tensile stresses can lead to crack extension and damage growth. Principal stress includes volumetric as well as deviatoric stress components. A damage model that represents material fracture and damage due to both these components is therefore sought. Figure 2 highlights the possible mechanism for damage progression in a brittle material; severely damaged (comminuted material) caused by shearing ahead of the projectile localizes into discrete cracks which then propagate due to tensile stresses in the material.

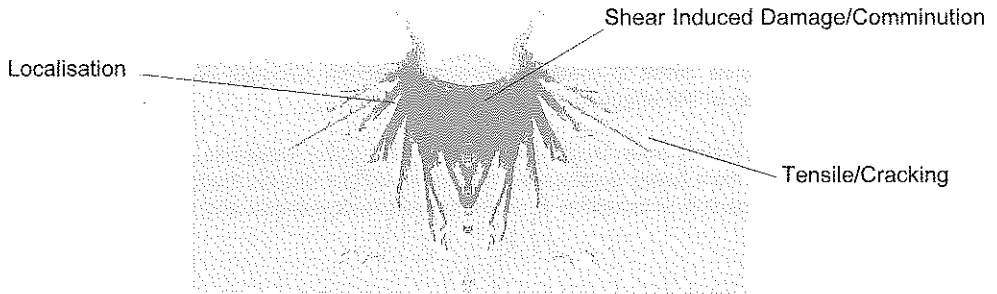


Figure 2 Failure Modes

TENSILE "CRACK SOFTENING" DAMAGE MODEL

Tensile crack softening models, in various forms, have been used for many years in the structural finite element community for modelling failure in brittle materials, such as concrete [7]. Here we have chosen to implement a Rankine plasticity model for brittle cracking based on the work by Feenstra and de Borst [6].

Tensile failure is initiated via maximum principal stress criteria defined through a Rankine failure surface. This failure surface is superimposed onto the traditional constitutive strength model, for example the JH2 model, Figure 3a. A distinctive feature of the Rankine failure surface is its triangular form in π -space, Fig. 3b.

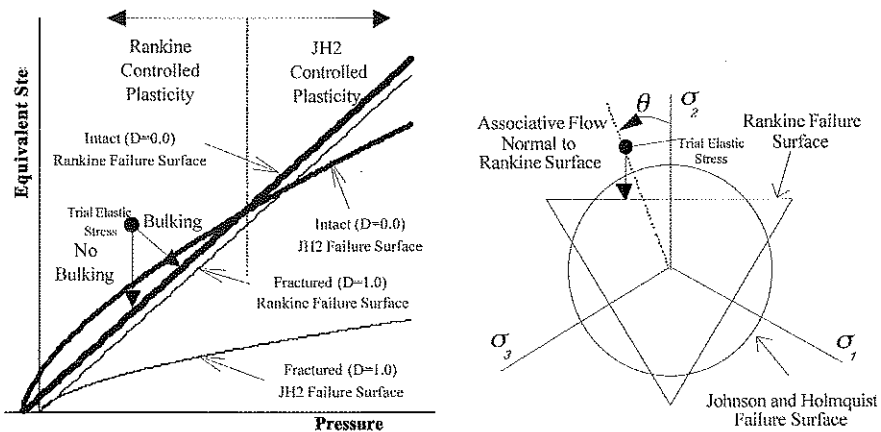


Figure 3 Rankine and JH2 failure surfaces in a) meridional plane b) π -space

The Rankine failure surface provides a limit for the maximum principal tensile stress in the material. When the trial elastic stress state violates the Rankine failure criteria, the stress is returned to the

failure surface using an associative backward-Euler method, similar to that described by Crisfield [8]. An option to force the return to take place at constant pressure, thus avoiding bulking, has also been implemented, Figure 3.

The return to the Rankine failure surface reduces the trial elastic stresses. The associated loss in strain energy results in an increase in the effective tensile crack strain, $\Delta\varepsilon_{cr}$. The rate of crack growth, hence damage, is controlled by the material critical strain energy release rate, G_c , the initial failure stress, T_{max} , and the local characteristic dimension, L_c , of the numerical cell representing the volume of fractured material. The resulting damage equation (1) is formulated such that the work required to extend a crack by a unit length is relatively insensitive to the local element size.

$$D = \sum \frac{L_c T_{max}^2}{2G_c} \Delta\varepsilon_{cr} \quad (1)$$

It is assumed that damage contributions from deviatoric straining (JH2 or RHT model) and tensile cracking (crack softening model) are additive.

EXAMPLES

The tensile crack softening model described above has been applied to a wide range of impact problems at velocities ranging from 10m/s to 15km/s. Here we present three examples in the ballistic velocity regime.

STEEL BALL IMPACT ONTO CERAMIC

Simulations of the impact of steel spheres on Sintox-FA (95% pure) alumina have been carried out and compared with experimental data presented by Hazell [3]. The results for a 6.35mm diameter sphere impacting a 25mm thick Sintox-FA alumina target at 1449m/s are discussed. The meshfree SPH (Smooth Particle Hydrodynamics) solution technique of AUTODYN [13] was used. Uniform particles of smoothing length 0.125mm were used to discretise the domain. The target geometry and response were assumed axisymmetric.

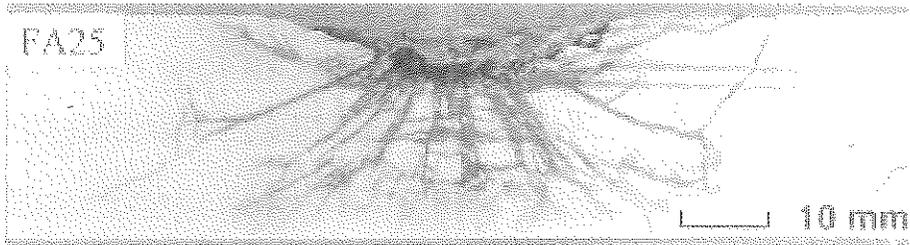
The 25mm Sintox-FA material was represented using the JH2 model with input data derived from [3] and [9]. The tensile crack softening model was used with failure initiation based on a maximum principal tensile stress of 0.1GPa. A fracture energy release rate of 68.7J/m² was assumed [3]. In the calculation shown, the "No Bulking" option was used for the plastic return algorithm. The steel projectile and target outer support frame were modelled using a shock equation state and Johnson-Cook strength model [5].

The simulated material failure 0.02ms after impact is shown in Figure 4a. On impact, the large contact stresses lead to rapid fragmentation of the material immediately ahead of the projectile. Central to the impact site the fragmentation is mainly due to deviatoric stresses. Moving radially outward from this region, the failure initiation mechanism quickly changes to principal tensile stress. Distinct cone cracks initiated by maximum principal stresses at the edge of the central impact site propagate through the ceramic. Lateral cracks are also predicted to grow from this central region and eventually break the surface of the ceramic. Finally, at late times, spall like cracks develop towards the back surface of the target.

These simulated modes of fracture compare encouragingly well with the experimental observations made by Hazell [3]. The results of an experimental firing on the simulated configuration are reproduced here in Figure 4b for comparison. The simulated depth of penetration, 6.5mm, compares well with the experimentally measured value, 6.1mm.



a) AUTODYN simulation results at 0.02ms



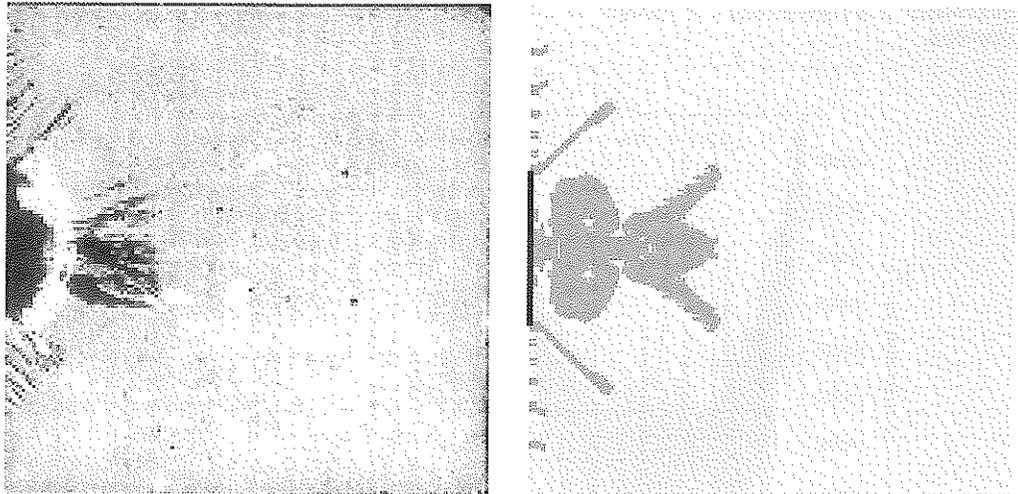
b) . Results from an Experimental firing, Hazell [Error! No se encuentra el origen de la referencia.]

Figure 4 25mm Sintox-FA after impact at 1449m/s by a 6.35mm steel ball

CERAMIC EDGE ON IMPACTS

Simulations of the edge on impact (EOI) experiments onto SiC targets reported by Strassburger[10] have been carried out. The experiments consisted of a cylindrical steel projectile ($r = 15\text{mm}$, $L = 23\text{mm}$) impacting a SiC target of size ($10\text{mm} \times 100\text{mm} \times 100\text{mm}$). The simulations were carried out in AUTODYN-3D assuming quarter symmetry about the axis of impact. The Lagrange solver was used to represent the steel projectile while the SiC target was represented using a uniform lattice of SPH particles with diameter 0.5mm . Interaction between the Lagrange and SPH regions was achieved using the standard contact logic. The material input parameters for SiC were derived from the data given by Holmquist[14].

Results for an impact velocity of 185m/s , at $4.6\mu\text{s}$ after impact, are shown in Figure 5. Comparison between the simulated crack pattern and that of the experiment [10] are again very encouraging.



a) Results from Experimental firing, Strassburger[17], b) AUTODYN-3D Simulation

Figure 5 Steel projectile impacting SiC at 185m/s

KEP PENETRATOR ONTO REINFORCED CONCRETE

Simulations of KEP impacts onto concrete using the Lagrange, SPH and Euler processors of AUTODYN-2D have previously been compared against experiment [11], [12]. Here the case of a 20kg KEP penetrator impacting a concrete target normally at 520m/s is used. The penetrator has a calibre of 90mm, an overall length of 388mm, and an ogive nose with calibre head radius (CHR) of 2.5. The plain concrete target was 1m thick with diameter 3m. The deceleration of the penetrator during the trial firing was recorded via onboard accelerometers. Simulations of these experiments have now been repeated in AUTODYN-2D using the latest constitutive models; RHT concrete [2] with tensile crack softening.

The Lagrange processor was used to represent the KEP penetrator. The penetrator was observed to undergo little or no deformation during the trial firings. A linear equation of state and elastic strength model was used to represent the penetrator material.

The concrete experiences large deformation local to the penetrator and cracking occurs over large regions of the target. The SPH solver is used in the target region that experiences large deformations. Further, a size (smoothing length) of 10mm was used for the SPH particles in all simulations. Regions that are not expected to experience large distortions were modelled using the Lagrange solver. Uniform square cells of side 10mm were used in all cases to a radius of 750mm. The cell radial size was then gradually increased to the radial extent of the target (1500mm). The meshfree and element based regions of the model are coupled using the technique described in [12].

The constitutive relations used to describe the concrete material contain three components: Firstly, the volumetric compaction of the material under high pressure was modelled using a "p-alpha" equation of state. Secondly the RHT concrete model was used to represent the material deviatoric behaviour in compression. Finally, the tensile crack softening model is used to represent the tensile material fracture and failure. The material data input was taken from that derived in [2].

Comparisons of the simulated penetrator deceleration and trial are given in Figure 6 along with the experimental result [11]. The simulation results show good correlation with the trial readings up to approximately 0.5m penetration. After this time, the predicted deceleration follows a similar path to that of the trial but at a slightly lower level. Note that the spike in the trial deceleration trace at

approximately 0.3m penetration is thought to be due to the instrumentation rather than physical phenomena.

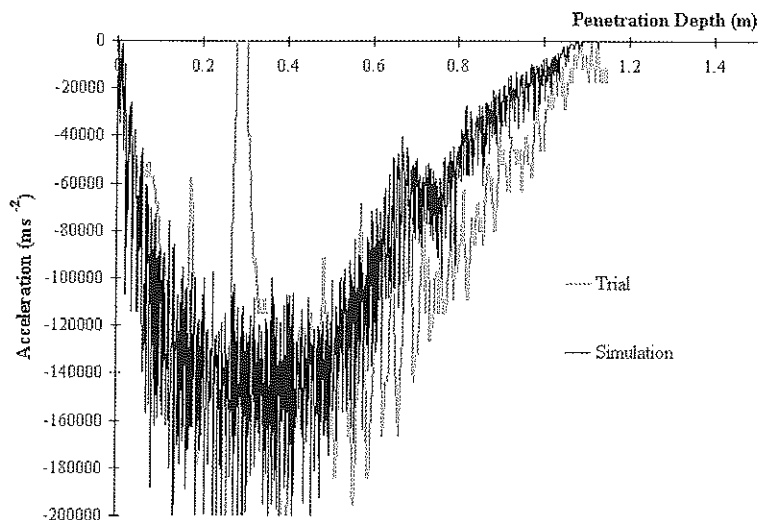


Figure 6 KEP Impact onto Concrete at 520m/s, Deceleration of projectile

The simulated concrete damage is shown in Figure 7. The dark regions indicate material in which tensile damage (cracking) covers more than 95% of the volume of the integration point.

The simulated back face spall diameters are in close agreement with the measured trial values of 2200mm±200 [11]. The front face spall diameters are slightly over predicted compared with the measured trial values of 1500mm ±150 [11].

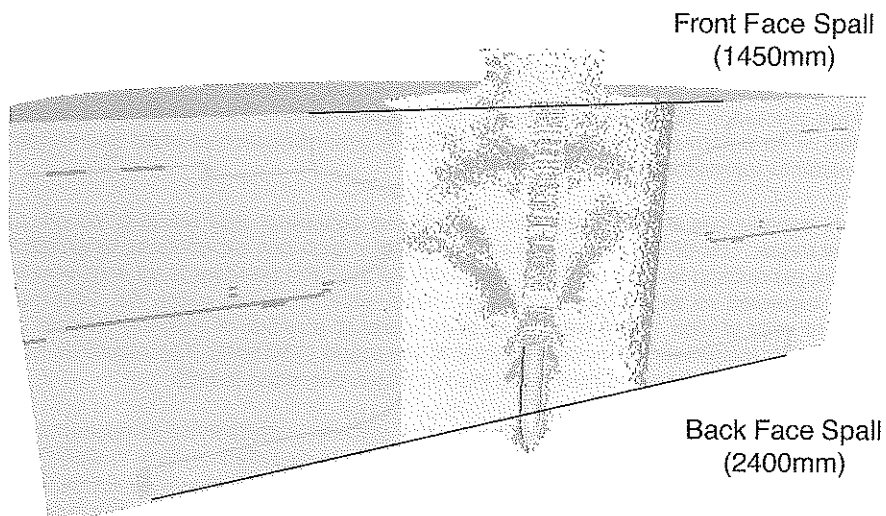


Figure 7 KEP Impact onto Concrete at 520m/s, Concrete Damage

CONCLUSION

The implementation and application of a tensile crack softening model in AUTODYN has been described. This model allows a continuum representation of fracture and crack growth in brittle materials due to principal tensile stresses. The model can be combined with any elastic-plastic constitutive relations for brittle materials in which damage is assumed to result from only deviatoric stresses. The damage law associated with the tensile crack softening model requires a single material input parameter, the critical strain energy release rate. Application of the tensile crack softening model to several ballistic impact problems on ceramic and concrete materials has been described.

For the two presented ceramic impact cases, the model is combined with the JH2 model for brittle glass/ceramic materials. The simulated extent of comminution, orientation and distribution of cone cracks, lateral cracking and spall regions compare encouragingly well with the experimental observations.

For the concrete impact case, the model is combined with the RHT model which was designed for concrete, and brittle materials in general. The simulation results again show good correlation with experiments in terms of penetrator deceleration and material fracture.

The tensile crack softening model described above is now available in the general release versions of AUTODYN-2D and 3D and continues to be applied to a wide range of applications both internally at Century Dynamics and externally by users of AUTODYN.

ACKNOWLEDGMENTS

The authors wish to thank Dr A.J. Sheridan of DSTL, UK for part funding the initial model development work on crack softening.

REFERENCES

1. Johnson G.R., and Holmquist T.J., "An Improved Computational Constitutive Model for Brittle Materials", in *High Pressure Science and Technology-1993*, AIP Press, 1994, pp.981-984.
2. W. Riedel, "Beton unter dynamischen lasten, Meso- und makromechanische modelle und ihre parameter", PhD Thesis, EMI report no. 6/00, Freiburg, Germany, July 2000.
3. Hazell P.J., "The Failure of Ceramic Armour Subjected to High Velocity Impact", *EngD Thesis*, Royal Military College of Science, UK, 1998.
4. Hayhurst C.J., Clegg R.A. "The Application of SPH Techniques in AUTODYN-2D ...", in *Proc. 16th Int. Symp. on Ballistics*, San Francisco, 1996, pp.409-417.
5. Johnson G.R., Cook W.H., "A Constitutive Model and Data for Metals ...", in *Proc. 7th Int. Symp. on Ballistics*, The Hague, 1983.
6. Feenstra P.H., deBorst R., "The Rankine Plasticity Model for Concrete Cracking", in *Computational Plasticity, Theory and Applications*, edited by Owen and Onate, Pineridy Press, UK, 1992, pp. 657-668.
7. Bazant Z.P., "Fracture Mechanics of Concrete Structures....", in *FraMCoS*, Elsevier Applied Science, 1992.
8. Crisfield M.A., *Non-linear Finite Element Analysis of Solids and Structures*, John Wiley, Chichester, 1997.
9. Anderson C.E., Johnson G.R., Holmquist T.J., "Ballistic Experiments and", in *Proc. 15th Int. Symp. on Ballistics*, Israel, 1995, pp65-72.
10. Strassburger E., Senf H., "Experimental Investigation of Wave and Fracture Phenomena in Impacted Ceramics", EMI report 3/94.
11. Clegg, R.A., Sheridan, A.J., Hayhurst, C.J. The application of SPH techniques in AUTODYN-2D to kinetic energy penetrator impacts on multi-layered soil and concrete targets. *Proc. of the 8th Int. Symp. Interaction of the Effects of Munitions on Structures. 1997.*
12. Clegg R.A., Hayhurst C.J., Meuric O.F. Combined Mesh and Meshfree Numerical Techniques to Efficiently Predict the Response of Concrete Structures to Impact. *In Proc of Structures under Shock and Impact. 2000.*

13. AUTODYN-2D & 3D User Documentation, Century Dynamics, 2002
14. Holmquist T.J., Johnson G.R., Response of silicon carbide to high velocity impact. J. Appl. Phys, vol 91, no 9, May 2002.
15. Hayhurst C.J., Clegg R.A., Cowler M.S., New generation 3D Hydrocode Developments including Advanced Visualisation, Parallelisation and Coupled Solvers, New Models and Hydrocodes for Shock Wave Processes in Condensed Matter, Edinburgh, Scotland, 19-24 May 2002.
16. M. S. Cowler, O. La'adan, T. Ohta, High Performance Computing using AUTODYN-3D, 6th International Conference on Applications of High-Performance Computers HPC 2000, Maui, Hawaii, 26-28 Jan 2000.

CONTACT

For further information about the material models and numerical methods contained in this paper, please send an email to richard.clegg@centurydynamcis.co.uk / colin.hayhurst@centurydynamcis.co.uk or visit www.centdyn.com.

Experimental and Numerical Investigations on Size Effect of Impact Taylor Testing

Hervé Couque and Lionel Cazenave

Giat Industries, Weapon and Ammunition Division, 7 route de Guerry, 18023 Bourges Cedex, France

ABSTRACT

Taylor testing has been recently used to compare dynamic compression failure properties of ductile materials initiating through shear banding. Comparison of failure data generated with different specimen sizes has been examined through an experimental-numerical investigation. Symmetric Taylor testing of a tungsten alloy was conducted with specimen 6 and 9 mm in diameter and 24 and 36 mm in length. Simulations were conducted with the finite element hydrocode AUTODYN 2D. A Johnson-Cook law calibrated with compression tests conducted at strain rates ranging from 1 to 5000 s^{-1} and at temperatures ranging from 23 to 320 °C was used. Results indicate a decrease of the impact speed characterizing the onset of failure either with the increase of the specimen diameter or with the decrease of the specimen length. Within the size range investigated, the increase of the specimen length implies an increase of the final diameter on initial diameter ratio associated to an increase of the effective plastic strain. The increase of the specimen diameter results in an increase of the maximum shear stress along the radial and tangential directions.

INTRODUCTION

Over the past fifty years, the Taylor test has been used as a mean to evaluate dynamic mechanical properties [1,2]. It has been primarily used to estimate the dynamic strength of metallic materials. Because the Taylor test involved stress and strain rate singularities, the Hopkinson pressure bars test generating dynamic stress-strain responses under a constant strain rate is currently employed to provide precise dynamic strength data. However, the strain rate limitations of the Hopkinson test of the order of $5 \times 10^3 s^{-1}$ motivate Taylor testing for which local strain rates up to $7.5 \times 10^4 s^{-1}$ can be achieved. Today Taylor tests are conducted to validate constitutive models of ductile materials calibrated with Hopkinson tests for strain rates ranging from 10^2 to $10^4 s^{-1}$. The validation is carried out by comparing experimental and numerical deformed profiles of the Taylor specimen. Another application is the evaluation of dynamic compression failure properties of ductile metals. By varying the impact speed from 200 to 350 m/s, Taylor testing is shown to be a mean of monitoring dynamic compression failure of ductile tungsten alloys occurring through shear banding [3].

While the specimen size effect on the estimate of the dynamic strength was found to be dependant on the material strain rate sensitivity [2,4], nothing is available on the two main Taylor specimen sizes, the length and the diameter, on the dynamic failure properties. The aim of this paper is to investigate the effect of the two main Taylor sizes on the failure properties of a ductile tungsten alloy. First, symmetric Taylor testing was conducted with specimen 6 and 9 mm diameters and 24 and 36 mm lengths. Second, a numerical investigation was conducted to establish the loading conditions associated with the failure initiation sites.

EXPERIMENTAL PROCEDURE

Taylor testing has been intensively used in the original configuration consisting of one cylindrical specimen impacting an anvil made of hard steel as to reproduce a rigid wall and usually referred as the single Taylor test [1]. To simulate the single Taylor test it requires to guess the friction coefficient between the specimen and anvil as well as to assume that the anvil is a rigid wall. With the symmetric loading procedure introduced by Erlich and al. [5], such hypotheses are no longer needed. When compared to single Taylor testing, symmetric Taylor testing involves one cylindrical specimen sent with a gas gun against another cylindrical specimen of identical shape and material sitting at the gun muzzle. Both specimens deformed without friction and the impact loading interface can be assimilated as a perfectly rigid wall. For the symmetric Taylor test, it is equivalent either to send two specimens against each other at a given speed V or, as in Erlich's configuration, to send one specimen at a speed $2V$ against a second specimen at rest. To allow direct comparisons between the two Taylor testing configurations, an equivalent impact speed, V_{eq} , is introduced corresponding to the impact speed for the single Taylor test and half the impact speed of the launched specimen for the symmetric Taylor test.

One inconvenient of Erlich's approach is the use of ceramic pins to locate the specimen sitting at the gun muzzle making difficult coaxial and planar impact of the two specimens. To facilitate planar and coaxial impacts, testing procedures involving Teflon sabots were developed [6]. These procedures address materials of strength ranging from 400 to 2000 MPa where Teflon sabots deforms along with the Taylor specimens.

Taylor data were generated by conducting symmetric Taylor testing using two specimens made of a tungsten alloy with 90% tungsten content in mass launched with a Teflon sabot following the procedure for high strength materials described in Ref. [6], see Figure 1. The Taylor experiments were conducted with specimens of lengths 36 mm and 24 mm and diameters 6 and 9 mm. The loading system consist of a 25 mm caliber gas gun launching, at impact velocities, V_i , ranging from 200 to 350 m s^{-1} , one Taylor specimen guided with a Teflon sabot against a second Taylor specimen located at the gun muzzle and positioned with another Teflon sabot, see Figure 1. The use of these Teflon sabots during the launch and during the loading phase of the Taylor specimens provides specimen guidance without interfering with the loading phase. A 18 mm two-laser beam device positioned 30 mm prior impact was used to measure the impact velocity V_i . X-rays observations were generated prior impact to identify the impact time and during the loading phase to provide intermediate specimen profiles.

Failure in tungsten alloys occurred along the maximum shear stress direction located at 45° from the principal stress direction which are the axial, radial and tangential directions of the Taylor specimen, Figure 2. For most of the tungsten alloys, the associated shear crack is preceded by an adiabatic shear band, see Figure 2b. To quantify the amount of shear fracture, shear crack lengths, a , were measured, Figure 2a. An average shear crack length, a_s , equal to the sum of the shear crack lengths divided by the number of shear cracks was deduced.

NUMERICAL PROCEDURE

Numerical simulations were conducted with the Lagrange processor of the finite-difference finite element hydrocode AUTODYN-2D [7]. Taylor simulations were conducted with a numerical model simulating the Taylor specimens, the Teflon sabots and the steel gun, see Figure 3. The mesh of the Taylor specimens was optimized by conducting simulations with different number of radial cells.

Convergence was obtained for a number of cells exceeding 32. As shown in Figure 4, the use of 41 cells indicate that the radius is about 5 μm less than the radius that one might obtained with an infinite number of cells. Such difference corresponds to a final diameter over initial diameter ratio, D_f/D_o , underestimated by 0.1%. Consequently, both 6 and 9 mm diameter specimens were composed of 41 cells in the plastically loaded region giving cells 73 μm and 110 μm in size for the 6 and 9 mm diameter specimens, respectively, see Figure 3c. The elastically loaded region was composed of coarser cells 220 μm in size.

High strain rate and temperature was taken into account using Johnson and Cook constitutive models [8]. The models express the equivalent stress as:

$$\sigma = (A + B \varepsilon_p^n) (1 + C \ln(\dot{\varepsilon}^\circ)) (1 - (T - 300) / (T_m - 300))^m$$

with ε_p , $\dot{\varepsilon}^\circ$, and T the equivalent plastic strain, the strain rate, and the temperature, respectively. The melting temperature, T_m , was chosen to be the melting temperature of the gamma phase, i. e. 1758 $^\circ\text{K}$ instead of the alpha phase, i. e. 3683 $^\circ\text{K}$. To calculate the temperature rise due to plastic deformation a Quinney coefficient of 0.9 was used along with a specific heat coefficient, C_{pe} , of 165 $\text{J/kg}^\circ\text{K}$. The model was calibrated to reproduce intermediate to high strain rates : 1, 2000 and 5000 s^{-1} at 20 $^\circ\text{C}$ and 2000 s^{-1} at 320 $^\circ\text{C}$. The five constants A, B, n, C and m were chosen to be 1350 MPa, 400 MPa, 0.4, 0.025, 1.27 as to reproduce by less than 5% the high strain rate and high temperature data as shown in Figure 5.

EXPERIMENTAL RESULTS

The influence of specimen size on shear crack formation of the tungsten alloy is shown in Figure 6 for the Taylor specimens of diameter 9 mm and length 36 mm (configuration 9x36) and for the Taylor specimens of diameter 6 mm and length 24 mm (configuration 6x24) and 36 mm (configuration 6x36). The data generated with the impacted specimen are identified as "impacted" and with the specimen sent with the gas gun as "projectile". The average shear cracks for the two specimens tested are also indicated. The decrease of the initial diameter or initial length implied an increase of the impact velocity. From these data, one can deduced a threshold impact speed, V_{co} , at which shear cracks initiate which is about 222 m/s for the 6 x 24 configuration, 209 m/s for the 6 x 36 configuration and 202 m/s for the 9 x 36 configuration.

The decrease of the threshold impact speed, V_{co} , with the increase of the Taylor diameter was first analyzed through the variation of the final diameter over the initial diameter ratio, D_f/D_o and the final length over the initial length ratio, L_f/L_o .

No significant differences were observed with regard to the final length over initial length ratio, L_f/L_o , between the three configurations. In an another hand, a significant increase of the ratio, D_f/D_o , is observed with the increase of the specimen length as shown in Figure 7. For an impact velocity of 243 m/s, the ratio D_f/D_o increase of 3% with the increase of the specimen length from 24 mm to 36 mm.

These differences appear to be associated with the loading duration increasing with the length implying a significant increase of the effective plastic strength of the specimen. Since shear band initiation occurs at a given effective plastic strain, different threshold impact speeds are reached with the 6 x 24 and 6 x 36 configurations. However, no explanation is provided for the differences observed with the diameter change.

NUMERICAL RESULTS

To provide insights of the effect of specimen sizes, a numerical investigation was undertaken with specimen sizes ranging from 6 to 18 mm in diameter and 24 to 36 mm in length. A large diameter configuration, 18 mm, for which no experimental data are available was considered to confirm the eventual dependence of the physical variables on the diameter.

The simulations were conducted at an impacted speed of 243 m/s for which final length and diameter are available. Table 1 reports a good agreement of the experimental and numerical ratios D_f/D_0 . In despite of the facts that no damage criteria as well no as no detailed strain rate dependence in the 10^3 10^4 s^{-1} regime was used. The numerical model confirms the increase of the ratio D_f/D_0 with the Taylor length. The experimental and numerical ratios L_f/L_0 are about constant. The overestimated numerical value of L_f/L_0 comes from the non detailed strain rate dependence in the 10^3 10^4 s^{-1} regime of the constitutive model based on numerical studies comparing experimental and numerical profiles conducted with single and symmetric Taylor tests [9].

Table 1. Experimental and numerical ratios D_f/D_0 and L_f/L_0 for an impact speed of 243 m/s.

Configuration	D_f/D_0		L_f/L_0	
	Experimental	Numerical	Experimental	Numerical
6 x 24	1.250	1.240	0.945	0.913
6 x 36	1.275	1.260	0.945	0.907
9 x 36	1.275	1.270	0.945	0.907

The increase of the ratio D_f/D_0 increase of 3% with the increase of the specimen length from 24 mm to 36 mm is confirmed to be associated with the loading duration as shown in Figure 8. The 6 x 24 configuration is deformed plastically up to 22 μs while the 6 x 36 and 9 x 36 are deformed plastically up to 30 and 34 μs , respectively. Up to 9 mm in diameter the strain rate histories are similar implying an effective plastic strain increasing with the loading duration i.e. the specimen length.

The plastic strain rate, axial stress, and pressure histories at shear band initiation sites located on the outside of the impacted diameter were not found to be significantly different. Differences were observed for the tangentials and radials stresses as revealed in the Figures 9 and 10. The tangential stresses increase of 200 MPa with the diameter increasing from 6 to 9 mm and of 500 MPa with the diameter increasing from 6 to 18 mm. The radial stress was found to decrease with the specimen diameter as expected due to inertia but to a less significant amount, i. e. 30 MPa. These variations imply a significant variation of the maximum shear stress along the tangential and radial directions with the increase of the diameter from 6 to 9 mm as shown in Table 2.

Table 1. Calculated maximum stresses in MPa at shear band initiation sites.

Configuration	σ_{XY}	σ_{XT}	σ_{YT}
6 x 36	500	900	260
9 x 36	450	850	390

CONCLUSION

Symmetric Taylor testing was conducted with specimen 6 and 9 mm in diameter and 24 and 36 mm in length to investigate dynamic compression failure properties of a tungsten alloy. Simulations were conducted with the finite element hydrocode AUTODYN 2D with a Johnson-Cook law calibrated with compression tests conducted at strain rates ranging from 1 to 5000 s⁻¹ and at temperatures ranging from 23 to 320 °C.

The impact speed characterizing the onset of failure initiated through shear banding decreases either with the increase of the specimen diameter or with the decrease of the specimen length. The increase of the specimen length implies an increase of the final diameter on initial diameter ratio associated to an increase of the effective plastic strain. The increase of the specimen diameter results in an increase of the maximum shear stress along the radial and tangential directions. Because critical effective plastic strain and critical shear stresses varied with the Taylor specimen sizes, it is necessary to compare failure data involving shear banding generated with different specimens sizes through numerical simulations of the Taylor tests.

ACKNOWLEDGMENTS

The authors express their thanks to J. P. Duparc, B. Salesse and F. Blier for their supports in the experimental work.

REFERENCES

1. G. I. Taylor, "The use of flat ended projectiles for determining yield stress. I: Theoretical considerations" G. I., Proc. Roy. Soc. London A 194 pp. 289-299, 1948.
2. M. L. Wilkins and M. W. Guinan, "Impact of cylinders on a rigid boundary", J. Appl. Phys., Vol. 44, N°3, pp. 1200-1206, 1973.
3. H. Couque, "On the Use of the Symmetric Taylor Test to Evaluate Dynamic Ductile Compression Fracture Properties of Metals", SUSI 1998, Computational Mechanics Pub., pp. 579-589, 1998.
4. J. U. Cazamias and S. J. Bless, "Scaling effects in penetration: a Taylor test approach", DYMAT 1997 Cf., J. Phys. IV France 7, pp. 115-120, 1997.
5. D. C. Erlich, D. A. Shockey and L. Seaman, "Symmetric rod impact technique for dynamic yield determination", Shock Waves Condensed Matter Cf., Amer. Inst. Phys. Eds., pp. 402-406, 1982.
6. H. Couque, "Symmetric Taylor testing procedures for material strength ranging from 400 to 2000 MPa", DYMAT 2000 Cf., J. Phys. IV France 10, pp. 179-184, 2000.
7. N. K. Birnbaum and M. S. Cowler, "Numerical simulation of impact phenomena in an interactive computing environment", IMPACT 1987 Cf., C. Chiem and all. Eds, pp. 881-888, 1987.
8. G. R. Johnson and W. H. Cook, "A constitutive model and data for metals subjected to large strains, high strain rates and high temperatures", 7th Int. Symp. Ballistics, pp. 541-547, 1983.
9. H. Couque, A. Lichtenberger and B. Salesse, "Study of dynamic plastic deformation of a nitrogen alloyed steel using single and symmetric Taylor testing", DYMAT 2000 Cf., J. Phys. IV France 10, pp. 353-358, 2000.

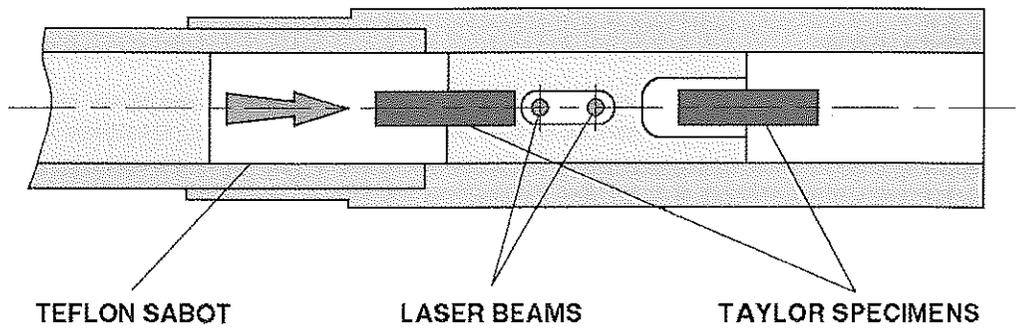


Fig. 1 Symmetric Taylor test schematic for the 9 x 36 specimens.

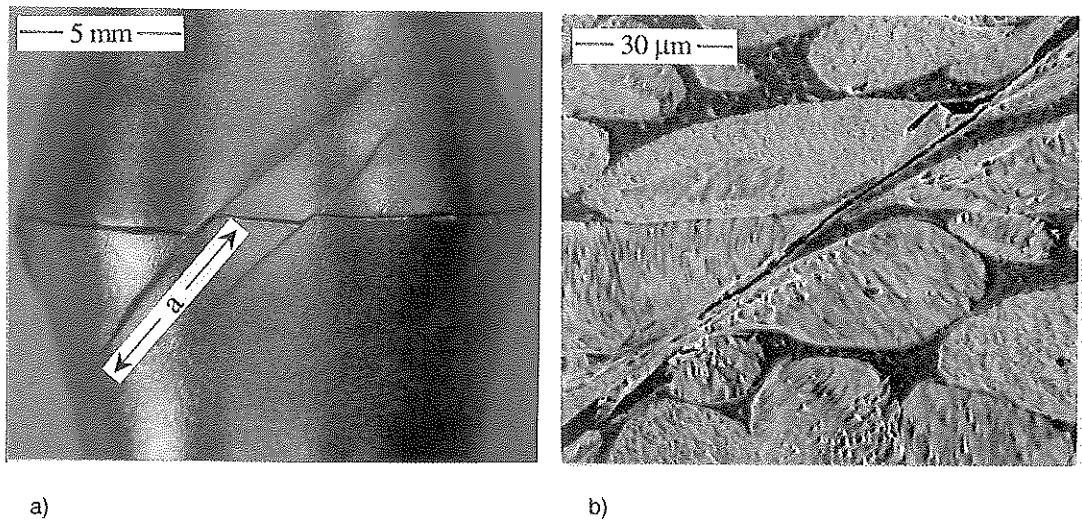
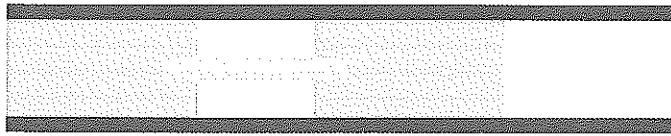


Fig. 2 Shear cracks observed on a swaged tungsten alloy Taylor specimen :
a) shear crack length a , b) shear crack path going through an adiabatic shear band.

4340 STEEL

TEFLON

W 6 X 24

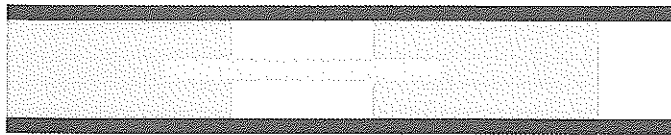


a)

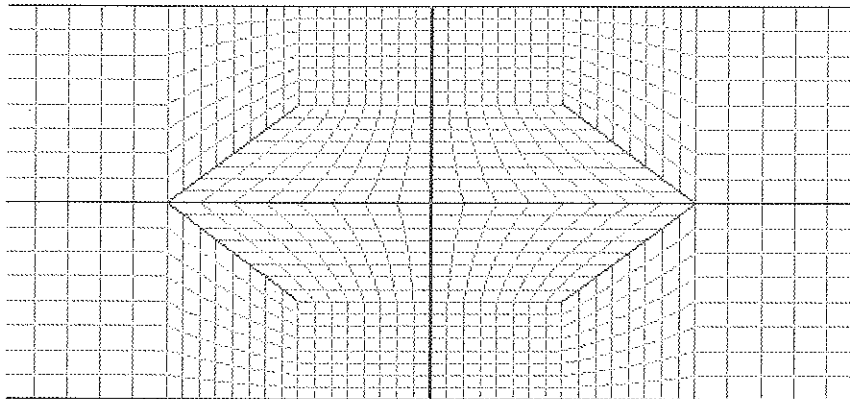
4340 STEEL

TEFLON

W 6 X 36



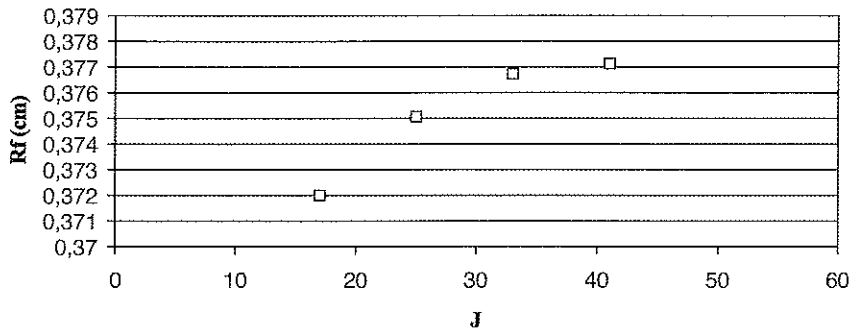
b)



c)

Fig. 3 Numerical schemes for the Taylor test :
a) 6 x 24 configuration b) 6 x 36 configuration c) refined zone at the impact location.

6 x 36



9 x 36

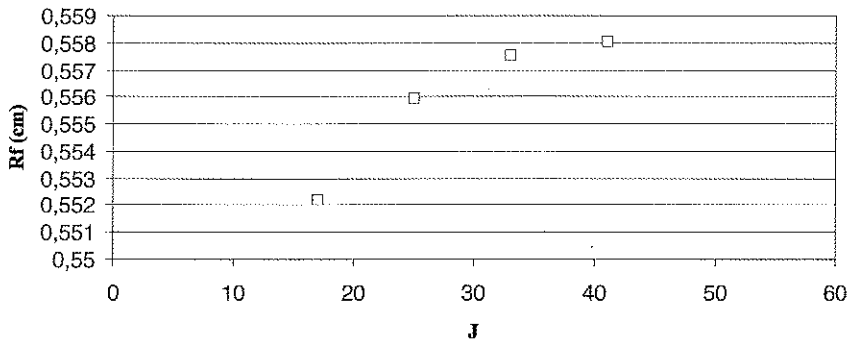


Fig. 4 Influence of the number of radial cells J on the final radius R_f for 6 x 36 and 9 x 36 Taylor configurations.

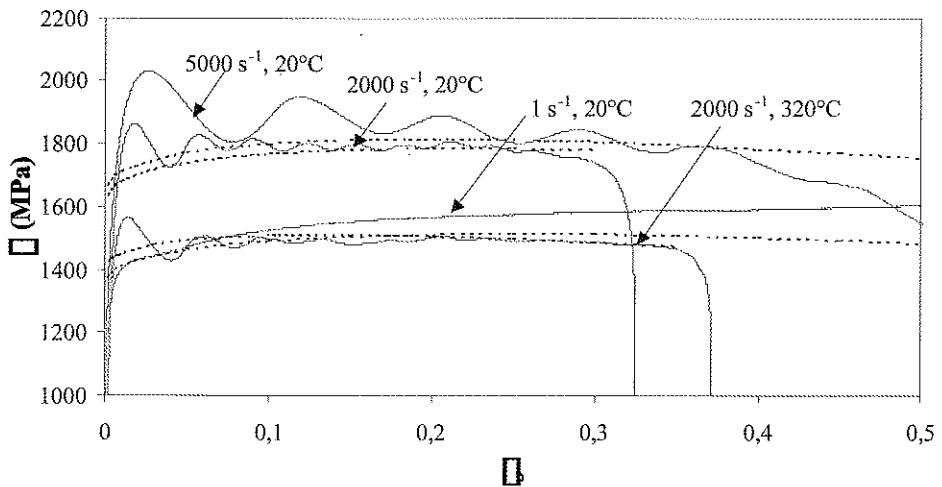


Fig. 5 Experimental and constitutive model stress-strain responses of the tungsten alloy.

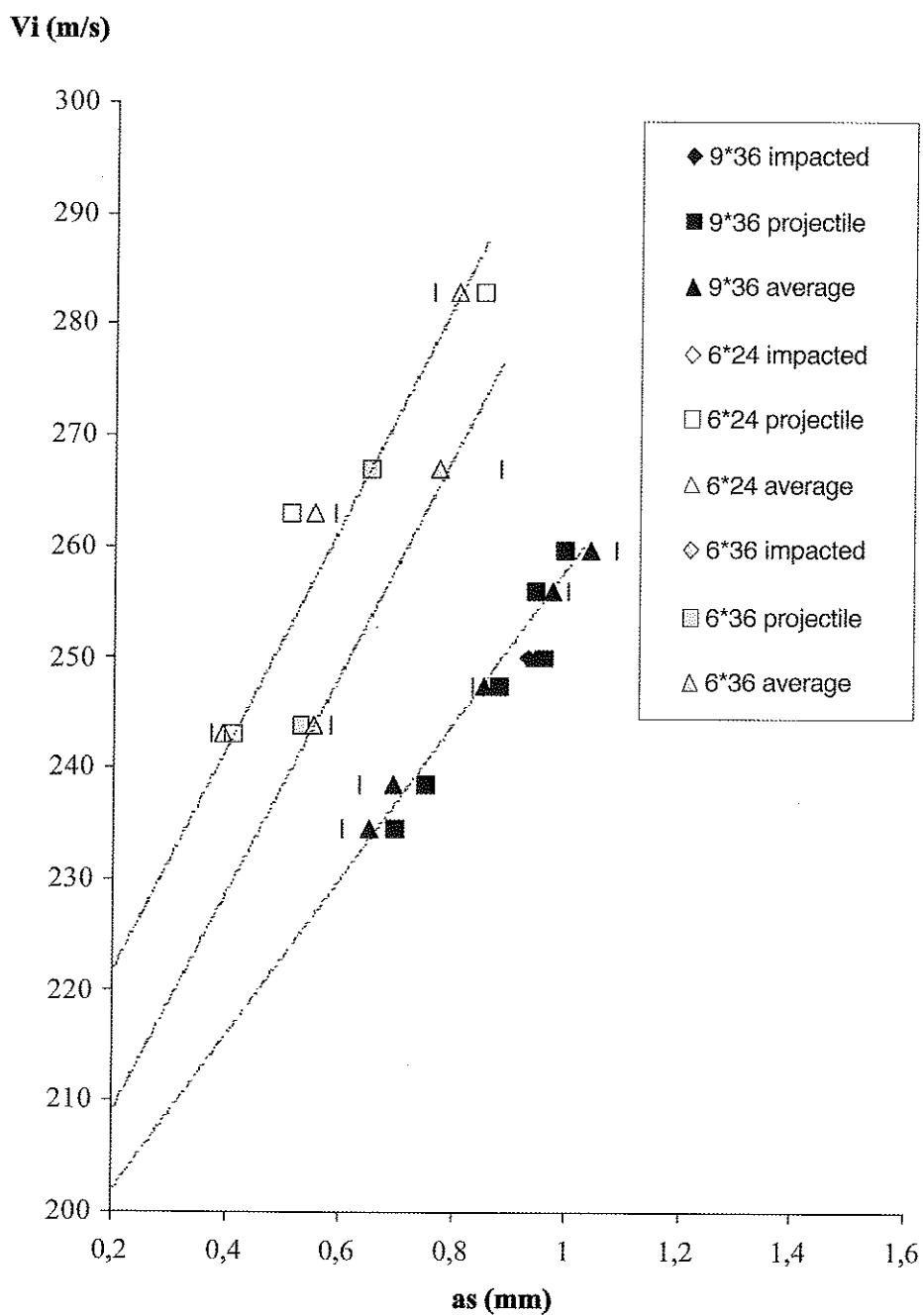


Fig. 6 Impact velocity as a function of the average shear crack length a_s for the 6 x 24, 6 x 36, 9 x 36 Taylor configurations.

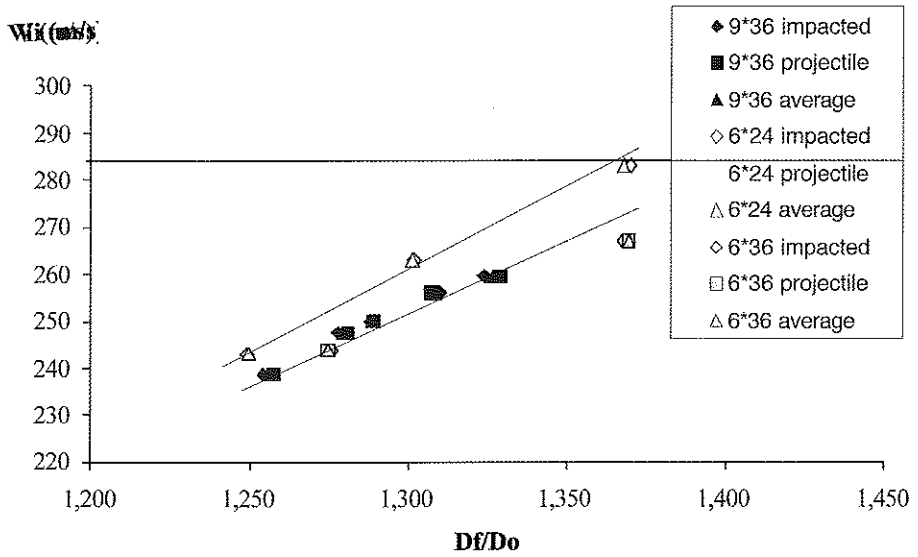


Fig. 7 Impact velocity as a function of the diameter ratio D_f/D_o for the 6 x 24, 6 x 36 and 9 x 36 configurations.

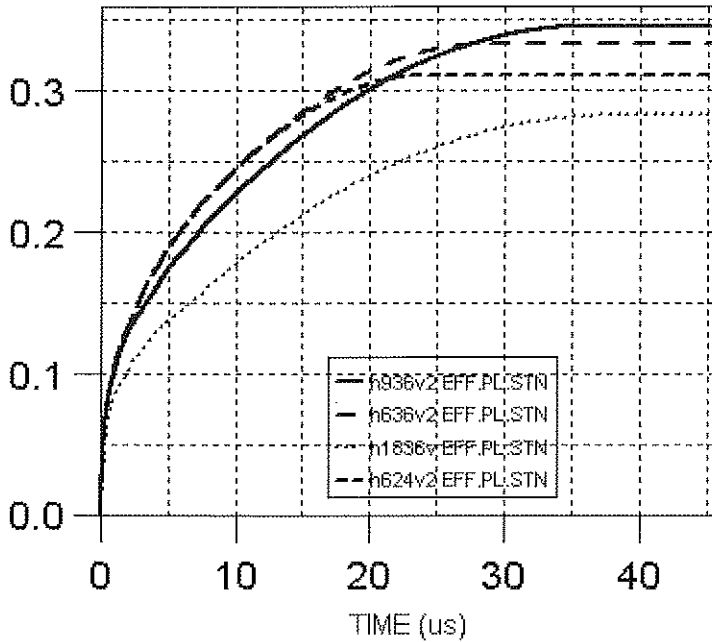


Fig. 8 Effective plastic strain at shear band initiation sites for the 6 x 24, 6 x 36, 9 x 36 and 18 x 36 configurations. The impact velocity is 243 m/s.

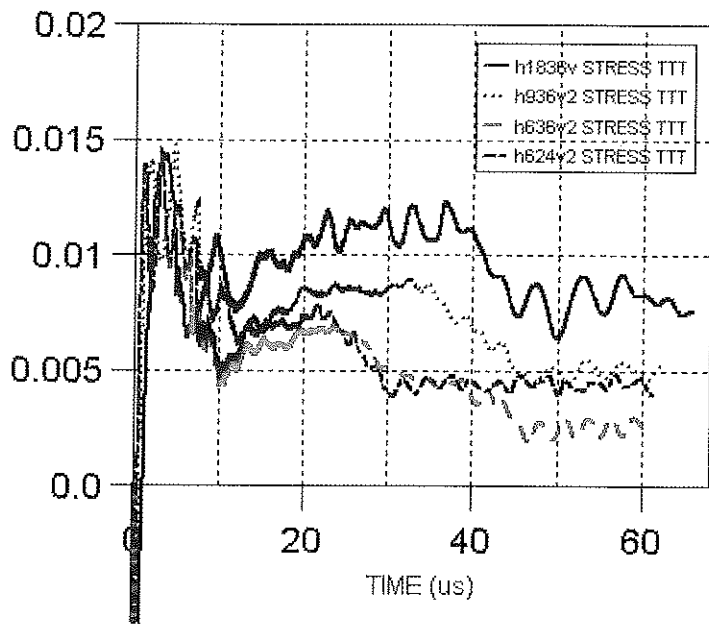


Fig. 9 Tangential stress ($\times 10^9$ MPa) at shear band initiation sites for the 6 x 24, 6 x 36, 9 x 36 and 18 x 36 configurations. The impact velocity is 243 m/s.

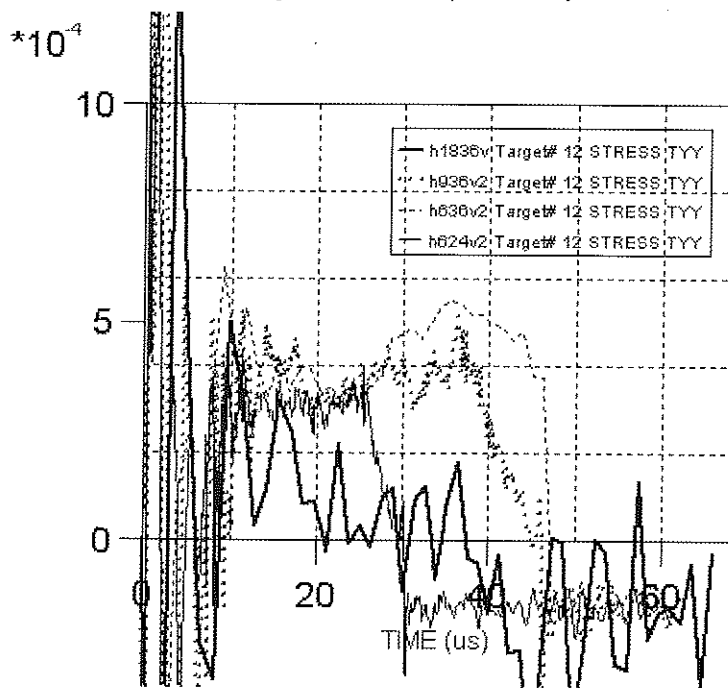


Fig. 10 Radial stress ($\times 10^5$ MPa) at shear band initiation sites for the 6 x 24, 6 x 36, 9 x 36 and 18 x 36 configurations. The impact velocity is 243 m/s.

A new shell element for composite structures with realistic transverse shear distribution: applications in static and dynamic.

F.Dau - LAMEFIP - ENSAM

Esplanade des Arts et Métiers - 33405 Talence - France

O. Polit - LMPX - Université Paris X

1 Chemin Desvallières - 92410 Ville d'Avray - France

M.Touratier - LMSP - UMR CNRS - ENSAM/ESEM

151 Bd de l'Hôpital - 75013 Paris - France

ABSTRACT

This paper deals with a new triangular finite element to analyse the behaviour of multilayered shells. This element is based on a refined kinematical model and uses both conforming finite element method and higher order approximations. Including a non-linear distribution with respect to the normal co-ordinate for transverse shear stresses and continuity requirements between layers for both transverse shear stresses and displacements, this model does not require any shear correction factors and allows to satisfy the boundary conditions at the top and bottom surfaces of the shell. Results in linear static, free vibrations and transient dynamic response for multilayered shells structures show the efficiency of this new shell finite element.

1 Introduction

Multilayered beam, plate and shell models are needed in structural mechanics for analyzing, dimensioning and designing this kind of structures. In the field of multilayered shells where transverse shear stress effects are of great importance, many high order shell theories exist, see for example [1] [2] [3] [4] [5], but a very few numerical tools have been developed.

In the recent litterature, a layer-wise technique has been used to develop a triangle finite element based on condensation technique at the pre-processing level in order to reduce the computational cost [6]. A three-dimensional shell element is presented by Klinkel [7]. These numerical tools are not pure structural models and suffer of the classical shear and membrane locking problems.

The aim of this work is to present a new finite element, simple to use, free from classical numerical problems and very efficient for computing both displacements and stresses for multilayered shell applications. This new C^1 shell finite element is based on the refined kinematic model given in [8] which incorporates :

- a cosine distribution for the transverse shear strains avoiding the use of shear correction factors ;
- the continuity conditions between layers of the laminate for both displacements and transverse shear stresses ;
- the satisfaction of the boundary conditions at the top and bottom surfaces of the shell ;

- the use of only five independent generalized displacements (three translations and two rotations),

A new finite element has been developed using both a conforming finite element method and high-order finite element approximations (Argyris interpolation for the transverse displacement and Ganev interpolation for membranes and transverse shear rotations). Some unavoidable geometric shell considerations are firstly presented to introduce necessary tools for shell description. In the second part of this paper, the shell model based on a kinematic approach is developed. The next part is dedicated to the finite element approximations and the present triangular finite element. Finally, some linear static tests for multilayered plates and shells are described. Linear free vibration and transient dynamic response tests are also evaluated in order to show the efficiency of this new finite element. It must be noticed that this efficiency is demonstrated for both convergence velocity and accuracy for displacements and stresses.

2 Geometric considerations

The shell \mathcal{C} with a middle surface \mathcal{S} and a constant thickness e is defined by :

$$\mathcal{C} = \left\{ M \in \mathcal{R}^3 : OM(\xi, \xi^3) = \vec{\Phi}(\xi) + \xi^3 \vec{a}_3; \xi \in \Omega; -\frac{1}{2}e(\xi) \leq \xi^3 \leq \frac{1}{2}e(\xi) \right\}$$

where the middle surface is described by a map $\vec{\Phi}$ from a bidimensional domain Ω as :

$$\begin{aligned} \vec{\Phi} &: \Omega \subset \mathcal{R}^2 \longrightarrow \mathcal{S} \subset \mathcal{R}^3 \\ \xi = (\xi^1, \xi^2) &\longmapsto \vec{\Phi}(\xi) \end{aligned}$$

At any point of the shell middle surface, the covariant basis vectors are usually obtained

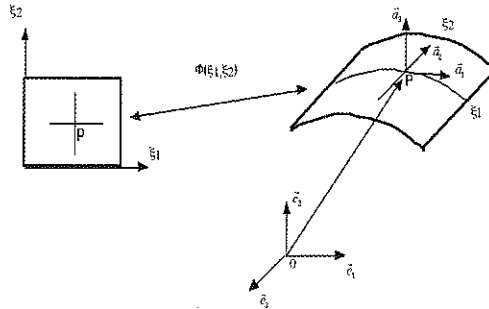


Figure 1: geometric transformation

as :

$$\vec{a}_\alpha = \vec{\Phi}(\xi)_{,\alpha} \quad ; \quad \vec{a}_3 = \frac{\vec{a}_1 \times \vec{a}_2}{\|\vec{a}_1 \times \vec{a}_2\|} \quad (1)$$

From these local covariant basis vectors, coefficients of the first and second fundamental forms are deduced, and we have :

$$\begin{aligned} a_{\alpha\beta} &= \vec{a}_\alpha \cdot \vec{a}_\beta \\ b_{\alpha\beta} &= -\vec{a}_\alpha \cdot \vec{a}_{3,\beta} = \vec{a}_3 \cdot \vec{a}_{\beta,\alpha} \end{aligned} \quad (2)$$

In Eq. (1) and further on, latin indices i, j, \dots take their values in the set $\{1, 2, 3\}$, while greek indices α, β, \dots take their values in the set $\{1, 2\}$. The summation convention on repeated indices and the classic notation $(\)_{,\alpha} = \frac{\partial(\)}{\partial \xi^\alpha}$ are used.

For any point of the shell, covariant base vectors are now expressed as follow :

$$\vec{g}_\alpha = \overrightarrow{OM}(\xi, \xi^3)_{,\alpha} = (\delta_\alpha^\beta - \xi^3 b_\alpha^\beta) \vec{a}_\beta = \mu_\alpha^\beta \vec{a}_\beta \quad \text{and} \quad \vec{g}_3 = \vec{a}_3 \quad (3)$$

where curvature tensor is defined by b_α^β .

The mixed tensor m_α^β must also be introduced. It is defined by the relation :

$$m_\alpha^\beta = (\mu^{-1})_\alpha^\beta = \frac{1}{\mu} \{ \delta_\alpha^\beta + \xi^3 (b_\alpha^\beta - 2H \delta_\alpha^\beta) \} \quad (4)$$

where $\mu = \det(\mu_\alpha^\beta) = 1 - 2H\xi^3 + (\xi^3)^2 K$; $H = \frac{1}{2} \text{tr}(b_\alpha^\beta)$; $K = \det(b_\alpha^\beta)$.

Finally, the contravariant vectors are constructed from the covariant vectors using the following equations :

$$\vec{a}^\alpha \cdot \vec{a}_\beta = \delta_\beta^\alpha \quad \vec{a}^3 = \vec{a}_3 \quad ; \quad \vec{g}^\alpha \cdot \vec{g}_\beta = \delta_\beta^\alpha \quad \vec{g}^3 = \vec{g}_3 \quad (5)$$

All these relations are classic and it is not necessary to give more details in order to obtain the Christoffel symbols and other differential geometric entities, see Bernadou [9].

3 The shell model

In order to define different shell models developed in this work, the displacement field is firstly introduced. Next, the methodology permitting to ensure continuity conditions and satisfaction of the boundary conditions at the top and bottom surfaces of the shell is presented. Finally, several strain models are presented according to usual assumptions.

3.1 The displacement field

From Beakou and Touratier [10], the displacement field of a shell point, for each elastic layer denoted (k) , is defined with respect to the contravariant base vectors \vec{a}^i by :

$$\begin{aligned} \vec{u}(\xi_1, \xi_2, \xi^3 = z, t)^{(k)} &= u_i(\xi_1, \xi_2, \xi^3 = z, t)^{(k)} \vec{a}^i \quad \text{where} \\ \begin{cases} u_\alpha(\xi_1, \xi_2, \xi^3 = z, t)^{(k)} &= \mu_\alpha^\beta v_\beta(\xi_1, \xi_2, t) - z v_{3,\alpha}(\xi_1, \xi_2, t) + F_\alpha^\beta(z)^{(k)} \gamma_\beta^0(\xi_1, \xi_2, t) \\ u_3(\xi_1, \xi_2, \xi^3 = z, t)^{(k)} &= v_3(\xi_1, \xi_2, t) \end{cases} \end{aligned} \quad (6)$$

In this expression, $\gamma_\alpha^0 = \theta_\alpha + b_\alpha^\beta v_\beta + v_{3,\alpha}$ are the two transverse shear strain components at the middle surface of the shell ($z = 0$) and we denote v_α the in-surface displacements, v_3 the transverse displacement and θ_α the two rotations of the transverse shell fiber. The functions $F_\alpha^\beta(z)^{(k)}$ of the transverse co-ordinate z , based on trigonometric functions, are determined from the boundary conditions on the top and bottom surfaces of the shell, and from the continuity requirements at each layer interfaces for displacements and stresses.

Eq. (6) for the displacement field is based on shallow shell theory and is extended hereafter to deep shells. Strains and stresses are classically denoted by $\epsilon_{ij}^{(k)}$ and $\sigma_{ij}^{(k)}$ for the k^{th} layer. Furthermore, the transverse normal strain ϵ_{33} is negligible according to the moderately thick shell hypothesis. The material behaviour is admitted linearly elastic and the shell lamination may be nonsymmetric and having angle ply layers.

From Beakou and Touratier [10], expressions for functions $F_\alpha^{\beta(k)}(z)$ are given by :

$$\begin{aligned} F_1^{1(k)}(z) &= f_1(z) + g_1^{(k)}(z) \quad ; \quad F_1^{2(k)}(z) = g_2^{(k)}(z) \\ F_2^{1(k)}(z) &= g_3^{(k)}(z) \quad ; \quad F_2^{2(k)}(z) = f_2(z) + g_4^{(k)}(z) \end{aligned} \quad (7)$$

where :

$$\begin{aligned} f_1(z) &= f(z) - \frac{e}{\pi} b_{55} f'(z) \\ f_2(z) &= f(z) - \frac{e}{\pi} b_{44} f'(z) \\ g_i^{(k)}(z) &= a_i^{(k)} z + d_i^{(k)} \quad i = 1, 2, 3, 4. \quad \text{and} \quad k = 1, 2, 3, \dots, N. \end{aligned} \quad (8)$$

with $f(z) = \frac{e}{\pi} \sin \frac{\pi z}{e}$ and N represents the number of layers. The present Sinus model, called (SIN-C), allows analyzing effects of interlayer requirements.

Classic shell models can be derived from this formulation :

- the present Sinus model without interlayer continuity (SIN) : $f_1(z) = f_2(z) = f(z)$, $g_i^{(k)}(z) = 0$
- the Reissner-Mindlin – Naghdi model (RM-N) : $f_1(z) = f_2(z) = z$, $g_i^{(k)}(z) = 0$
- the Kirchoff-Love – Koiter model (KL-K) : $f_1(z) = f_2(z) = 0$, $g_i^{(k)}(z) = 0$

Hereafter, the superscript (k) for $u_\alpha^{(k)}$ components is omitted in order to lighten notations.

3.2 The strain tensor

General expressions of the strain tensor are established from the displacement field of the shell model. The strain tensor is expressed with respect to the contravariant basis vectors and after some algebraic manipulations, the strain components are deduced as :

$$\begin{aligned} \epsilon &= \epsilon_{ij}(a^i \otimes a^j) \quad \text{with} \\ 2\epsilon_{\alpha\beta} &= \frac{1}{\mu} \left(\epsilon_{\alpha\beta}^0 + \epsilon_{\beta\alpha}^0 + F_\alpha^\nu(z) \epsilon_{\nu\beta}^1 + F_\beta^\nu(z) \epsilon_{\nu\alpha}^1 + G_\alpha^\nu(z) \epsilon_{\nu\beta}^2 + G_\beta^\nu(z) \epsilon_{\nu\alpha}^2 \right. \\ &\quad \left. + z \left\{ (b_\beta^\lambda - 2H\delta_\beta^\lambda) (\epsilon_{\alpha\lambda}^0 + F_\alpha^\nu(z) \epsilon_{\nu\lambda}^1 + G_\alpha^\nu(z) \epsilon_{\nu\lambda}^2) + \right. \right. \\ &\quad \left. \left. (b_\alpha^\lambda - 2H\delta_\alpha^\lambda) (\epsilon_{\beta\lambda}^0 + F_\beta^\nu(z) \epsilon_{\nu\lambda}^1 + G_\beta^\nu(z) \epsilon_{\nu\lambda}^2) \right\} \right) \\ 2\epsilon_{\alpha 3} &= \frac{1}{\mu} \left(F_\alpha^\nu(z) \gamma_\nu^0 + b_\alpha^\nu (F_\nu^\beta(z) - zF_\nu^{\beta'}) \gamma_\beta^0 \right. \\ &\quad \left. + z(b_\alpha^\nu - 2H\delta_\alpha^\nu) \left\{ F_\nu^{\beta'}(z) \gamma_\beta^0 + b_\nu^\beta (F_\beta^\lambda(z) - zF_\beta^{\lambda'}) \gamma_\lambda^0 \right\} \right) \end{aligned} \quad (9)$$

with $G_\alpha^\nu(z) = F_\alpha^\nu(z) - \delta_\alpha^\nu z$.

Furthermore, $H = \frac{1}{2}(b_1^1 + b_2^2)$ and $F_\nu^{\beta'}$ denotes z -derivative of F_ν^β .

By convenience, the following notations have been introduced in Eq. (9) to characterize the mechanical effects :

membrane strain : $\epsilon_{\alpha\beta}^0 = v_{\alpha|\beta} - b_{\alpha\beta} v_3$

bending strain 1 : $\epsilon_{\alpha\beta}^1 = \beta_{\alpha|\beta}$

bending strain 2 : $\epsilon_{\alpha\beta}^2 = b_\alpha^\lambda v_{\lambda|\beta} + b_{\alpha|\beta}^\lambda v_\lambda + v_{3|\alpha\beta}$

transverse shear strain : $\gamma_\alpha^0 = \beta_\alpha + b_\alpha^\beta v_\beta + v_{3,\alpha}$

where the notation $v_{\alpha|\beta}$ stands for the covariant derivation with respect to the ξ^β curvilinear co-ordinate.

At this stage, no hypothesis is carried out on the strain components : the coefficient $1/\mu$ which depends on the transverse co-ordinate z and curvature tensor components and all terms coming from the displacement field are preserved in the transverse shear strain expressions. This model is called the **complete model**. (SIN-C) model can be deduced from the **complete model** setting the transverse shear strains components to ensure **continuity** requirements.

$$\begin{aligned}
2\epsilon_{\alpha\beta} &= \frac{1}{\mu} \left(\epsilon_{\alpha\beta}^0 + \epsilon_{\beta\alpha}^0 + F_\alpha^\nu(z)\epsilon_{\nu\beta}^1 + F_\beta^\nu(z)\epsilon_{\nu\alpha}^1 + G_\alpha^\nu(z)\epsilon_{\nu\beta}^2 + G_\beta^\nu(z)\epsilon_{\nu\alpha}^2 \right. \\
&\quad \left. + z \left\{ (b_\beta^\lambda - 2H\delta_\beta^\lambda) (\epsilon_{\alpha\lambda}^0 + F_\alpha^\nu(z)\epsilon_{\nu\lambda}^1 + G_\alpha^\nu(z)\epsilon_{\nu\lambda}^2) + \right. \right. \\
&\quad \left. \left. (b_\alpha^\lambda - 2H\delta_\alpha^\lambda) (\epsilon_{\beta\lambda}^0 + F_\beta^\nu(z)\epsilon_{\nu\lambda}^1 + G_\beta^\nu(z)\epsilon_{\nu\lambda}^2) \right\} \right) \\
2\epsilon_{\alpha 3} &= \frac{1}{\mu} \left(F_\alpha^\nu(z)\gamma_\nu^0 \right)
\end{aligned} \tag{10}$$

4 The triangular six node finite element

The discrete formulation of the boundary value problem for the shells is deduced from the standard functional :

$$a(\bar{u}^h, \bar{u}^{*h})_{\cup\Omega_e} = f(\bar{u}^{*h})_{\cup\Omega_e} + F(\bar{u}^{*h})_{\cup\mathcal{C}_e}, \quad \forall \bar{u}^{*h} \tag{11}$$

In Eq. (11), $\cup\Omega_e$ is the triangulation of the multilayered structure and $\cup\mathcal{C}_e$ is its edges. In addition, \bar{u}^h is the finite element approximation of the displacement field \bar{u} given by Eq. (6) and \bar{u}^{*h} is the finite element approximation of the corresponding virtual velocity field \bar{u}^* . Linear functions f and F represent the body (including inertia terms) and surface loads, actually surface and line loads respectively due to the integration performed throughout the thickness of the shell. The superscript h introduced in Eq. (11) which indicates the finite element approximation, is also used for the finite element approximation of the generalized displacements v_i^h and θ_α^h shown in Eq. (6).

4.1 The finite element approximations

The geometry is approximated using the classic linear three nodes triangle.

In a conforming finite element approach, the displacement field, given by Eq. (6) requires that v_3^h has to be approximated by a C^1 -continuous function, while the other generalized displacements v_α^h and θ_α^h require a C^0 -continuous.

Therefore, we choose the Argyris [11] interpolation for the deflexion and the Ganev [12] interpolation, for the other generalized displacements. Note that the Argyris interpolation is exactly of continuity C^1 and the Ganev interpolation involves a semi- C^1 continuity which is not needed here.

The degrees of freedom associated with this kind of finite element in the local curvilinear base are :

- at a corner node :

$$\begin{array}{cccccc}
v_1 & v_{1,1} & v_{1,2} & v_2 & v_{2,1} & v_{2,2} \\
v_3 & v_{3,1} & v_{3,2} & v_{3,11} & v_{3,22} & v_{3,12} \\
\theta_1 & \theta_{1,1} & \theta_{1,2} & \theta_2 & \theta_{2,1} & \theta_{2,2}
\end{array} \tag{12}$$

- at a mid-side node :

$$\begin{aligned} & v_1 \quad v_{1,n} \quad v_2 \quad v_{2,n} \\ & v_{3,n} \\ & \theta_1 \quad \theta_{1,n} \quad \theta_2 \quad \theta_{2,n} \end{aligned} \quad (13)$$

where $p_{,n}$ is the derivative with respect to the normal direction of the edge of the element.

4.2 The elementary matrices

4.2.1 Elementary stiffness matrix

The elementary stiffness matrix $[K_e]$ is obtained by computing the bilinear form given in Eq. (11) at the elementary level as :

$$\begin{aligned} a(\vec{u}^h, \vec{u}^{*h})_{\Omega_e} &= \int_{\Omega_e} \int_{-e/2}^{e/2} [\epsilon_e^{*h}]^T [\bar{C}^{(k)}] [\epsilon_e^h] \mu dz \sqrt{ad} \Omega_e \\ &= \int_{\Omega_e} [E_e^{*h}]^T \left(\int_{-e/2}^{e/2} [B_e]^T [\bar{C}^{(k)}] [B_e] \mu dz \right) [E_e^h] \sqrt{ad} \Omega_e \\ &= \int_{\Omega_e} [E_e^{*h}]^T [A_e] [E_e^h] \sqrt{ad} \Omega_e \\ &= [Q_e^*]^T [K_e] [Q_e] \end{aligned} \quad (14)$$

Using the displacement field \vec{u} in Eq. (6) and the strain components in Eq. (9), the matrix $[B_e]$ can easily be deduced. The vector $[E_e^h]$ (identically for $[E_e^{*h}]$ adding the asterisk superscript), which may be seen as a generalized strain vector, is given by :

$$\begin{aligned} [E_e^h]^T &= \begin{bmatrix} v_1^h & v_{1,1}^h & v_{1,2}^h & : & v_2^h & v_{2,1}^h & v_{2,2}^h & : \\ v_3^h & v_{3,1}^h & v_{3,2}^h & v_{3,11}^h & v_{3,12}^h & v_{3,22}^h & : \\ \theta_1^h & \theta_{1,1}^h & \theta_{1,2}^h & : & \theta_2^h & \theta_{2,1}^h & \theta_{2,2}^h &] \end{bmatrix} \end{aligned} \quad (15)$$

The finite element approximations, defined at the above Section 4.1, are directly used to express the matrix $[E_e^h]$ as a function of the degrees of freedom vector $[Q_e]$ at the element level (see Eq. (14) and Eq. (15)).

Finally, $[A_e]$ contains the linearly elastic material behaviour matrix for a multilayered shell which results of the integration with respect to the thickness co-ordinate. This matrix incorporates also the classic geometrical characteristics of shells.

4.2.2 Elementary mass matrix

The consistent elementary mass matrix $[M_e]$ is immediately computed, using the same method that for the stiffness one, and we have :

$$\int_{\Omega_e} \int_{-e/2}^{e/2} \rho_e [u^{*h}]^T [\ddot{u}^h] \mu dz \sqrt{ad} \Omega_e = [Q_e^*]^T [M_e] [\ddot{Q}_e] \quad (16)$$

In this equation, $(\ddot{\cdot}) = \partial^2(\cdot)/\partial t^2$ and ρ_e is the mass density of the element Ω_e .

Finally, the load vector is similarly deduced and there is no need to develop its expression. All the mass and stiffness matrices, as well as the load vector, are integrated using 16 points.

5 Numerical evaluations

This new finite element has already been evaluated on classical shell tests for homogeneous structures [13] have . and very good results have been obtained.

This section is dedicated to numerical evaluations of this new finite element on multilayered structures.

The aim of the numerical tests is to characterize accuracy and convergence properties for both displacements and stresses in a multilayered case.

As indicated before (see Section ??), the Sinus model permits recovering other classical models specifying values for $f_\alpha(z)$ and $(g_i(z)^{(k)})$ for $i = 1, 4$. Numerical developments associated to the present six node triangular finite element, denoted GAG (for Ganev-Argyris-Ganev finite element approximations), give the opportunity to compare various models.

5.1 Static linear test on a cylindrical shell panel

R/a	a/e	models	\bar{v}_3	$\bar{\sigma}_{11}$	$\bar{\sigma}_{22}$	$\bar{\sigma}_{12}$	$\bar{\sigma}_{13}$	$\bar{\sigma}_{23}$
1	5	Elas.	2.716	-1.293	2.411	0.4371	0.4447	0.3442
		SIN-C	2.551	-1.250	2.239	0.4151	0.4352	0.3020
		SIN	2.193	-1.016	1.927	0.3563	0.3072	0.3187
1	10	Elas.	1.153	-0.8534	1.602	0.2725	0.4697	0.1848
		SIN-C	1.168	-0.8638	1.617	0.2799	0.4803	0.1819
		SIN	0.982	-0.7498	1.365	0.2376	0.3143	0.1891
4	5	Elas.	2.118	-1.022	1.116	0.2588	0.3867	0.2729
		SIN-C	2.048	-1.043	1.079	0.2508	0.4048	0.2489
		SIN	1.937	-0.923	1.024	0.2358	0.2930	0.2858
4	10	Elas.	0.9396	-0.7463	0.6468	0.1510	0.4271	0.1555
		SIN-C	0.9318	-0.7432	0.6415	0.1494	0.4434	0.1524
		SIN	0.8763	-0.7026	0.6076	0.1412	0.3029	0.1734

Table 1: Simply supported cross-ply cylindrical shell panel : finite element results for SIN and SIN-C models. Non dimensionalized deflexion and stresses are computed as in [14]

Numerical results are presented in this section for a simply supported cross-ply cylindrical shell panel, see Fig. 2. The geometry of this cylindrical panel is defined by means of its radius R , its length b , its circumferential length $a = R\phi$. Geometrical, material and loading properties have been chosen as follows :

geometry : a rectangular shell with $R = 10.$, ratio $b/a = 3.$ and two ratios $R/a = 1, 4.$, is considered. Two thickness ratios $a/e = 5, 10$ are used.

boundary conditions and loading : this cross-ply cylindrical shell panel is simply supported at its edges, and is loaded by a transverse doubly sinusoidal pressure,

material properties : the shell has got three layers ($0^\circ, 90^\circ, 0^\circ$) of equal thickness and the lamina material properties are taken from Pagano [15] as :

$$E_1 = 25E_2 \quad G_{12} = G_{13} = 0.5E_2 \quad G_{23} = 0.2E_2 \\ \nu_{12} = 0.25$$

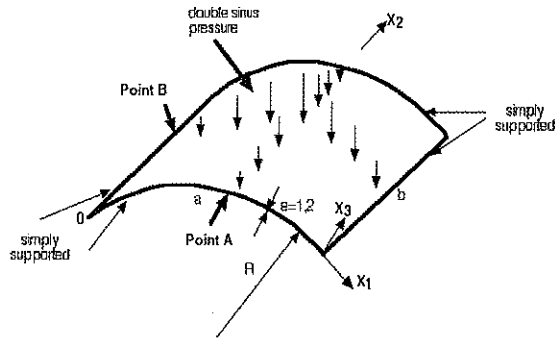


Figure 2: Three layers cylindrical panel under transverse doubly sinusoidal pressure

Numerical results obtained on this test with the present finite element (mesh $N=4$) are compared in Tab. 1 with the elasticity solution given by Huang [14].

Results from the present finite element are in good agreement with elasticity solutions for both transverse displacement and stresses, and the effect of the continuity condition is one more time very significant. For the most difficult case, $R/a = 1$ and $a/e = 5$ which is a deep thick shell, numerical results present the following deviations in comparison to an elasticity solution : $-6. \%$ for the transverse displacement, $(3., -7., -5.) \%$ for the stresses $(\sigma_{11}, \sigma_{22}, \sigma_{12})$, and finally $(-2., -12) \%$ for the transverse shear stresses $(\sigma_{13}, \sigma_{23})$.

5.2 Free vibration tests

For this test, a simply supported two-layer cross-ply cylindrical panel is considered and the first dimensionless natural frequency is compared with an analytical value given in [16]. Characteristics of this cylindrical panel are as follows :

geometry : a rectangular shell with $R = 4.$, $a = 2.$ and different ratios $L/a = 1, 2, 3, 4, 5$ are considered. The thickness is given by $e = 0.1$;

boundary conditions : this cross-ply cylindrical shell panel is simply supported at its edges ;

material properties : two layers $(0^\circ, 90^\circ)$ of equal thickness are considered and the lamina material properties are taken from [15] :

$$E_1 = 25E_2 \quad G_{12} = G_{13} = 0.5E_2 \quad G_{23} = 0.2E_2 \\ \nu_{12} = 0.25$$

Results from the present finite element, shown in Tab. 2, are in good agreement with the reference solution. One can observe that the KL-K model overestimates the first natural frequency for all the ratios while RM-N model underestimates this natural frequency. Deviations in comparison to analytical solution never exceeds 2% for SIN-C model.

5.3 Transient response

Implicit and explicit time integration schemes have been implemented to evaluate the capabilities in dynamics of this new finite element. Some tests have been performed on homogeneous plates and finally on multilayered shells. Parametric studies such as

L/a	Ref. [ber82]	SIN-C	KL-K	RM-N
1	11.71	11.66	11.74	11.54
2	7.35	7.28	7.42	7.24
3	6.58	6.49	6.65	6.43
4	6.32	6.23	6.40	6.19
5	6.22	6.11	6.28	6.08

Table 2: Free vibrations of a simply supported two layers cylindrical panel. Firstflexural eigenfrequency and comparison with an analytical solution.

sensitivity to the time integration on the transient response or damping factor influence on the dynamic behaviour have been accomplished validating the implementation. Uniform pressure and Dirac loading have been tested on simply supported cylindrical shell panel. The results obtained under Dirac loading are presented here.

Geometrical and material characteristics of this cylindrical panel, see Fig. 3, are as follows :

geometry : a rectangular shell with $R = 10.$, ratio $b/a = 3.$ and ratio $R/a = 1,$ is considered. Ratio $a/e = 10$ is used in this case.

boundary conditions and loading : this cross-ply cylindrical shell panel is simply supported at its edges, and is subjected to an impulsive normal load at its center.

material properties : the shell has got three layers ($0^\circ, 90^\circ, 0^\circ$) of equal thickness and the lamina material properties are taken from Pagano [15] as :

$$E_1 = 25E_2 \quad G_{12} = G_{13} = 0.5E_2 \quad G_{23} = 0.2E_2 \\ \nu_{12} = 0.25$$

Transient responses have been achieved on this multilayered panel. For each simulation, the results are in good agreement in comparison with 3D solid or shell finite element computations from Ansys Software.

The transient responses given by the present element and Shell93 element from Ansys Software are compared in Fig. 4. For this simulation, the Rayleigh damping factor value is $\beta = 0.001.$ A good agreement for the global dynamic responses of the panel is observed. On the other hand, Fig. 5 shows the evolution of the dynamic response when rayleigh damping factor increases. Responses are in agreement with theoretical results again. Finally, these first investigations in dynamics are very encouraging for future work, especially for impacts and damage studies in dynamics.

6 Conclusions

In this paper, a new triangular finite element has been presented to analyze the linear behaviour of multilayered shells in statics and dynamics.

The higher order shell theory used, which contains only five independent generalized displacements, allows satisfying exactly all the boundary conditions at the top and bottom surfaces of the shell and involves a non-linear transverse shear stress distribution avoiding the use of shear correction factors. Furthermore, interlaminar continuity for displacements and transverse shear stresses are taken into account with this model.

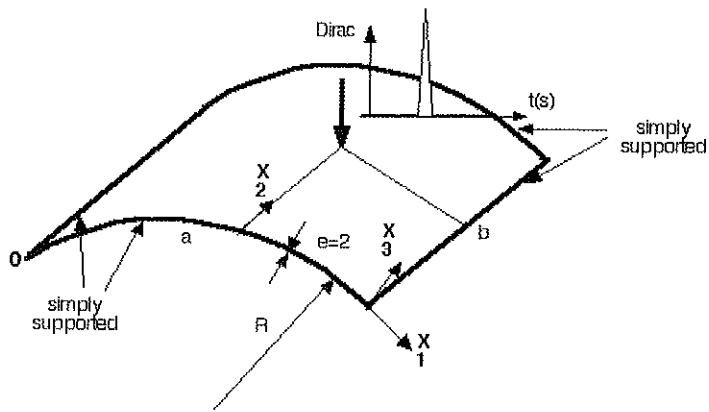


Figure 3: Laminated cylindrical panel for dynamic tests

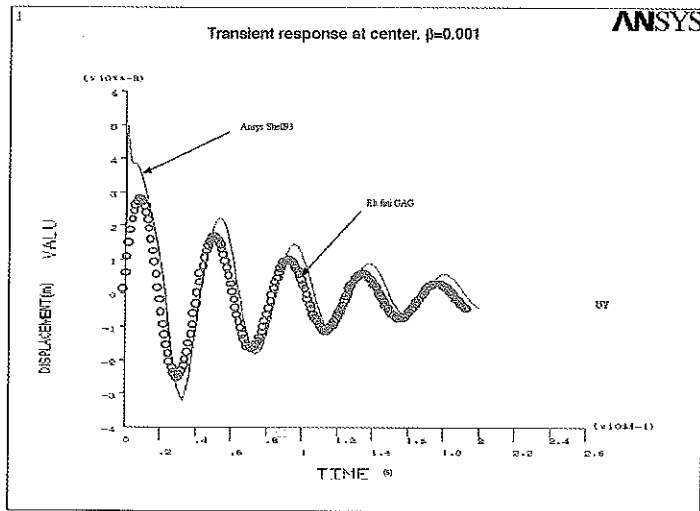


Figure 4: Compared response with numerical simulation from Ansys.

On the other hand, this finite element is free of transverse shear and membrane lockings, and several tests have shown its efficiency.

Present works have recently been followed by the introduction of a moderately large transverse displacement (von-Karman assumptions) for geometrically non linear applications.

References

- [1] J.N. Reddy and C.F. Liu. A higher-order shear deformation theory of laminated elastic shells. *Int. J. Eng. Sci.*, 23:319-330, 1985.
- [2] L.-H. He. A linear theory of laminated shells accounting for continuity of displacements and transverse shear stresses at layer interfaces. *Int. J. Solids Struct.*, 31(5):613-627, 1994.

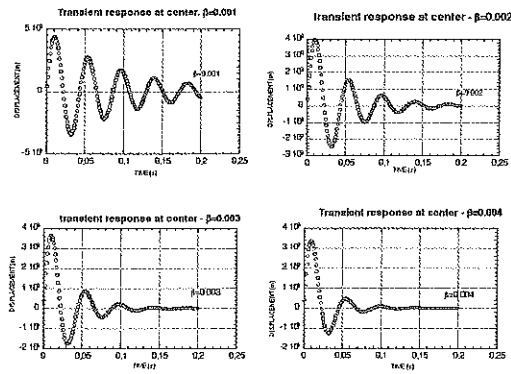


Figure 5: Transient response of cylindrical panel under impulsive excitation on its center - Rayleigh damping

- [3] M. Di Sciuva. A third order triangular multilayered plate finite element with continuous interlaminar stresses. *Int. Jour. Num. Meth. Eng.*, 38:1–26, 1995.
- [4] X.-P. Shu. A refined theory of laminated shells with higher order transverse shear deformation. *Int. J. Solids Struc.*, 34(6):673–683, 1997.
- [5] E. Carrera. Multilayered shells theories accounting for layerwise mixed description, part 1 : governing equations. *AIAA J.*, 37(9):1107–1116, 1999.
- [6] S. Botello, E. Onate, and J.M. Canet. A layer-wise triangle for analysis of laminated composite plates and shells. *Comp. and Struc.*, 70:635–646, 1999.
- [7] S. Klinkel, F. Gruttmann, and W. Wagner. A continuum based three dimensional shell element for laminated structures. *Comp. and Struc.*, 71:43–62, 1999.
- [8] M. Touratier. A refined theory of laminated shallow shells. *Int. J. Solids Struc.*, 29(11):1401–1415, 1992.
- [9] M. Bernadou. *Finite Element Methods for Thin Shell Problems*. John Wiley et Sons, 1996.
- [10] A. Béakou and M. Touratier. A rectangular finite element for analysing composite multilayered shallow shells in statics, vibration and buckling. *Int. Jour. Num. Meth. Eng.*, 36:627–653, 1993.
- [11] J.H. Argyris, I. Fried, and D.W. Scharpf. The tuba family of plate elements for the matrix displacement method. *Aero. J. Royal Aeronaut. Soc.*, 72:701–709, 1968.
- [12] H.G. Ganeev and Tch.T. Dimitrov. Calculation of arch dams as a shell using an ibm-370 computer and curved finite elements. In *Theory of shells*, pages 691–696. North-Holland, Amsterdam, 1980.
- [13] J.L. Batoz and G. Dhatt. *Modelling of structures by finite elements*. Hermès, Paris, 1992. (in french).
- [14] N. N. Huang. Influence of shear correction factors in the higher order shear deformation theory. *Int. J. Solids Struc.*, 31(9):1263–1277, 1994.

- [15] N.J. Pagano. Exact solutions for rectangular bidirectional composites and sandwich plates. *J. Comp. Materials*, 4:20-34, 1970.
- [16] C.W. Bert and M. Kumar. Vibration of cylindrical shells of bimodulus composite materials. *J. Sound Vibr.*, 81(1):107-121, 1982.

Modelling of material behaviour at high strain rates and temperatures for numerical simulations

E. El-Magd, C. Treppmann, M. Korthäuer

Department of Materials Science, RWTH Aachen (Germany)

ABSTRACT

Continuous constitutive equations for wide ranges of strain rates and temperatures are gaining increasing importance for adequate simulation of dynamic deformation processes. The flow behaviour of the carbon steel CK45N and the Titanium Alloy Ti6Al4V is studied at different strain rates between 0.001 s^{-1} and 10000 s^{-1} with temperatures varying 23°C and 1000°C .

In order to describe the material behaviour over this wide range different physical deformation mechanisms have to be considered. In addition to plastic deformation mechanism with relatively low strain rate sensitivity and weak temperature dependence, creep deformation processes have to be taken into consideration that are dominant in the range of high temperatures and low strain rates. Furthermore an additional stress increase caused by damping controlled mechanism is considered which accounts for the increase of strain rate sensitivity in the range of high strain rates. In case of steel a dynamic age hardening mechanism is superimposed leading to a stress increase between 300°C and 600°C according to strain rate. However a continuous description is achieved assuming that the different mechanisms are simultaneously active and hence they can be superimposed.

INTRODUCTION

The mechanical behaviour of materials at high strain rates is characterised by increased strain rate sensitivity, by the adiabatic character of the deformation process, by increasing effects of mass inertia forces and by the reflections of mechanical waves at the material boundaries. In this paper these effects are studied on CK45N and Ti6Al4V in dynamic compression tests on cylindrical specimens. The test temperature is varied between room temperature and 1000°C at strain rates up to 10000 s^{-1} .

EXPERIMENTAL INVESTIGATION OF THE MECHANICAL BEHAVIOUR

TEST PROCEDURE

The material behaviour of CK45N and Ti6Al4V at strain rates lower than 1000 s^{-1} was investigated using servo-hydraulic testing machines. At strain rates higher than 1000 s^{-1} the tests were realized with impact compression tests on a Split-Hopkinson bar arrangement. The start temperature can be increased up to 1000°C .

EXPERIMENTAL RESULTS

Figure 1 shows the flow curves of CK45N in quasi-static tests at strain rates of 0.001 s^{-1} and in dynamic tests at about 5000 s^{-1} in a temperature range from room temperature up to 1000°C . For the steel Ck45N a dynamic strain age hardening effect is observed at strain rates 0.001 s^{-1} at a temperature range between 250°C and 400°C leading to an increase of stress in this region. Also in the dynamic range of strain rates strain age hardening cannot be neglected. At 500°C the flow stress decreases while at 600°C a rising behaviour of the flow stress is noticeable.

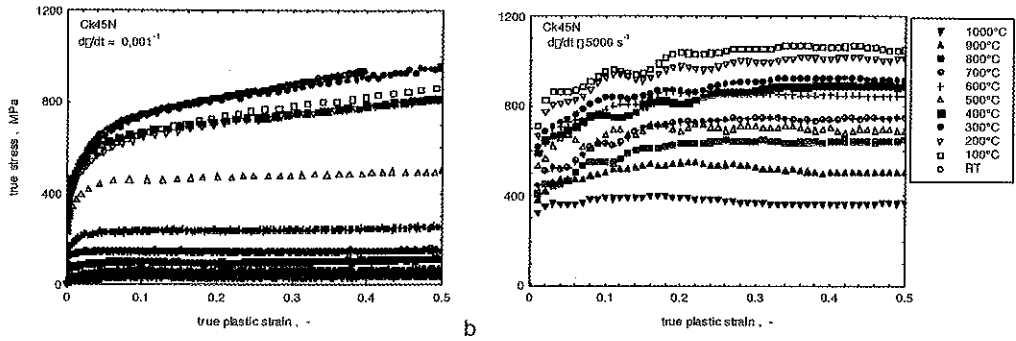


Figure 1: Comparison of flow curves of CK45N at strain rates 0.001 s^{-1} and 5000 s^{-1}

The material behaviour of Ti6Al4V is presented in Figure 2. The quasi-static flow curves with strain rates at 0.01 s^{-1} are represented in Figure 2a whereas the results of the impact compression tests determined using a Split-Hopkinson bar arrangement with strain rates of nearly 3000 s^{-1} are shown in Figure 2b. There are great differences between the flow stresses of each tested temperature. The influence of the strain rate on the flow stress depends to a great extent on the test temperature. At 900°C the true stress reaches a value of 500 MPa while in the quasi-static test this value is less than 80 MPa .

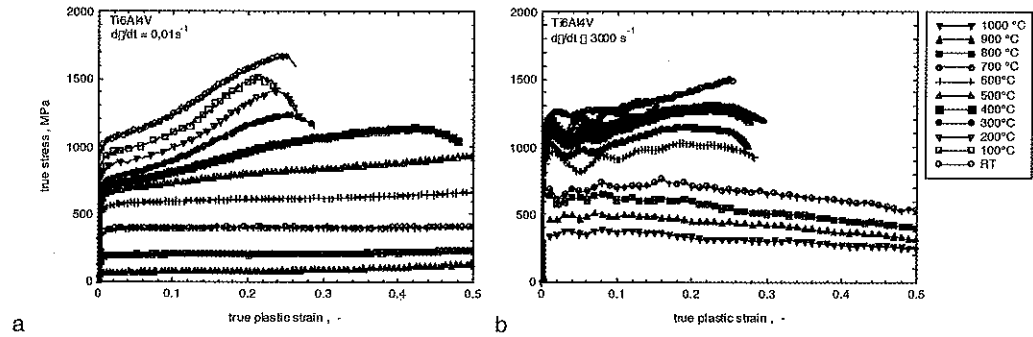


Figure 2: Comparison of flow curves of Ti6Al4V at strain rates 0.01 s^{-1} and 3000 s^{-1}

The temperature dependency for CK45N is shown in Figure 3a. Depending on the strain rate the material indicates an increase of the flow stress to a maximum lying between 300°C and 600°C due to dynamic age hardening effect. With increasing strain rate this stress maximum is shifted to higher temperatures at which the velocity of interstitial soluted atoms equals the dislocation velocity at this strain rate.

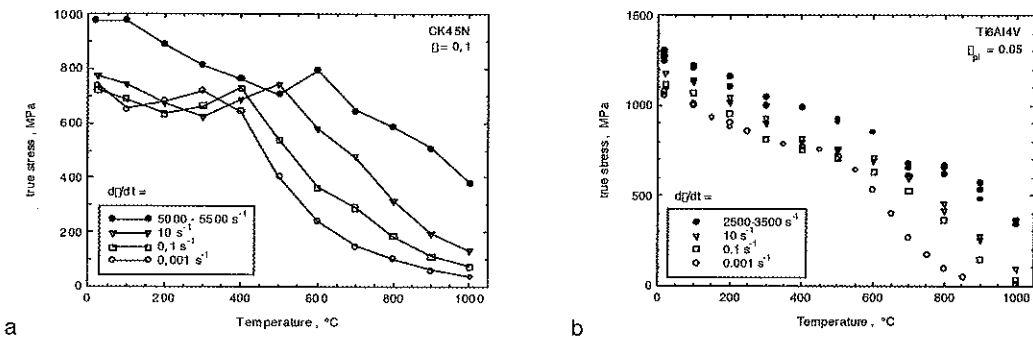


Figure 3: Temperature dependency of CK45N and Ti6Al4V at quasi-static and dynamic tests

Figure 3a presents the corresponding temperature dependency of the flow stress of Ti6Al4V at a plastic strain of 0.05. Over the whole investigated range of the temperature, the values of the flow stress determined in the dynamic tests are much higher than those determined in quasi-static tests. The difference increases with increasing temperature. Therefore no unique temperature function can be applied to the whole range of strain rates.

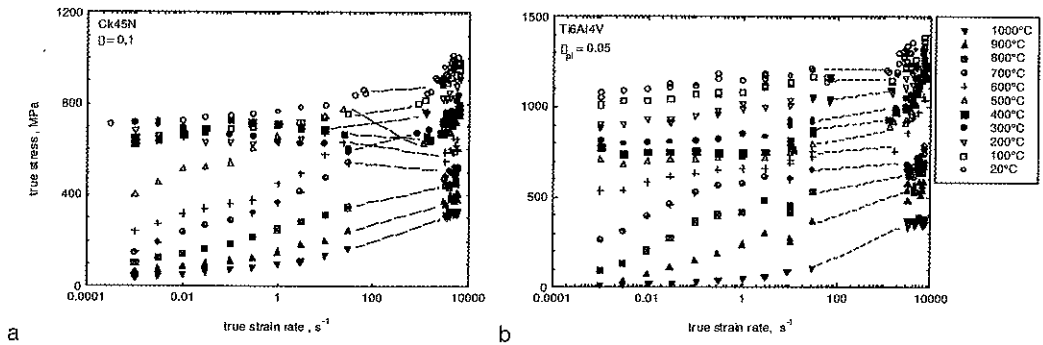


Figure 4: Temperature and strain rate dependency of CK45N and Ti6Al4V from $0.001 s^{-1}$ to $10000 s^{-1}$

Figure 4 shows the temperature and strain rate dependency of CK45N and Ti6Al4V in a range of strain rates between $0.001 s^{-1}$ and $10000 s^{-1}$ at a true plastic strain of $\epsilon = 0.1$ and $\epsilon = 0.05$. Three different regions can be distinguished in the figure. In the region of low temperatures and moderate strain rates, only a slight dependence of the flow stress on strain rate and temperature is observed. The usual plastic deformation mechanism dominates in this region. The strain hardening as well as the strain rate dependence can be described by power laws. At temperature higher than about $500^{\circ}C$, a greater influence of strain rate and temperature can be observed at low and moderate strain rates. This is caused by additional creep strains arising during the deformation tests. They can be considered either as an increase of strain for a given flow stress value, or as a reduction of the flow stress by stress relaxation. At high strain rates ($\dot{\epsilon} > 2000 s^{-1}$), the viscous damping deformation mechanism can be considered as dominant.

The presentation of the temperature and strain rate dependency of CK45 and Ti6Al4V under dynamic conditions of strain rate is shown in Figure 5. The stress for different values of strain follows a linear relation with the strain rate. The slope $\partial\sigma/\partial\dot{\epsilon}$ remains nearly constant between room temperature and $600^{\circ}C$, thereafter it decreases continuously with increasing temperature.

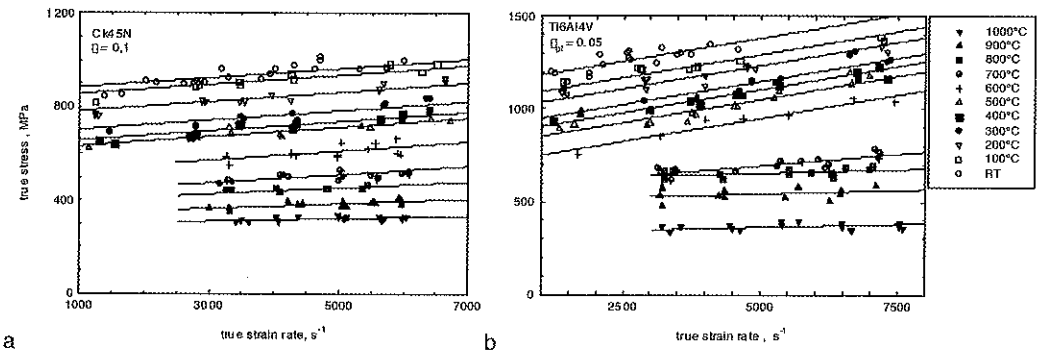


Figure 5: Temperature and strain rate dependency of CK45N and Ti6Al4V in a dynamic range of strain rate

CONSTITUTIVE EQUATIONS FOR THE WHOLE RANGE OF STRAIN RATE AND TEMPERATURE

Under dynamic conditions the mechanical behaviour can be described with damping controlled gliding according to [1,2]

$$\sigma = \sigma_G(T, \varepsilon) + \eta \cdot \dot{\varepsilon} \quad (1)$$

with

$$\eta = \frac{M_T B}{b^2 N_m} \quad (2)$$

where M_T , B , b , N_m are the Taylor factor, a damping constant, the burgers vector and the mobile dislocation density, respectively.

At lower strain rates the deformation is controlled by a combination of creep processes and plastic flow. So the complete strain rate range can be described as a combination of different strain rates [3,4]:

$$\dot{\varepsilon} = (1-M) \left(\dot{\varepsilon}_{cr} + \dot{\varepsilon}_{pl} \right) + M \cdot \dot{\varepsilon}_{damping} \quad (3)$$

where $M(T, \varepsilon, \dot{\varepsilon})$ is a transition function between dynamic and lower strain rates. Finally the following equation can describe the material behaviour in the whole range of strain rate and temperature:

$$\dot{\varepsilon} = (1-M) \left(\left(\frac{\sigma}{\sigma_o(T, \varepsilon)} \right)^{N(T)} + \left(\frac{\sigma}{\sigma_H(T, \varepsilon)} \right)^{1/n(T)} \right) + M \cdot \left(\frac{\sigma - \sigma_G(T, \varepsilon)}{\eta} + \dot{\varepsilon}_G \right) \quad (5)$$

This material model has the disadvantage that on the one hand the evaluation of many constants is necessary and on the other hand this description is only a transcendent function of stress. Thus there was a great demand of a reduction of parameters and a description like $\sigma = f(\varepsilon, \dot{\varepsilon}, T)$. The next part shows a possible solution for these demands.

The dependency $\sigma(\varepsilon)$ can be described by a strain hardening power law e.g. by Hollomon [5]

$$\sigma = K \varepsilon^n \quad (6)$$

Besides the influence of velocity at the range of low strain rates has to be considered with an exponential function [6].

$$\sigma = \sigma(\varepsilon, T) \cdot \dot{\varepsilon}^m \quad (7)$$

The linear damping effects should be described as known !Error! Marcador no definido.

$$\sigma = \sigma(\varepsilon) + \eta \cdot \dot{\varepsilon} \quad (8)$$

With the temperature dependency $\psi(T)$ the flow function can be given by

$$\sigma_o = \left(\sigma_h \varepsilon^m \varepsilon^n + \eta \dot{\varepsilon} \right) \Psi(T) \quad (9)$$

The creep behaviour at high temperatures and low strain rates should be roughly described in consideration of stress relaxation:

$$\sigma = \frac{\sigma_0}{\left(1 + \frac{(\sigma_0/\sigma^*)^v \dot{\epsilon}^*}{\exp(-T/T^*) \epsilon}\right)^{1/v}} \quad \text{with } \sigma^* = 1 \text{ MPa} \quad (10)$$

The following parameters can be used with CK45N:

$$\begin{aligned} T^* &= 202,84K & \sigma_h &= 605 \text{ MPa} \\ \dot{\epsilon}^* &= 15262 \cdot 10^{-32} \text{ s}^{-1} & m &= 0.01 \\ \nu &= 7 & n &= 0.17 \\ & & \eta &= 00242 \text{ MPa}\cdot\text{s} \end{aligned}$$

The temperature dependency $\psi(T)$ can be described by e.g.

$$\Psi(T) = \left[\exp\left(-\frac{T}{T_1}\right) + A \exp\left(-\frac{T}{T_2}\right)^7 \right] \quad (11)$$

with the following parameters:

$$A = 0.278, \quad T_1 = 1300 \text{ K}, \quad T_2 = 700 \text{ K}$$

Thereby the number of parameters of the constitutive equation for the whole range of strain rate and temperature could be halved. Besides the stress values can be calculated direct without any iterations.

For CK45N the dynamic strain age hardening effect should be considered with $\sigma = \sigma + R$

$$R = 140 \cdot \exp\left[-\left(\frac{T-700}{130}\right)^6\right] \cdot \exp\left[-\left(\frac{\ln(\dot{\epsilon}) - 0.023 \cdot T + 16.5}{9.0 - 0.01 \cdot T}\right)^2\right] \quad (10)$$

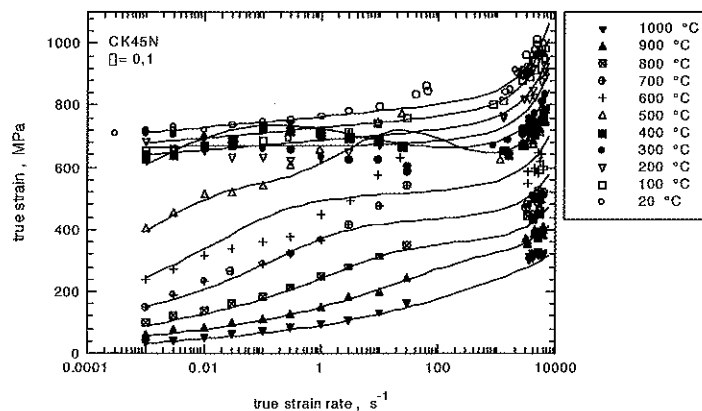


Figure 6: Description of the material behaviour of CK45N with the new model for the whole range of strain rate and temperature

APPLICATION: SIMULATION OF IMPACT SHEAR TESTS

Hat shaped specimens [7] were tested using a Split-Hopkinson Bar arrangement, in order to realize high strain rate deformation up to large strains under controlled conditions. The specimen is axisymmetrical with a narrow region of concentrated shear deformation. These tests were simulated with the explicit time integration finite element code Abaqus/Explicit in order to validate the material model eq. (5) at highest strain rates up to 300000 s^{-1} . Figure 7 shows the idealization of the specimen with boundary conditions. The motion of the upper bar was given by measured data from the experiment. The output bar was idealized with infinite elements, so no reflection of mechanical waves occurs during the simulation.

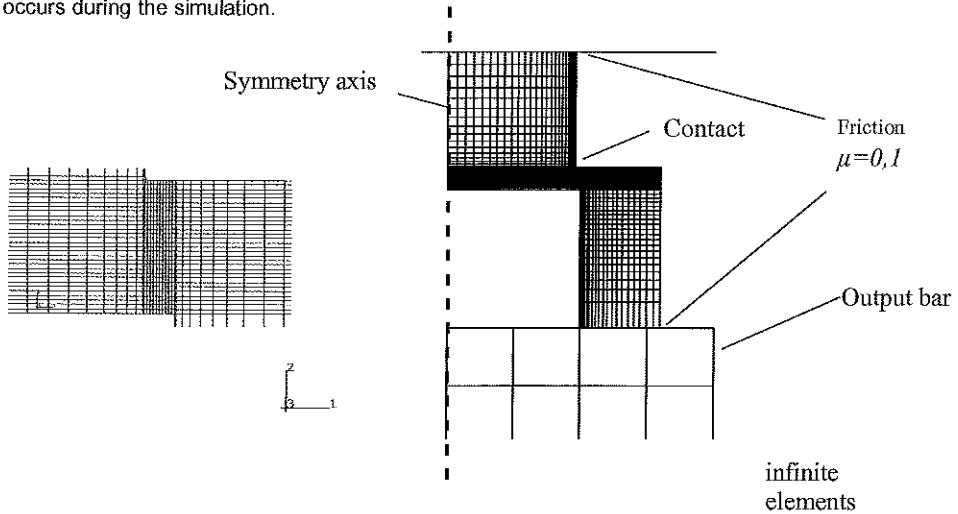


Figure 7: Idealisation of the hat-shaped specimen

The results of the measured data (symbols) and the numerical simulation (lines) are shown in Figure 8.

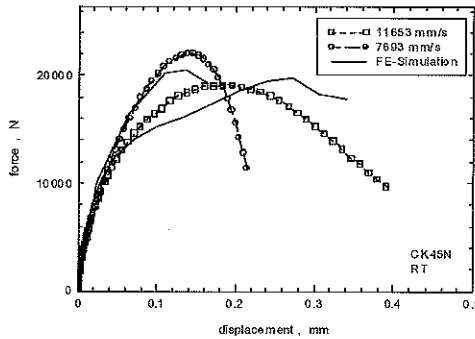


Figure 8: Comparison between simulation and material model of CK45N

CONCLUSION

Split-Hopkinson Bar and quasi-static compression tests were carried out on cylindrical specimens at different temperatures and strain rates between 0.001 s^{-1} and 10000 s^{-1} . The temperature dependency for CK45N and Ti6Al4V is measured in quasi-static and dynamic compression tests. For CK45N, strain age hardening effects are found at a temperature about 250°C up to 500°C at all investigated strain rates. Considering this temperature dependency, the material behaviour could be described for CK45N using a new material model based on Hollomon combined with the structure mechanical viscous damping behaviour and creep processes. The FE-Simulation is compared with the results of the experiments on hat shaped specimens using extrapolated flow curves up to strain rates of $3 \cdot 10^5 \text{ s}^{-1}$.

REFERENCES

- [1] El-Magd, E.: Journal de Physique III, Vol. 4, 1994, C8-149-170
- [2] Kumar, A., Hauser, F.E. and Dorn, J.E.: Act. met. 16(1968), 1189-1197
- [3] Treppmann, C.: PhD-Thesis, RWTH Aachen, Germany, 2001
- [4] El-Magd, E, Treppmann, C.: Dehnratenabhängige Beschreibung der Fließkurven bei erhöhten Temperaturen, Z. Metallkd., 92 (2001) 8, 888-893
- [5] Hollomon, J.: Tensile deformation, Trans. AIME, 162(1945), 268-290
- [6] Ludwik, P.: Über den Einfluß der Deformationsgeschwindigkeit bei bleibenden Deformationen mit besonderer Berücksichtigung der Nachwirkungserscheinungen, Physikalische Zeitschrift, 10 (1909) 12, 411-417
- [7] Hartmann, K.-H.; Kunze, H.-D.; Meyer, L.W.: Metallurgical Effects on Impact Loaded Materials, in: Shock Waves and High Strain Rate Phenomena in Metals, Eds.: M.A. Meyers and L.E. Murr, Plenum Press, New York 1981, p. 325-337

Dynamic Fragmentation of R-SiC Ceramics during Edge-On Impact Tests

Pascal Forquin, Lisa Tran, Pierre-François Louvigné, Laurent Rota

DGA/Centre Technique d'Arcueil
16 bis avenue Prieur de la Côte d'Or, F-94114 Arcueil Cedex, France

François Hild

LMT-Cachan, ENS de Cachan / CNRS-UMR 8535 / Université Paris 6
61 avenue du Président Wilson, F-94235 Cachan Cedex, France

ABSTRACT

The threat of small to medium caliber armor piercing projectiles requires efficient protections that can be achieved by using bilayered configurations. They consist in a front face made of a hard material and a backing made of a ductile material. These solutions are among the most interesting in terms of mass efficiency. To design such bilayered concepts, one needs to understand and model fragmentation of the ceramic during the first microseconds after impact. This cracking pattern may significantly influence the projectile / target interaction and reduce the multi-hit capability of the armor. A new material made of porous silicon carbide infiltrated with aluminum is considered. The presence of an aluminum skeleton may improve the residual strength after impact. The present study deals with a comparison of fragmentation properties of this new material with those of porous silicon carbide. Quasi-static experiments and edge-on-impact tests are performed. The role of aluminum is discussed. An anisotropic damage model coupled with a fragmentation study is used to analyze the experimental observations.

INTRODUCTION

Bilayered armors using hard materials such as ceramics (e.g., alumina, silicon carbide) as front plate and ductile materials (e.g., steel, aluminum alloy, composite or polycarbonate) as backing face have been studied for several years to improve the efficiency of light or medium armors [1]. This configuration was successfully explored by den Reijer [1]: a bilayered armor using an 8.1 mm thick alumina tile as front plate and a 6mm thick aluminum plate as backing face was able to stop a 7.62 mm AP projectile. Radiographs of the projectile / target interaction shot with an x-ray pulsers set-up (600 kV) permitted the observation of the entire projectile erosion. This projectile failure and erosion is made possible by the high strength of ceramic materials in compression (more than twenty times greater than the tensile strength) [2]. Moreover a wide deformation of the aluminum plate was observed within a zone approximately 75 mm large. Two functions of the backing face are met: first, to absorb the impact energy as much as possible by plastic dissipation, second, to increase the confinement of the damaged ceramic tile. The weight of the armor is then reduced in comparison to an armor made of steel only with this combination. It is especially appealing when dealing with small to medium armor piercing calibers (e.g., 7.62 mm AP or 12.7 mm AP). More recently, a silicon carbide ceramic combined by a 50-mm thick honeycomb aluminum also led to interesting results [3].

Furthermore, Riou [4] performed experiments on bilayered configurations with different thicknesses of the SiC ceramic layer. A significant degradation of the ceramic called fragmentation and characterized by numerous radial micro-cracks was observed in a normal impact test. The fragmentation is caused by tensile hoop stresses and strains induced by the radial motion of the ceramic after impact. To visualize fragmentation, a so-called edge-on-impact (EOI) configuration can be used. These configurations were developed by the Ernst-Mach-Institut (EMI) in Germany [5-7] and

more recently by the Centre Technique d'Arcueil (CTA) in France [4,8]. The same damage mechanism (i.e., multiple cracking) was observed by Riou [4] in EOI and in normal impact configurations for bilayered and monolithic ceramics. This result was also obtained numerically [10]. To allow for post-mortem observations, a sarcophagus configuration was designed [9] (Fig. 1-a). These studies enabled for a comparison between different ceramics in terms of fragmentation features (Fig. 1-b) [11]. To limit the perforation of the ceramic, a material leading to a small crack density is recommended [2]. Yet, the multi-hit strength is still low with these material combinations.

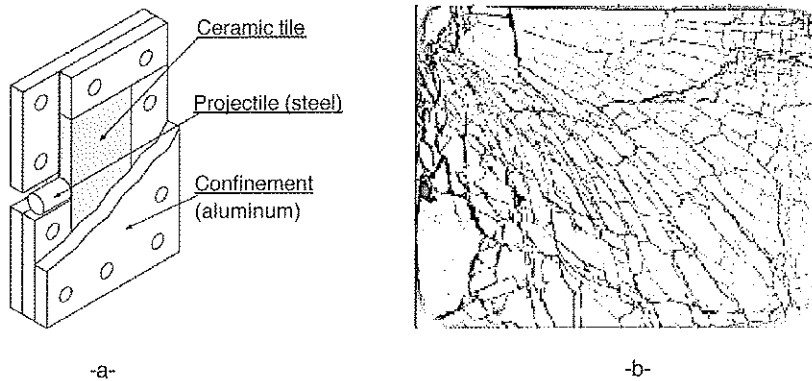


Fig. 1. Schematic of a sarcophagus configuration (a) and post-mortem observation of a SiC-100 ceramic impacted by a steel projectile (AFNOR 100C6, AISI 52 100) at 330 m/s (b) [2].

Another route can be followed to improve the multi-hit capability of a bilayered armor. It consists in avoiding or reducing the motion of the fragments [12]. To achieve this property, a porous SiC ceramic is infiltrated by aluminum. Aluminum induces a better cohesion to the impacted material thereby increasing the residual strength after impact. To illustrate this feature, Fig. 2 shows a block of armor made of 3 tiles of infiltrated ceramic encased in a 15 mm thick aluminum layer that was impacted by an AP 7.62 mm projectile travelling at 847 m/s [12]. One can note no penetration even though a very dense cracking occurred in the first layer (see micrographs of Fig. 2).

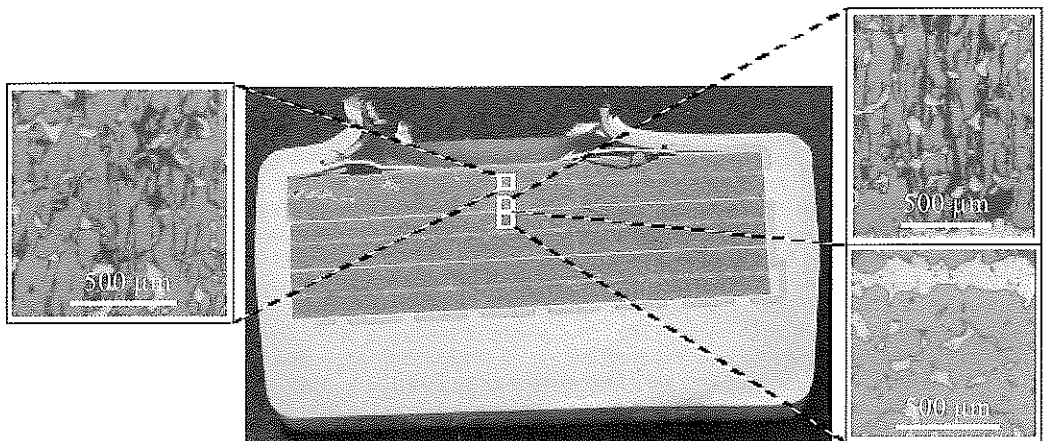


Fig. 2. View of a multilayered armor made of RSiC-Al ceramics impacted by an AP 7.62-mm bullet. No perforation can be observed and the fragmentation process is confined around the impact zone (see zooms of three different zones).

To design bilayered armors, one has to model damage caused by impact in the brittle material. To achieve this goal, a comparison of the fragmentation features of the infiltrated ceramic with those of the porous SiC material is performed. The two materials studied herein are presented. Mechanical and failure properties are obtained under quasi-static loading conditions. EOI experiments are then discussed. Two sets of data are obtained. Based upon a fragmentation theory, a so-called local damage model [11] is used to analyze the different fragmentation conditions observed.

STUDIED MATERIALS

The armor concept consists in a compact aluminum box of size $160 \times 90 \times 45 \text{ mm}^3$ [13]. The box contains one or several ceramic tiles surrounded by a steel casing on the first half of its thickness, located close to the impacted surface (Fig. 2). The steel casing has two functions: first, to maintain the ceramic tiles in position during squeeze casting, and second, to constrain the ceramic during impact. The RSiC tiles, which are obtained by sintering of SiC powder by Saint-Gobain industrial ceramics (commercial name: Crystar[®]), are porous (Fig. 2). The open porosity of the RSiC tiles is regular and continuous from one side to the other one, in such a way that aluminum will fill most of the open cavities during the squeeze-casting process. An initial porosity of the order of 17% was measured [14]. The second half of the thickness of the box is pure aluminum. The density of the box is close to 2.8, depending on the number of R-SiC tiles used.

Elaboration of compact boxes has been carried out at LKR laboratory by infiltration of the porous R-SiC tiles using UBE HVSC 350 indirect squeeze casting equipment. Before infiltration, the ceramic tiles are encased in a steel canister perforated by numerous holes to allow for the penetration of liquid aluminum. The boxes are heated up in a furnace to allow for a complete filling of the pores during infiltration. After preheating, the boxes are put in a die of the squeeze casting equipment and infiltrated with liquid aluminum or an aluminum-silicon alloy by applying a pressure of about 70 MPa. The same processing parameters are used to make infiltrated R-SiC-Al alone. Image analyses of micrographs of the RSiC-Al material are used to determine the volume fraction of aluminum (*i.e.*, 14.5%) and the remaining porosity (*i.e.*, 2.5%) [14].

The elastic properties of the two materials are obtained by using ultrasound experiments. The celerities of longitudinal and transverse waves are measured and the elastic properties of an isotropic and elastic material can be deduced [15]. Table 1 summarizes the results obtained for the two ceramics. A comparison is given with a steel to be used in the EOI experiments. The presence of aluminum increases the Young's modulus of the material as well as the density when compared to the raw R-SiC ceramic.

Table 1. Mechanical properties of materials used during edge-on impact tests.

Material	R-SiC	R-SiC-Al	35NCD16 steel
Young's Modulus (GPa)	260	317	210
Poisson's ratio ν	0.159	0.167	0.3
Density	2.64	2.99	7.89
Porosity	17%	2.5%	0
Yield stress σ_y (MPa)	–	–	1300
Weibull modulus m	26.5	24	–
Mean strength α_w (MPa)	113	222	–
Effective volume V_{eff} (mm^3)	0.084	0.12	–
Number of samples	19	12	–

To evaluate the fracture properties under quasi-static loading condition, 3-point flexural experiments are carried out. The failure load is scattered so that a Weibull model [16,17] is used. The failure probability P_F is expressed as

$$P_F = 1 - \exp \left[-V_{eff} \lambda_0 \left(\frac{\sigma_F}{S_0} \right)^m \right], \quad (1)$$

where V_{eff} denotes the effective volume [18]

$$V_{eff} = \int_{\Omega} \left[\frac{\sigma_1(\underline{x})}{\sigma_F} \right]^m d\omega \quad \text{with} \quad \sigma_F = \max_{\Omega} \sigma^*(\underline{x}) \quad (2)$$

corresponding to an equivalent stress σ^* (e.g., maximum principal stress) at a given point \underline{x} . The parameter m is the Weibull modulus (i.e., it measures the scatter, the lower m , the higher the scatter), S_0 the scale parameter relative to a reference density λ_0 , and $\langle * \rangle$ the Macauley brackets (i.e., the positive part of $*$). The constant S_0^m / λ_0 is the Weibull scale parameter. By using a beam theory, the effective volume can be calculated in 3-point flexure

$$V_{eff} = \frac{V}{2(m+1)^2}, \quad (3)$$

where V is the loaded volume (i.e., $V = 20 \times 3 \times 3 \text{ mm}^3$). The surfaces in tension were polished prior to the experiments and two chamfers were ground. 19 experiments are performed for the raw R-SiC ceramic and 12 for the infiltrated R-SiC. A stroke rate of 0.1 mm/min was applied. Table 1 shows that the Weibull moduli are similar for the two materials. Consequently, it is expected that the defect population is identical in both cases. For the Weibull model, the average failure stress σ_w is given by

$$\sigma_w = \sigma_0 (V_{eff} \lambda_0)^{-\frac{1}{m}} \Gamma \left(\frac{m+1}{m} \right), \quad (4)$$

where Γ is the Euler function of the second kind. It can be noted that a significant increase is observed when the two materials are compared. The effect of aluminum infiltration is clearly evidenced by these results. A strong bond can be expected between the R-SiC skeleton and aluminum in EOI experiments.

EDGE-ON-IMPACT EXPERIMENTS

The dynamic fragmentation is studied by using EOI configurations. It consists in impacting a ceramic (or a glass) on the edge so that a ultra-high speed camera can be used to visualize the kinetics of the fragmentation process or microscopic analyses can be carried out to observe the post-mortem cracking pattern. The interframe time can be as low as 0.2 μs . A projectile made of high strength steel (AFNOR designation: 35NCD16) is fired by a gas launcher with velocities ranging from 100 to 450 m/s for a steel projectile (length: 15 mm, diameter: 11 mm). The sample is put in an aluminum container. The projectile speed is measured by two optical cells 50 mm apart. When the bullet reaches the second cell, the flashlight is triggered, and when it impacts the target, it activates the camera to take pictures. To get a good contrast, a very thin aluminum layer is deposited on the surface of interest. The size of the tested tiles is $60 \times 30 \times 8 \text{ mm}^3$.

Figure 3 shows two series of pictures obtained for the two ceramics when impacted at 200 m/s. For the raw ceramic (Fig. 3, top view), one can see a very intense damage front invading the tile ($t = 4 \mu\text{s}$) until it reaches half of tile ($t = 6 \mu\text{s}$) followed by numerous radial macro-cracks that propagate as time increases. The same observations can be made for the infiltrated ceramic (Fig. 3, bottom view). This first series of experiments does not allow us to differentiate significantly the fragmentation

features of the two materials even though the damage zone is less extended for R-SiC-Al than R-SiC ceramics. However, when analyzed after the experiment, R-SiC ceramics were fully fragmented whereas the R-SiC-Al tile had intact parts. A second EOI configuration is used to analyze dynamic fragmentation.

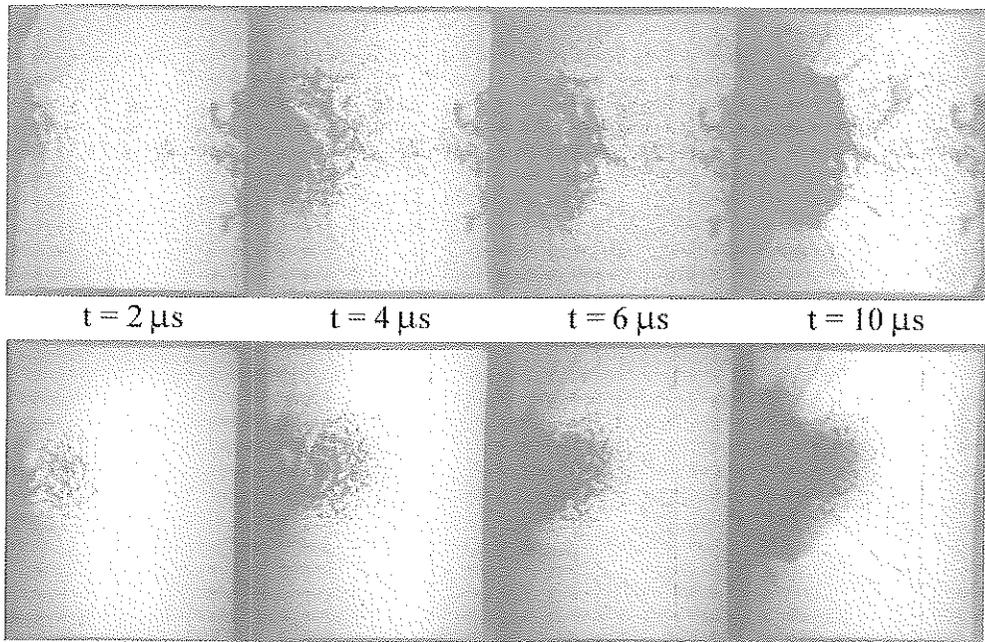


Fig. 3. Comparison of damage patterns for R-SiC (top) and R-SiC-Al (bottom) ceramics impacted by a steel projectile travelling at 200 m/s.

A so-called sarcophagus configuration is used (see Fig. 1-b). Instead of utilizing a high-speed camera, the present configuration enables us to maintain the fragments in place. The impedance of the confinement needs to be less than that of the ceramic so that the "confinement" does not interfere with the impacted ceramic. After impact, the tile is infiltrated by a hyper-fluid resin and polished for macroscopic and microscopic analyses. Two different experiments are reported for the same impact velocity (i.e., 200 m/s). The same sample geometry as before is used here. The macroscopic and microscopic post-mortem cracking pattern is shown in Fig. 4. Different zones can be separated with respect to the crack density. The top views of Fig. 4 show that in front of the projectile, a first zone experiences a very fine cracking pattern. In a second zone, one can observe long radial cracks. This result is comparable with the high-speed camera observations. For the raw SiC, the first zone has a size of the order of $20 \times 25 \text{ mm}^2$. For the infiltrated ceramic, the size of the first zone is significantly reduced (i.e., $15 \times 15 \text{ mm}^2$).

Furthermore, the erosion of the raw SiC is more important compared with the infiltrated ceramic. The bottom views of Fig. 4 show that in the first zone the cracking pattern is mainly oriented along the radial direction. These micrographs correspond to the same location (i.e., 13 mm ahead of the impact center). Smaller cracks can be seen in the infiltrated material. This trend was also observed for another SiC-Al material [19] for which it was concluded that only a limited number of cracks was generated when compared to dense SiC-100 and hipped SiC. All these observations are now analyzed with a damage model based upon a fragmentation analysis.

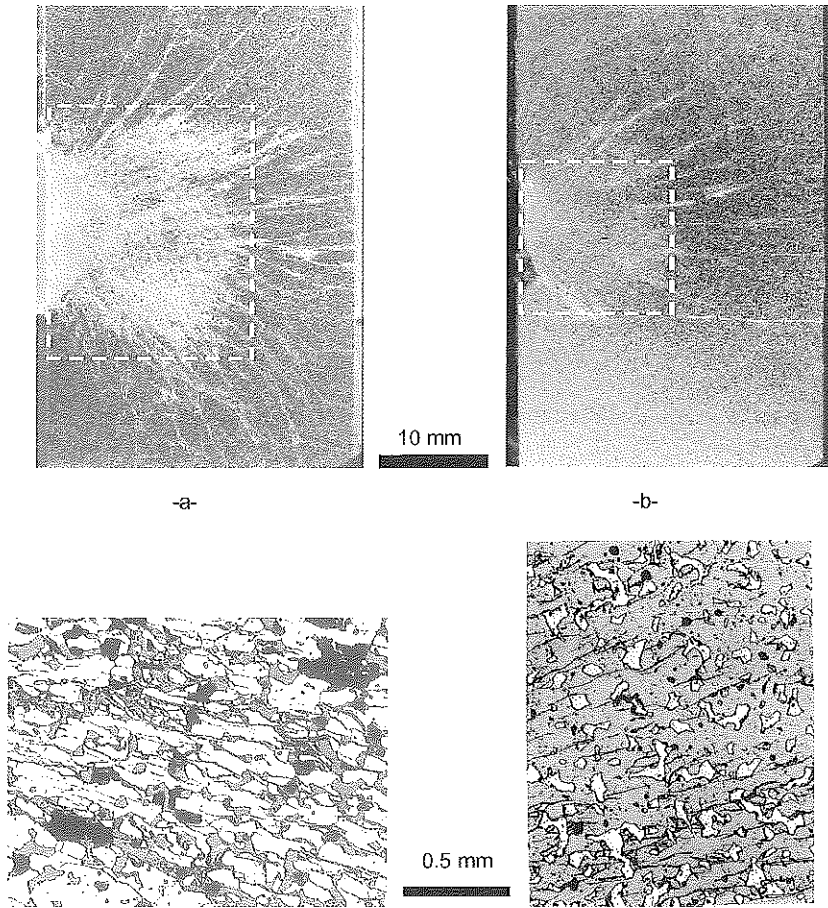


Fig. 4. Post-mortem observations and zoom around a central zone located 13 mm from the impact point: R-SiC impacted at 200 m/s (a), R-SiC-Al impacted at 200 m/s (b).

NUMERICAL ANALYSIS OF THE FRAGMENTATION IN SiC CERAMICS

The fragmentation process is discrete by essence. Continuum Damage Mechanics can be used with an isotropic [20-23] or anisotropic [24] damage description to account for multiple fragmentation. Consequently, in the numerical simulations, the medium is assumed to be continuum on the scale of a finite element in which numerous cracks are expected to form. In the following, a damage model based upon a fragmentation analysis is used.

DAMAGE MODEL

For brittle materials, the analysis of failure depends upon the microstructure in terms of flaw density and failure stress distribution [25]. In the present analysis, it is assumed that cracking occurs normal to three directions d_i ($i = 1, 2, 3$). The microstructure is approximated by point defects of *density* λ_i with *random* locations. It can be described by a Poisson point process of intensity λ_i , [26,27]

$$\lambda_i(\sigma_i) = \lambda_0 \left(\frac{\langle \sigma_i \rangle}{S_0} \right)^m. \quad (5)$$

Equation (5) shows that the higher the local principal stress σ_i , the more defects can break. Under impact, a whole cracking pattern is observed as shown in Fig. 4. In the following, it is assumed that the defect population leading to damage and failure is identical when the material is subjected to quasi-static and dynamic loading conditions [25,28]. To understand why a crack nucleates, one has to model the interaction of a nucleated defect and other defects that would nucleate. The crack propagation velocity is assumed to be constant and equal to a fraction k of the longitudinal wave speed C_0 [29,8]. Therefore, one may define a relaxation or obscuration domain of volume V_0 around a crack (i.e., a zone in which the stresses are less than the applied stresses, thus do not cause new crack initiations)

$$V_0 = S(kC_0(t-\tau))^3, \quad (6)$$

which is a function of a shape parameter S , the present time t and the time to nucleation $\tau < t$. The shape parameter S may depend on the Poisson's ratio ν but it is independent of time so that the relaxed zones are self-similar. New cracks will initiate only if the defect exists in the considered zone and if the flaw does not belong to any relaxed zone. It can be noted that the relaxation volumes are associated with a cracking normal d_i . The total flaw density λ_i can be split into two parts: namely, λ_b , the cracking density and the obscured flaw density. The increment of the cracking density λ_b can be related to that of total flaw density λ_i by [30]

$$\frac{d\lambda_b}{dt}[\sigma(t)] = \frac{d\lambda_i}{dt}[\sigma(t)](1 - P_0(t)), \quad (7)$$

with $\lambda_b(0) = \lambda_i(0) = 0$ and P_0 the probability of obscuration associated to the cracking normal d_i

$$P_0 = 1 - \exp\left(-\int_0^t V_0(t-\tau) \frac{d\lambda_i}{d\tau}(\sigma_i) d\tau\right). \quad (8)$$

It can be noted that Eqn. (8) accounts for overlappings of obscuration zones. Based upon the fragmentation analysis, a damage model is now developed. The variable P_0 can be used to define a damage variable in the framework of Continuum Damage Mechanics [30]. The probability P_0 is assumed to be equal to the damage variable D_i associated to the direction d_i . It is interesting to mention that the first order approximation of Eqn. (8) leads to the differential equation proposed by Grady and Kipp [21] to describe the kinetics of an isotropic damage variable. In the present analysis, an anisotropic description is used. The kinetics of each damage variable D_i is based upon the defect density λ_i and is derived by using Eqn. (8)

$$\frac{d^2}{dt^2} \left(\frac{1}{1 - D_i} \frac{dD_i}{dt} \right) = 6\lambda_i(\sigma_i) S(kC_0)^3 \quad \text{when } \sigma_i > 0 \quad \text{and} \quad \frac{d\sigma_i}{dt} > 0 \quad (9)$$

where no index summation is used. The cracking velocity kC_0 is about 20-40% the longitudinal wave velocity C_0 (i.e., k is ranging between 0.2 and 0.4), and S is a dimensionless shape factor: in 3D situations $S = 3.74$ [11]. The microscopic and macroscopic stresses are related by the classical effective stress concept [31] associated to each cracking direction d_i

$$\sigma_i = \frac{\Sigma_i}{1 - D_i}, \quad (10)$$

Once the elastic properties and the Weibull parameters are known, the constant k is chosen equal to 0.38 as for other SiC ceramics [8,11], the model has no other parameters to tune. The following numerical simulations are therefore predictions.

FINITE ELEMENT COMPUTATIONS

Finite element simulations are performed with the commercial code Pamshock [32] in which the fragmentation and damage models are implemented. For each step, the strain increment is given so that the local or microscopic stresses can be computed (since these stresses are elastic). From this information, the damage kinetics is obtained (Eqn. (9)) as well as the cracking density increment (Eqn. (7)). At the end of each step, the user has access to the damage variables along the three cracking normals, the macroscopic stresses as well as the density of cracking. Depending on the problem, any of these quantities can be visualized. In the present case, we will focus on the cracking density along the maximum principal stress direction.

The mesh uses 8-node elements with reduced integration (i.e., only one integration point per element). The two symmetry conditions lead to a mesh of one quarter of the geometry made of 5200 elements. The material parameters used in the simulations are given in Table 1 for the tile and the projectile. Figures 5 and 6 show maps of cracking densities associated with the first (maximum) principal stress for the different cases used in the EOI experiments. The dashed boxes correspond to those found experimentally (Fig. 4). When $t = 4 \mu\text{s}$, the cracking density is greater than $10^{2.5} \text{ mm}^{-3}$ in the boxes (Figs. 5-a and 6-a). A damage front gradually invades about one half to two thirds of the tile in less than $4 \mu\text{s}$. The pictures obtained with the high-speed camera show a very dense damage pattern created around $4 \mu\text{s}$, then followed by long cracks visible after $6 \mu\text{s}$. The simulation is able to find the development of the first damage front. However, there is a time lag of about $2 \mu\text{s}$ for the second phase of the cracking pattern. One may argue that the cracks are too small to be observed by the high-speed camera at their inception. It can also be noted that the cracking density is very similar when the maps corresponding to the external surfaces (Figs. 5-a and 6-a) are compared with those of the mid-height (Figs. 5-b and 6-b).

The cracking density in the porous R-SiC is significantly greater than that of the infiltrated R-SiC. This result is consistent with the post-mortem observations and confirms the beneficial effect of aluminum infiltration on fragmentation.

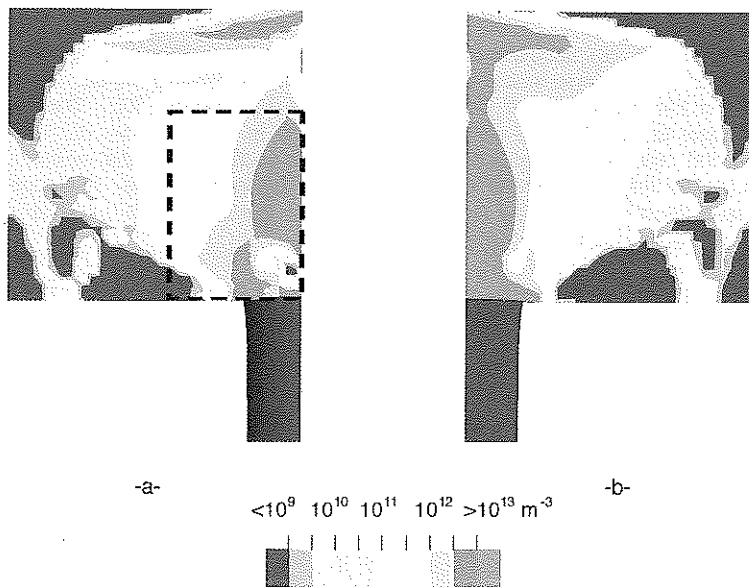


Fig. 5. Cracking density $4\mu\text{s}$ after a 200 m/s impact of one quarter of an RSiC ceramic tile: (a) external surface, (b): mid-height of the tile.

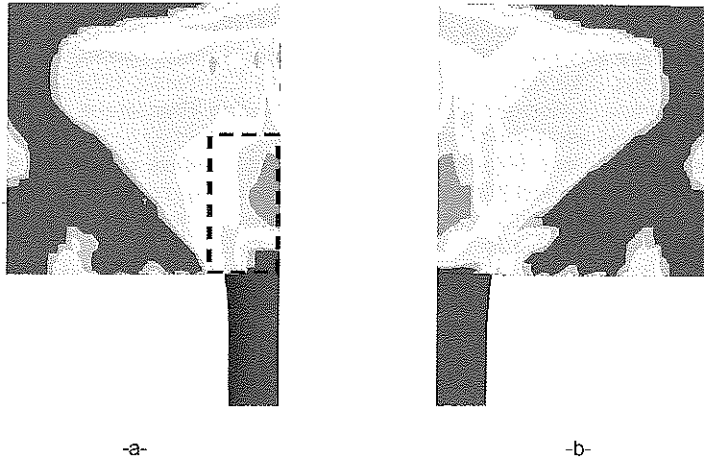


Fig. 6. Cracking density $4\mu\text{s}$ after a 200 m/s impact of one quarter of an R-SiC-Al ceramic tile: (a) external surface, (b): mid-height of the tile.

CONCLUSION

A new SiC ceramic infiltrated by aluminum has been studied herein. In terms of density and Young's modulus, lower values are found for raw R-SiC compared to infiltrated R-SiC-Al when the two materials are tested under quasi-static loading conditions.

Edge-on-impact experiments were performed on the two R-SiC grades. When using a high-speed camera, no significant differences could be observed. A sarcophagus configuration was then used to perform post-mortem analyses that are more precise in terms of observations of the cracking pattern. Macroscopic and microscopic examinations show that, when subjected to impact loadings leading to dynamic fragmentation, the R-SiC ceramic infiltrated with aluminum shows a significant reduction in cracking density when compared to the raw R-SiC material. Under this type of loading conditions, the aluminum skeleton provides sufficient cohesion for the cracks to be stopped.

The material parameters, which were determined under quasi-static loading conditions, are the only ones needed for the fragmentation model used herein. A damage model is then deduced. The finite element simulations using the damage and fragmentation models are able to predict the trends observed in the experiments for the two R-SiC grades. The numerical simulation of edge-on-impacts shows damage patterns in agreement with experimental observations, even though the second stage is slightly ahead of experimental observations. The infiltration has a strong influence on the initiation of cracks and a lesser effect on their propagation as it was assumed in the simulations. This is however going to be different when the residual strength will be assessed. This work is still in progress.

ACKNOWLEDGMENTS

This work was funded by DGA and is a collaboration within the network 'Pôle Francilien de Dynamique' (DGA / Centre Technique d'Arcueil, LMS / Ecole Polytechnique and LMT-Cachan / ENS de Cachan).

REFERENCES

1. P. C. den Reijer, Impact on Ceramic Faced Armor, (PhD thesis, Delft Technical University, 1991).
2. C. Denoual, Approche probabiliste du comportement à l'impact du carbure de silicium: application aux blindages moyens, (Ph.D. thesis, École Normale Supérieure de Cachan, 1998).

3. Internal data, (CTA, Arcueil (France), 2002).
4. P. Riou, Contribution à l'étude de l'endommagement du carbure de silicium lors d'un impact de basse énergie : application aux blindages, (Ph.D. thesis, École Nationale Supérieure des Mines de Paris, 1996).
5. U. Hornemann, J. F. Kalthoff, H. Rothenhäusler, H. Senf and S. Winkler, Experimental Investigation of Wave and Fracture Propagation in Glass - Slabs Loaded by Steel Cylinders at High Impact Velocities, (EMI report E 4/84, Weil am Rhein (Germany), 1984).
6. S. Winkler, H. Senf and H. Rothenhäusler, Wave and Fracture Phenomena in Impacted Ceramics, (EMI report V 5/89, Weil am Rhein (Germany), 1989).
7. E. Strassburger and H. Senf, Experimental Investigations of Wave and Fracture Phenomena in Impacted Ceramics, (EMI report 3/94, Weil am Rhein (Germany), 1994).
8. P. Riou, C. Denoual and C. E. Cottenot, Visualization of the Damage Evolution in Impacted Silicon Carbide Ceramics, *Int. J. Impact Eng.* 21 [4] (1998) 225-235.
9. C. Denoual, C. E. Cottenot and F. Hild, Analysis of the Degradation Mechanisms in an Impacted Ceramic, in: S. C. Schmidt, D. P. Dandekar and J. W. Forbes, eds., *Proc. Shock Compression of Condensed Matter*, (AIP Press, New York (USA), 1998), 427-430.
10. C. Denoual, C. E. Cottenot and F. Hild, On the Identification of Damage during Impact of a Ceramic by a Hard Projectile, *Proc. 16th International Conference on BALLISTICS*, (APDS, Arlington, VA (USA), 1996), 541-550.
11. C. Denoual and F. Hild, Dynamic Fragmentation of Brittle Solids: A Multi-Scale Model, *Eur. J. Mech. A/Solids* 21 [1] (2002) 105-120.
12. P.-F. Louvigné and P. Schulz, MMC for Armour Application : New Concept, *Proc. of ICCE8 conference*, Tenerife, Canary Islands, Spain (2001), 2p.
13. P.-F. Louvigné, F. Feuchtenschlager, J. Reiter, G. Rettenbacher and P. Schulz, Blindage composite multicouche, PCT patent, PCT/FR02/024767 (2002).
14. L. Tran, Étude de la fragmentation générée dans les céramiques R-SiC au cours d'essais d'impact sur la tranche, (M.Sc. dissertation, University Paris 6, 2002).
15. H. Kolsky, *Stress Waves in Solids*, (Dover Publications, New York (USA), 1963).
16. W. Weibull, A Statistical Theory of the Strength of Materials, (*Roy. Swed. Inst. Eng. Res.*, 151, 1939).
17. W. Weibull, A Statistical Distribution Function of Wide Applicability, *ASME J. Appl. Mech.* 18 [3] (1951) 293-297.
18. D. G. S. Davies, The Statistical Approach to Engineering Design in Ceramics, *Proc. Brit. Ceram. Soc.* 22 (1973) 429-452.
19. E. Strassburger, B. Lexow, H. Ashuach, Y. Yeshurun, S. Bar-Ziv, Y. Hachamo and H. Gedon, Impact on Ceramic-Metal-Composites – Ballistic Resistance and Fracture Behavior, *Proc. of 20th Symposium on Ballistics*, (2002), 8p.
20. H. D. Espinosa, P. D. Zavattieri and S. K. Dwivedi, A Finite Deformation Continuum/Discrete Model for the Description of Fragmentation and Damage in Brittle Materials, *J. Mech. Phys. Solids* 46 (1998) 1909-1942.
21. D. E. Grady and M. E. Kipp, Continuum Modeling of Explosive Fracture in Oil Shale, *Int. J. Rock Min. Sci. & Geomech. Abstr.* 17 (1980) 147-157.
22. L. G. Margolin, Elasticity Moduli of a Cracked Body, *Int. J. Fract.* 22 (1983) 65-79.
23. A. M. Rajendran, Modeling the Impact Behavior of AD85 Ceramic under Multiaxial Loading, *Int. J. Impact Eng.* 15 [6] (1994) 749-768.
24. C. Denoual and F. Hild, A Damage Model for the Dynamic Fragmentation of Brittle Solids, *Comp. Meth. Appl. Mech. Eng.* 183 (2000) 247-258.
25. D. A. Shockey, D. R. Curran, L. Seaman, J. T. Rosenberg and C. F. Petersen, Fragmentation of Rocks under Dynamic Loads, *Int. J. Rock Mech. Min. Sci.* 11 (1974) 303-317.
26. R. Gulino and S. L. Phoenix, Weibull Strength Statistics for Graphite Fibres Measured from the Break Progression in a Model Graphite/Glass/Epoxy Microcomposite, *J. Mater. Sci.* 26 [11] (1991) 3107-3118.
27. D. Jeulin, Modèles morphologiques de structures aléatoires et changement d'échelle, (thèse d'État, University of Caen, 1991).
28. C. Denoual and P. Riou, Comportement à l'impact de céramiques techniques pour blindages légers, (CREA report 95 R 005, Arcueil (France), 1995).
29. L. B. Freund, Crack Propagation in an Elastic Solid Subjected to General Loading - Constant Rate of Extension, *J. Mech. Phys. Solids* 20 (1972) 129-140.

30. C. Denoual, G. Barbier and F. Hild, A Probabilistic Approach for Fragmentation of Ceramics under Impact Loading, C. R. Acad. Sci. Paris 325 [Série IIb] (1997) 685-691.
31. J. Lemaitre, A Course on Damage Mechanics, (Springer Verlag, Berlin (Germany), 1992).
32. Pamshock, User's Manual, ESI (1996).

Numerical modeling of high velocity impact on CFRPs at low temperature

J. López-Puente, R. Zaera, C. Navarro

Department of Continuum Mechanics and Structural Analysis, University Carlos III of Madrid
Avda. de la Universidad 30, 28911 Leganés, Madrid, Spain

ABSTRACT

The influence of low temperature on the damage to CFRPs caused by intermediate and high velocity impacts was investigated by launching spherical projectiles against quasi-isotropic carbon fiber/epoxy laminates. Tests were done at temperatures between 25 °C and -150 °C.

The extension of the damage was measured by C-Scan. The results show a clear dependence of damage on temperature and impact velocity. In the numerical simulations of the test, a multi-damage criterion was adopted that considered delamination, matrix cracking and fibre failure.

INTRODUCTION

Future generations of launch vehicles will have to be completely reusable to give reliable access to space at a much lower cost than is possible with the present expendable vehicles (type Ariane 5) or the semi-expendable Space Shuttle type. This means a reduction of the structural mass of the vehicles since dry weight is a major cost driver; fuel tanks and propellant masses form an important fraction (about 90%) of the total mass. Fibre Reinforced Plastics (FRPs) are widely used in this application. Their excellent specific mechanical properties and their resistance to fatigue offer many advantages over conventional metallic materials; high stiffness, high strength and anisotropic behaviour clear the way to optimized designing for specific loading conditions. Among the high performance FRPs, Carbon Fibre Reinforced Plastics (CFRPs) are outstanding for their mechanical properties, but unfortunately they have a very low capacity of energy absorption when subjected to impulsive loads normal to the laminate plane, a condition that may arise at high velocity in the case, for example, of an impact of debris on a spacecraft. This low capacity of energy absorption is due mainly to the brittleness of the epoxy matrix and the low failure strain and shear strength of the carbon fibres. Engineers try to reduce the impact damage by means of matrix toughening [4], fibre toughening [2], hybridizing [3] and through-thickness reinforcement [4]. Different types of impact damage may be found in CFRP laminates: fibre breaking, matrix cracking, matrix crushing, fibre pull-out and delamination, the last being the most ominous in the reduction of the compression and of the bending and buckling strengths [5] since it causes a separation of the plies, and therefore an overall reduction of the laminate stiffness.

CFRPs are widely used for structural components in the aeronautical and aerospace industries, applications in which they may be subjected to very low temperatures. CFRPs are also commonly used in the construction of cryogenic tanks on account of their low thermal conductivity and high dimensional stability, so the static properties of carbon fibre composites at cryogenic temperatures have been the subject of several investigations. Usami et al [6] studied the behaviour of various epoxy resins at temperatures from -269 °C to 100 °C, and found that strength increases and failure strain decreases as the temperature falls. Korab et al [7] and Rogers et al [8] did tests to obtain thermal expansion coefficients for cross-ply, woven and unidirectional laminates. Giesy [9] described the variation of the laminate strength with temperature from -269°C to 23°C and found a slight increase in tension and a small decrease in compression at low temperature as compared with those at room

temperature, while Schutz [10] observed an increase in both tensile and compressive strengths. Morino et al [11] and Aoki et al [12] studied the process of interlaminar fracture and showed that matrix cracking is the main problem when CFRPs are considered for cryogenic applications.

The behaviour under impact loading at low temperatures has so far received little attention. Here we examine the effect of low temperature (-150 °C to 25 °C) on the extension of damage produced by intermediate and high velocity impact (60 m/s to 529 m/s) on quasi-isotropic CF/Epoxy laminates. C-Scan measurement showed how the damaged area of the composite for a given impact mass and velocity varies with temperature and with the type of laminate. Finally we made numerical simulations of the test.

IMPACT EXPERIMENTS: PROJECTILE AND TESTED MATERIALS

For the impact tests we used a tempered steel projectile of 1.73 g mass, spherical to avoid scattered results due to changes in the yaw angle. The laminated we tested was tape AS4/3501-6 with stacking sequence $[-45.0.90]_s$, a material widely used in the aeronautical and aerospace industries. The material was provided by SACESA (Spain) from prepegs manufactured by HEXCEL, with a volumetric fibre content of 60%. The elastic and strength properties of these prepegs are given in Table 1 and Table 2. The specimen size was 80 x 80 mm².

Prepreg	Thickness (mm)	E_1 (Gpa)	E_2 (Gpa)	G_{12} (Gpa)	ν_{12}
AS4/3501-6	0.175	131	8	3.7	0.33

Table 1: elastic properties.

Prepreg	X_t (Mpa)	X_c (Mpa)	Y_t (Mpa)	Y_c (Mpa)	S (Mpa)
AS4/3501-6	2105	1656	74	175	114

Table 2: strength properties.

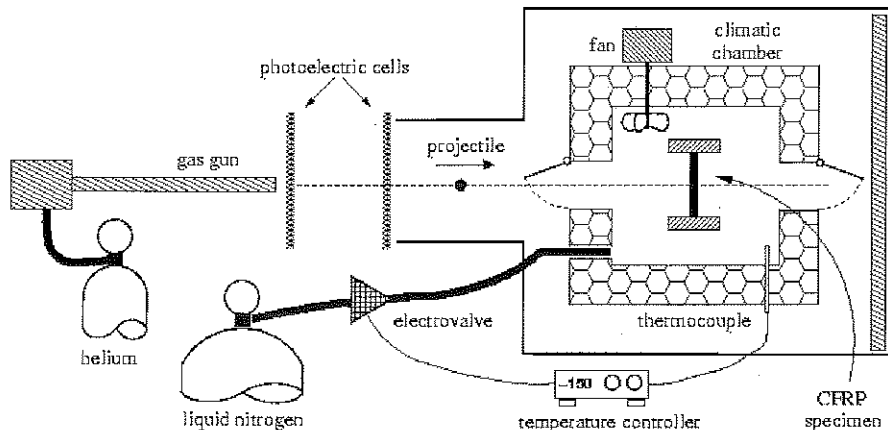


Figure 1: Sketch of the experimental device: gas gun and climatic chamber inside.

EXPERIMENTAL DEVICE

A SABRE gas gun was used to launch the spherical projectile. For the impact test at different temperatures a climatic chamber was coupled to the gas gun. The experimental device is depicted in Fig. 1.

GAS GUN

The gas gun uses a 7.62 mm caliber canon coupled to a helium gas bottle at a pressure of 200 bar. When the exhaust valve opens, the helium impels the spherical projectile at velocities of up to 525 m/s. The fragment expelled from the canon travels a distance of 2 m along a $40 \times 60 \text{ cm}^2$ gallery in which its passage is detected by two photoelectric cells from which the impact velocity is obtained. At the end of the gallery, the projectile reaches an armoured box ($1 \times 1 \times 1 \text{ m}^3$) in which the climatic chamber is located.

CLIMATIC CHAMBER

A cryogenic chamber (Fig. 2) was manufactured to provide temperatures down to $-150 \text{ }^\circ\text{C}$. A flow of liquid nitrogen inside the chamber was regulated by an electrovalve controlled by a thermocouple placed next to the composite specimen. A fan ensured that the inside atmosphere was in constant recirculation. The CFRP specimen was placed in a special tool to clamp its border. To be certain of the homogeneity of the temperature in the specimen, we cooled it in the chamber for 20 minutes at $-60 \text{ }^\circ\text{C}$ or for 30 minutes at $-150 \text{ }^\circ\text{C}$, (determined by previous thermal analyses).

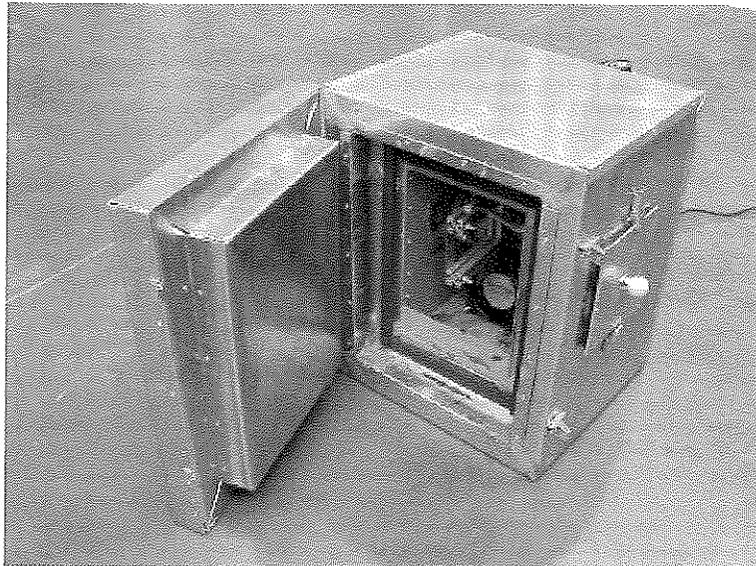


Figure 2: cryogenic chamber.

EXPERIMENTAL RESULTS

We ran the impact tests at between 60 and 525 m/s and at three temperatures (25°C , -60°C and -150°C). After the tests, we measured the damaged area of the specimens by C-Scan, and found that it was very large in this type of laminate, reaching the border in the most badly damaged specimens since the laminate fibres are oriented in different directions in each ply. Most experimental evidence has shown that delamination occurs mainly between plies with different fibre orientation [5] and hence with different bending behaviour of the plies.

Fig. 3 shows the C-Scan images of the damaged areas around the impacts, at different velocities and temperatures, in tests done at velocities above and below the ballistic limit. Perforations are identified by the hole made on penetration. There, the attenuation of the ultrasonic signal becomes zero, so a white area appears in the laminate.

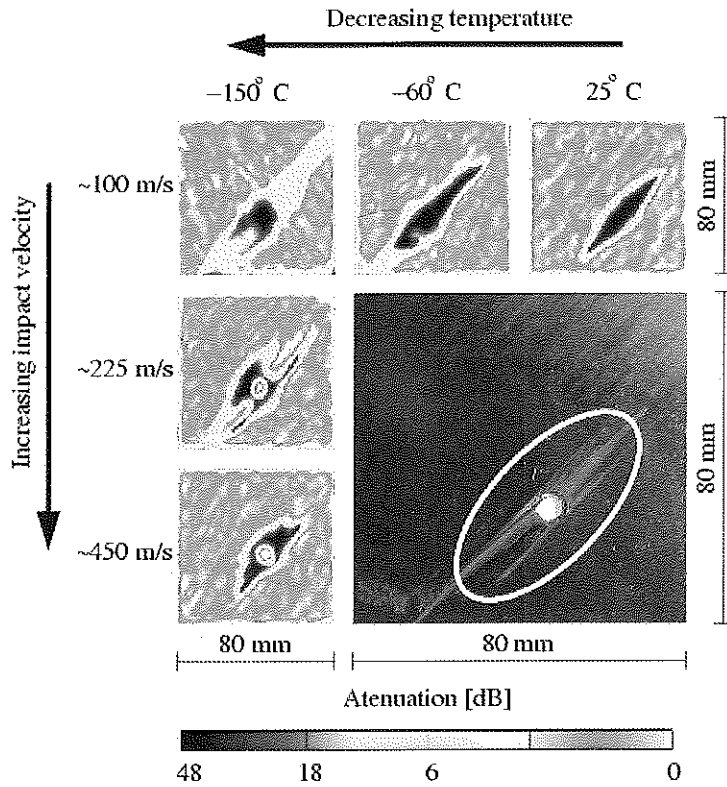


Figure 3: C-Scan damage contours in quasi-isotropic laminates as a function of impact velocity and temperature. External aspect of the damage in a perforation case.

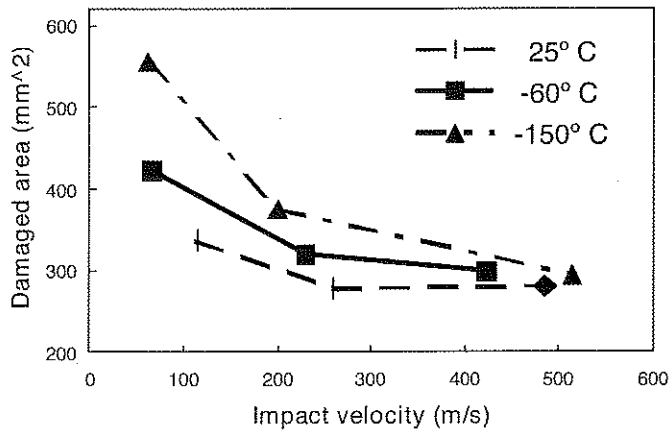


Figure 4: Damage extension in quasi-isotropic laminates vs impact velocity and energy at three different temperatures.

We used an image analyser programme to measure the damage areas from the C-Scan images, recognizing delamination when the signal attenuation was above 4 dB. Average values are plotted in Fig. 4 as a function of the impact velocity, at the three temperatures of the tests. Below the ballistic limit, the impact energy is absorbed mainly by local bending of the laminate, which allows energy transfer away from the impact zone. Without perforation, the impact energy is dissipated mainly by delamination and fibre failure [13]. However, above the ballistic limit the structural laminate response is much more localized around the point of impact because loading induces shear plugging with no global bending of the laminate, as is sketched in Fig. 5. Damage extension diminished as impact velocity increased, tending to a limit value and showing a saturation effect. In these conditions the damage area was independent of the impact velocity, and temperature did not significantly affect the damage extension (Fig. 4).

The effect of temperature was more pronounced (Fig. 3). Damage extension grew significantly at the lower temperatures but on account of the prevalence of inertial effects, the thermal conditions did not affect the mechanical response of the laminate at higher velocities.

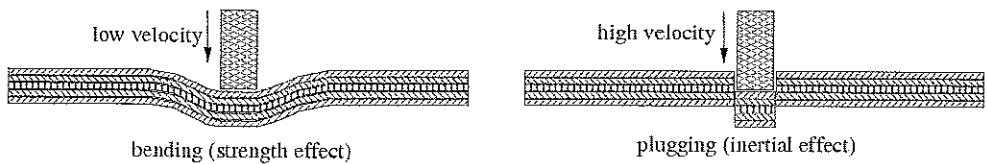


Figure 5: Effect of velocity on the response of laminates.

NUMERICAL SIMULATION

We chose the commercial finite element code ABAQUS for the numerical simulation as it allows the introduction of user sub-routines with the programme language Fortran. We made two kinds of simulation: a static one to determine the thermal tensions in the material at 25, -60 and -150 °C, and then a dynamic simulation of the impact to screen the progression of the damage.

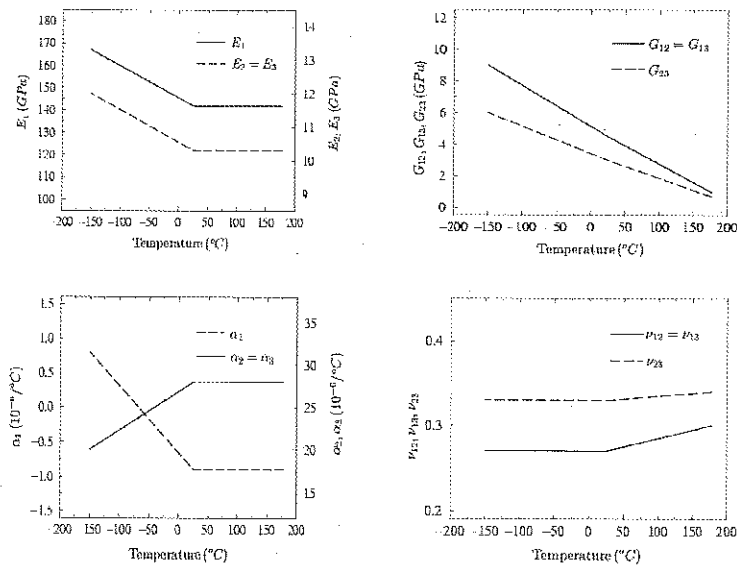


Figure 6: Evaluation of the laminate elastic and thermal properties with temperature.

MODELLING THE MATERIAL

We introduced a model of anisotropic behaviour that covers the appearance of the damage. Several investigators have described the thermoelastic properties (Fig. 6) as a function of temperature [6, 8, 12, 14].

The damage criterion we adopted was based on the one proposed by Hou et al [15] which is in turn based on that of Chang et al [16]. It considers four different kinds of damage (Fig. 7), each with a damage parameter d_i . When the value of the parameter is below unity, it is considered that no damage exists, whereas above unity, the material will lose stiffness in certain directions. These are enumerated below.

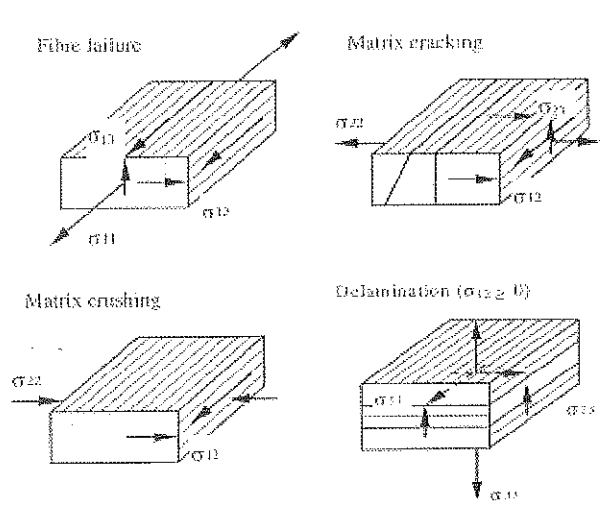


Figure 7: Failure modes.

- Fibre failure:

$$d_f = \left(\frac{\sigma_{11}}{X_T} \right)^2 + \left(\frac{\sigma_{12}^2 + \sigma_{13}^2}{S_f^2} \right)$$

where the constants X_T and S_f are characteristic of each material and represent the resistance in each direction. On failure, the material loses its rigidity in all directions.

- Matrix cracking: This is the first of the two that simulate the breaking of the matrix – shear fracture perpendicular to the fibres in the plane of the laminate.

$$d_{mc} = \left(\frac{\sigma_{22}}{Y_T} \right)^2 + \left(\frac{\sigma_{12}}{S_{12}} \right)^2 + \left(\frac{\sigma_{23}}{S_{m23}} \right)^2 \quad \text{with } \sigma_{22} \geq 0$$

in which Y_T , S_{12} and S_{m23} are constants of the material. On failure, the strains σ_{22} and σ_{12} are eliminated.

- Matrix crushing: Material breakage under compression.

$$d_{mc} = \frac{1}{4} \left(\frac{\sigma_{22}}{S_{12}} \right)^2 + \frac{Y_c \cdot \sigma_{22}}{4 \cdot S_{12}^2} - \frac{\sigma_{22}}{Y_c} + \left(\frac{\sigma_{12}}{S_{12}} \right)^2 \quad \text{with } \sigma_{22} \leq 0$$

where Y_c is another material constant. The stress eliminated by crushing is σ_{22} .

- Delamination: This is the form of breakage that weighs most heavily in reducing the mechanical strength since it is the most likely form of fracture, the weakest zone being the interlaminar. Delamination occurs when stress is applied perpendicularly to the laminate.

$$d_d = \left(\frac{\sigma_{33}}{Z_r}\right)^2 + \left(\frac{\sigma_{23}}{S_{123}}\right)^2 + \left(\frac{\sigma_{31}}{S_{31}}\right)^2 \quad \text{with } \sigma_{33} \geq 0$$

The constants in this equation are Z_r , S_{123} and S_{31} . The stress eliminated are σ_{33} , σ_{23} and σ_{13} .

STATIC SIMULATION

We used the ABAQUS/Standard code to calculate the thermal stresses, taking the curing temperature, 170 °C, as that of free stress state. The strains should be fairly high since the coefficients of thermal dilatation are very different in the fibre direction and in the perpendicular direction, and this difference increases as the temperature is reduced (Fig. 6).

It seems that matrix cracks contribute little to energy absorption or to a reduction of the residual properties. However [5], before delamination at the ply interfaces, the damage process is initiated by this matrix cracking failure mode. We observed large differences in the contours of matrix cracking between those at room temperature and those at cryogenic temperatures. The magnitude of this parameter at $T=25$ °C is not significant in any ply (about 0.04, Fig. 8), but at $T=-150$ °C is rises to about 0.5 and gives rise to faster damage development on impact

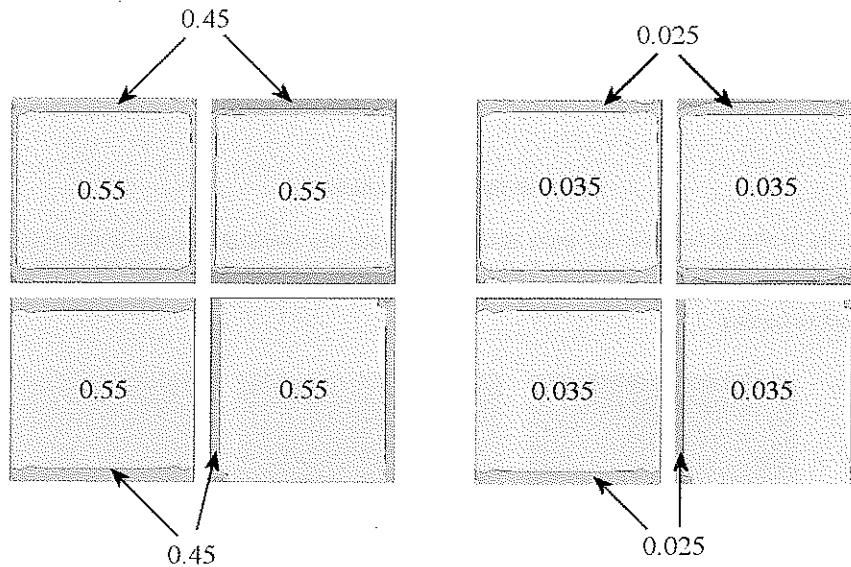


Figure 8: Values of matrix cracking damage at -150 °C (left) and 25 °C (right) due to thermal stresses. Ply +45 (top left), ply -45 (top right), ply 0 (bottom left), ply 90 (bottom right).

To study the progress of damage during high-velocity impact, we simulated it with the finite element programme ABAQUS/Explicit. Large deformations, and even perforations, appear in this analysis, so we had to establish a criterion to eliminate elements.

It is clear from the models described above that fibre failure is the only type of damage that nullifies the capacity of resistance in every direction, so we chose this stress as a condition for erosion. And

given the brittleness of the CGRPs, we adopted also a deformation criterion on the basis of equivalent strain.

$$\bar{\epsilon}_{eff} = \sqrt{\left[\frac{2}{3} (\epsilon_{xx}^2 + \epsilon_{yy}^2 + \epsilon_{zz}^2 + \epsilon_{xy}^2 + \epsilon_{xz}^2 + \epsilon_{yz}^2) \right]}$$

When either of these variables – (fibre failure or equivalent deformation) – reaches a limit value, the element is eliminated by the user sub-routine.

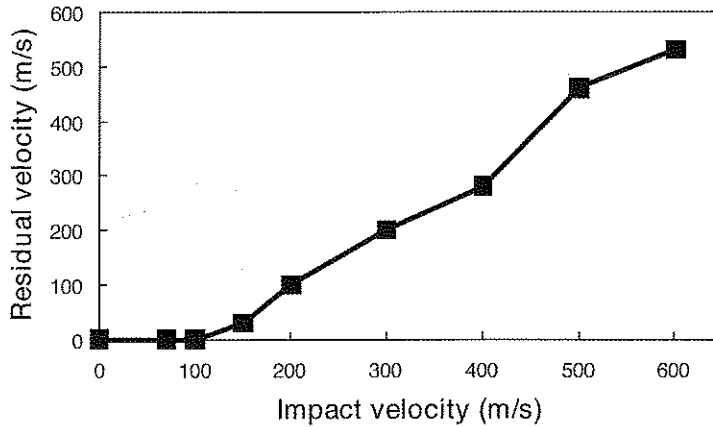


Figure 9: dynamic simulation

From the results of this simulation we were able to calculate the residual velocity of the projectile in cases of perforation. The Figure 9 shows that the ballistic limit forecast by the model is around 100 m/s, very similar to our experimental finding. We also obtained final contours of the fibre failure at different impact velocities.

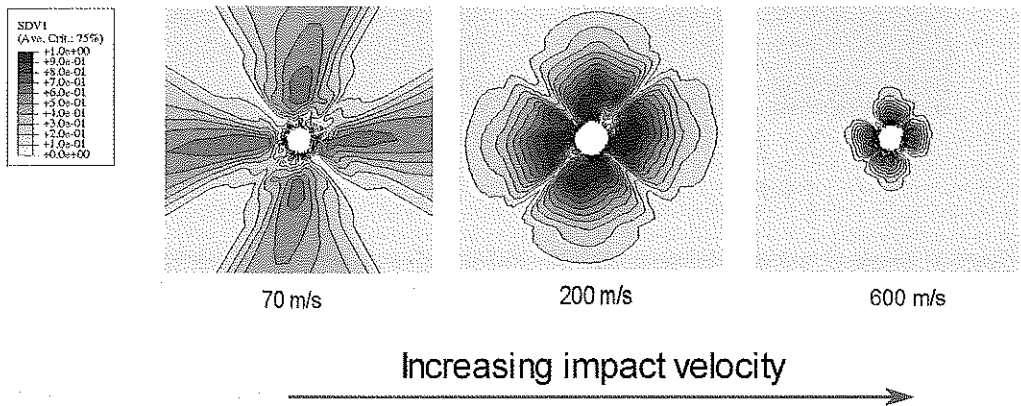


Figure 10: Contour of fibre failure for different impact velocities.

CONCLUSION

CFRP laminates are susceptible to damage after impact. It is often difficult to localize the damage, which can have a strong influence on the mechanical properties of structural components. This explains the interest of studying the parameters that affect the type and the extension of the damage.

Our study of the effect of impact velocity and temperature on the mechanical response of CFRP laminates shows that low temperatures detract from the impact behaviour of the laminate as a result of high in-plane thermal stresses. Our tests showed a damage saturation effect as the velocity increased above the ballistic limit; in this velocity range, temperature has no influence on damage extension. For aeronautical and aerospace applications, in which velocities can exceed those considered in this paper, the damage extension could well be determined from impact tests at room temperature.

The Chang-Chang model predicts realistic damage trends in a CFRP laminate subjected to high velocity impact. The ballistic limit is well reflected in this numerical model.

ACKNOWLEDGMENTS

The authors are indebted to the Comisión Interministerial de Ciencia y Tecnología of Spain for financial support of this work (Project MAT98-0273). They also thank EADS-CASA for assistance in C-Scan measurements.

REFERENCES

1. J. C. Hedrick, M. P. Nirajan, J. E. McGrath, Toughening of epoxy resin networks with functionalized engineering thermoplastics, *Advances in Chemistry* 208 (1993) 293–304.
2. W. J. Cantwell, P. T. Curtis, J. Morton, An assessment of the impact performance of {CFRP} reinforced with high-strain carbon fibers, *Composite Science and Technology* 25 (1986) 133–148.
3. G. Marom, E. Drukker, A. Weinberg, J. Banbaji, Impact behaviour of carbon/kevlar hybrid composites, *Composites* 17 (2) (1986) 150–153.
4. T. J. Kang, S. H. Lee, Effect of stitching on the mechanical and impact properties of woven laminate composite, *Journal of Composite Materials* 28 (16) (1994) 1574–1587.
5. S. Abrate, *Impact on composite structures*, Cambridge University Press, Cambridge, UK, 1998.
6. S. Usami, H. Ejima, T. Suzuki, K. Asano, Cryogenic small-flaw strength and creep deformation of epoxy resins, *Cryogenics* 39 (1999) 729–738.
7. J. Korab, P. Stefanik, S. Kavecky, P. Sebo, G. Korb, Thermal expansion of cross-ply and woven carbon fibre-copper matrix composites, *Composites A* 33 (2002) 133–136.
8. K. F. Rogers, L. N. Phillips, M. Kingston-Lee, B. Yates, M. J. Overy, J. P. Sargent, B. A. McCalla, The thermal expansion of carbon fiber-reinforced plastics, *Journal of Materials Science* 12 (1977) 718–734.
9. R. K. Giesy, Advanced composite materials for cryogenic support structures, in: *ICEC16/ICMC Proceedings*, Vol. 60, Kitakyushu (Japan), 1996, pp. 2053–2056.
10. J. B. Schutz, Properties of composite materials for cryogenic applications, *Cryogenics* 38 (1) (1998) 3–12.
11. Y. Morino, T. Ishikawa, T. Aoki, H. Kumazawa, Y. Hayashi, Feasibility study of {CFRP} material application to the cryogenic propellant tank of reusable launch vehicles, in: *Proceeding of 21st International Symposium of Space Technology and Science*, Omiya (Japan), 1998.
12. T. Aoki, T. Ishikawa, H. Kumazawa, Y. Morino, Mechanical behavior of cf/polymer composite laminates under cryogenic environment, in: *International Conference on Composite Materials ICCM 12th*, Paris (France), 1999.
13. R. H. Zee, C. Y. Hsieh, Energy loss partitioning during ballistic impact of polymer composites, *Polymer Composites* 14 (3) (1993) 265–271.
14. R. P. Reed, M. Golda, Cryogenic properties of unidirectional composites, *Cryogenics* 34 (11) (1994) 909–928.
15. J. P. Hou, N. Petrinic, C. Ruiz, S. R. Hallet, Prediction of impact damage in composite plates, *Composites Science and Technology* 60 (2000) 273–281.
16. F. Chang, K. A. Chang, A progressive damage model for laminated composites containing stress concentrations, *Journal of Composite Materials* 21 (1987) 834–855.

Analysis of the numerical instabilities in the hydrocodes when using an elasto-viscoplastic behaviour.

Pierre Mouro
PSA Peugeot Citroën

G rard Gary
LMS Ecole Polytechnique

ABSTRACT

An analysis of instabilities observed in numerical integration made with hydrocodes is made in this paper. This instability mostly affect the calculated strain-rate inside the elements. It is shown that it is due to the approximations used in the integration scheme in order to minimize the time consumption. A stability criterion is proposed. It is the generalization of the Courant condition to viscoplastic unloading situations. Some solutions are evaluated, including those used in commercial hydrocodes.

INTRODUCTION

In order to simulate the response of metallic structures under dynamic loading, it is usually necessary to take account of the viscous property of materials such as steel. In the commercial hydrocodes such as "Radioss" or "LS-DYNA" the constitutive models that are available are based on the classical elasto-plasticity theory. In order to integrate step by step the constitutive equations they use approximate schemes. The aim of this paper is to examine the effects that these algorithmic approximations induce and, in particular, how they can lead to numerical instabilities. A more detailed presentation of this work is found in [Mouro, 2002].

GENERAL DESCRIPTION OF THE CONSTITUTIVE MODEL

In the frame of the classical plasticity theory, it is assumed that the loading produce a plastic flow when a given level of stress is reached. This plastic flow is assumed incompressible. After unloading, a residual strain is observed. This assumption induce that the strain-rate tensor is written in the form of an elastic part and an added purely deviatoric non-elastic part [Hughes, 1984].

Most of tests are conducted under uniaxial loading. Consequently, a simple way to describe the constitutive law is to assume the validity of a yield criterion and to define a simple scalar relation between "equivalent" (related to the chosen plasticity criterion) mechanical parameters that are the stress, the strain and the plastic strain rate. For technical reasons, this relation is generally given by a function k written in the general following form:

$$k = f(\sigma, \dot{\epsilon}^p) \quad (1)$$

Due to the general lack of more precise information, the Von Mises yield criterion is chosen for purely numerical reasons. It is associated with an isotropic strain hardening. It leads to the following set of equations:

$$\dot{\epsilon}_{ij}^p = \frac{3}{2} \dot{p} \frac{s_{ij}}{\sigma_{eq}} s_{ij} \quad (2)$$

$$\sigma_{eq} - k(p, \dot{p}) = 0 \quad (3)$$

$$\text{with: } \dot{p} = \left(\frac{2}{3} \dot{\epsilon}_{ij}^p \dot{\epsilon}_{ij}^p \right)^{\frac{1}{2}} \dots \text{et } \sigma_{eq} = \left(\frac{3}{2} s_{ij} s_{ij} \right)^{\frac{1}{2}} \quad (4)$$

Johnson and Cook [Johnson and Cook, 1983] have proposed the following expression for the function k .

$$k(p, \dot{p}) = (A + Bp^n) \left(1 + C \ln \left(\frac{\dot{p}}{\dot{p}_0} \right) \right) \quad (5)$$

In this law, five parameters (A, B, n, C, \dot{p}_0) have to be determined. This constitutive law is probably the one the more generally used in numerical crash simulations. Its limitations are related to two main points:

- the stress and the strain rate are increasing (or decreasing) in the same manner. It means that an increase of the stress with the strain rate automatically induces an increase of the strain hardening.
- The relation between the stress and the logarithm of the strain rate is bi-linear. It does not permit to describe correctly the real experimental situation over a large range of strain rates.

Nevertheless, it appears as a good compromise between a relatively easy identification of its parameters and an acceptable description of the behaviour of real metals. This law will be considered in the following as it does not interfere with the general purpose of this paper.

ANALYSIS OF THE NUMERICAL INSTABILITY

ALGORITHMIC OF HYDROCODES.

In commercial hydrocodes, the global integration scheme introduces the question of the constitutive law of the material in the following context:

At a given step, the strain rate tensor is known and is assumed to be constant during the corresponding time step. All other mechanical values are known at the previous step. The only remaining values to be calculated at the present step (step $n+1$) are the components of the Cauchy stress tensor $\sigma_{ij}(n+1)$.

INTEGRATION OF CONSTITUTIVE EQUATIONS

The integration scheme is known under the name of "radial return scheme". It has been developed by Wilkins [Wilkins, 1964] in the case of perfect plasticity and generalised (to the case with strain hardening) by Krieg R.D and Krieg D.B [Krieg and Krieg, 1977].

In order to use it with strain-rate sensitive models the following hypothesis is used. The equivalent plastic strain-rate ($\dot{\epsilon}_p$) is taken equal to the total equivalent strain rate ($\dot{\epsilon}$) as it is known at the beginning of the time step.

In a first step, it is assumed that the strain increment is purely elastic. The stress is then computed and it is checked whether this assumption was valid or not by comparison of this computed stress with the known yield criterion. When the computed stress is greater than the criterion, the strain is split in two

parts: an elastic part and a (purely deviatoric) plastic part. From this consideration, a relation is obtained for the deviatoric part of the stress tensor, between the estimated stress and the one to be calculated.

$$s_{ij}(n+1) = s_{ij}^{estimated} + 2G\Delta\varepsilon_{ij}^p(n+1) \quad (6)$$

The plastic strain increment is then directly calculated by the normality rule. This rule (the plastic stress increment is in the direction of the vector orthogonal at its origin to the yield criterion) gives an equation to be added with a second one given by the combination of the Von Mises criterion and an isotropic strain hardening. Both equations allow for the calculation of the two unknown arguments in equation (6). The calculation of the increment of the equivalent plastic strain is made easy with the use of the linear expansion of the k function around the known value of $\dot{\varepsilon}_p(n)$, the second argument of this function being constant. The final equivalent total plastic strain is then obtained. The components of the deviatoric stress tensor are deduced by a simple homothetic transformation.

SHOWING THE INSTABILITY.

A finite element calculation is made for the simple case of a pure traction test. The specimen is meshed with shell elements in plane stress. The specimen is loaded at one end with a speed given in the following form:

$$v(t) = v(0)e^{\kappa t} \quad (7)$$

The other end is fixed. A tensile state at a constant strain rate κ is rapidly obtained in the specimen (when the parameters are correctly chosen).

Two simulations are made. In one simulation, a strain-rate sensitive model is used. In a second one, the model is not strain-rate sensitive with a choice of fixed parameters giving a correct behaviour at the strain rate of the test.

In fig 1, the stress and the cumulated plastic strain are shown for an element in the middle of the specimen.

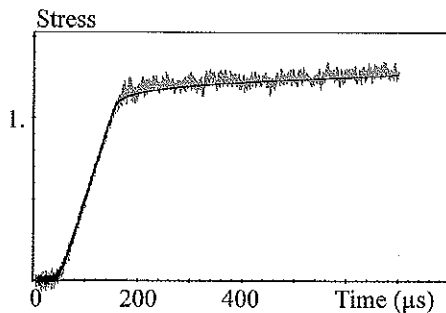


fig 1a. Stress in an element

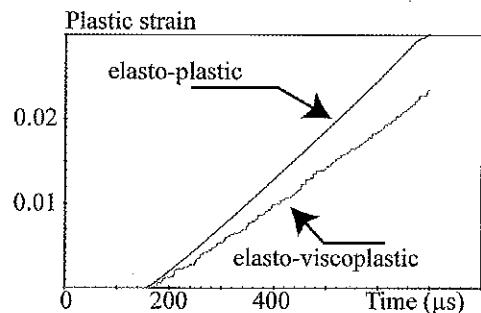


fig 1b. plastic strain in an element.

The viscoplastic model (strain-rate sensitive - grey curve) gives a noisy stress response which is, in average, slightly greater than the one of the purely plastic model. For the stresses, the difference is small. The situation is completely different when considering the total plastic strain which is smaller in the case of the viscoplastic model. Moreover, its increase is not exactly smooth as it should be expected from the chosen loading.

ONE DIMENSIONAL ANALYSIS.

The response observed above using the program Radioss is now reproduced by means of a one-dimensional totally open explicit code - hydrocode -(written in "Matlab" language). The specimen is divided in four elements. The last node is clamped while a sinusoidal speed is applied at the first node, in order to reach rapidly an equilibrium state (stress and strain fields constant in the space domain) and a time dependant strain-rate. After half a period, the speed of the first node is set to zero. It induces then a relaxation process. The calculation shown in fig. 2 (underneath : showing the stress, the plastic strain and the strain rate) is made with a time step 40% smaller than the time step given by the stability condition (Courant condition).

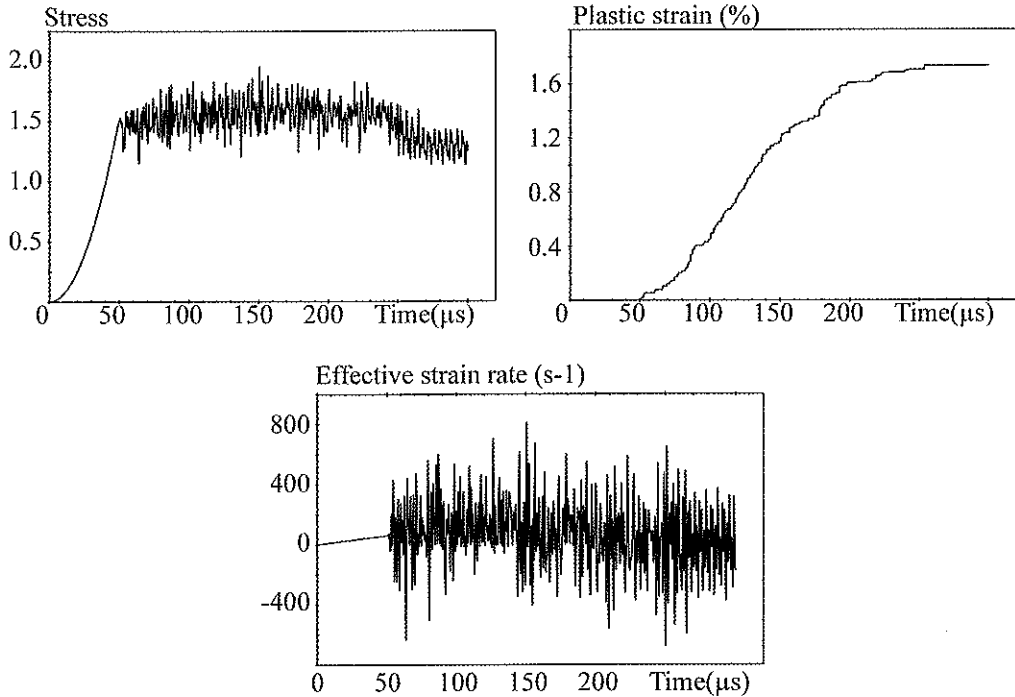


fig 2a: (upper left) : stress

fig2b: (upper right) plastic strain

fig 2c. (middle) : strain rate.

These figures (2a and 2c) show that an instability appears very early, in the phase of viscoplastic loading. The same features as observed in the calculation with Radioss are seen: the strain rate is very noisy (the average strain rate is 100 and the amplitude of the noise is close to 1000), and the cumulated plastic strain shows an irregular increase, reaching a maximum around 1.73%.

When the time step is reduced under the same loading conditions, it is observed that the unstable response is delayed. It can then be verified, in a more precise manner, that the unstable response is initiated when the calculated stress is outside an interval defined, in the incremental process, in the following way :

$$[\sigma^- = \sigma(t) - K_{crit} \dot{\epsilon} dt \quad , \quad \sigma^+ = \sigma(t) + K_{crit} \dot{\epsilon} dt] \quad (8)$$

where $K_{crit} = \rho \frac{l^2}{(dt_{calcul})^2}$ (ρ mass density, dt_{calcul} time step, l element size)

It shows that a viscous unloading can introduce a tangent modulus the absolute value of which is greater than Young's Modulus. Consequently, the stability condition required for the integration scheme is more severe than the Courant condition alone.

The link between the numerical instability and the stability condition of the numerical scheme clearly appears. Nevertheless, one can find surprising that such an event happens in the studied example where the applied strain-rate is softly changing under a state of equilibrium. The rate sensitivity of steels is indeed relatively weak and should require a significant strain-rate step to induce an unloading leading to the violation of the stability criterion.

It is then worth showing that, in the present conditions, this breaking is not a consequence of the real loading situation but a consequence of the approximations used in the integration scheme. In particular, it is related to the integration scheme used to describe the material behaviour.

SOLUTIONS FOR THE INSTABILITY PROBLEM.

SOLUTION PROPOSED IN RADIOSS

The program Radioss (in its version 4.1) proposes to filter the strain-rate used as an argument in the stress calculation scheme. Using this modification (and by comparison with fig.1), the stress and strain history appear to be improved in fig. 3.

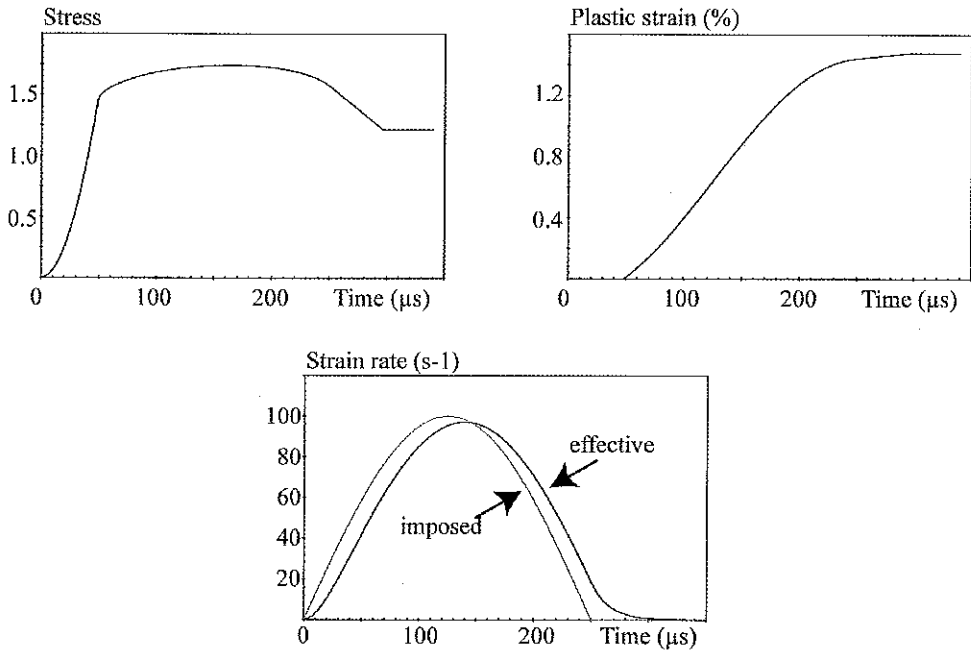


Fig 3a (upper left): stress

Fig 3b (upper right) : plastic strain

Fig 3c (middle) : strain rate.

The main negative effect of this correction is the phase shift (shown in fig. 3c) between the applied strain rate and the one finally used in the calculation.

The final plastic strain (1.48%) is very close to the final plastic strain obtained with the basic calculation when a small enough time step is used to prevent the instability.

SOLUTION PROPOSED BY NEMAT-NASSER

Nemat-Nasser and Li [Nemat-Nasser and Li, 1992] have proposed an alternative integration scheme which avoids the simplifications of the classical one when dealing with a viscoplastic step.

The method is based on the following analysis: In a situation where the stress increment is mostly viscoplastic, the stress given by the elastic trial is far from the solution. It is then more natural to use a viscoplastic prediction of the stress (viscoplastic trial). The viscoplastic increment of the total strain is then given by the routine dealing with the constitutive law. A correction taking account of the elastic strain is added afterwards.

It is shown in fig.4, under the same loading conditions, that this method gives a nice result.

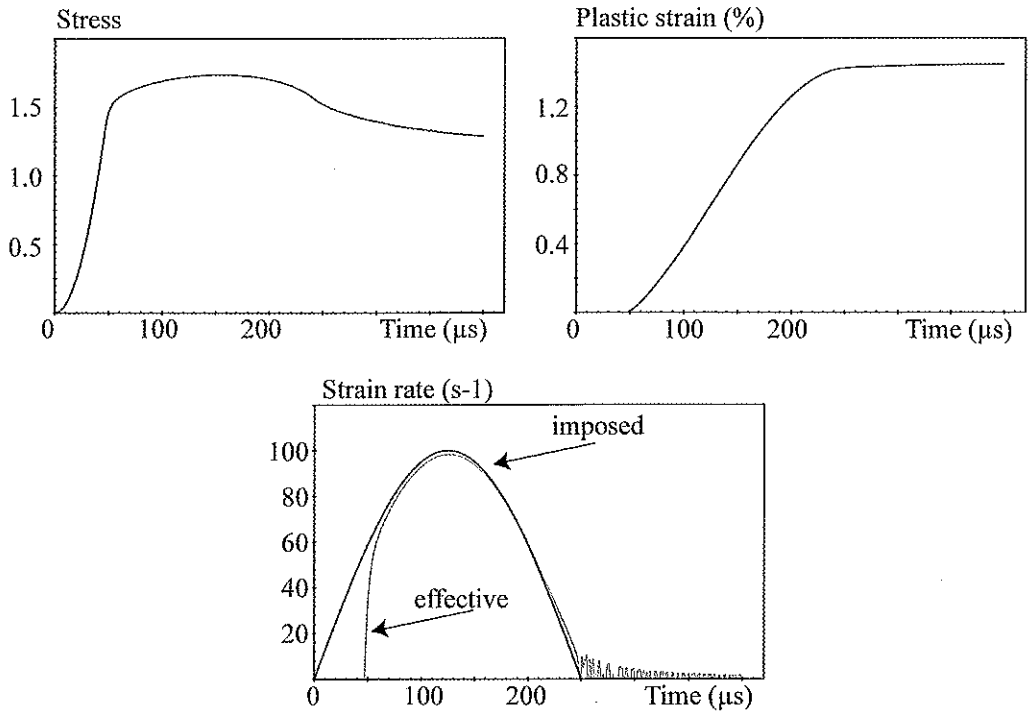


Fig 4a (upper left):stress

Fig 4b (upper right) : plastic strain

Fig 4c (middle) : strain rate.

The final plastic strain reaches here the value of 1.45%, very close to the estimated ideal one.

INTRODUCTION OF A CONVERGENCE CRITERION.

There is not a major reason to reject the use of the elastic prediction provided that it leads to a solution close enough to the theoretical one. It is then necessary to use a convergence criterion. This is done by means of an iterative scheme. A scalar equation in which the solution is the unknown parameter is then solved using the Newton method. This method is available in the DYNA-3D explicit code. Its only limitation is that it is more time consuming than the others.

CONCLUSION

In fig 5, a comparison between the 3 proposed methods is shown. Considering this figure, the following remarks arise:

The approximation made with the standard integration method for the constitutive law does not introduce a significant error in the loading phases.

The numerical instability is due to the fact that the stability condition (generalized Courant condition) is not verified because of algorithmic reasons. Anyway, it only induces small errors in the global response.

All the corrections introduced in this study induce a stronger resistance in the element where a relaxation occurs.

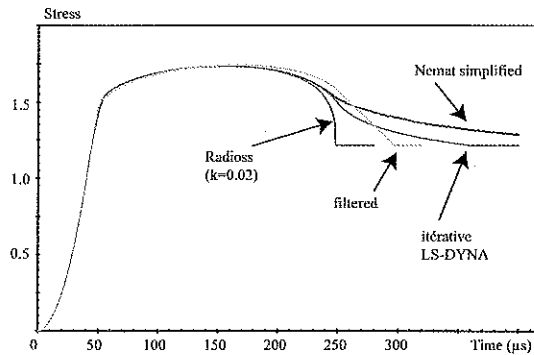


Fig. 5. Comparison between the three correction methods.

This study shows that the formulation of the viscoplastic behavior used in the hydrocodes is mechanically correct. In most cases, the oscillations observed in the strain-rate are only due to the approximations used in the integration scheme in order to minimize the time consumption. This effect could induce significant errors in a problem where a general structural instability could appear (local-global buckling) but it does not induce very important errors in most industrial situations.

REFERENCES

- T.J.R. Hughes. Numerical implementation of constitutive models, rate independent deviatoric plasticity. In *Theoretical Foundation of Large-Scale Computations for Nonlinear material behavior*, Martinus Nijhoff, pp 29-63, 1984
- G.R. Johnson and W.H. Cook. A constitutive model and data for metals subjected to large strains, high strain rates and high temperatures. In *Proc. 7th International Symposium on Ballistics, The Hague, Netherlands*, pp 541-547, 1983
- R.D. Krieg and D.B. Krieg. Accuracies of numerical solution methods for the elastic perfectly plastic model. *Trans. ASME, J. Pressure Vessel Technology*, vol 99 pp 510-515, 1977
- P. Mouro. Comportement dynamique des tôles d'acier pour le calcul de crash. *Thèse de l'Ecole Polytechnique*, 2002
- S. Nemat-Nasser, Y.F. Li. A new explicit algorithm for finite deformation elastoplasticity and elastoviscoplasticity : performance evaluation. *Computers & Structures*, vol 44 n°5 pp 937-963, 1992
- M.L. Wilkins. Calculation of elastic plastic flow. *Meth. Comput. Physics*, vol 3, 1964

Soil Stiffness Determination by Experimental and Numerical Methods

M. Parvizi, C.M. Merrifield

Manchester School of Engineering, University of Manchester, UK

M.M. Shakib

Dept. of Mechanical Engineering, UMIST

ABSTRACT

A study has been undertaken at unit gravity in the laboratory as part of a larger multi-gravity test programme in a large geotechnical centrifuge, to simulate the consolidation of a soil bed by dynamic compaction. This was achieved by allowing a tamper mass of 875 gm to fall through 100mm onto a stiff aluminum target, having a mass 268 gm and a diameter of 100mm. Since the frequencies generated by this process are very low the dynamic stiffness derived approximates the static value derived from a monotonic load test. The results of this experiment were validated by the application of a numerical model to simulate a static load test to derive a static stiffness. This paper shows that even at unit gravity with the influence of soil surface covering the stiffness obtained in the impact test by Fast Fourier Transform analysis (WAK Test) and the stiffness by static load test by numerical method are reasonably close.

INTRODUCTION

Dynamic compaction is defined as the densification of soil deposits by means of repeatedly dropping a heavy weight onto the ground surface. Historically this has been achieved by dropping a weight of between 5 and 30 tones through a height of between 10 and 40 metres onto the ground surface in a predetermined pattern over the area to be treated (Merrifield et al, 1998).

A recent development of this process is the Low Energy Dynamic Compaction (LEDC) method which has been developed for the rapid improvement of a foundation soil to a modest depth. It is termed 'low energy' because the energy input per blow is low compared with that imparted by traditional dynamic compaction techniques. The field apparatus for this method was designed originally for the rapid repair of bomb damaged airfield runways, but later adopted as a method of ground improvement (Allen, 1996).

MODEL PREPARATION

A soil bed of fine Mersey River sand ($D_{50}=0.2\text{mm}$, Coefficient of uniformity, $C_u=1.5$) was constructed by dry pluviation into a rigid model container having sides of 580mm and a depth of 460mm. The model comprised a uniform bed of loose sand having a relative density of about 38%. A stiff aluminium target (dia.=100mm), instrumented with an accelerometer active in the vertical axis, was placed on the sand surface at the location of impact. Impact was applied to this target by a pounder instrumented with a dynamic load cell. High frequency signals were buffered by covering the target with a thin rubber sheet. The frequency of impact in this test was of the order of 0.01 Hz (Parvizi & Merrifield, 2000). In addition the soil bed surface was covered by a thick rubber sheet to prevent soil disruption during application of the dynamic load. This sheet also was used to locate the target on the point of impact.

ANALYSIS

An adoption of the Wave Activation Stiffness (K) or WAK Test, a non-destructive test originally designed to assess the static stiffness of soil beneath a rigid footing (Briaud and Lepert, 1990), developed further by Allen (1996), was used to predict the increase in static stiffness of the target/soil system, the mass of the vibrated, system damping coefficient and the depth of improvement due to the dynamic compaction (Parvizi & Merrifield, 2002).

The test was performed by applying a blow of known magnitude to the rigid target or footing near its centre. This impact caused the footing and soil immediately beneath it to vibrate. The velocity signal of this vibration, derived from the accelerometer data, and the force input signal from the drop weight were used to calculate the frequency response function by taking the ratio of the Fourier transform of the response of the response signal, $v(t)$, to the Fourier transform of the input signal, $F(t)$. This transfer function is a measure of the mobility, v/F , of the system.

This analysis, which assumes a single degree of freedom system to model the footing/soil behaviour, is used to determine the internal damping of the system, C , the stiffness of the soil underlying the footing, K , and the theoretical mass of soil and footing, M , which contributes to the behaviour of the system (Tschirhart & Briaud, 1992). In the calculation of the transfer function account was not taken of the influence of the thick rubber sheet covering the soil bed surrounding the target. At low stress levels characteristic of those found in mesoscale experiments at unit gravity this would have tended to overestimate the stiffness of the system.

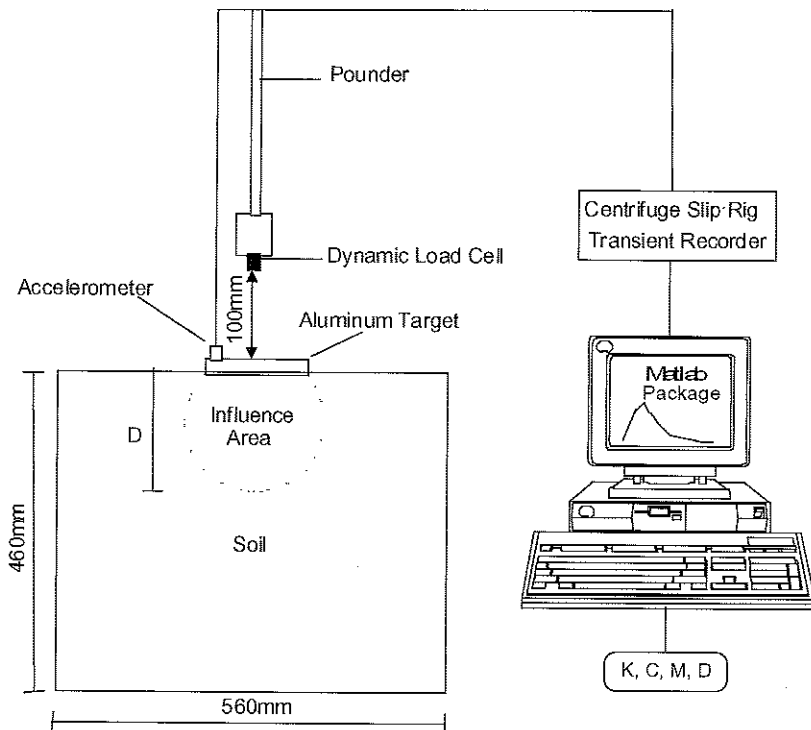


Figure1. The WAK Test applied and model box to LEDC in the centrifuge

Measurement by the load cell of the input force, F , due to the impact of the falling drop weight and resultant acceleration response of the target measured by an accelerometer placed on the target itself, provided the required output data for the analysis.

Impact data and WAK Test Results	
Date of Test:	13/3/98
Blow No.:	5
Centrifuge Test G Level:	1 g
Number of Samples:	2048
Sampling Period:	2 microseconds
WAK Test Sampling Duration:	4098 microseconds

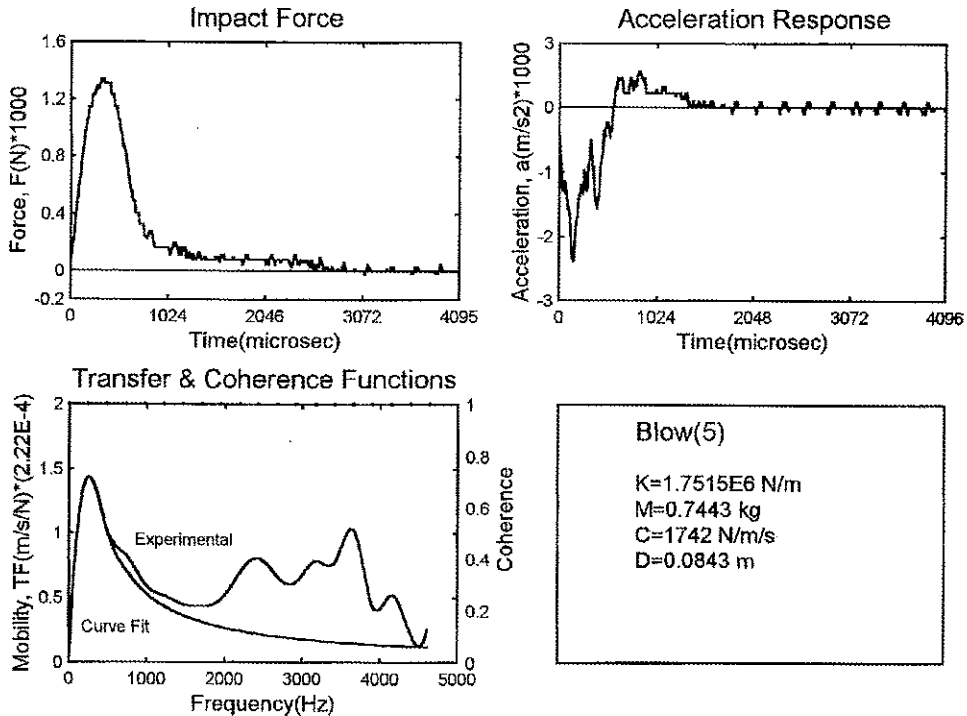


Figure 2. Typical impact data and parameters derived from the WAK Test, blow 5.

The stiffness of the soil and drop-weight combined system, the mass and the damping of the system are expressed by expansion of the transfer function, i.e.

$$\left| \frac{v}{F}(\omega) \right| = \frac{\omega}{[(K - M\omega^2)^2 + C^2\omega^2]^{1/2}} \quad 1$$

(Tshirhart & Briaud, 1992; Alien et al, 1994)

Differentiating with respect to frequency and setting to zero gives the relationship between K, and M at the undamped natural frequency of the system ω_n , i.e.

$$\frac{1}{[(K - M\omega^2)^2 + C^2\omega^2]^{1/2}} - \frac{4M^2\omega^4 - 4KM\omega^2 + C^2\omega^2}{2[(K - M\omega^2)^2 + C^2\omega^2]^{3/2}} = 0 \quad 2$$

Hence;
$$\omega = \omega_n = \sqrt{\frac{K}{M}} \quad 3$$

Substituting equation 3 into equation 2 gives

$$\left. \frac{v}{F}(\omega) \right|_{\omega=\omega_n} = \frac{1}{C} \quad 4$$

Investigation of another point on the curve, i.e. ω , $\left. \frac{v}{F}(\omega) \right|_{\omega=\omega_2}$ allows the calculation of the mass, M, by the solution of equation 1, and K by subsequent substitution into equation 3.

The theoretical depth of influence (D) due to the dynamic loading may be calculated by assuming a volumetric characteristic for the mass of soil contributing to the vibration. This is normally assumed to be truncated-spherical. Since the transient signal is aperiodic it is necessary to represent it by means of a discrete Fourier Transform. Using Matlab, a commercially available signal-processing package, the transfer function derived from the experimental data may be found (Parvizi, 1999).

Likewise the coherence function may be determined to assess the reliability of the data. A value of unity for the coherence function will be returned for a perfect relationship between input (F_ω) and the output (v_ω) signals.

Since the transfer function is inevitably irregular an iterative process of curve fitting was used to determine the best-fit values for K, M and the damping factor, C (Tshirhart & Briaud, 1992).

Figure 2 shows typical data (force input, F and accelerations output, a) and derived transfer function for a single blow (blow 5 in a series of blows). From these data the average mechanical properties for first five blows are; soil stiffness, $k = 1.646 \times 10^3$ kN/m, damping factor, $C = 1640$ N/m/sec, mass of vibrated soil, $M = 0.6993$ kg and depth of improvement, $D = 0.0815$ m.

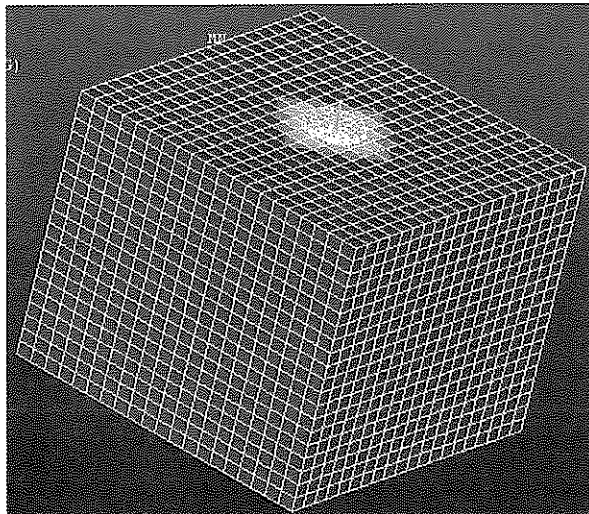


Figure3. Schematic mesh for monotonic load test

NUMERICAL MODELLING OF THE MONOTONIC LOAD-DISPLACEMENT TEST

The mesh describing the soil bed and footing system in 3-D developed for the FE analysis has been prepared by the ANSYS software package for monotonic load test (see Figure 3). The monotonic load test was simulated by the application of a series of load steps. Each load step was equal to 5N and for each step the displacement was recorded (Figure, 4). The static stiffness of the system was derived from the slope of the load-displacement curve at low loads magnitudes.

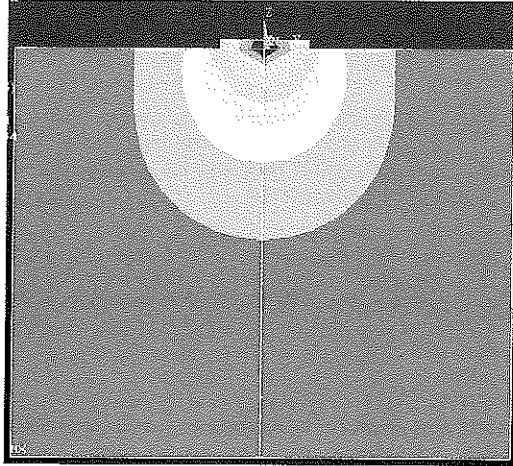


Figure 4. Contours of typical displacement due to monotonic loading (load step $F = 5\text{N}$, displacement = $0.134\text{E-}4\text{m}$)

NUMERICAL RESULTS

It was assumed that within the load range the soil behaviour was linear-elastic. The load-displacement curve is plotted in Figure 5, confirming this assumption. The stiffness calculated from this relationship was $K_{\text{Numerical}} = 1.12 \times 10^9 \text{ kN/m}$. Comparison between the value of k derived from the WAK test with that from the numerical model is shown in Table 1.

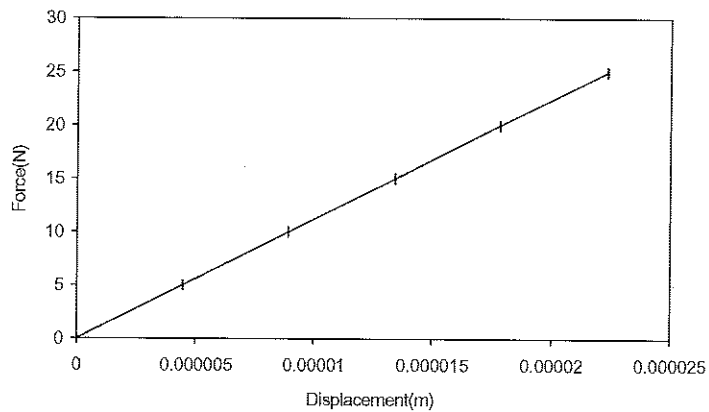


Figure 5. Load-displacement curve for the static load test numerical model

Table 1. Stiffness from the WAK Test compared to that from the numerical model.

$K_{WAK\ Test}$ kN/m x 10^3	$K_{Numerical\ model}$ KN/m x 10^3	$K_{WAK\ Test}/K_{Numerical\ model}$
1.65	1.12	1.47

CONCLUSIONS

This paper shows that notwithstanding the influence of a rubber sheet restraining the soil bed displacement at unit gravity, in essentially a multi-gravity test programme, the stiffness obtained in an impact test by a Fourier transform analysis (WAK Test) and the stiffness derived from a static load test by a numerical analysis (ANSIS) are reasonably close.

ACKNOWLEDGEMENTS

The support of the Ministry of Culture and Higher Education of the Islamic Republic of Iran is acknowledged.

REFERENCES

1. Allen, S., Davies M.C.R. & Brandon J.A. In process assessment of the stiffness of soil footing during dynamic compaction. Proceedings 19th international seminar on modal analysis, Leuven, Belgium, Sept. 1994, pp 935-946.
2. Allen, S. The low energy dynamic compaction of soil. PhD Thesis. University of Wales, College of Cardiff, 1996.
3. Briaud, J.L & Lepert, L. WAK Test to find spread footing stiffness. ASCE, Vol. 116, No. GE3,(1990), 415-432.
4. Merrifield, C.M., Cruickshank, M. & Parvizi, 1998, Modeling of low energy dynamic compaction. Proc. Int. Confr. On Geotechnical Centrifuge Modelling.
5. Parvizi, M. & Merrifield, C.M. 2000. Mechanical behaviour of a sand bed subjected to low energy dynamic compaction, 6th international conference on mechanical and physical behaviour of materials under dynamic loading, France, pp 131-135 dymat (2000).
6. Parvizi, M & Merrifield, C.M. 2002. Centrifuge modeling of soil improvement by low energy dynamic compaction. Physical Modelling in Geotechnics: ICPMG, 20002, John's /Newfoundland/ Canada.10-12 July 2002.
7. Parvizi, M. Centrifuge modeling of low energy dynamic compaction, PhD thesis, University of Manchester, 1999.
8. Tschirart A.R. & Briaud J.L., 1992. Users manual for the WAK Test- A Method of Measuring the Static Stiffness of Soil. Texas A& M University Report.

Numerical simulation of strain rate behavior of high-strength steels for impact applications

N. Peixinho; A. Pinho
University of Minho

N. Jones
University of Liverpool

ABSTRACT

This work presents results of tensile testing of a Dual-Phase steel in view of obtaining properties for constitutive models, namely Johnson-Cook equation and a modified version. Mechanical properties were obtained at strain rates ranging from 0.0001 to 141 /s. Coefficients for the studied constitutive equations were determined and the models were critically analyzed regarding their suitability for use in numerical simulation.

INTRODUCTION

The knowledge of material behavior in dynamic loading should be translated to constitutive models capable of providing a description of that behavior in analytical or numerical calculations. Hence the study of constitutive models is currently of interest for this subject. The Johnson-Cook model is widely used in crashworthiness simulations in codes such as LS-DYNA and was therefore selected. A modified version was also used in this study with the intent of evaluating its ability to provide a more accurate description of the stress-strain response for a broader range of strain-rates.

Obtaining coefficients for these material models is of particular interest in the case of Dual-Phase steels because this material is a strong candidate for use in crashworthy components. The knowledge of the strain-rate dependence coupled with the efficient use of constitutive equations is a key factor for designing energy absorbing structures using high-strength steels.

EXPERIMENTAL PROCEDURE

This study examines a cold-rolled Dual-Phase steel, having the commercial designation: DP600. This type of steel is generally considered to have a good balance between strength properties and ductility. According to some authors, Dual-Phase steels also exhibit stronger strain rate dependence and higher values of absorbed energy at high strain rates than other high-tensile steels of the same strength [1,2]. Specimens were cut in the rolling direction from material supplied by SSAB. Material thicknesses was 1mm. Tests were performed at different speeds using distinct techniques:

1. Servo-hydraulic testing machine (DARTEC, 600kN capacity), existing at University of Minho, used for lower loading speeds (0.01 mm/s) here referred as quasi-static loading. Values of engineering stress and strain were determined using the strain gauge load cell of the test machine (DARTEC, M1000 RD, 600kN), and a strain-gauge extensometer clip-gauge, SANDNER model EXA 100-10, with a gauge length of 100mm. Data were recorded digitally and stored on a personal computer.
2. High-speed servo-hydraulic tensile testing machine (ESH, 50kN capacity), existing at University of Liverpool, used for speeds ranging from 50mm/s to 3000mm/s. The machine includes a slack-

response bracket, allowing the pull-rod to accelerate before commencing to load the specimen. The internal measuring equipment of the ESH tensile testing machine included a vertical displacement transducer for the stroke of the pull-rod. Load measurements were performed using a piezo-electric load cell (Kistler model 9361B). An optical displacement transducer (ZIMMER, model 200X-20) was used to obtain measurements of absolute displacement of contrast marks (flags) placed on the specimen. This allowed strain calculation. These flags were placed at the beginning of the head region of the test specimens. This was necessary in order to avoid excessive fluctuation of the signal when the flags were placed in the gauge length distance. To improve strain measurements in the initial phase of deformation strain gauges were attached to the main body. Output signals from the equilibrated Wheatstone circuits were amplified using Tektronix model AM502 amplifiers. Readings from the measuring systems were recorded using a transient recorder Kontron, model TRA-800 and subsequently analyzed on a personal computer. Strain gauges were also placed in the head of the specimen. Since this region remains elastic these gauges were used to determine load at higher speeds. By comparing head gauge and load cell signals at low speeds, a constant factor *load signal/strain gauge signal* was calculated. By knowing this factor and the strain gauge signal the load can be determined for higher speeds. This procedure is necessary because the load cell signal shows strong fluctuation at higher speeds. This method works well, and was confirmed by analysing data in regions where the load cell and head gauge signals do not present a significant variation.

The nominal strain rates in the tests ranged from 0.0001/s to strain rates close to 150/s. The nominal strain rate was calculated by dividing the linear speed of the testing machine v_0 by the parallel length of the specimen L_C according to equation (1):

$$\dot{\epsilon} = \frac{v_0}{L_C} \quad (1)$$

EXPERIMENTAL RESULTS

Results of quasi-static and dynamic uniaxial tensile tests are presented in figures 1 and 2. The strength values generally present a moderate variation with increasing strain rate. This behaviour is expected considering the high strength values of these steels and the general decrease in strain rate dependence with increasing strength grades.

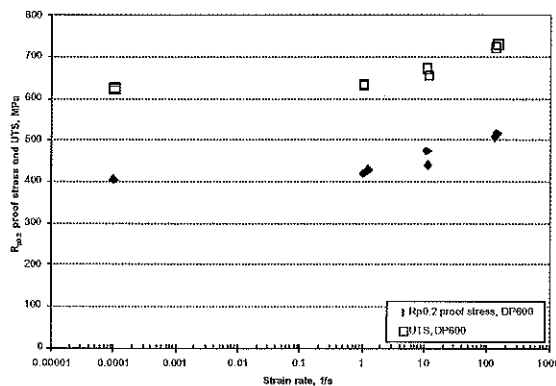


Figure 1. Variation of strength properties with strain rate

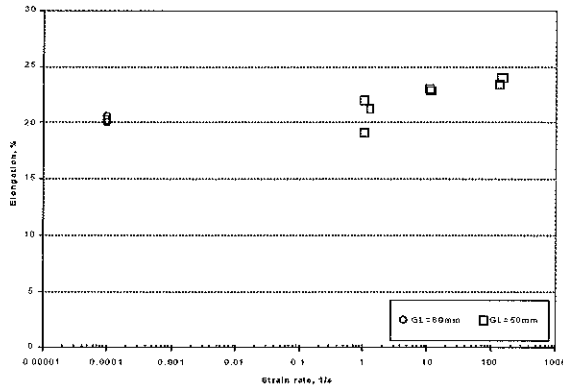


Figure 2. Variation of elongation to fracture with strain rate

The evaluation of the elongation to fracture should be considered with care since different specimen sizes were used at quasi-static loading and higher strain rates. However it is evident that the steel does not suffer a degradation of ductility with increasing loading speeds. The observed increase of elongation at the higher strain rates was obtained in specimens with the same gauge length (GL=50mm).

CONSTITUTIVE EQUATIONS

JOHNSON-COOK EQUATION

The strain rate behavior of materials is frequently described with the Johnson-Cook constitutive equation, in the original form [3]:

$$\sigma = (A + B\varepsilon^n)(1 + C \ln \dot{\varepsilon})(1 - T^{*m}) \quad (2)$$

that contains five material constants, i.e., A , B , n , C , and m , which are to be determined. The first bracket in the equation is the strain hardening term, the second is the strain rate hardening term, and the third is the thermal softening term. T^* is the homologous temperature represented by equation (3):

$$T^* = \frac{T - T_{room}}{T_{melt} - T_{room}}, \quad (3)$$

where T is the temperature of the specimen and T_{melt} is the melting temperature of the specimen material. With the present results, the temperature dependence term was neglected since all the tests were performed at room temperature and the heat resulting from plastic strain is allowed to dissipate at this strain-rates.

The strain hardening parameters A , B and n are determined at a strain rate of 1/sec. To determine parameter C in the second term a trial and error process was adopted seeking to find a good fit between the experimental true stress-true strain curves and the equation at intermediate strain rates, that is between, 1/s and 150/s.

In table 1 the determined constants are presented. Figure 3 compares the experimental results with equation (2) having empirical coefficients. The true stress-true strain curves presented do not include any correction for necking effects. In this case the analysis of results is valid only until the beginning of necking phenomena, usually near to the strain at UTS.

Table 1. Constants in the original Johnson-Cook constitutive equation

	A	B	n	C
DP600	425	915	0.52	0.025

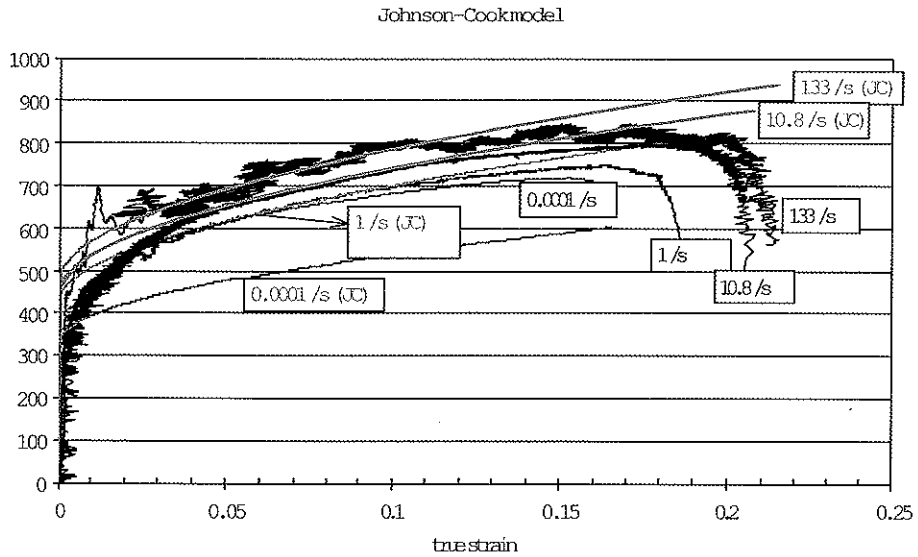


Figure 3. Results of stress-strain curves modeling using Johnson-Cook equation

MODIFIED JOHNSON-COOK EQUATION

After experimental testing with different steels, Kang et al. [4] suggested that the linear interpolation in the strain rate hardening term might not be appropriate for sheet metals. These authors suggested using a quadratic curve to interpolate experimental data, modifying the original Johnson-Cook constitutive equation to the following form:

$$\sigma = (A + B\epsilon^n) \left(1 + C_1 \ln \dot{\epsilon} + C_2 (\ln \dot{\epsilon})^2 \right) \left(1 - T^{*m} \right) \quad (4)$$

In figure 4 and table 2 the results of using equation (4) to fit experimental data are presented for the DP600 steel.

Table 2. Constants in the Modified Johnson-Cook constitutive equation

	A	B	n	C_1	C_2
DP600	425	915	0.52	0.018	0.0019

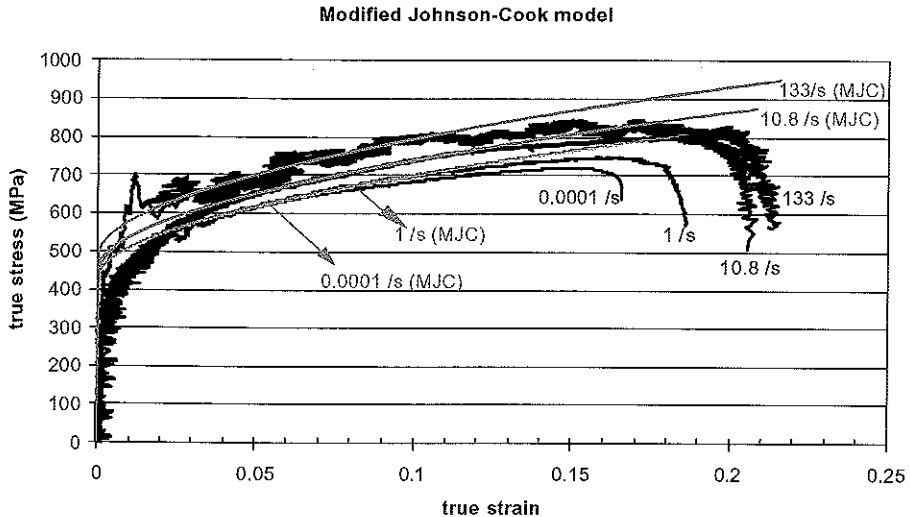


Figure 4. Results of stress-strain curves modelling using Modified Johnson-Cook equation

ANALYSIS OF RESULTS

Modelling using the Johnson-Cook equation is usually a compromise exercise since one needs to choose for which range of strain rates the better correlation is required as it is not generally possible to obtain a good fit over a broad range of strain rates. In this case, the constants in equation (2) were chosen in order to obtain a better fit at strain rates in the range 1-150 /s. With the tested steel a good correlation in the targeted range of strain rates was obtained. However, that was possible at the expense of a worse fit for the 0.0001 /s strain rate.

The use of equation (4) is a definitive improvement in relation to the original Johnson-Cook equation. The principal benefit is the ability to incorporate strain rate dependence from strain-rates as low as 0.0001 /s up to around 150 /s in our tests. This improvement is very useful for numerical analyses since the strain rate in a crushed component varies with the geometric location, it being possible to have at an instant very high localized strain rates and very low strain rates at other locations. The results of using the modified Johnson-Cook equation were very encouraging. Figure 4 displays a remarkable fit between experimental results and the curves obtained with equation (4).

CONCLUSIONS

This work presented results of testing of a dual-phase steel at different strain rates. This material is considered a strong candidate for crashworthy applications. The experimental program for the tested steel revealed results of strain-rate sensitivity in accordance with the expected behavior of such material. Also the effect of strain rate in ductility is of interest for crashworthiness applications since the elongation to fracture does not decrease at the highest strain rates. The Modified Johnson-Cook equation showed improvements over the original equation, mainly in describing behavior at lower strain rates.

ACKNOWLEDGEMENTS

We express our gratitude to SSAB Tunplatt AB for supplying the tested steels. This work was sponsored by Portuguese Foundation for Science and Technology through project POCTI/EME/39389/2001.

REFERENCES

1. K. Miura, S. Takagi, T. Hira, O. Furukumi, S. Tanimura, *High Strain Rate Deformation of High Strength Sheet Steels for Automotive Parts*, SAE paper n° 980952, 1998.
2. E. Nakanishi, H. Tateno, Y. Hishida, K. Shibata, *New Materials Technology for Achieving Both Crashworthiness and Weight Reduction Using Energy-Absorbing Steel with Higher Strain-Rate Sensitivity*, SAE paper n° 980953, 1998.
3. G. R. Johnson, W. H. Cook, *A Constitutive Model and Data for Metals Subjected to Large Strains, High Strain Rates and High Temperatures*, Proc. of 7th Int. Symposium on Ballistics, pp. 115-120, 1983.
4. W. J. Kang, S. S. Cho, H. Huh, D. T. Chung, *Modified Johnson-Cook Model for Vehicle Body Crashworthiness Simulation*, Int. J. Vehicle Design, Vol. 21, (4/5), pp. 424-435, 1999.

THE ROLE OF EXPERIMENTS IN THE DEVELOPMENT OF DEFORMATION AND FAILURE ALGORITHMS FOR NUMERICAL MODELLING SCHEMES

D.D. Radford

Cambridge University, Department of Engineering, Trumpington St., Cambridge, CB2 1PZ, UK

P.D. Church and W.G. Proud[†]

QinetiQ, Fort Halstead, Sevenoaks, Kent, TN14 7BP, UK

[†] PCS, Cavendish Laboratory, Madingley Road, Cambridge, CB3 0HE, UK

ABSTRACT

The role of experiments in the overall development of constitutive and damage relations used in numerical simulations is reviewed. The process of model development considered includes initial formulation based on the physics of material deformation and failure, calibration, validation and verification. Specific reference is made to deformation and failure algorithms that are currently used to describe material behaviour during high strain rate and impact loading. Recent results that involve a novel approach to the development of accurate numerical schemes for high strain rate and impact loading are presented.

INTRODUCTION

The availability of modern high-speed computers allows for the implementation of complicated, physically based algorithms into codes for solving complex problems involving the deformation and failure of engineering structures. Some examples that specifically involve high strain rate loading conditions include structural impacts, foreign object damage, metal-forming processes, ballistic penetration, and vehicle crash worthiness. Although it is possible to accurately simulate such problems numerically, experimental data is still required to characterise the behaviour of materials and verify the actual response of structures. The main "perceived" advantage of numerical analysis over experimentation is cost: It is generally accepted that numerically predicting the behaviour of an event is cheaper than performing an experiment. One must consider, however, the costs associated with the time and effort required in the development of accurate mathematical algorithms and performing the calculations.

The algorithms used to describe the deformation and failure processes of materials require insight that can only be obtained through experimental observations. This is the case whether the algorithms are highly empirical, analytical, or completely theoretical in nature. Once a model has been formulated, precise experiments must be performed in order to measure the physical parameters required to apply the model to specific materials. The model should then be validated against experimental data, otherwise it cannot be used for predicting the response of structures exposed to complicated loading conditions with any confidence.

In this paper, a brief overview of deformation and failure algorithms is presented. The role of experiments in the development of such models and the validation of their predictive capability is

discussed. Recent results involving numerical simulations of symmetric Taylor impact experiments are presented.

DEFORMATION AND FAILURE MODELS

The mathematical formulation describing the macroscopic response of a material to applied forces is known as a constitutive relation, or deformation model. In the most general form, deformation models relate the stress of a material to the strain, strain rate, temperature, and loading history experienced by the material. This type of relationship is applicable for ductile and brittle materials. In a similar fashion, failure, or damage models relate the current state of the material to the amount of damage that has accumulated throughout the deformation. Once a critical threshold is reached, the material can no longer withstand any stress and catastrophic failure occurs. The manner in which failure manifests itself in the calculation, depends upon the specific model.

Under dynamic loading conditions, the failure process is strongly influenced by the state of stress, strain rate and loading history for both ductile and brittle materials. In reality, both the deformation of a material and the amount of damage accumulation are intrinsically coupled and interact on a fundamental physical level. As a result, it is ideal if the deformation and failure models used in numerical simulations are mathematically coupled.

It is not possible for a single relationship to completely describe the deformation behaviour or failure process of a material for all combinations of loading conditions and histories. Depending on the intended use, availability of experimental data, and the desired accuracy of the description, a decision must be made as to the amount of effort to be invested. Typically, the effort required to describe the material behaviour is proportional to the degree of accuracy with which the governing physical mechanisms are modelled.

DEFORMATION MODELS USED IN COMPUTER CODES

Three of the most widely [1, 2, 3] used deformation models in numerical codes that do account for strain rate effects are the Johnson-Cook [4, 5], the Zerilli-Armstrong [6 - 9], and the mechanical threshold stress (MTS) [10] constitutive relations. The Johnson-Cook and the Zerilli-Armstrong constitutive relations are relatively simple, one dimensional models that account for the effects of strain, strain rate, and thermal softening on flow stress and utilise a von Mises yield criterion [1, 2, 3]. They both describe the material hardening behaviour based on the well-known power-law function introduced by Ludwick [11]. That is,

$$\sigma = \sigma_0 + K \cdot \epsilon^n \quad (1)$$

where, σ_0 , K , and n , are material constants.

The Johnson-Cook constitutive relation is an empirical relation that is relatively simple to calibrate for a given material. That is, very few experimental results in the form of stress-strain curves covering the loading conditions are required to determine the parameters. It is relatively easy to implement into computer codes, inexpensive to use and produces reasonably accurate predictions for a range of materials if loading conditions do not exceed those used to determine the material parameters.

The Zerilli-Armstrong constitutive relations are semi-empirical models based on the concept of dislocation dynamics. Separate relations were developed to describe the deformation behaviour of copper, which is FCC, and iron, which is BCC. A subsequent relation was introduced for HCP materials, which generally exhibit behaviour between that of BCC and FCC materials. Overall, the Zerilli-Armstrong relations tend to give a slightly better correlation to experimental results when compared to the Johnson-Cook relation [1, 3]. The Zerilli-Armstrong relation, however, requires slightly more data to calibrate than the Johnson-Cook relation, but is still relatively easy to implement into computer codes and inexpensive to use. Similar to the Johnson-Cook relation, however, it is not very accurate when used outside of the range of loading conditions that it was calibrated for, or for large strain calculations [3].

The MTS relation is a more advanced and physically based model that relates the macroscopic mechanical response of a material to microscopic properties [10]. It accounts for the evolution of sub-structures as a function of plastic deformation and loading history. It generally is more accurate than both the Johnson-Cook and Zerilli-Armstrong relations. Once it is calibrated for a particular material, it can be used to accurately predict deformation outside the range of calibration loading conditions [3], which has been attributed to the form used to represent the work hardening behaviour. Rather than use a power-law form [11], which yields a continuously increasing stress for increases in strain, the stress function "saturates" to a maximum level for increasing strain. This concept was based on the observation [12] that at large strains most metallic materials tend to approach a finite "saturation stress", or approach a constant, but small hardening rate at large strains [13, 14]. It should be noted, however, that the form of the equation used to describe the work hardening behaviour is not strictly physically based and, therefore, the MTS relation is also semi-empirical.

The main disadvantages of the MTS relation are that it requires an extensive experimental data base to determine the material parameters, it is more difficult to incorporate into computer codes and more computationally expensive.

Another classification of deformation models that are used in problems involving high strain rate deformation are unified viscoplastic relations. These relations are generally formulated in three-dimensions and are based on the decomposition of strain rate into elastic and plastic components, where the plastic strain rate is time dependent and can represent all possible non-elastic material processes. Significant experimental effort is also required to characterise these models for a given material. The main disadvantages of viscoplastic relations, however, are that they are more difficult to incorporate into codes and require iterative solutions making them computationally expensive. Consequently, they have seen limited use in codes utilised for high strain rate material modelling [1].

FAILURE MODELS

The response of a material or structure to extreme external forces is dramatically affected by the manner in which damage accumulates during deformation. In numerical simulations, nucleation and growth of damage leading to ultimate failure is calculated using a failure model. Although the process of dynamic failure has been extensively studied over the past few decades, it remains as one of the most challenging fields in physics, materials science and engineering due to its complex nature. As a result, most of the models introduced to date are empirically based and require large amounts of experimental data to characterise parameters for individual materials. This results in limiting the range of applicability and further increases the need for experiments to verify the accuracy and predictive capability.

During dynamic or impact loading, metals generally fail under tension due to microvoid and microcrack growth. This applies for both ductile and brittle metals. Non-metallic, brittle materials like ceramics, however, typically fail in a compressive mode. Shear banding is another failure mechanism that occurs in metallic and non-metallic ductile materials subjected to high strain rates. During dynamic loading, plastic work is converted to heat. If the material and loading conditions are such that the heat is not conducted away fast enough, deformation can localise along narrow regions, or bands, known as shear bands.

Regardless of the material type or level of ductility, failure algorithms used in codes can be loosely grouped as either (i) instantaneous failure models, or (ii) damage evolution models.

Instantaneous failure models are based on the simple idea that once some critical value of stress or strain is reached in the material, failure occurs instantaneously. This technique is employed in numerical codes by physically separating the material once the critical threshold is reached. In contrast, failure occurs in a progressive, continuous manner in damage evolution models.

Damage, in the context of failure algorithms, is generally defined as the total amount of void content per unit volume in a material and depends on stress, plastic strain, plastic work, pressure, strain rate and temperature. As the damage level increases, the effective cross-sectional area of load-bearing material is reduced, thereby decreasing the overall load-carrying capacity. The amount of void nucleation, growth and coalescence is based on the current state of the material. The state of the material is then updated in the deformation model based on the newly calculated level of damage.

The deformation and damage models are, therefore, coupled providing a positive feed back mechanism to determine the overall response of the material.

An extensive review of both deformation and failure models covering classical works and recent developments is provided in [1].

THE DEVELOPMENT, CHARACTERISATION AND VALIDATION OF MODELS

Experimental observations provide insight into the physical aspects of deformation and the process of failure that are invaluable in the development of mathematical algorithms. Such information is generally used as the foundation whether the model is highly theoretical or completely empirical. Once the foundation of a model has been constructed, precise experiments focusing on individual physical phenomena further extend the understanding of the underlying physics and are required to quantify the critical parameters in the model.

The behaviour of materials under high strain rate loading conditions can be investigated through the use of a fairly large number of experimental techniques. An excellent review on the general subject can be found in [15]. The techniques most commonly used to obtain precise data for the characterisation of materials, however, are based on two experiments: the Kolsky pressure bar, or split Hopkinson bar experiment, and the plate impact experiment. These experimental techniques provide data in strain rate regimes of 10^2 - 10^4 s⁻¹ and 10^4 - 10^7 s⁻¹, respectively.

Ideally, models should be developed and the materials characterised for the range of conditions that the material will be subjected to in the actual event of interest. In this circumstance, the deformation and failure models are not forced to extrapolate the behaviour of the material into regions that have not been verified. Generally, this is not possible due to the large range of loading conditions and complex material states associated with dynamic events. As a result, it is imperative that the models are validated to assess the true predictive capability outside the range of conditions that they were developed.

Accurately predicting the deformation and failure of materials during high strain rate and impact events represents a major challenge for numerical simulations. The approach adopted by our group involves fully integrating material testing, simulations and precise experiments. This is accomplished by representing the underlying physics in a simple manner, thereby capturing the major mechanisms, rather than attempting to simulate the vast complexity of the micro-mechanics (dislocations, etc.) at the meso-scale. The methodology involves describing the material behaviour at the computational cell level and the failure process within the cell analytically, thereby linking the macroscopic and microscopic scales [16, 17]. Although this novel approach has been quite successful at predicting high rate deformation and fracture [18, 19], it is recognised that these algorithms must be exercised in order to understand the limits of applicability. The "symmetric" version of the classic Taylor test [20] is widely used for this purpose and can be designed to produce fracture along the axis of the specimen. In a recent investigation, symmetric Taylor experiments were performed and modelled in attempt to understand the limits of our numerical techniques.

In that investigation, symmetric Taylor impact tests were performed on a proprietary material designated XM-copper, using a single-stage, light gas gun at the Cavendish Laboratory. The specimens were 12.7 mm diameter rods, 64 mm in length. The flyer rods were mounted in polycarbonate sabots and fired into stationary target rods at velocities ranging from 0.1 to 0.5 km s⁻¹. High-speed photographic sequences were taken using a DRS-Hadland Ltd. high-speed camera. Numerical simulations were performed using DYNA2D. The deformation behaviour of the rods were modelled using the Goldthorpe path-dependent deformation model [21] and the process of fracture was calculated using the Goldthorpe path-dependent fracture model [16] defined by:

$$dS = 0.67 \exp(1.5\sigma_n - 0.04\sigma_n^{-1.5})d\varepsilon \quad (2)$$

Here, σ_n is the stress triaxiality (pressure/flow stress), $d\varepsilon$ is the effective plastic strain, and S is the damage parameter, which is incremented by $S' = S + dS$. Fracture occurs when the damage reaches a critical value (S_c), which is obtained from analysis of the neck in a quasi-static tension test.

Fracture is accommodated by element removal. For iron and copper S_c is 5.4 and 4.7, respectively. The sabot was modelled using an elastic/perfectly plastic model with $E=2$ GPa, $\nu = 0.26$, and $\sigma_y = 57$ MPa. A mesh resolution study was conducted in an iterative manner producing a converging solution, based on the calculated stress within the rods. The sabot was modelled by fixing the nodes to the flyer rod using a tied slide line.

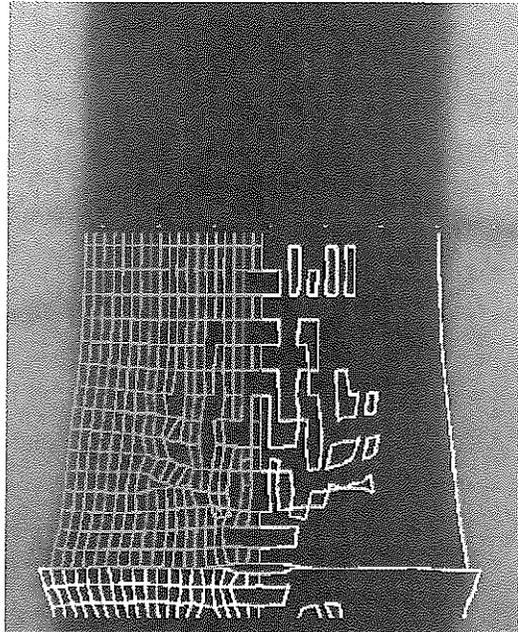


Figure 1: Photograph of deformed target (top) rod at $26 \mu\text{s}$ after impact, and calculated profile/damage (impact velocity, $V_0=255 \text{ m s}^{-1}$).

Simulations of the experiments were performed and it was determined that the deformed profile was accurately calculated in all cases and that damage evolution was complete within $10 \mu\text{s}$ after impact. Figure 1 shows a single frame of a high-speed photographic sequence at ca. $26 \mu\text{s}$ after impact for an experiment performed at 255 ms^{-1} . Included in Figure 1 is the calculated profile and the accumulated damage from a simulation. It is interesting to note that the flyer rod (bottom) has deformed more along the impact face than the target rod, despite the fact that the incident stress wave could not have propagated to the end of the rod and reflected back. Post-test measurements of the impact face diameters confirmed this phenomenon. It is believed that the experimental configuration is non-symmetric in a momentum frame of reference, as reported in [19], and is causing the asymmetric deformation. Research efforts are ongoing in this area and will be presented in future publications.

The damage accumulated along the centre-line of the specimen tested is shown in Figure 2b). Comparing Figures. 1 and 2b) it is seen that the model over-predicts the amount of damage. The general distribution of voids and the dimple on the impact face, however, is captured. Comparing Figures 2a and 2b), it is seen that the amount of damage increases as the impact velocity was increased from 200 to 255 ms^{-1} , as expected. Analytical calculations showed that the stress system leading to fracture in the specimen is mainly due to the propagation of the plastic wave. However, current calculations show that damage occurs within $10 \mu\text{s}$ after impact and, therefore, is due to release waves arriving from the outer surface of the rods. A detailed study involving meshes fine enough to resolve all waves is underway.

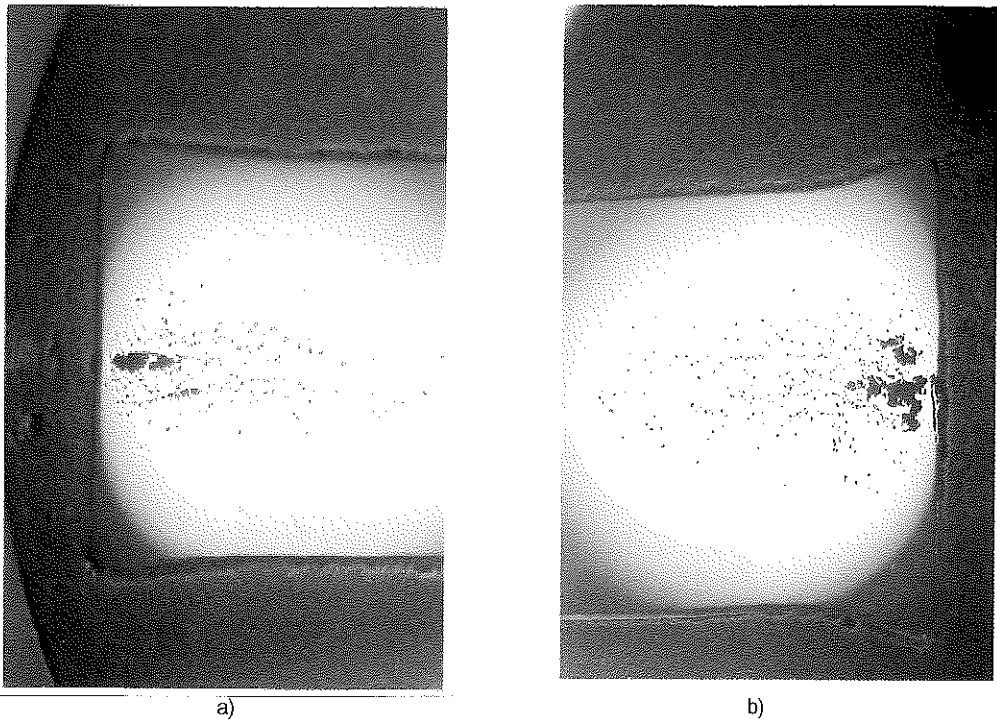


Figure 2: Damage accumulation along centre-line of target rod from symmetric Taylor impact specimens for impact velocities (V_0) of a) $V_0=200\text{ ms}^{-1}$ and b) $V_0=255\text{ ms}^{-1}$.

CONCLUSIONS

It is well established that experiments play a central role in the development of theoretical and phenomenological models used to describe the deformation and failure behaviour of materials. This role is enhanced when considering high strain rate and impact loading due to the increase in complexity of the state of stress imposed in the materials. Once a model has been developed, it must then be calibrated for the material of interest. Ideally, this process involves the use of extensive experimental data obtained over the range of applicable loading conditions. These models should then be validated by comparing results from simulations with precise experimental data. These results should be obtained for loading conditions outside those used in calibrating the models to determine the predictive capability. Finally, by maintaining a close link between experiments and theory/modelling it is possible to refine models as new experimental techniques are developed.

ACKNOWLEDGEMENTS

This work was performed under the auspices of QinetiQ. The authors would like to thank Dr. S.M Walley and Professor J.E. Field for valuable discussions.

REFERENCES

1. Nicholas, T. and Rajendran, A.M., Ch.3 in: High Velocity Impact Dynamics, Zukas, J.A. (ed.), Wiley Interscience, New York, 1990.
2. Cook, W.H., Rajendran, A.M. and Grove, D.J., *Engng Fract. Mech.* **41**, 607-623, 1992.
3. Chen S.R. and G.T. Gray III, *Metall. Mater. Trans. A*, **27** 2994-3006, 1996.
4. Johnson, G.R. and Cook, W.H., *Proceedings of the Seventh International Symposium on Ballistics*, The Hague, The Netherlands, pp. 541-547, 1983.
5. Johnson, G.R. and Cook, W.H., *Engng. Fracture Mech.* **21** 31-48, 1985.
6. Zerilli, F.J. and Armstrong, R.W., *J. Appl. Phys.* **61** 1816-1825, 1987.
7. Zerilli, F.J. and Armstrong, R.W., in *Shock Waves in Condensed Matter*, Schmidt, S.C. and Holmes, N.C. (eds.), publ. Elsevier, pp. 273-276, 1988.
8. Zerilli, F.J. and Armstrong, R.W., in *Shock Compression of Condensed Matter*, Schmidt, S.C., Tao, W.C. (eds), publ. American Institute of Physics, pp. 315-318, 1996.
9. Zerilli, F.J. and Armstrong, R.W., in *High Strain Rate Effects on Polymer, Metal and Ceramic Matrix Composites and Other Advanced Materials*, Rajapakse, Y.D.S., Vinson, J.R. (eds), publ. ASME, **48**, p.121, 1995.
10. Follansbee, P.S. and Kocks, U.F., *Acta Metall.* **36** 81-93, 1988.
11. Ludwick, P., *Elemente der technologischen Mechanik*, publ. Springer, Berlin, 1909.
12. Kocks, U.F., *Trans. ASME: J. Engng Mater. Technol.* **98** 76-85, 1976
13. Hughes, D.A. and Nix, W.D., *Metall. Trans. A* **19** 3013-3024, 1988.
14. Rollett, A.D., Ph.D. Thesis, Drexel University, Philadelphia, PA, 1988.
15. Field, J.E., Walley, S.M., Bourne, N.K. and Huntley, J.M., *J. Phys. IV France* **4** Colloq. C8 (DYMAT 94) 3-22, 1994.
16. Goldthorpe, B. D. A path dependent model for ductile fracture, *J. Phys. IV France* **7** Colloq. C3 (EURODYMAT 97) 705-710, 1997.
17. Church, P.D., T. Andrews, B.D. Goldthorpe, in *Structures under Extreme Loading Conditions (PVP 394)*, D.M. Jerome (ed.), publ. New York, American Society of Mechanical Engineers: pp. 113-120, 1999.
18. Church, P. D., J. Macmahon, I. Softley, C. Cameron, *J. Phys. IV France* **10** Pr. 9 (DYMAT 2000) 391-396, 2000.
19. Walley, S. M., P. D. Church, R. Townsley, J.E. Field, *J. Phys. IV France* **10** Pr. 9 (DYMAT 2000): 69-74, 2000.
20. Taylor, G. I. *J. Inst. Civil Engrs* **26** 486-519, 1946.
21. Gould, P. J. and B. D. Goldthorpe, *J. Phys. IV France* **10** Pr. 9 (DYMAT 2000) 39-44, 2000.

CONTACT

Darren D. Radford, dr244@eng.cam.ac.uk
Cambridge University, Department of Engineering, Trumpington St., Cambridge, CB21PZ, UK

Contribution of Computational Simulation to define the Design Drivers of a Pyrotechnic Device

Fabien RONDOT

ISL, French-German Research Institute of Saint-Louis, 68301 Saint-Louis, France

ABSTRACT

Results of a computational investigation on the parametric functional evaluation of a pyrotechnic separation device are presented.

Examples are given of some design drivers and their influence upon stresses and strains induced in the structure. Using the erosion algorithm implemented into the Lagrangian finite element code LS-DYNA to deal with failure, results are also discussed in terms of rupture capability.

A satisfactory agreement between preliminary experimental results and predictions suggests that the numerical approach has in fact been accurate in the modeling of the system functioning. Trends were drawn that give the ground rules to optimize the device.

INTRODUCTION

Use of a pyrotechnic expanding tube to separate two structures is a suitable solution for space applications. Indeed, two main advantages over a pyromechanical device can be argued: the tightness of the device and the limitation of the resultant shock. This technology is commonly used near by commercial load of space launchers.

The expanding tube includes a stainless steel tube, a lead-hexogen detonating fuse and a stuffing material. A booster is used at each extremity to facilitate ignition. The tube is inserted inside a structure in order to separate it into two pieces. When initiated, the tube expands under effect of shock wave and gas pressure. It applies stress on the structure, and cuts it with regards to a weakened notched section.

The system investigated has to do with the separation of equipment case. Numerical simulations are requested to give a parametric functional evaluation of the tube, to know more precisely the combined functioning of cutting, and particularly the influence of design drivers over the efficiency of cutting and resultant shock.

NUMERICAL APPROACH

Hydrocode calculations were carried out using the Lagrangian finite element code LS-DYNA2D [1]. As shown by Figure 1, the simulation involves the expanding tube and the two metallic sheets to be separated. A 2D plane geometry is selected: calculations are carried out for a section. The system is supposed infinite in the third dimension. Termination time was fixed to 40 μ s after ignition of the explosive.

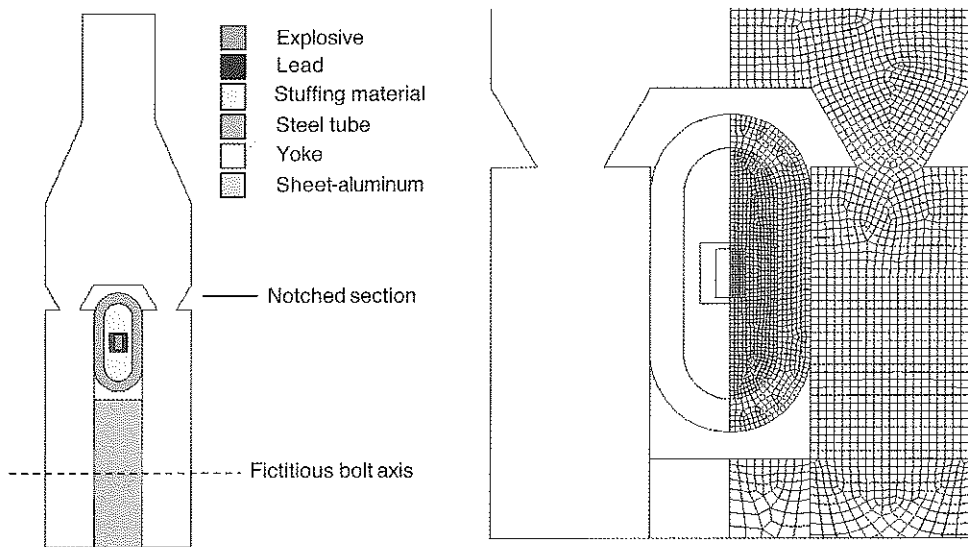


Figure 1. 2D plane geometry and details of the lagrangian mesh

The pyrotechnic tube components are meshed using elements of size ranging from $0.1 \times 0.1 \text{ mm}^2$ to $0.2 \times 0.2 \text{ mm}^2$. Around the notched section, the density of meshing is about $0.3 \times 0.3 \text{ mm}^2$.

The assembling bolt between the yoke and the sheet-aluminum is treated as a continuity of structure. Common interface nodes over the bolt size are merged.

The explosive is modeled using a JWL equation of state. Pressure "p" is related to specific relative volume V and internal volumic energy E as:

$$p(V, E) = A(1 - \omega/R_1V) e^{-R_1V} + B(1 - \omega/R_2V) e^{-R_2V} + \omega E/V$$

To take into account the physical release along the axis of propagation of the detonation wave, an instantaneous release of the entire section of the explosive is simulated. The explosive is modeled as a hydrodynamic material. The initial energy E_0 is reduced by the quantity " $\rho_0 (0,06 D)^2 / 2$ " [2].

Table I. Modeling of explosive

ρ_0 (g / cm ³)	JWL Parameters					E_0 (GPa cm ³ / cm ³)
	A (GPa)	B (GPa)	R ₁	R ₂	ω	
1.55	503.14	15.16	4.94	1.38	0.40	9.15

Inert materials are modeled using an isotropic-elastic-plastic constitutive law based on the Von Mises yield criterion. The Mie-Gruneisen equation of state, with linear shock velocity (U_s) - particle velocity (u_p) relationship, defines pressure for compressed material as:

$$p = \rho_0 C_0^2 \mu [1 + (1 - \gamma_0/2) \mu - a \mu^2/2] / [1 - (S - 1)\mu]^2 + (\gamma_0 + a \mu) E$$

and for expanded material as:

$$p = \rho_0 C_0^2 \mu + (\gamma_0 + a \mu) E$$

where C_0 and S are respectively the intercept and the slope of the U_s-u_p curve. γ_0 is the Gruneisen parameter at the ambient condition and a is the first order volume correction to γ_0 . μ is the reduced density ($\mu = \rho / \rho_0 - 1$) and E denotes the internal energy.

Figure 2 indicates the levels of strain rate recorded in the structure at selected times during a typical run. A more detailed examination reveals a peak of $3.1 \cdot 10^5 \text{ s}^{-1}$, while the notched section suffers from a maximum of $1.2 \cdot 10^5 \text{ s}^{-1}$. The "mean" strain rate regime in the structure ranges between $2 \cdot 10^4 \text{ s}^{-1}$ and $4 \cdot 10^4 \text{ s}^{-1}$.

Parameters used in the simulations are listed in Table II. The constitutive law is fully defined with the shear modulus "G" and yield strength "Y". The bulk modulus is set to " $K = \rho_0 C_0^2$ ".

Table II. Modeling of inert materials

Material	ρ_0 (g / cm ³)	G (MPa)	Y (MPa)	C_0 (m/s)	S	γ_0	a
Lead	11.34	8600	100	2092	1.452	2.74	0.54
Nylon	1.14	770	50	2290	1.630	0.87	0
Steel	7.80	77000	600	4570	1.490	1.93	0.50
7075	2.80	26700	440	5200	1.360	2.20	0.48

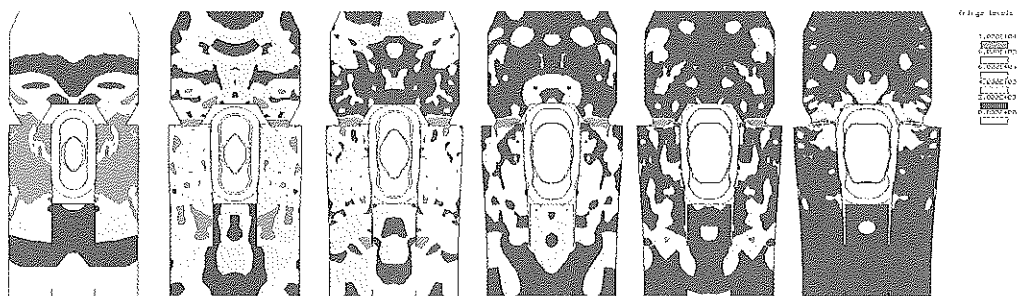


Figure 2. Fringes of effective strain rate (units in s^{-1}) in the structure at selected times

Interaction between the tube and the structure is treated using "eroding automatic" slideline.

To deal with failure of the notched section, calculations are carried out using the erosion algorithm implemented into the hydrocode. Failure is approached by a user defined erosion strain, i.e. critical plastic strain required for an element to be deleted. Erosion strain of 80% is applied to the yoke. This value has to be explained as a local degree of elementary distortion of the mesh at high strain rates. Comparison with global values obtained from a classic static tensile test is not instructive.

Different steps of the separation process are illustrated by Figure 3. Failure starts on the internal side of the notched section 10-15 μs after ignition of the explosive. The separation is achieved under 3 μs .

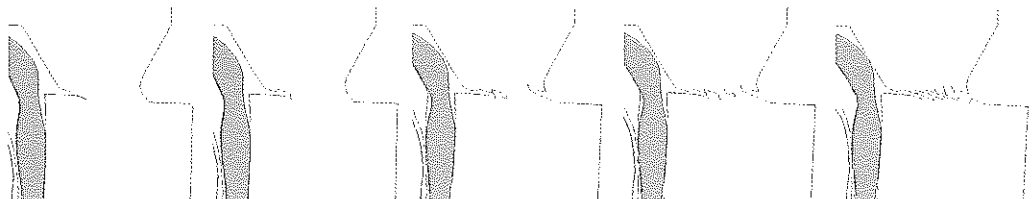


Figure 3. Typical separation process (less than 3 μs between first and last snapshots)

DISCUSSION

The parametric investigation includes tube components (amount of explosive, type of stuffing material, thickness and length of the tube), structure characteristics (rigidity of the yoke, location of the notch) and technological aspect as the permissible clearance between the tube and the structure.

AMOUNT OF EXPLOSIVE

Figure 4 shows different results obtained from variation by as much as -30% to $+50\%$ around a selected value. A minimal amount of explosive is needed to achieve separation. The major plastic strain is observed at the vicinity of the notch. Near the bolt, 15 % of plastic strain is locally showed at termination time.

When the amount of explosive is increased, failure of the notched section is initiated earlier. The shock transmitted to the structure is amplified and risk of tearing is not negligible near the bolt.

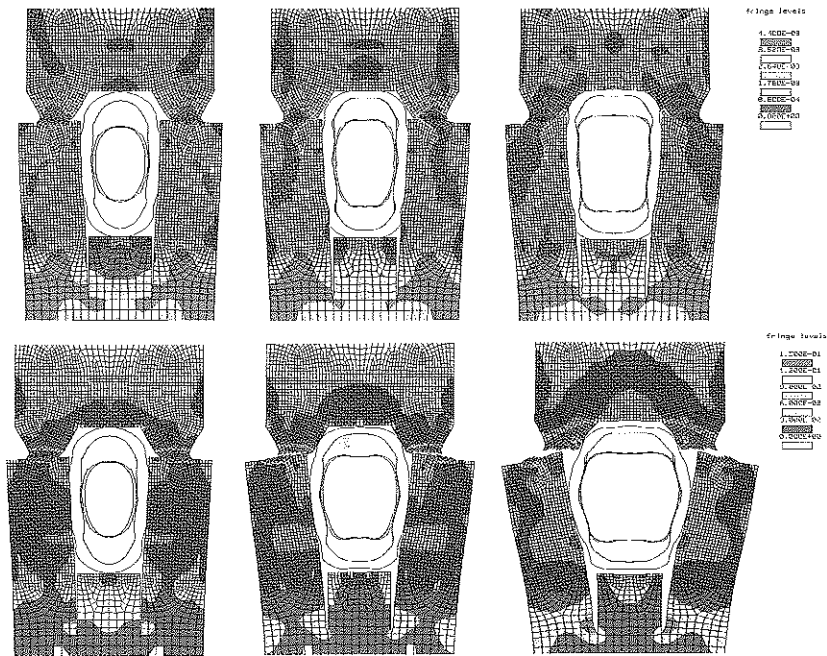


Figure 4. Influence of the amount of explosive upon the Von Mises stress 15 μ s after ignition (top) and plastic strain induced in the structure at termination time (bottom). Increasing amount from left to right.

TYPE OF STUFFING MATERIAL

Due to differences in impedance and mass, the type of stuffing material has direct effects on the expansion of the tube (Figure 5). By replacing, for instance, nylon with lead, the separation occurs earlier, but stresses applied on the structure are more important, especially at the assembling between the yoke and the sheet (Figure 6). Another criterion has to be regarded: the ultimate mechanical strength of the tube. Fringes of plastic strain of Figure 7 exhibit a very distorted tube. Breaking is likely to happen, and as a result the tightness of the system would not be ensured.

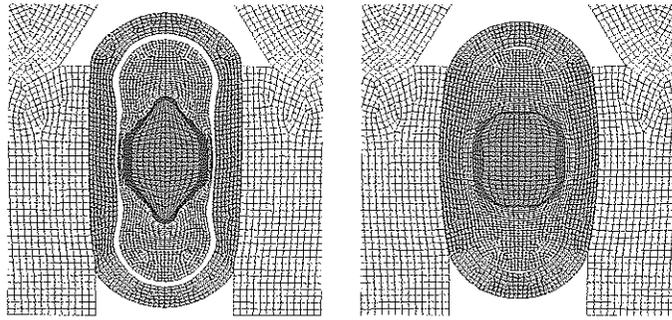


Figure 5. Tube expansion vs. stuffing material: Nylon (left) and Lead (right)

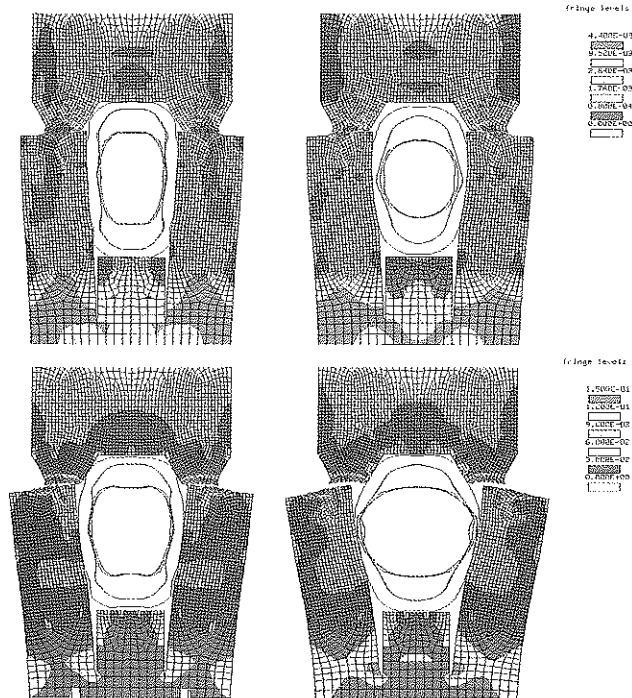


Figure 6. Effective stress at 15 μ s and plastic strain at 40 μ s: Nylon (left) and Lead (right)

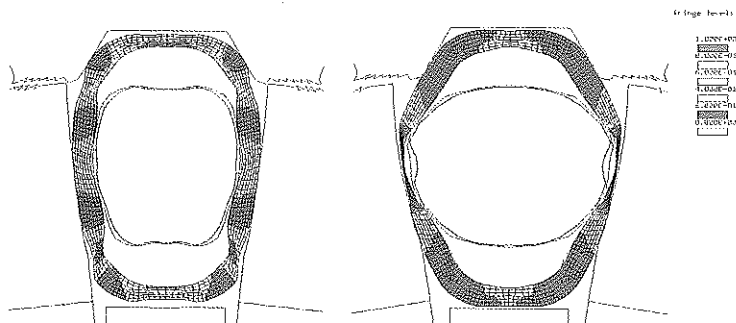


Figure 7. Tube distortion at 40 μ s when stuffing material is Nylon (left) or Lead (right)

THICKNESS OF THE TUBE

Keeping constant the external dimensions of the tube and the amount of explosive, the thickness parameter plays a minor role on the separation process (variations by 20% around a selected dimension were considered). Fringes of plastic strain of Figure 8 indicate that a thicker tube confers more homogeneity. The breaking risk of the tube, and consequently the perviousness of the system, is certainly more critic using a thin tube.

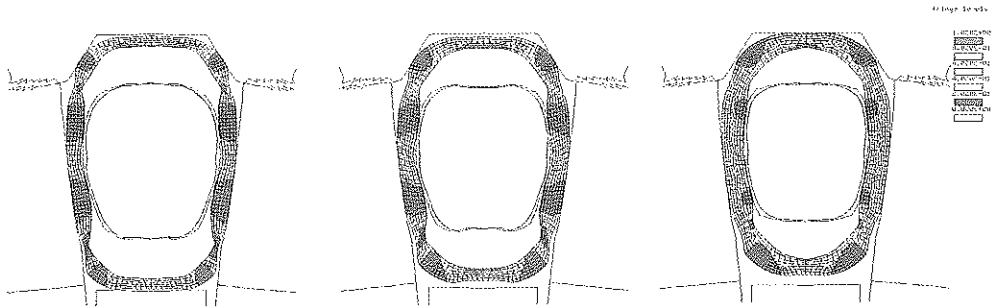


Figure 8. Tube distortion at 40 μ s (increasing thickness from left to right)

LENGTH OF THE TUBE

Shortening of the tube has a negative effect over cutting capability. Moreover, if the separation seems achieved more rapidly in case of an elongated tube, the structure is then strongly stressed, in particular at assembling zone between metallic sheets, as seen in Figure 9. An optimum length of the tube exists.

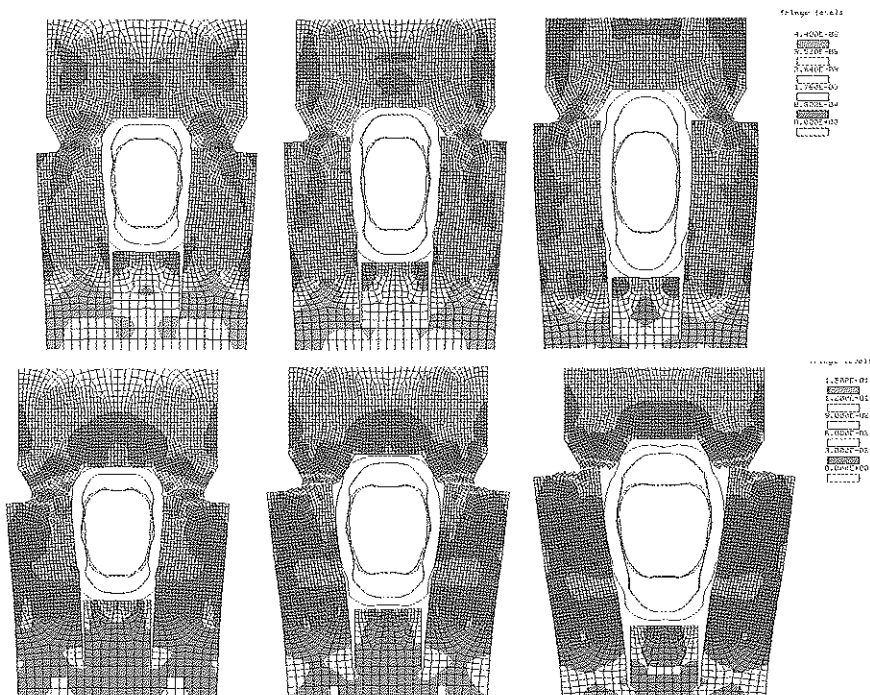


Figure 9. Influence of the length of the tube.
Variations by 20% around a selected value (middle)

RIGIDITY OF THE YOKE

Keeping constant the width of the notched section, separation is not achieved with a too thin flank. As shown by Figure 10, the plastic strain is maximal near the notch, but the global expansion of the structure leads to levels ranging between 10 and 30 % in the central part. At the "bolt", up to 30 % of plastic strain is reached at the termination time. There exists an optimal thickness for the flanks of the yoke:

- too thin and the flanks expand in a homogeneous way;
- too thick and the tube expansion is dominated.

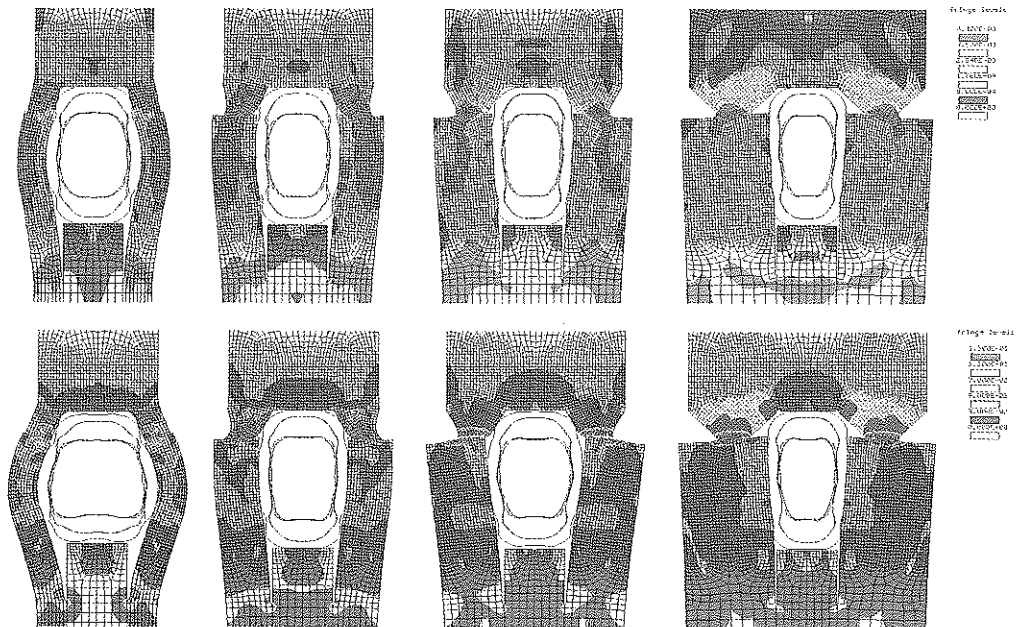


Figure 10. Von Mises stress at 15 μ s and plastic strain at 40 μ s depending on the rigidity of the yoke

ALIGNMENT OF THE NOTCH

Alignment of the notch with the tube is not worth the trouble. No failure is initiated and a larger part of the structure enters plasticity (Figure 11). The plastic strain is not only limited to the vicinity of the notch. The upper part of the yoke is also concerned (Figure 12).

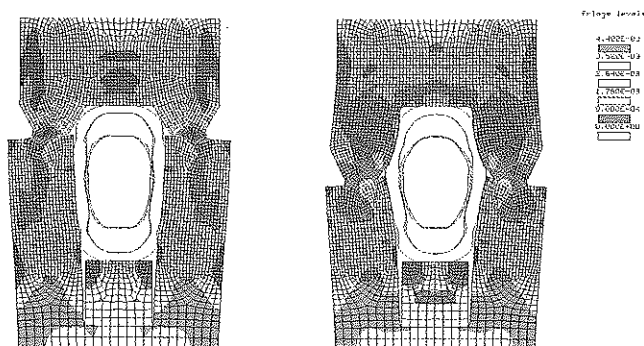


Figure 11. Effective stress at 15 μ s with in line notch (left) and out of line notch (right)

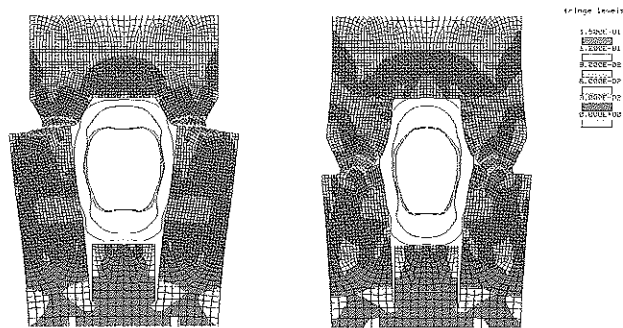


Figure 12. Plastic strain at 40 μ s with in line notch (left) and out of line notch (right)

CLEARANCE BETWEEN THE TUBE AND THE STRUCTURE

Clearance between the expandible tube and the structure is a crucial parameter. The more important it is, the more focused is the transmitted shock on the explosive centerline and the less loaded is the notched section. A permissible clearance can be predicted. Figure 13 shows that a 0.5 mm symmetrical lateral clearance is not acceptable, separation is not achieved.

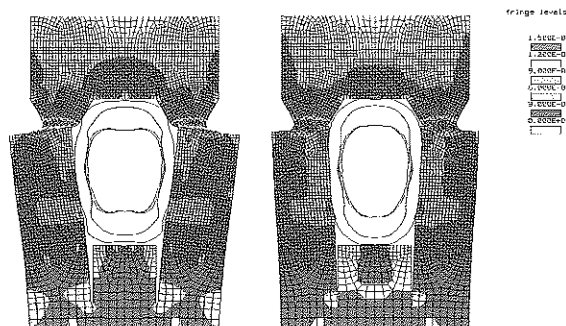


Figure 13. Effects of clearance: initial contact (left) and 0.5 mm gap (right)

COMPARISON WITH EXPERIMENTAL RESULTS

Using the same numerical erosion strain, the predicted limits in thickness of the notched section for different amounts of explosive were found to match the experimental results within a margin of 10%. This agreement suggests that the numerical approach has in fact been accurate in the modeling of the system functioning. One has to keep in mind the "warranted" reproducibility of numerical simulations, while the formula "other things being equal" is hardly, if not impossible, to be complied with during a series of trials.

CONCLUSION

A series of Lagrange simulations using an erosion algorithm was conducted to evaluate the influence of design drivers of a separation pyrotechnic device. The parametric investigation included tube components (amount of explosive, type of stuffing material, thickness and length of the tube), structure characteristics (rigidity of the yoke, location of the notch) and technological aspect as the permissible clearance between the tube and the structure.

A satisfactory agreement between preliminary experimental results and predictions suggests that the numerical approach has in fact been accurate in the modeling of the system functioning. Trends were

drawn that give the ground rules to optimize the device. By means of numerical simulation, the number of experiments are reduced significantly, and consequently the cost of a study.

REFERENCES

1. J.O. HALLQUIST. "LS-DYNA2D. An Explicit Two-Dimensional Hydrodynamic Finite Element Code With Interactive Rezoning and Graphical Display", LSTC Report 1004, April 1990.
2. IGA DEFOURNEAUX. Cours de détonique, Stage ENSTA D01 "Détonique théorique".

Size Effects in Dynamic Tension Test, Numerical Approach

A. Rusinek & J.R. Klepaczko

Laboratory of Physics and Mechanics of Materials, Metz University, Ile du Saulcy, 57045 Metz, France

ABSTRACT

Advances in experimental techniques and numerical codes have allowed during the last decades for a more detailed analysis of specimen behavior during high strain rate and impact testing for variety of materials like advanced industrial alloys, composites and ceramics. It is well known that a specimen for impact materials testing must be optimized concerning its dimensions. The main reason is to reduce strain gradients due to the effects of elastic-plastic wave propagation. On the other hand, when a Split Hopkinson Bar (SHB) in tension is applied, the net displacement of the specimen ends is very limited, usually from 2.0 to 3.0 mm. In order to reach relatively large deformations the specimen gage length must be very short, for example to reach maximum strain 0.5 the specimen length must be reduced to dimensions from 4.0 mm to 6.0 mm. Consequently small diameters or lateral dimensions must be applied to assure one dimensional deformation. Such small lengths substantially perturb idealized material behavior to be determined. For example, Lüders bands typical for materials with the upper and lower yield point disappear and formation of necking is perturbed as well. Since the authors of this contribution are interested in testing of sheet metals at high strain rates the situation is even worse, because reduction in length causes transition from one-dimensional strain to plane strain conditions where the instability mode is substantially perturbed. In this paper a numerical analysis of the effect of the initial length l_0 and the initial velocities on the elastic and plastic wave propagation in tension of thin steel sheets is reported. The purpose was to analyse the maximum impact velocity above which the process of plastic deformation is disturbed by propagation of plastic waves and the appearance of the thermoviscoplastic instability. The limit is found and analysed by a numerical methods. One of such limits in the form of so called the Critical Impact Velocity in tension has been analysed. A new approach to the CIV which takes into account the temperature coupling with plastic deformation is proposed. A precise constitutive relation which takes into account strain hardening, rate and temperature sensitivity is developed. This relation has been introduced to the FE code ABAQUS™. The FE analysis has been applied to the dynamic tension of the sheet steel ES. Existence of the CIV in tension has been confirmed numerically for different initial gage lengths l_0 as an intrinsic property.

THERMOVISCOLASTIC MODELLING

To study the dynamic deformation of sheet metals, a constitutive relation has been implemented in a FEM. Several processes have been studied as perforation [1], double shear by direct impact [2], Taylor test and tension test [3]. With the constitutive relation in the form of Eq. (1) the effects of temperature and the strain rate on the flow stress may be considered and analyzed. It is clear that the temperature increase, including adiabatic heating, has a substantial effect on the flow stress and typically it induces a decrease of flow stress with plastic strain. The thermo-visco-plastic relation applied here takes into account strain hardening, strain rate sensitivity and thermal softening. In order to describe more precisely the visco-plastic behavior the tensile stress σ is assumed to be a sum of two components σ_{h} and σ^* , which are respectively the internal and the effective stress, [9]. The first component is directly related to the strain hardening of the material and the second one defines the contribution due to the thermal activation (combination of temperature and strain rate). Thus, the flow stress is written as:

$$\sigma(\varepsilon, \dot{\varepsilon}, T) = \frac{E(T)}{E_0} [\sigma_p(\varepsilon, \dot{\varepsilon}, T) + \sigma'(\dot{\varepsilon}, T)] \quad (1)$$

where E_0 is the Young's modulus at $T = 0$ K and $E(T)$ is the evolution of the Young's modulus as a function of temperature, this expression is based to some extent on physical considerations, [9].

The final expressions for both stress components are the following :

$$\sigma_p(\varepsilon, \dot{\varepsilon}, T) = B(\dot{\varepsilon}, T) (\varepsilon_0 + \varepsilon)^{n(\dot{\varepsilon}, T)} \quad (2)$$

$$n(\dot{\varepsilon}, T) = n_0 \left(1 - D_2 \left(\frac{T}{T_m} \right) \log \left(\frac{\dot{\varepsilon}}{\dot{\varepsilon}^{\min}} \right) \right) \quad (3)$$

where $B(\dot{\varepsilon}, T)$ and $n(\dot{\varepsilon}, T)$ are respectively the modulus of plasticity and the strain hardening exponent.

In Eq. (3) n_0 and D_2 are material constants and $\dot{\varepsilon}^{\min}$ is the minimum strain rate, which defines the quasi-static stress-strain relation.

The formula for $B(\dot{\varepsilon}, T)$ is a function of the homologous temperature modified by strain rate, [5].

$$B(\dot{\varepsilon}, T) = B_0 \left(\left(\frac{T}{T_m} \right) \log \left(\frac{\dot{\varepsilon}^{\max}}{\dot{\varepsilon}} \right) \right)^{-\nu} \quad (4)$$

where B_0 is the material constant and ν is the temperature sensitivity.

The strain-hardening exponent $n(\dot{\varepsilon}, T)$ and the modulus of plasticity $B(\dot{\varepsilon}, T)$ are defined respectively by relations (3) and (4), they take into account the experimental observations that the strain hardening itself depends on temperature and strain rate. Thus, for the ES steel the strain-hardening exponent substantially changes with temperature, particularly in the adiabatic conditions, [4]. Moreover, the strain rate $\dot{\varepsilon}$, that corresponds to the complete adiabatic conditions is estimated as $\dot{\varepsilon} \approx 10 \text{ s}^{-1}$. For strain rates higher or equal to 10^2 s^{-1} , a significant temperature increase ΔT is observed during plastic deformation, it accelerates the thermal softening of the material. The process of plastic deformation is then close to the adiabatic one and the flow stress is coupled with temperature as it is discussed latter.

The explicit form for the effective stress is given below, it is similar to the equation of Arrhenius that describes the kinetics of thermally activated processes.

$$\sigma^*(\dot{\varepsilon}, T) = \sigma_0^* \left(1 - D_1 \left(\frac{T}{T_m} \right) \log \frac{\dot{\varepsilon}^{\max}}{\dot{\varepsilon}} \right)^{m^*} \quad \text{with} \quad \sigma^*(\dot{\varepsilon}, T) \geq 0 \quad \text{and} \quad \dot{\varepsilon} \leq \dot{\varepsilon}^{\max} \quad (5)$$

where σ_0^* is the effective stress at $T = 0$ K, D_1 is a constant, $\dot{\varepsilon}^{\max}$ is the maximum strain rate of validity of the model and m^* is a coefficient which characterizes the temperature and strain rate sensitivity. In adiabatic conditions, the quantities which are function of the temperature are coupled via, Eq. (6), which describes the plastic work converted into heat.

$$\Delta T_{\text{adia}} = \frac{\beta}{\rho C_v} \int_0^{\varepsilon} \sigma(\xi, \dot{\varepsilon}, T) d\xi \quad (6)$$

where β is the Taylor-Quinney coefficient of stored energy, ρ is the density and C_v is the specific heat at constant volume.

The adiabatic increase of temperature triggers the thermal softening phenomenon and reduces the rate of strain hardening. The analytical results obtained by the constitutive relations outlined above is shown in Fig. 1, for strain rates varying from $10^{-4} \leq \dot{\epsilon} \leq 10^3 \text{ s}^{-1}$.

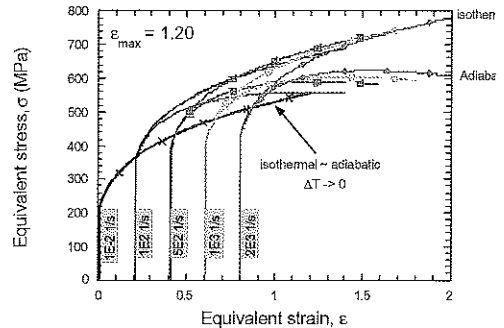
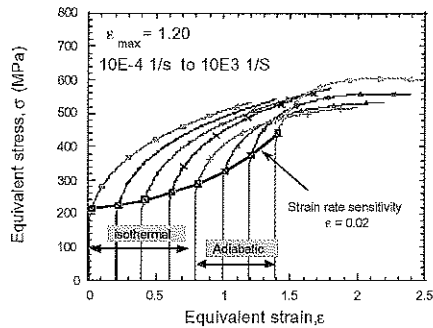


Fig. 1. Effect of the strain rate, analytical results Fig. 2. Effect of the adiabatic heating during plastic deformation

In Fig. 1 is shown that the strain rate induces an increase of the yield stress. The rate sensitivity is the most important during the modeling of the thermo-visco-plastic behavior of materials. Generally the logarithmic rate sensitivity is defined by Eq. (7), in the present case is equal to $m = 0.02$ (ES sheet steel).

$$m = \left. \frac{\partial \log \sigma}{\partial \log \dot{\epsilon}} \right|_{\epsilon} \quad (7)$$

The experimental results have permitted to estimate the logarithmic strain rate sensitivity. For the low strain rates $10^{-4} \leq \dot{\epsilon} \leq 10^{-1} \text{ s}^{-1}$, the strain rate sensitivity is equal to $m = 0.023$ and increases to $m = 0.05$ for higher strain rates $1 \leq \dot{\epsilon} \leq 10^3 \text{ s}^{-1}$, both for strain level $\epsilon = 0.1$. However, in the adiabatic conditions the first formal observation is a decrease of the strain rate sensitivity with plastic strain as shown in Fig. 2. This is induced by the thermal softening of the material that is more important when the strain rate increases. In conclusion, the strain rate sensitivity m is strongly dependent on the plastic work accumulated during plastic deformation. However, the apparent values of the strain rate sensitivity can change with the geometry of the specimen at high strain rates, as it will be shown latter during the numerical analysis.

NUMERICAL APPROACH

In order to verify the effect of the specimen geometry at different strain rates and temperatures with the visco-plastic model a series of numerical simulations have been performed with ABAQUS Explicit [6]. The aim was to simulate the tensile test and analyze the phenomenon of elastic and plastic wave propagation as a function of the initial length of the specimen used during the experiments. Three geometries have been assumed: $l_0 = 10 \text{ mm}$, $l_0 = 20 \text{ mm}$ and $l_0 = 40 \text{ mm}$. The meshes used without defect along the specimens together with all dimensions used are given below, Fig. 3.

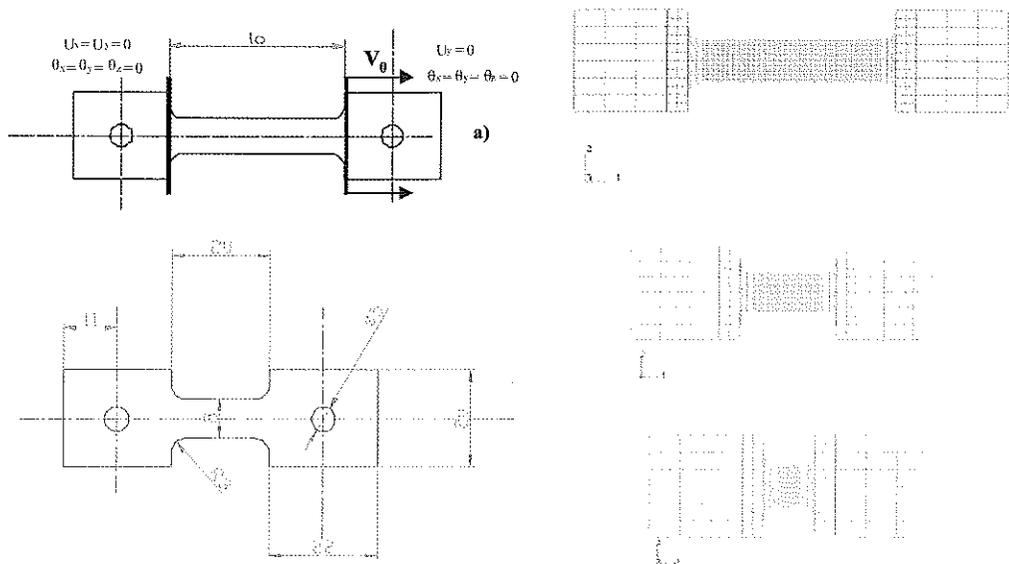


Fig. 3. Initial conditions, dimensions of the specimens and meshes used during the numerical simulations with ABAQUS Explicit

During the numerical simulations the loading profile in velocity that was assumed is an instantaneous increase from zero to the impact velocity (rectangular loading) and a constant velocity during the process of dynamic tension. The constitutive relations adopted to approximate behaviour of the mild steel ES, [1], with thickness of 0.8 mm, is discussed above, Eq. (1), and all material constants are given in [1]. The left specimen side is blocked in displacement and the right side is load by velocity.

The first series of calculations was a comparison between the constitutive behavior at isothermal and adiabatic conditions for strain rate varying from 10^2 s^{-1} to 10^4 s^{-1} where the adiabatic softening takes place. In fact, for ES steel the strain rate which defines the transition isothermal-adiabatic is equal to $\sim 10 \text{ s}^{-1}$, as it has been mentioned previously on the basis of the experimental results. Above this strain rate a change of the hardening coefficient caused by thermal softening is observed, but for the strain rates lower than $\sim 10 \text{ s}^{-1}$ the surface $\sigma(\epsilon, \dot{\epsilon}, T)$ represent the same isothermal shape, Fig. 2. To compare the numerical predictions, the curve $\sigma - \log(\dot{\epsilon})$ has been plotted for different levels of strain varying from 0.05 to 0.1.

In FE calculations the time variation of stress has been defined for two cases. In the first case the force has been defined on the opposite side of the impact and in the second case the force has been calculated on the impact side. The results are shown in Fig.4-a and Fig.4-b. A good agreement is observed at lower strain rates between the constitutive relation and numerical results. However, for strain rates higher than $5 \cdot 10^3 \text{ s}^{-1}$, the numerical results predict a decrease of the stress in comparison with the constitutive relation which assume a continuously increase. In fact, the numerical results are much realistic in the sense which it take into account the boundary conditions and the strong gradient as the temperature increase caused by the plastic strain localization and the local high strain rate. This numerical observation is made for all geometries used.

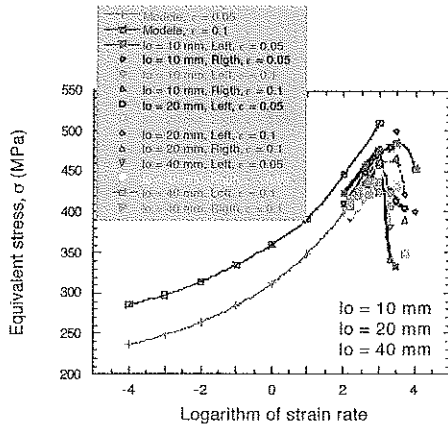


Fig. 4. Effect of the initial length at different strain rates , numerical results

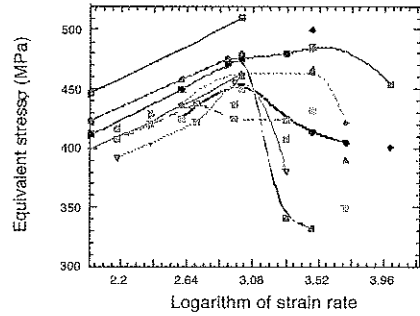


Fig. 5. Effect of the initial length at different strain rates, numerical results

The second step in FE calculations was an analysis of the initial length effect for the same strain rate equal 100 1/s. Thus, a substantial difference in behavior is observed for $l_0 = 10$ mm where the stress level is much higher, Fig. 6, and at the same time the instability ($\partial\sigma/\partial\varepsilon = \sigma$) appears earlier for all strain rates, Fig. 7. However, for the two lengths : $l_0 = 20$ mm and $l_0 = 40$ mm, very close hardening rate and stress level are found. The length of $l_0 = 20$ mm , or the range from $20 \leq l_0 \leq 40$ mm , seems to be a good compromise to study behavior of sheet metal at high and low strain rates.

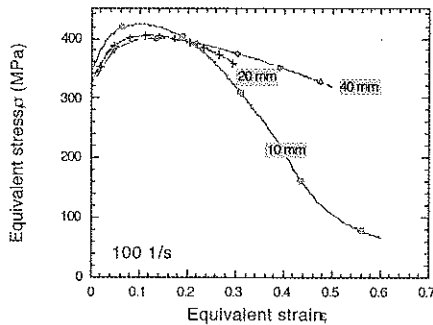


Fig. 6. Effect of initial length on reconstituted behavior of sheet steel, numerical results

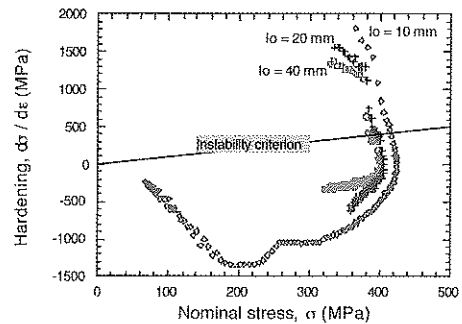


Fig. 7. Hardening rates vs. stress level for all three geometries, numerical results

At high strain rates, for example for strain rate $\dot{\varepsilon} = 10^3 \text{ s}^{-1}$, for the initial length $l_0 = 40$ mm a delay at the beginning of loading determined in the clamped end is observed on the $\sigma - \varepsilon$ curve, Fig. 8 and Fig. 9. This delay is characteristic due to wave propagation along specimen. In addition, the plastic wave trapping near the impact end may occur, such behavior is discussed latter. A disturbance of the strain gradients in the form of transmitted plastic wave along the specimen lead to the so called the Critical Impact Velocity in tension, [3].

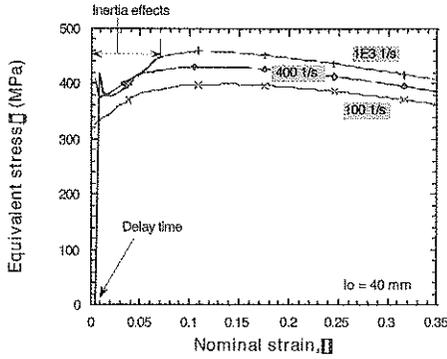


Fig. 8. Rate sensitivity of the ES steel for initial length 40 mm, numerical results

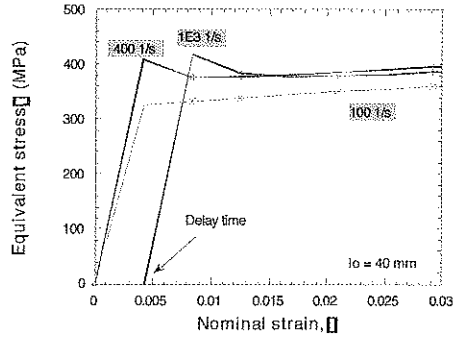


Fig. 9. Analysis of peak stress at different strain rates for initial length 40 mm, numerical results

The numerical results have permitted for an analysis of the logarithmic rate sensitivity m defined by Eq. (7), such analysis was performed for several levels of strain and for three lengths 10, 20 and 40 mm, the result is shown in Fig. 10. The mean slope is a coefficient which is equal or similar for all geometries, at strain rate varying within the limits : $100 \leq \dot{\epsilon} \leq 400 \text{ s}^{-1}$, and without effect of the strain level. In this case, m is equal to the mean value $m = 0.06$. However, when the strain rate is higher than 400 1/s differences appear between the numerical results for the different initial lengths, Fig. 10, the logarithmic rate sensitivity is varying within the limits : $0.027 \leq m \leq 0.1$ for strain level : $0.1 \leq \epsilon \leq 0.12$.

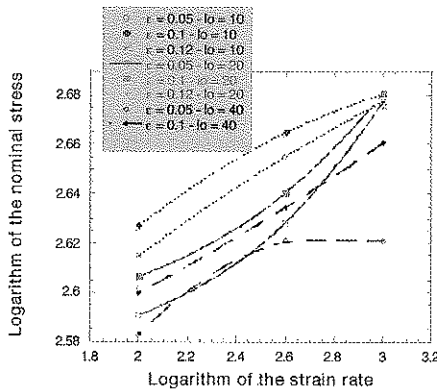


Fig. 8. Strain rate sensitivity of ES steel for all initial lengths, numerical results

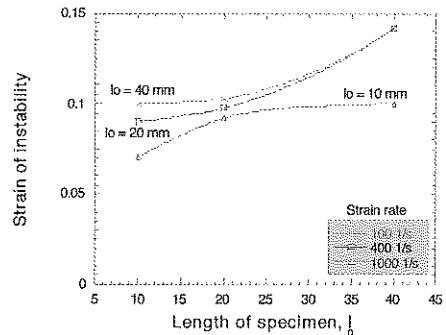


Fig. 9. Analysis of maximal strain to reach the necking for all geometries, numerical results

Due to a substantial adiabatic coupling the values of m change at high strain rates which are close to $\dot{\epsilon} = 10^3 \text{ s}^{-1}$. However at low strain, $\dot{\epsilon} = 0.05$, where the adiabatic increase of temperature is relatively small, and for the initial length $l_0 = 40 \text{ mm}$, the apparent strain rate sensitivity reaches zero for the high strain rate $\dot{\epsilon} \rightarrow 10^3 \text{ s}^{-1}$. The apparent strain rate sensitivity m equal to zero is due to the impedance mismatch effect causing wave reflections from the clamped end. This induces an inertia pick at the beginning of loading creating at the same time a decrease of the stress level determined at the clamped end at the strain level varying from $0.008 \leq \epsilon \leq 0.07$. In conclusion, finding of the "true" material behavior in the range of small strains for a longer specimen is very limited since the strain of instability for this geometry $l_0=40 \text{ mm}$ is equal to $\epsilon_{inst} = 0.1$, Fig. 9. In such case is not very easy to

study the behavior of materials and deduce experimental parameters to propose a constitutive relation. In general, an optimal specimen length deduced from Fig. 9 is 20 mm.

In the following picture, Fig. 10, a comparison is made between the constitutive relation and the numerical results for strain rates varying within the limits: $10^{-4} \leq \dot{\epsilon} \leq 10^3 s^{-1}$ and for the initial length $l_0 = 20$ mm. In this case the logarithmic strain rate sensitivity m stays relatively low with an average value equal to $m \approx 0.03$.

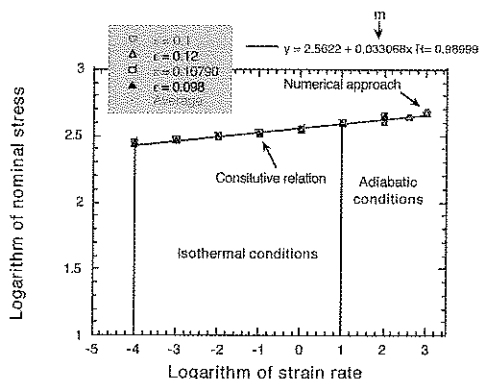


Fig. 10. Strain rate sensitivity for initial length $l_0 = 20$ mm, analytical and numerical results

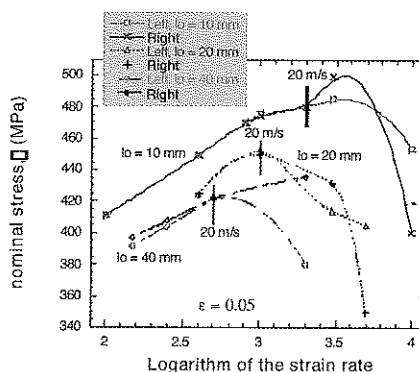


Fig. 11. Analysis of force equilibrium during dynamic tension test, numerical results

Moreover, during the numerical simulation the equilibrium of forces induced by the elastic and plastic wave propagation along the specimen by comparing the force level on the impacted side (right side) and the force level on the opposite side (left side). Thus, a critical strain rate is found for all specimen geometries above which no force equilibrium is observed between two specimen sides. Impact velocities corresponding to this critical strain rate are $V = l_0 \dot{\epsilon}$, Fig. 11. This critical strain rate is reduced when the initial length of the specimen increases, as it is shown in the figure. This phenomenon appears when the plastic waves begin inducing strain gradients along the specimen created by the strong thermal softening. In this case a part of the transmitted signal to the clamped end is disturbed by the trapping of the plastic waves caused by a substantial reduction of plastic wave speed in adiabatic conditions, $\lim C_p \rightarrow 0$, [3]. Therefore, it is very important to know the limit of the strain rate for each specimen geometry applied in impact testing. Knowing this strain rate an analysis of the dynamic behavior of a material tested is limited to the strain rates lower than this value. Above such strain rate the effects of plastic wave propagation may lead to the fact that the experimental observations are erroneously interpreted. In fact, it is suggested that all specimen geometries and set ups should be coupled with numerical analyses. Such methodology would permit to analyze the complete problem and to find an intrinsic behavior of the material. The following factors play an important role in dynamic tension test: the elastic and plastic wave propagation, the geometry of the specimen and the boundary conditions.

The main motivation of this study was to perform a systematic analysis, numerical and analytical, to find differences in behavior of short and long specimens loaded in impact tension. For this purpose precise constitutive relations were applied which include effects of strain hardening, rate and temperature sensitivity on the flow stress, [2]. The FE explicit code ABAQUS has been applied that include thermal coupling by application of adiabatic conditions of deformation. Several specimen lengths from 10 mm to 40 mm, and several velocities from 10 m/s to 120 m/s were assumed in FE calculations. It has been confirmed that too short gage lengths substantially perturbs the "material behavior" to be determined. Moreover, the second part of this study is focussed on the effect of the initial length on the triggering of instability during the process of elastic and plastic wave propagation.

SIZE EFFECTS ON THE ELASTIC AND PLASTIC WAVE PROPAGATION

In early fifties and later the Critical Impact Velocity (CIV) in tension of round specimens has been confirmed as a material property [7,9,10-12]. The latest stage of specimen deformation is, of course, failure by necking near the impact end. A complete study of an impact tension test may be classified as an example of Dynamic Failure Mechanics, a discipline in the stage of early development. The DFM is characterized that no initial cracks are present but the impact loading leads to failure. A solid is loaded in a short time interval and a more or less uniform plasticity field develops. But after a short time, because of local stress concentrations due to inertia and a particular geometry, temperature gradients appear caused by adiabatic heating, and localization of plastic field leads to failure. Thus in the case of impact tension the thermal softening appears locally leading to decrease of the strain hardening, and in the final stage the plastic wave speed C_p is reduced to zero, [3]. The final result is that the plastic deformation is concentrated close the impact end causing almost instantaneous failure of the specimen, Fig. 12. This phenomenon is called the Critical Impact Velocity (CIV). Early analytic modeling of the CIV in tension at different temperatures was reported in [12]. More recent analysis of CIV with a complete thermal coupling, that is in the adiabatic conditions, was reported in [3].

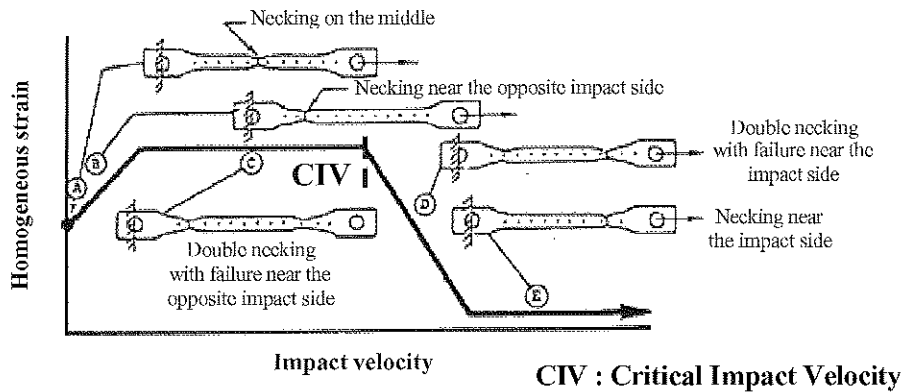
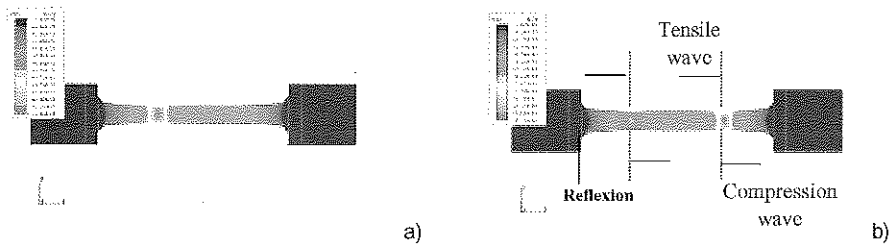


Fig. 12. Scheme of the development of the Critical Impact Velocity for a long specimen, [7].

The numerical results obtained in dynamic loading for a long specimen, $l_0 = 40$ mm, are shown in Fig. 13. In this case, the same observations as reported by Wood [7] are found where the point of instability or necking move along the specimen as a function of the initial impact velocity. Moreover, for a specific strain rate equal to 800 s^{-1} double necking appears, Fig.13-b.



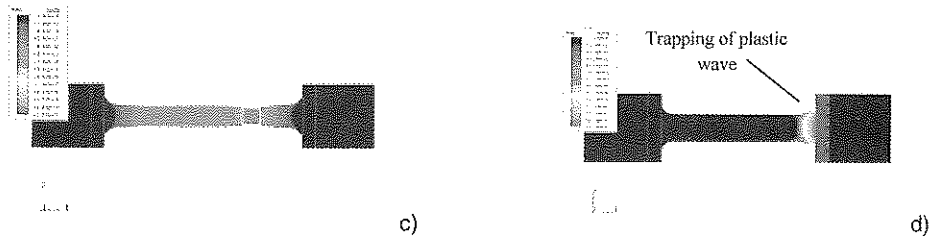


Fig. 13. Determination of the position of necking at different impact velocity V_0 , initial length $l_0 = 40$ mm,
 a - $V_0 = 10$ m/s , b - $V_0 = 32$ m/s , $V_0 = 36$ m/s , $V_0 = 120$ m/s

The distribution of plastic strain along the specimen for the impact velocity $V_0 = 10$ m/s appears as homogeneous at the beginning and also during further stages of loading, Fig. 13-a. The neck is close to the center of symmetry. At this impact velocity the homogeneity is better along a more longer specimen, 40 mm, in comparison with a short specimen, 10 mm, where the localization is more rapid. At relatively low impact velocity a longer specimen is advantageous because of reduced strain gradients. However, this is not the case at higher impact velocities where the plastic deformation gradients increase, this is shown in Fig. 13-b where the double necking develops.

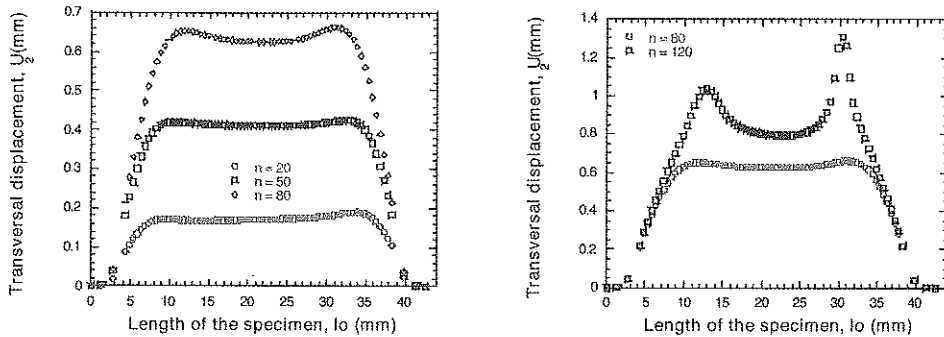


Fig. 14. a-b. Apparition of the double necking during dynamic tension, numerical results,
 $V_0 = 32$ m/s, $e^{\max} = 0.6$ with a loading time $t = 7.5 * 10^{-4}$ s

The following picture, Fig.14a-b, shows the development of the double necking at different time intervals given in μ s which appears for impact velocity $V_0 = 32$ m/s . In fact, for this impact velocity the two point of instability corresponds to a zone where a superposition appears between tensile and compressive waves inducing a strong gradient of strain. At the beginning of loading a homogeneous distribution of the transversal strain is observed, Fig. 14-a, later on a double localization occurs but the second neck located near the impact end is more important and the failure of the specimen will appear at this place as it has been shown by Wood [7], Fig. 12.

Concerning the phenomenon observed at high impact velocity, $V_0 \geq 100$ m/s , trapping of plastic waves occurs, Fig.13-d, defined as the Critical Impact Velocity. It appears that this phenomenon occurs for all specimen lengths studied, [8]. However, the double necking appears only for longer specimens beginning with the minimal length $l_0 = 40$ mm , Fig. 13-d. Thus, the Critical Impact Velocity is directly related to the behavior of material and not to the specimen geometry used during experiment. But for the short specimen, $l_0 = 10$ mm , Fig. 15 a-d, the plastic front is able to be propagate along the

specimen and it reaches the opposite side. In this case a more homogeneous strain distribution is observed with another neck appearing in the middle of the specimen, this is possible when the numerical analysis is performed without a failure criterion, Fig. 15 c-d.

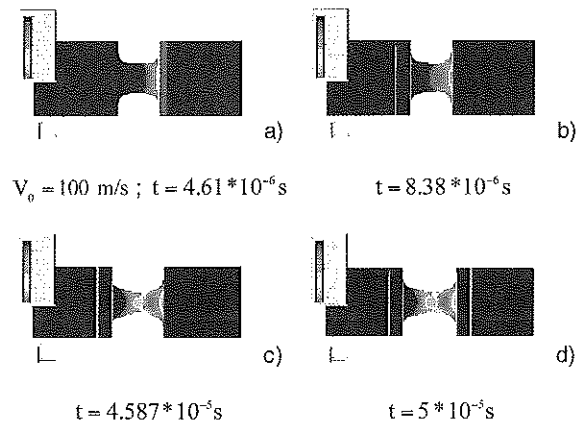


Fig. 15 a-d. Effect of the initial impact velocity for short specimen, numerical results,
 $l_0 = 10 \text{ mm}$, $V_0 = 100 \text{ m/s}$

The numerical results obtained for the standard geometry used in LPMM ($l_0 = 20 \text{ mm}$) for quasi-static and dynamic loading are shown in Fig. 16 a-b. The point of strain localization moves to the impact end at the impact velocity 100 m/s (nominal strain rate $5 \cdot 10^3 \text{ 1/s}$). The trapping of plastic waves for velocity close to $V_0 = 100 \text{ m/s}$ is obvious. For the impact velocity 60 m/s (nominal strain rate $3 \cdot 10^3 \text{ 1/s}$) the neck is situated close to the middle of the specimen. At lower strain rates the necking appears in the middle of the specimen as during standard experiments for the initial length $l_0 = 20 \text{ mm}$, Fig. 17.

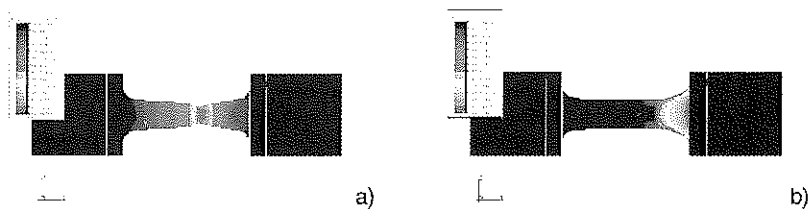
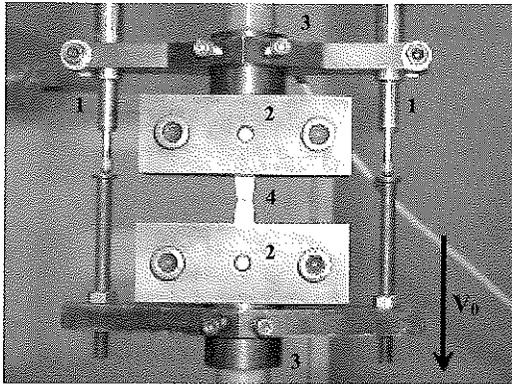


Fig. 16 a-b. Numerical results, effect of the initial impact velocity,
a) $V_0 = 60 \text{ m/s}$ – $t = 1.67 \cdot 10^{-5} \text{ s}^{-1}$ b) $V_0 = 100 \text{ m/s}$ – $t = 1 \cdot 10^{-5} \text{ s}^{-1}$

With the experimental set-up shown in Fig.17 as attached to a fast hydraulic machine (the setup designed by Klepaczko, [13]) it is possible to measure the tensile forces at both ends of the specimen and verify the force equilibrium imposed on the specimen during loading. In addition, the load cell of the machine permits also to measure the force to calibrate the system during slow loading and make a comparison with the local cells of force at fast loading. The local displacements due to specimen elongation are precisely measured, precision less than $1.0 \mu\text{m}$, by two LVDT displacement gages with the band pass 1.0 kHz. The total number of channels to be recorded is 6, that is two signals from the local load cells, two displacement signals from LVDT and two signals from the test machine: the force and displacement of the actuator.



- 1) Linear Variable Differential Transducer
- 2) Mechanical grips
- 3) Local load cells
- 4) Specimen (metallic sheet)

Fig. 17. Experimental set-up used during fast tensile test, $l_0 = 20 \text{ mm}$ and $10^{-4} \leq \dot{\epsilon} \leq 100 \text{ s}^{-1}$

CONCLUSIONS

The numerical analyses by FE have permitted to demonstrate the effect of the initial length of the specimen during the impact tension of sheet metals. It was found that there is, as expected, a limiting value of strain rate for each specimen geometry. This parameter is very important since above such strain rate the material properties determined become "apparent", the shape of the hardening is affected by the plastic wave propagation which is directly related to this value of strain rate. Moreover, determined stress level is higher for an excessively short specimen caused by a more intensified end effects of the specimen sides. The second point to be discussed is a longer deformation time or larger strain, before necking for the long specimen. This is caused by a more homogeneous distribution of the plastic strain along the specimen in comparison with the short one.

The numerical analyses of the adiabatic processes of plastic deformation coupled with plastic wave propagation in tension performed for several initial specimen lengths have revealed many interesting features. One of the purposes was to find an order of the impact velocities above which the plastic wave propagation is disturbed by the appearance of an thermo-visco-plastic instability. For example, simulations of the tensile tests of sheet metals have shown that below the impact velocity, $V_0 < 50 \text{ m/s}$, the distribution of longitudinal plastic strain is very close in both sides of the short specimen. On the other hand, when the impact velocity is increased above 50 m/s, one observes from the beginning a loss of symmetry of plastic deformation along the specimen, Fig. 11-14. When the impact velocity reaches 100 m/s, the necking occurs near the impact end, and the CIV is reached, Fig. 11-14. It is interesting to note that at relatively high velocities the form of the hardening rate and the stress level in reconstituted curves are affected by the initial length of the specimen. It was also shown that the proposed constitutive relation allows to approximate correctly thermo-visco-plastic behavior of ES sheet metal up to 10^3 1/s .

REFERENCES

1. A. Rusinek & J.R. Klepaczko, Etude numérique de la propagation des ondes dues à un chargement par impact, *Revue Française de Mécanique*, Vol. 1 (2001), pp. 55-62.
2. A. Rusinek & J.R. Klepaczko, A double shear testing of a sheet steel at low and high strain rate in large deformation and a constitutive relation on the strain and temperature dependence of the flow stress, *International Journal of Plasticity*, Vol. 17 (2001), pp. 87-115.
3. A. Rusinek & J.R. Klepaczko, A numerical study on the wave propagation in tensile and perforation test, *Journal de Physique IV*, Vol. 10 (2000), pp. 653-658.
4. A. Rusinek, P. Gadaj, J.R. Klepaczko & W.K. Nowacki, Simulation of heat exchange during simple shear of sheet steel, *Journal of Theoretical and Applied Mechanics*, Vol. 40 (2002), pp. 317-337.
5. C.MacGregor and J.C.Fisher, A velocity modified temperature for the plastic flow of metals, *J. Appl. Mech.*, Vol. 13 (1946), pp. 11-16 .
6. ABAQUS – Explicit Manual, Version 5.8, Hibbit, Karlson and Sorensen Inc., Providence, RI, USA, (1995)
7. W.W. Wood, Experimental mechanics at velocity extremes - very high strain rates, *Experimental Mechanics*, Vol.5 (1965), pp.361-371.
8. A. Rusinek and J.R. Klepaczko, Numerical analysis of size effects in dynamic tension tests and thermo-visco-plastic instabilities, Part I, to be submitted (2002), *International Journal of Plasticity*, pp. 1-35
9. J.R.Klepaczko, Modeling of structural evolution at medium and high strain rates, FCC and BCC metals, in: *Constitutive Relations and Their Physical Basis*, Proc. 8-Th Riso Mater. Symp., Riso, (1987), pp.3 – 42.
10. Th.Karman and P.E.Duwez, The propagation of plastic deformation in solids, *J. Appl. Phys.*, Vol. 21 (1950), pp. 987- 993.
11. D.S.Clark and W.W.Wood, Tensile impact properties of some metals and alloys, *Proc. ASTM*, Vol.42 (1950), pp.45-52.
12. J.R.Klepaczko, Generalized conditions for stability in tension test, *Int. J. Mech. Sci.*, Vol. 10 (1968), pp. 297-313.
13. J.R.Klepaczko, Methodology of a fast tension test with the hydraulic machine Zwick-REL-Amsler, Internal Technical Report, ISGMP-LPMM, prepared for SOLLAC, Metz, (1989).

CONTACT

Alexis Rusinek : rusinek@lpmm.univ-metz.fr,

Tél : + (0033) 3. 87. 31. 50. 20, Fax : + (0033) 3. 87. 31. 53. 66

Constitutive Equations at High Rates of Loading

Julia V. Suvorova

MERI, RAS, Moscow, Russia

Irina V. Viktorova

Clemson University, Clemson, USA

ABSTRACT

The stress-strain-time dependence for some metals and alloys based on the idea of non-linear heredity is proposed. In particular the theory can be applied to the metals with delayed yielding (low carbon mild steels). It is shown that the phenomenon of yield delay affects the slope of stress-strain diagram in any loading program considered. The proposed theory is applied to the analysis of the results of the tests for some metals under various loading and unloading rates and also to the creep and relaxation experimental data. Using some additional assumption the basic equation can be applied to the description of material behavior under repeated loading and to incremental elastic wave propagation. The problem of the longitudinal wave propagation in non-linear hereditary type medium has been solved using the Laplace transform technique. An asymptotic expansion of the solution in the vicinity of the wave front has been obtained.

INTRODUCTION

The non-linear hereditary theory has found wide application for description of time effects in polymers, including reinforced polymer composites. It turned out that such processes as creep, relaxation, creep recovery may be rather accurately described within the wide range of variation of stresses, time and temperature [1]. This presentation is intended to show that the nonlinear-hereditary theory of viscoelasticity may be, with some modifications applied to the behavioral analysis of metals.

There are two basic models for metals accounting for the loading effect. The simplest model according to Karman - Taylor - Rakhmatulin [2-3] is based on two stress-strain curves, namely static and dynamic. The dynamic diagram is assumed to be independent of the loading rate. This assumption works for the description of wave propagation in bars. However, the principle of differentiation between the "static" and "dynamic" diagrams is not available; moreover, this model is unable to describe the observed stress-strain curves rate variation.

The second type model, according to Malvern - Sokolovsky [4-5], is based on the assumption that there exists a lower static curve, which corresponds to loading at an infinitely low rate. Various generalizations and refinements were offered to develop this approach. For the specific loading case the appropriate selection of the parameters for the constitutive equation give satisfactory results, but as a rule turn out to be impractical with the change of the loading conditions. Moreover, the concept of the static yield stress is vaguely specified. Usually that is understood as the stress, which is measured during the ordinary tests on a standard tensile testing machine. However, should the loading rate be some decreased, the yield stress also decreases. Thus the position of the static curve, which should be constructed for loading at the infinitely low rate, is not clearly specified.

There exist one more fact that favored the idea of implementation of the hereditary theory. That is the functional relationship between yield stress and the history of loading in the elastic range. Originally it was observed in the experiments with low-carbon steels demonstrating the yield delay effect. The effect of delay is studied rather thoroughly at present [6] with few models describing the above phenomenon, one of which, proposed in [7], is the generalization of Taylor – Karman – Rakhmatulin model. The process of wave propagation in the bars, which was analyzed on the basis of this model, is described in [8]. When constant velocity V_0 is applied at the end of the semi-infinite bar, an elastic overstress wave propagates through the whole length of the bar first; the rear front of the wave is determined by condition of exhaustion of the yield delay capacity and moves at the velocity of an elastic wave. Since delay time is the same for all sections, the elastic relief takes place at this front down to stress σ_s , which is conditionally termed lower yield stress. Strain ε_s , corresponding to stress σ_s , remains constant for some time before the plastic wave front comes. However the value of ε_s was found to be higher than the value of the strain corresponding to the static yield stress. This cannot be caused by the rate effect, because the strain rate in the constant value region is zero. But depending on the loading rate, i.e. on the value of the overstress, both: σ_s and ε_s were found to be different. Thus the history of loading in the elastic range affects the shape of the diagram of the subsequent plastic strain and the value of the yield stress. A similar effect was discovered for high strain rate testing of the titanium alloy, which does not possess the yield delay capacity; it was demonstrated that the yield stress depends on the tension rate in the elastic range [9].

CONSTITUTIVE EQUATIONS

As it is known, the hereditary theory of viscoelasticity is based on the hypothesis of existence of the upper instantaneous straining diagram from which "slipping down" takes place with time. This circumstance played a major role in choosing the hereditary theory for the basis of the model for describing the mechanics of metals at higher rates of loading [10,11]. The peculiarity of application of the theory to metals consists in replacement the values of the total strain in the constitutive equation as suggested in [1,12] by plastic components

$$\varphi(p) = (1 + K^*)\sigma$$

$$K^*\sigma = \int_0^t K(t-s)\sigma(s)ds \quad (1)$$

Equation $\sigma = \varphi(p)$ determines the instantaneous straining diagram, $p = \varepsilon - \sigma/E$, ε is a total strain. The function $\varphi(p)$ is determined only for the positive values of the argument, $\varphi(0)$ being the dynamic yield stress at an infinitely high strain rate. The beginning of the loading process corresponds to $t = 0$; consequently, the integral term takes into account the entire history of loading in the elastic range. Apparently, some internal processes in elastic materials affect the progress of the subsequent plastic strain. At small t the integral on the right-hand side of (1) becomes extremely small and transition to the dynamic curve $\sigma = \varphi(\varepsilon - \sigma/E)$ takes place. The equation (1) is the simplest nonlinear hereditary type relationship between values of p and σ .

ACTIVE LOADING PROCESSES

At first we shall discuss the problems related to the transition from elastic to plastic state, considering separately the materials with and without the delayed yielding.

Materials without delayed yielding.

If the material does not possess the yield delay capacity, time t_0 of transition to the plastic state is to be found directly from eqn. (1); the material remains elastic until

$$\sigma + \int_0^t K(t-s)\sigma(s)ds \leq \varphi(0) \quad (2)$$

At the instant t when the equality becomes valid in (2), the material enters the plastic stage. The instant and the corresponding stress are determined as follows. If the machine grips move at a constant velocity, then

$$\sigma / E + \lambda p = Vt, V = const \quad (3)$$

Variable λ characterizes the loading system rigidity, at $\lambda = 0, V$ is the loading rate, at $\lambda = 1, V$ is the total strain rate. In general case $0 < \lambda < 1$. It follows from eon. (1)

$$\varphi(p) = \sigma + \int_0^t K(t-s)(Vs - \lambda p)ds$$

Let us assume

$$\int_0^t K(t-s)sds = G_1(t)$$

Then

$$\varphi(p) = \sigma - \lambda \int_0^t K(t-s)p(s)ds + VG_1(t) \quad (4)$$

Thus, we obtained the nonlinear integral equation for the function $p(t)$. The eon. (1) becomes valid beginning from the moment t_0 . Therefore, if $t > t_0, \varphi(p) > \varphi(0)$; if $t < t_0, p = 0$. At $t = t_0, p = 0, \sigma = \sigma_0 = VE t_0$. From eon. (4) it also follows, that

$$\varphi(0) = \sigma_0 + VG_1(\sigma_0 / VE) \quad (5)$$

The relation (5) defines yield stress σ_0 , i.e. the initial point of the plastic curve corresponding to the tension rate V . As an example Table1 gives the relationship between the yield stress and the loading rate for titanium alloy [13], obtained experimentally and calculated from (5); it was assumed that $K(t) = k/(t-s)^\alpha$, the material's parameters were: $\alpha = 0.9, k = 0.023$

Table1

$\varepsilon, 1/s$	1.5×10^{-5}	1.8×10^{-3}	5×10^{-1}	5
$\sigma_{1exp}, kg/mm^2$	31.0	34.2	38.5	40.0
$\sigma_{1calc}, kg/mm^2$	30.3	34.8	39.1	40.5

To construct the stress-strain curve in the plastic range, it is necessary to solve the integral equation (4). The case when $\lambda = 0$ (constant loading rate) is an exception, then

$$\varphi(p) = \sigma + VG_1(\sigma / VE) \quad (6)$$

The instantaneous curve calculated from the straining diagrams [9] and diagrams of tension at various rates $\dot{\varepsilon}$ are shown in Fig.1. The piece-wise linear function was taken for the approximation of the stress variation in time.

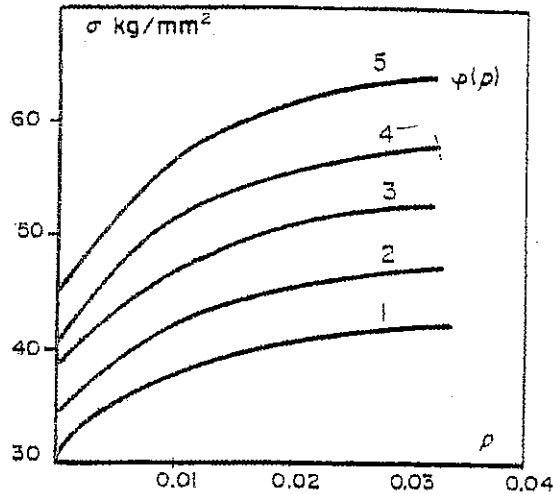


Fig. 1. (1) $\dot{p} = 1.5 \cdot 10^{-3} \text{ sec}^{-1}$; (2) $\dot{p} = 1.8 \cdot 10^{-3} \text{ sec}^{-1}$; (3) $\dot{p} = 5.0 \cdot 10^{-1} \text{ sec}^{-1}$; (4) $\dot{p} = 5.0 \cdot 10^0 \text{ sec}^{-1}$.

Materials with delayed yielding

As is known, the yield delay capacity is associated with the extension of the plastic part of the diagram and involves the existence of two branches in some region. The value of the upper yield stress is determined by the selected criterion of delay. Transition from the elastic to plastic branch may be carried out in different ways and is determined by the conditions of the loading process. It will be shown that the plateau on the stress-strain diagram appears only for the specimens with long working part in tension and the dimensions of the plateau are naturally associated with the specimen length. However, under the specific loading conditions (the stress grows up in value all the loading time) the peak stress, i.e. the upper yield stress, is not observed. Hence, the obtained stress-strain diagram should be interpreted with great care, paying attention to both: the shape of the specimen and the loading conditions. The suggested model allows for the instantaneous variation of the specimen state – the appearance of the instantaneous plastic strain p and the stress drop. However the model suggests the stress drop not all the way to the static curve, but to the curve, determined by the history of the elastic loading. At the instant t_0 , yield delay capacity becomes exhausted

$$\sigma / E + \lambda p = Vt_0 = \sigma_{drop} / E \quad (7)$$

Since at $t < t_0$, $p = 0$, the eqn.(4) has the following form

$$\varphi(p) = \sigma + VG_1(t) - \lambda \int_0^t K(t-s)p(s)ds$$

At the instant $t = t_0$

$$\varphi(p) = \sigma + VG_1(\sigma_{drop} / VE) \quad (8)$$

Solving (7) and (8) together, we find the values of σ, p at the moment $t = t_0$ after the condition of yielding has been fulfilled. The curve 1 in Fig 2 is the instantaneous straining diagram $\sigma = \varphi(p)$. Curve 2 is obtained by parallel shift of the curve 1 downwards by the value of $G_1(\sigma_{drop} / VE)$. The equation of the straight line 3 is: $\sigma + \lambda Ep = \sigma_{drop}$. The point of intersection A of the curve 2 and the straight line 3 determines the observed lower yield stress σ_s and the respective instantaneous plastic strain. In this case, it is necessary to solve the integral equation to construct the strain-strain curve. If $\dot{\sigma} = const, \lambda = 0$, then eqn (6) holds. The approach described above can be applied to the elements (i.e. for the specimen with a very short working part). If the long specimen is stressed, the plastic strain front propagates from one end to the other. The strain gage fixed in some intermediate section indicates the following (Fig. 3): at first the specimen stretches uniformly remaining elastic, which is shown by part 1 on the diagram. The maximum elastic strain at the end determines the peak stress, i.e. the upper yield stress σ_{drop} . at $t = t_0$ the material yield delay capacity becomes exhausted, the stress drops down to the value of σ_s - the observed lower yield stress, and the strain remains elastic until the plastic front reaches the section (part 2). As soon as the plastic front reaches the gage, the strain increases up to the value p and remains constant until the front reaches the other end of the specimen (part 3). After that the specimen continues deforming uniformly with strain hardening (part 4). The plastic strain front registered by the gauge turns out to be increased. This can be explained by the inclination of the plastic strain front, which makes an angle of approximately $\pi/4$ to the specimen axis, whereas the narrow gauge had been fixed on the surface.

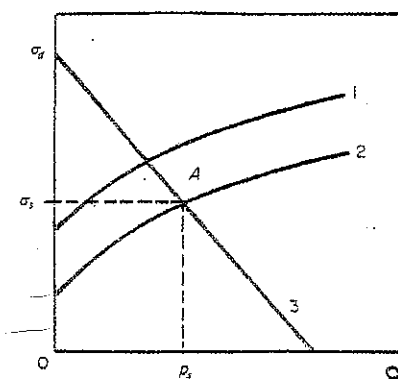


Fig. 2.

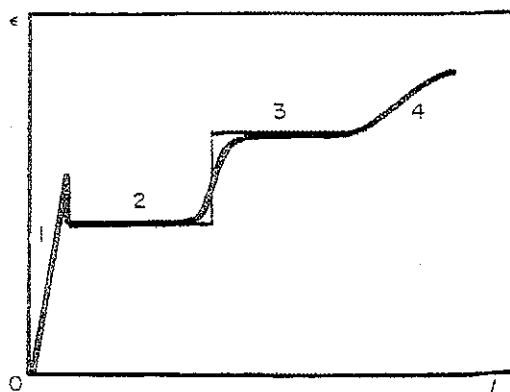


Fig. 3.

The further analysis should be taking into consideration the stress concentration (with the coefficient k_1) occurring at the specimen end near the grips (let it be section $x = 0$). Therefore the condition of delaying will be fulfilled primarily here. The stress drop at the end leads to the total stress drop down to the value of σ_s . The movement of the plastic front starts from the section $x = 0$ and is regulated by the condition of delaying. For some section x the plastic strain appears at the time when the condition of delaying is fulfilled in this section; that is to be written as follows:

$$\int_0^{t_0} g(\sigma) dt + \int_0^t g(\sigma_s) dt + \int_t^{t+\Delta t} g(k_2 \sigma_s) dt = \tau_0$$

The last integral is determined by concentration c_2 at the front of the moving plastic wave. Let 's take the function of delay as $g(\sigma) = (\sigma / \sigma^0)^n$ and assume $(\sigma_x / \sigma^0)^n = \tau_0 / t_s$ where t_s is the delay time corresponding to the constantly acting stress σ_x . Then, taking into account that $\Delta t = \Delta(dt/dx)$ (Δ is the section covered by the concentration) we obtain the following differential equation, which describes the front movement:

$$\frac{dx}{dt} = \frac{k_2'' \Delta}{(1 - k_1^{-n}) t_s + t_0 - t}$$

Neglecting the value of k_1^{-n} which is small compared with a unit and designating $\delta = k_2'' \Delta$, we obtain the following solution for the equation:

$$x = -\delta \ln \left[1 - \frac{t - t_0}{t_s} \right]$$

which satisfies the condition $x = x_0|_{t=t_0}$. If we take into account that $t_s \leq t_0, t_s \leq t$, then

$$x \approx \delta (t - t_0) / t_s \quad (9)$$

Expression (9) determines the constant velocity of the front movement; this conclusion had been verified experimentally.

In addition to the designation $G_1(t)$ introduced earlier, let us assume

$$G(t) = \int_0^t K(t-s) ds.$$

Then the constitutive equation for some section through which the plastic front has already passed will be written:

$$\varphi(p) = \sigma_s [1 + G(t) - G(t_0)] + \sigma_{drop} G_1(t_0) / t_0 \quad (10)$$

If the velocity of the machine grips is constant, then the loading rate in the elastic range is also constant and $\sigma = \eta t$, whereas $\sigma_{drop} = \eta t_0$. Assuming in (10) $t = t_0$ we obtain

$$\varphi(p) = \sigma_s + \eta G_1(\sigma_{drop} / \eta) \quad (11)$$

Expression (11) relates the lower yield stress σ_s and the plateau length p . The second equation for these two characteristics may be derived from the kinematic condition relating the grips velocity V with the front movement velocity

$$V(t) = (xp)' \quad (12)$$

To correlate (12) with expression (9) defining the front constant velocity, we should assume

$$\dot{p} = 0. \text{ Then } V = \dot{x} p. \quad (13)$$

Comparing (9),(13) and taking into account definition of t_0 , we obtain:

$$\sigma_s = \sigma^* \left(\frac{\sqrt{\tau_0}}{\delta p} \right)^{1/n} \quad (14)$$

Solving (11) and (14) together we can find p and σ_s . The graphic solution diagram remains the same as for the element analysis, but the straight line is replaced by the curve (14) of the hyperbolic type.

Having assumed that $p = 0$, we should believe that the time depending term in (10) is also negligible for $t > t_0$. This condition dictates the selection of the kernel type. For example, for Abel's kernel $K(t-s) = k(t-s)^{-\alpha}$ difference $G(t) - G(t_0)$ at any moment may be made as small as one wants, provided that the selected value of α is sufficiently close to 1. If we take the kernel as Abel's type and assume function $\varphi(p)$ is linear, $\varphi(p) = \varphi(0) + m^{-1}p$, the dependence between the lower and upper yield stresses can be derived from (11):

$$\varphi(0) + \frac{1}{m}p - \sigma_s = A / \sigma_{drop}^{n(1-\alpha)-1} \quad (15)$$

This dependence had been verified by experiments [8] on steel 50. The following parameters were calculated for this steel: $\alpha = 0.9$; $k = 0.02$; $\varphi(0) = 57.8$. The elastic strain rates were equal to 6×10^{-6} ; 1.1×10^{-4} ; $5 \times 10^{-3} s^{-1}$. The slight scatter was observed in each group of tests corresponding to the given rate. The average value of η was equal to 21. The exponent of σ_{drop} in (15) $n(1-\alpha) - 1 = 1.1$ differs but slightly from a unit. Figure 4 shows the dependence of the actually measured value $\sigma_p = \varphi(0) + m^{-1}p - \sigma_s$ on the value of $1/\sigma_{drop}$, the points are practically on the same straight line.

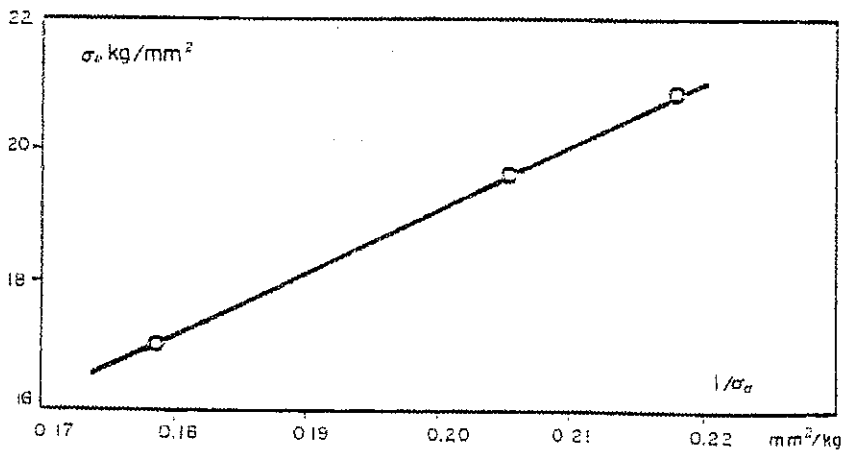


Fig. 4.

UNLOADING PROCESSES

According to the theory of Karman-Taylor-Rakhmatulin The unloading should be always elastic, whereas by Malvern-Sokolovsky theory, the process of unloading is viscous down to the static curve, but neither of them reflects the true situation with unloading process in metals. The constitutive equation (1) as distinct from the mentioned above types, makes it possible to describe the unloading

as well [13]. If the unloading starts at some moment $t = t_*$, the value of $\dot{\sigma}$ becomes negative, the stress drops but the strain may continue growing for some time. Plastic strain can not decrease, therefore the unloading yield stress should correspond to the extreme value of p , i.e. the condition $\dot{p} = 0$. Differentiating the equation (1) with respect to time, we obtain:

$$\varphi'(p) \dot{p} = \dot{\sigma} + \frac{d}{dt} \int_0^t K(t-s) \sigma(s) ds = 0 \quad (16)$$

If the law of unloading is known, eqn.(16) allows to determine both: the moment t_{**} when the plastic strain reaches its maximum as well as the stress value σ at this instant, i.e. the value of unloading yield stress. Upon reaching this stress level the further unloading is elastic.

If the loading process was taking place at the constant rate $\dot{\sigma}_l$ and the unloading was almost at the constant rate $\dot{\sigma}_u$ and if we select the Abel's kernel under the integral in (1), then, it follows from (16):

$$\frac{\dot{\sigma}_l}{\dot{\sigma}_u} t^{1-\alpha} + (1 - \frac{\dot{\sigma}_l}{\dot{\sigma}_u})(t - t_*)^{1-\alpha} + \frac{1-\alpha}{k} = 0 \quad (17)$$

Here t_* corresponds to the instant the unloading begins. Eqn.(17) allows to determine the rate $\dot{\sigma}_u$ at which the unloading is elastic and viscous parts should not be observed. For this purpose we introduce $t = t_*$ into eqn.(17) and then we obtain

$$\dot{\sigma}_u = -\dot{\sigma}_l t_*^{1-\alpha} \frac{k}{1-\alpha} \quad (18)$$

It is evident that this value depends on both: the loading rate and the value t_* , i.e. on the value of the maximum stress (or strain) which was achieved at the moment of the unloading start. The analysis of the experimental data [13] indicated that, if the unloading rate is the same as the loading, i.e.

$\dot{\sigma}_u = -\dot{\sigma}_l$, or exceeds it, viscous effects are practically insignificant and cannot be discovered.

However, if $\dot{\sigma}_u = -0.1 \dot{\sigma}_l$, the viscous effects are essential. As an example, Fig.5 shows a part of the diagram $\sigma \sim \varepsilon$ (continuous line) obtained at the loading rate $\dot{\sigma}_l = 0.385 \text{ kg/mm}^2 \text{ s}$; the unloading rate was $-0.0385 \text{ kg/mm}^2 \text{ s}$ [13]. The material tested was a low-carbon steel, the kernel parameters were the following: $\alpha = 0.93$; $k = 0.1$. The time of loading transition to the elastic state was $t_{**} = t_* + 27.5 \text{ s}$ in accordance with eqn (17). The dashed curve shown in Fig.5 is calculated by (1).

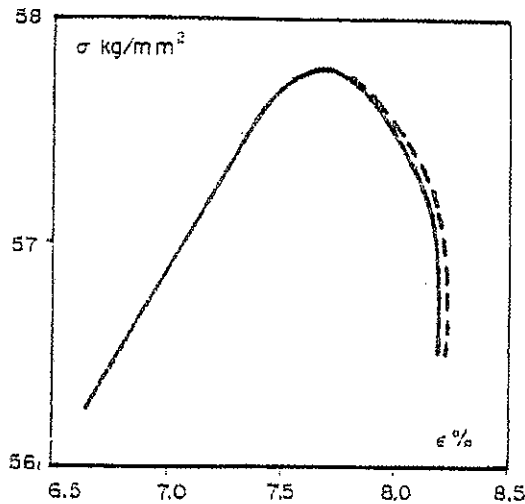


Fig. 5.

CONDITIONS OF PLASTIC STRAINING

The presence of pure elastic state with various elastic histories leads to the appearance of the distinctions in values of initial plasticity moduli, thus each stress-strain curve in the plasticity range is in fact characterized by two parameters – by the yield stress σ_0 and by the initial plasticity modulus

$$d\sigma / dp \Big|_{t=t_0}$$

From the described above yield determination it is seen, that $\sigma_0 < \varphi(0)$, therefore the possibility of repeated elastic straining is reserved at some straining conditions. If at any moment $t = t_*(\sigma = \sigma_*, p = p_*)$, the instantaneous additional loading is applied, the material behavior can be described by new instantaneous curve, which corresponds to p_* . Let $\psi(p) = \varphi(p) - \varphi(0)$, then the equation of the new instantaneous curve will be

$$\varphi^*(p) = \varphi^*(p_*) + \psi(p)$$

where $\varphi^*(p_*) = \varphi(0) - \sigma_0 + \sigma_*$.

From eqn.(1) the slope of the real stress-strain curve, i.e. $d\sigma / dp$ is always less than the slope of the instantaneous curve for the same point p :

$$\frac{d\sigma}{dp} = \varphi'(p) - \frac{d}{dp} K^* \sigma$$

If we have the ordinary viscoelasticity without pure elastic deformation, then, as is mentioned above, $\varphi'(0) = \sigma'(0)$. In this case the condition $d(K^* \sigma) / dp \geq 0$ characterizes the hardening process and is always satisfied. In our present case when there is the pure elastic strain in the beginning, the initial plasticity moduli of the curves are not equal. Therefore it is natural to assume the following for the condition of plastic straining:

$$\frac{d}{dp} K^{\alpha} \sigma \geq \frac{d}{dp} K^{\alpha} \sigma \Big|_{t=t_0} \quad (19)$$

When the condition (19) is disturbed, the material will be deformed in accordance with the new instantaneous curve, which was defined above. The appearance of the additional elastic strain is possible now. Performing differentiation in (19) and taking into account properties of the integral operator K^{α} , we obtain

$$\dot{\sigma} \leq \left[\frac{\varphi'(p)}{\varphi'(0)} \left[\int_0^{t_0} K(t-s) \sigma(s) ds + \sigma_0 \right] \right] \left[\int_0^{t_0} K(t-s) \dot{\sigma}(s) ds \right] - 1 \int_0^t K(t-s) \dot{\sigma}(s) ds \quad (20)$$

Here $\dot{\sigma}_0$ is the value of $\dot{\sigma}$ at the moment $t = t_0$. Condition (20) applies the limitations on the value of $\dot{\sigma}$ for the loading process conditions, remaining the plastic range. The limitations on the value of the loading rate allows to explain the propagation of the incremental waves at the elastic rate. Rates of the additional loads, as a rule are highly essential and exceed the permissible value of $\dot{\sigma}$. As an illustration we present the analysis of the torsional tests results [14]. The velocity of the initial torsion was $\dot{\gamma}_1 = 5 \times 10^{-5} s^{-1}$, the rate of increment $\dot{\gamma}_2 = 850 s^{-1}$. It turned out that part of incremental wave propagates at an elastic velocity; the new effect had been discovered – the drop of stresses upon the reaching of the yield stress during the application additional loading (Fig.6). Accounting for the constant rate of the additional loading and is applied at some instant $t = t_*$, then the rate $\dot{\sigma}$ at the moment when the material changes to the plastic state can be determined from the following equation:

$$\dot{\sigma} \left(1 + \frac{\varphi'(p_*)}{E} \right) = \varepsilon \left[\varphi'(p_*) - E \frac{k}{1-\alpha} (t_{**} - t_*)^{1-\alpha} \right] - k \frac{\sigma(t_*)}{(t_{**} - t_*)^{\alpha}} \quad (21)$$

It is clearly seen from (21) that for the certain combination of material parameters, the value of $\dot{\sigma}$ may be negative. Fig. 6 demonstrates the results of analysis based on experimental data from [14] (the solid curves are the experimental, the dashed lines are the calculated by (21)). Figure 7 shows the experimental results from [15], performed on the aluminum bars at torsion with the velocities $\dot{\gamma}_1 = 1.66 \times 10^{-5} s^{-1}$ and $\dot{\gamma}_2 = 6.24 \times 10^{-1} s^{-1}$. The initial loading took place at the rate of $\dot{\gamma}_2$ (curve2) to the values of $\gamma_1, \gamma_2, \gamma_3, \gamma_4$, with the subsequent unloading and repeated loading at the low rate $\dot{\gamma}_1$ (curve 2). Curve 3 in Fig.7 is the stimulated instantaneous curve. The dashed lines show the calculated curves for the repeated loading.

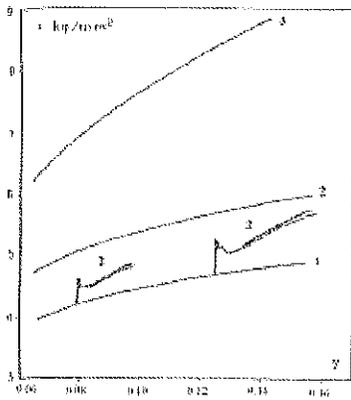


Fig. 6. (1) $\dot{\gamma} = 5.5 \cdot 10^{-2}$ sec $^{-1}$; (2) $\dot{\gamma} = 0.85$ sec $^{-1}$;
 (3) 91% γ - the hysteresis curve.

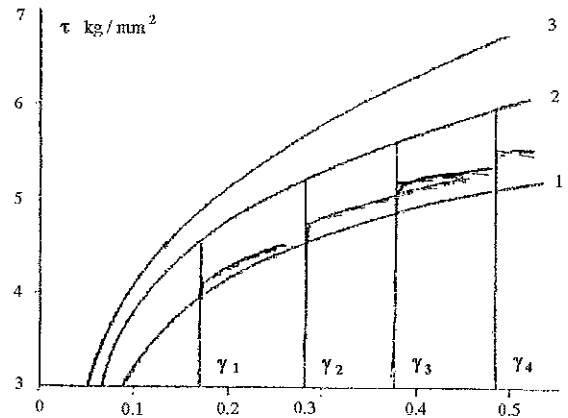


Fig. 7.

WAVE PROCESSES.

When investigating the wave processes in materials described by the suggested model, it is necessary to take into account the existence of two constitutive equations: while the material is elastic it is the Hooke's Law, while when the material goes into the plastic stage, it is the eqn. (1). In the elastic stage the solution is to be found by usual methods of the theory of elasticity, in the plastic range it can be constructed by summing up the solutions of relaxation and common visco-elasticity problems. The detailed results of such approach are given in [16].

CONCLUSION

The demonstrated results show the success of the hereditary type of approach to the mechanical behavioral modeling for the metals under the various loading conditions and rates including the wave propagation phenomenon.

REFERENCES

1. Yu.N.Rabotnov, Creep Problems in Structural Members. North Holland, Amsterdam (1969)
2. T.von Karman, On the propagation of plastic strains in solids. NRDC Rept.A29,OSRD(1942)
3. Kh.A.Rakhmatulin, On propagation of unloading wave. PMM,9(1),(1945)
4. V.V.Sokolovsky, Propagation of elastic-plastic waves in bars. PMM, 12(3) (1948)
5. L.E.Malvern, The propagation of longitudinal waves of plastic deformation in a bar of material exhibiting a strain-rate effect. J. Appl. Mech. 18(2), (1951)
6. J.V.Suvorova, Delayed yielding in steels (review of experiments). PMTF, No.3, 55-62 (1968)
7. Yu.N.Rabotnov, Model of elastic-plastic medium with delayed yielding. PMTF, No.3, 45-54 (1968)
8. Yu.N.Rabotnov and Yu.V.Suvorova. Dynamic problems for elastic-plastic solids with delayed yielding. Int.J. Solids and Structures 7, 143-159 (1971)
9. V.V.Viktorov and G.S.Shapiro. On determination of metal tension dynamic diagrams at moderately high strain rates, Inzh.zh.MTT, No.2 (1968)
10. Yu.N.Rabotnov and Yu.V.Suvorova. On Law of metal deforming in uni-axial loading, Izv. AN USSR, MTT, No.4, 41-54 (1972)
11. Yu.N.Rabotnov and Yu.V.Suvorova. Hereditary effects in loading of metals, In Successes of Deformed Media Mechanics, Nauka, Moscow, 470-477, (1975)
12. Yu.N.Rabotnov. Certain problems of creep theory, Vestnik MGU, No.10, (1948)
13. A.F.Melshonov, Yu.V.Suvorova and S.Yu.Khazanov. Experimental confirmation of constitutive equation for metals in loading and unloading, Izv. AN USSR, MTT, No.6, 166-170 (1974)
14. R.A.Frantz and J.Duffy. The dynamic stress-strain behavior in torsion of 1100-0 aluminum subjected to a sharp increase in strain rate, Trans. ASME, Ser.E.J.Appl.Mech., 39(4), (1972)

15. J.Klepaczko. Strain rate history effects for polycrystalline aluminum and theory of intersections, *J.Mech. and Phys. Solids*, 16, 255-266, (1968)
16. Yu.V.Suvorova. Propagation of loading impulse in nonlinear-hereditary material with delayed yielding. *Izv.An USSR, MTT*, No.3,87-91, (1973)

The Behavior of Sand under Shock Wave Loading: Experiments and Simulations

K. Tsembeles, W.G. Proud, B.A.M. Vaughan* and J.E. Field

Physics and Chemistry of Solids, Cavendish Laboratory, Madingley Road, Cambridge, CB3 0HE, UK

* Now at: Alvis Vickers Ltd., Hadley Castle Works, PO Box 106, Telford, TF1 6QW, UK

ABSTRACT

A series of plate impact experiments has been performed to determine the shock loading behavior of dry sand. The sand was placed inside a copper cell and the stress levels were measured by means of manganin gauges. A simple numerical model was constructed based on the experimental data and used in the CAST-EDEN™ hydrocode. Results indicate reasonable agreement between experiments and simulations given the relative simplicity of the model. Limitations and possible improvements of the model are discussed.

INTRODUCTION

The shock properties of geological materials have long been a source of interest. Traditionally, the main driving forces have been planetary impact and geological research. Recently, there has been a growing interest in the shock properties of concrete, where geological materials are added as aggregates [1-2]. In addition, there is a growing interest in the properties of sand because of applications such as destruction of ordnance and landmines [3-4].

Sand, like all porous materials, is still poorly understood compared to metals or liquids. There are only a handful of Hugoniot data [5] derived from tests in the 50s and 60s. The experiments reported here, were performed using the plate impact gas gun facility [6] of Cambridge University to assess the sand behavior under shock wave loading and establish the Hugoniot curve. The results were then used to construct a simple Mie-Gruneisen model which was used in conjunction with the CAST-EDEN hydrocode.

MATERIAL DATA

The sand used for the plate impact experiments was a quartz system originating from Weston-super-Mare in the United Kingdom and had a bulk density of 1450 kg m^{-3} at a porosity of $48 \pm 2 \%$ vol.

PARTICLE SIZE DISTRIBUTION

A series of sieves were used to define the grain sizes distribution. A sample of 100 g of dried sand was placed in the coarsest cut sieve and the sieve column left on a gently vibrating surface for half an hour. At this time the sieves were subjected to gross manual shaking for a few minutes then left to gently vibrate for a further 30 min. The mass of sand in each sieve was measured. The total mass of sand left unaccounted for after the masses found in all sieves was summed was found to be $< 0.3 \text{ g}$. Figure 1 shows the particle distribution obtained; the percentages given are based on the total mass of sand.

THEORETICAL MAXIMUM DENSITY

The theoretical maximum density of the sand was measured using a difference technique. A sample of sand, dried in an oven, was placed in a measuring cylinder of known mass. The mass of the sand and cylinder was recorded. Water was added to the sand until a layer of supernatant water was formed. The sand was agitated and air bubbles were eliminated. An ultrasonic bath was used in some of the measurements to eliminate small air bubbles but the results were not significantly affected. The volume occupied by the saturated sand and the volume of the supernatant liquid were measured from

the side of the measuring cylinder. Weighing the cylinder and its saturated contents, combined knowledge of the density of water allows the mass of the sand and its porosity to be obtained.

The density of six samples of sand was taken and the density of the sand material with no porosity was found to be $2550 \pm 50 \text{ kg m}^{-3}$

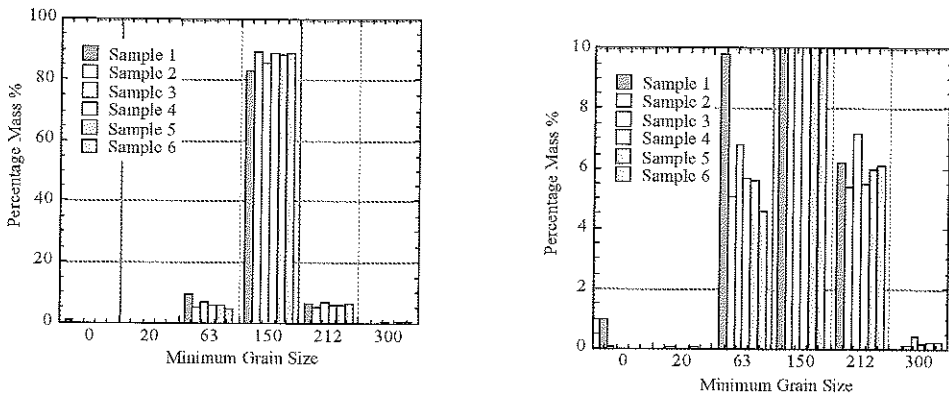


Figure 1. Size distribution in the sand studied. Note: sample 1 did not have the 20 μm cut sieve in the column.

EXPERIMENTAL METHOD

Experiments were performed using a single stage light gas gun (figure 2). This has a 5 m long, 50 mm bore barrel and uses air or helium at pressures of up to 350 atmospheres. It is capable of velocities up to 1200 m s^{-1} . The projectile consists of a plate of copper 10 mm thick mounted on the front of a polycarbonate sabot. A recess on the front of the sabot ensures that only the copper plate interacts with the sample on the time scale of the experiments. The thickness of the sample, the sound speeds of the materials used including the sand allow up to $9 \mu\text{s}$ of useful data to be gathered. The timescale and the impactor are towards the upper end of those commonly used in this area of shock studies.

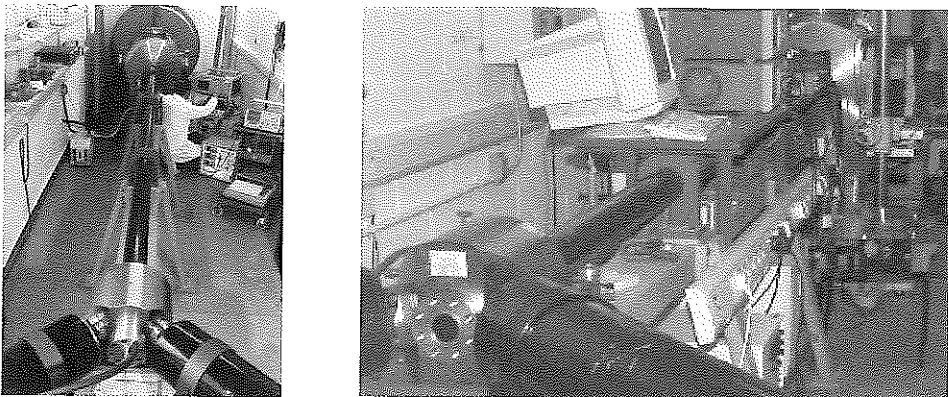


Figure 2. Two views of the plate impact facility. Left hand view shows the barrel with the driving reservoirs at the bottom of the image and the expansion chamber at the top. The right hand view shows the gauge box at knee height holds the VISAR system with gauge power supplies alongside. The box alongside the gun at knee height holds the VISAR system capable of recording velocity time histories with a time resolution of 2 ns. The device at waist height at the right hand side of the image is the ultracam FS501 camera capable of a framing rate of twenty million per second.

The sample consists of a 3mm bed of sand inside a copper cell. The cell is in four parts as shown in figure 3. A cover plate 2 mm thick fronts the cell, a gauge is mounted in epoxy between this plate and the 2-3 mm thick copper plate behind it. The next plate has a 3 mm recess in which the sand is mounted. The recessed plate has a 1 mm thick rear face after which a second gauge is mounted in epoxy. The rear plate is 10 mm copper.

In these experiments the sample mount was aligned to an accuracy of $<1 \mu\text{m}$, an angle of $<1 \text{ mrad}$, to the end of the barrel using a dial gauge prior to each experiment thus allowing a highly planar impact. The projectile is one half to two thirds within the barrel at impact so removing the effect of tumbling; a possibility, if the projectile was in free flight before impact. The impact velocity is measured using a sequential array of shorting pins mounted at the end of the barrel to an accuracy of 0.1%. The velocity of the impactors used was varied in steps of approximately 150 m s^{-1} from 200 to 960 m s^{-1} .

The gauges used are manganin piezoresistive gauges which alter resistance with pressure but not with any shock-induced temperature effects. The gauges are widely used and have been independently calibrated by several groups worldwide. In this configuration the time resolution of the gauge is of the order 200 ns.

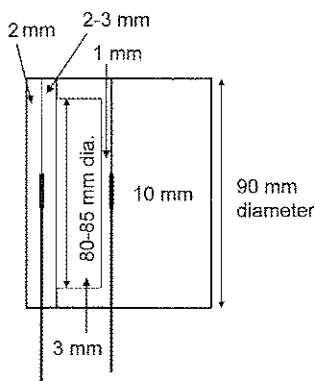


Figure 3. The Cell. All cell components are made from copper (Cu 101). In the experiments, all cell dimensions were recorded to an accuracy of $\pm 0.01 \text{ mm}$.

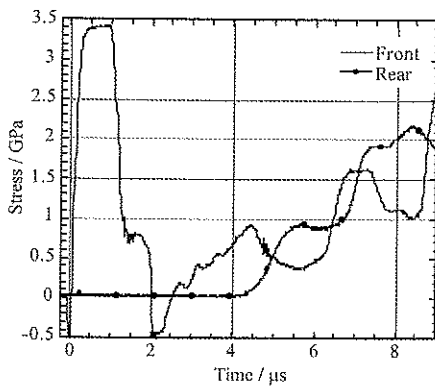
If the gauge is mounted in polymethylmethacrylate (PMMA, lucite, perspex, plexiglass) the time resolution is of the order 30 ns as the polymer components of the gauge are impedance matched to the PMMA. However, analysis of the gauge data requires an accurate knowledge of the coefficient for the stress transmission across the interface. This impedance mis-matched interface also introduces more wave reflections in the system thus complicating the analysis. It is normal and desirable to use the gauges in the embedded configuration first, to gain the Hugoniot stresses, then to perform experiments with the gauge in PMMA to obtain wave profiles with greater resolution. Alternatively, a velocity interferometric technique (VISAR) may be used.

In either configuration the gauges act as time of arrival sensors, a fact that is exploited in the data analysis presented later.

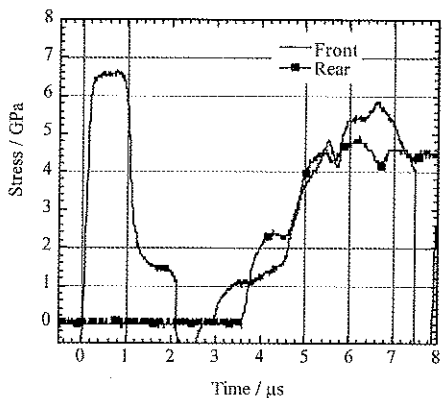
QUALITATIVE ASPECTS OF DATA PRODUCED

EXPERIMENTAL DATA

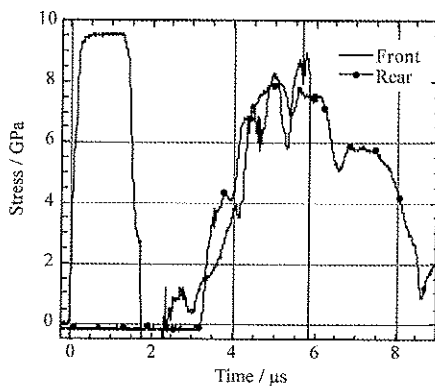
Figure 4 shows the data from shots at velocities of 200, 354, 505, 652, 812 and 969 m s^{-1} . There are similarities between the gauge outputs seen in all experiments. The front gauge shows a rapid rise to a flat topped pulse. The height of this pulse is defined by the copper Hugoniot as the impactor and the front plates of the target are copper. The stress level increases with velocity and the width of the pulse is defined by the thickness of second plate in the target, as will be shown later.



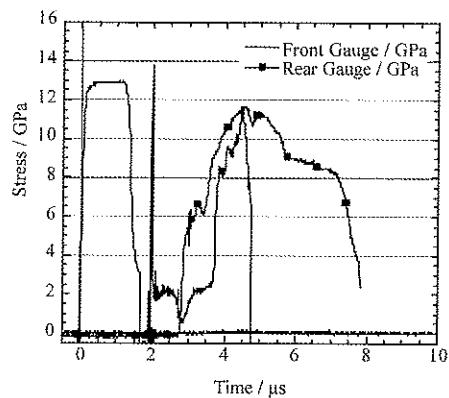
(a)



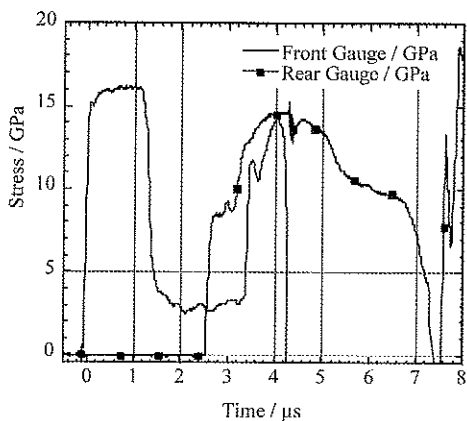
(b)



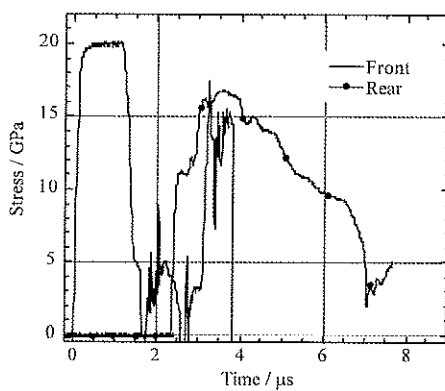
(c)



(d)



(e)



(f)

Figure 4. The output of the gauges from experiments with impact velocities of (a) 200 m s^{-1} , (b) 354 m s^{-1} , (c) 505 m s^{-1} , (d) 652 m s^{-1} , (e) 812 m s^{-1} and (f) 969 m s^{-1} . The time bases of all experiments are set so the initial rise of the front gauge is at $0 \mu\text{s}$. The stress measured is that in the copper cell.

The shock impedance of a material is defined as the density multiplied by the shock speed. In this experiment the copper impedance is of approximately 2.5 times that of the sand. This has important consequences in the reflection of waves in the system.

IDEALIZED APPROXIMATION

For an initial qualitative explanation, a homogeneous material is assumed. The shock wave geometry is dependent on the target configuration used in the experiments reported here. Figure 5 shows the basic wave structure which develops in the system. The initial impact produces a shock wave which propagates into the target and into the impactor.

A compression wave is partially transmitted and reflected as compressive waves when going from a low impedance material to a high impedance material. When a compressive wave transmits from a high impedance material into a low impedance material, the transmitted wave is compressive but the reflected wave is a partial release which takes the stress from a high state to a lower state. When a wave reaches a free surface, it is reflected as a full release which takes the material from a high stress state down to the ambient conditions prevailing around the sample. In this case, the ambient pressure was 1 mbar, as the shots take place in a rough vacuum.

Taking the processes occurring at the gauge locations as shown in figure 5 the gauge traces expected from this system can be predicted as shown in figures 6 and 7. When the traces in figures 6 and 7 are compared with the results seen in figure 4 the agreement is qualitatively correct however there are some differences.

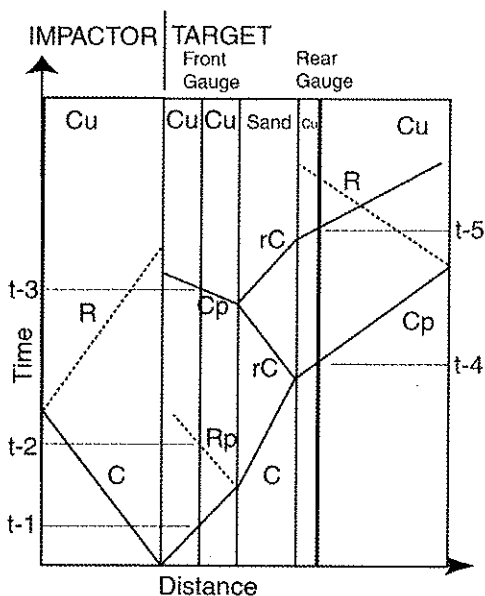


Figure 5. Wave propagation in the present experiment in distance/time space. Compression pulses are represented by solid lines and releases by dashed lines. Cp indicates a partially transmitted compression, rC indicates a recompression. R indicates a full release back to ambient conditions while Rp is a partial release.

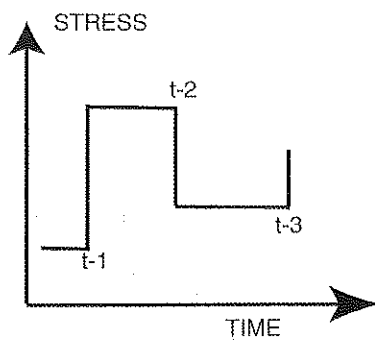


Figure 6. Idealized trace from front gauge based on wave diagram in figure 5

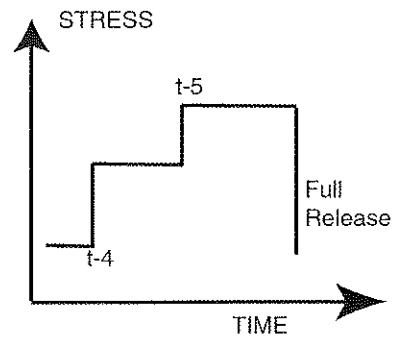


Figure 7. Idealised trace for rear gauge, on wave diagram in figure 5

FEATURES SEEN IN REAL DATA

In some of the front gauge traces there is a dip immediately before the steep initial rise. This is due to capacitive linking between the gauge, the epoxy surrounding, which acts as a dielectric, and the copper plates on either side of the gauge. If the plates are rapidly brought together there is a small change in the electrical environment of the gauge and this causes a current to flow, resulting a small dip in the trace. This has been seen in many plate impact traces and is widely reported.

In some cases, there is also a negative dip in the front gauge found when the partial release wave reaches it. This is not predicted by the idealized model and is a result of the slight difference in the particle velocity between the copper plates and the epoxy layer holding the gauge in place. This means that if the front gauge trace shows such a negative transient the data after this transient should be used with caution. The model follows the ideal case, without the negative dip.

Given the granular nature of sand the rising parts of traces are not instantaneous as the idealized case predicts. Instead a ramp is seen due to the collapse of pores in the system. A simple way of viewing this shape is outlined by Gilman and dates from the 1960's [7]. Gilman's argument is based on work done by the wave and can be summarized as waves which do little work travel fast and those which do predominantly plastic work travel slowly. In the case of a granular structure the pore collapse can be described as falling into three phases. The fastest traveling wave moves through the skeleton of the sand as illustrated in figure 8. This is followed by the main collapse of the bed which takes it to <5% porosity. Finally, the last few pores are closed by the higher pressure. In reality it would be unwise to regard these phases as distinct, as they blend into a single continuous wave shape.

REPRODUCIBILITY

Sand is a statistical material and therefore, some variation can be expected from sample to sample. Repeat shots were performed at velocities of 350 and 500 m s⁻¹. The degree of agreement between the rear gauge traces was excellent as shown in figure 9 for the repeats at 500 m s⁻¹.

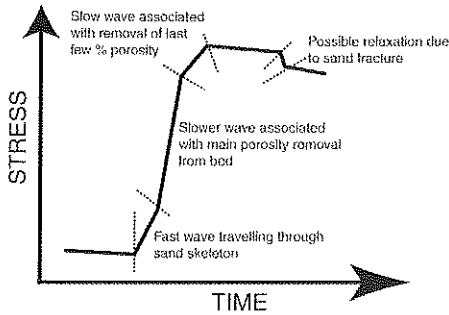


Figure 8. The wave shape for porous bed collapse the ideas of Gilman.

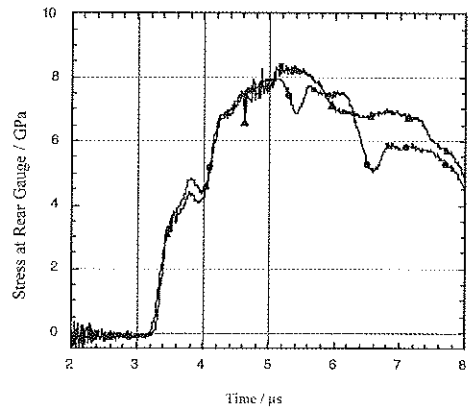


Figure 9. The reproducibility of shots following at 500 ms^{-1} . The rear gauge traces are shown.

OVERALL COMPARISON

Figure 10 shows the variation in the transmitted pulse for shots ranging from 354 to 969 m s^{-1} . Two features are immediately evident, at higher input stresses it takes less time for the shock pulse to be transmitted i.e. the sound speed increases. The other feature not so evident in the traces, is that the degree of attenuation caused by transmission through the sand decreases as the input stress increases. This can be seen in figure 5 (a) - (f) by comparing the maximum height of the input pulse and the maximum height of the output pulse. This is due to the sand having a finite and relatively fixed compression threshold, as the input stress increases in intensity comparatively less of its energy is required to collapse the bed and therefore more is transmitted.

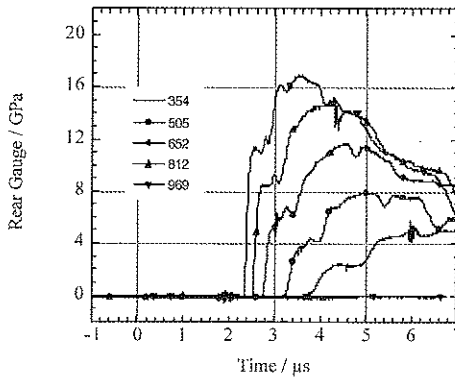


Figure 10. Output pulses from 3 mm sand beds of the impact velocity indicated in m s^{-1} by the legend.

THE SAND HUGONIOT

Figure 11 illustrates the sand and Copper Hugoniot interactions for the experimental set up. It can be seen that the only direct information extracted for the sand is the shock wave velocity. However, in order for the Hugoniot curve to be obtained an initial density value needs to be used. In normal materials this value corresponds to the elastic initial density. However for porous materials it is not certain if this value or the theoretical maximum density is appropriate. For that reason, two Hugoniot curves have been constructed. Figure 12 illustrate the Hugoniot on the shock wave velocity (U_s) - particle velocity (U_p) space while Figure 13 the Hugoniot is illustrated in the Stress - particle velocity space. In addition, previously published quartz sand data [5] are also plotted for comparison purposes.

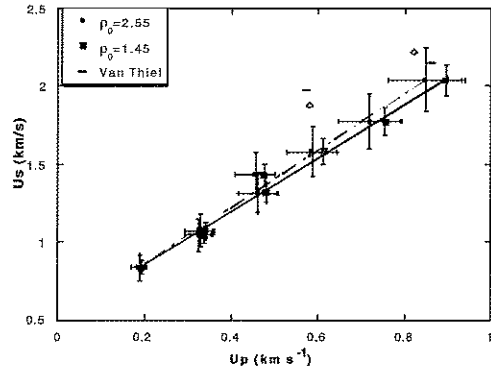
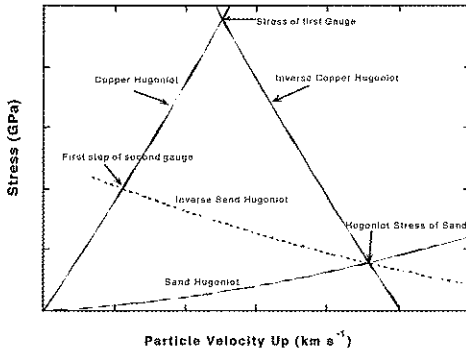


Figure 11: Hugoniot interactions of Sand and Copper Figure 12: Sand Hugoniot in U_s - U_p space

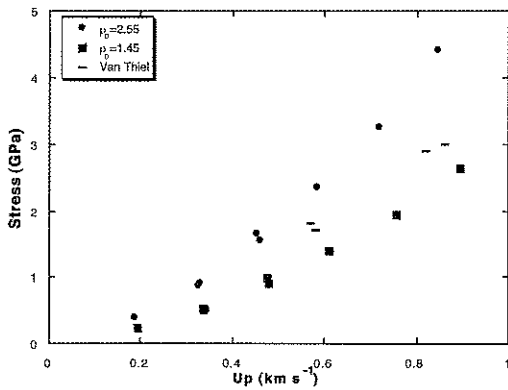


Figure 13: Sand Hugoniot in P - U_p space

Therefore, two Hugoniot curves are constructed:

- $U_s = 0.511 \text{ (km s}^{-1}\text{)} + 1.72 * U_p$ with initial density 1450 kg m^{-3} .
- $U_s = 0.475 \text{ (km s}^{-1}\text{)} + 1.83 * U_p$ with initial density 2550 kg m^{-3} .

HYDROCODE SIMULATIONS

The experiments were modelled using the 2-d version of CAST-EDEN hydrocode provided by QinetiQ and Fluid Gravity. It is an Eulerian code and runs under RedHat Linux 7.1. The computer has an AMD Athlon-Thunderbird 900 MHz CPU and 458 MB of SDRAM. The material model for Copper had an Extended Mie-Gruneisen Equation of State (EoS) and a Hull constitutive model.

For the sand, a standard Mie-Gruneisen EoS was used with a linear Us-up relationship with no constitutive relation. Hence the material was assumed to be hydrodynamic. The sand EoS parameters are given in table 1.

Table 1: Sand EoS parameters:

RHO - The ambient density (kg m^{-3})	1450	2550
C - The ambient bulk sound speed (km s^{-1})	0.511	0.475
S - The slope of the shock velocity/particle velocity curve	1.72	1.83
GAMMA - The initial Gruneisen gamma ratio (2S-1)	2.44	2.66

For all the calculations, symmetry was used along the propagation axis. The mesh had 5 cells per mm, and for 7 μs of experimental time, 15 minutes of computational time were needed. A single simulation was performed using 10 cells per mm for experiment with the impact velocity of 811 m s^{-1} , as illustrated in Figure 14 for 2.55 g cm^{-3} initial density. The computational time was 1 h 30 mins. It can be seen that the results are similar but the computational time is significantly higher for the finer mesh. For that reason, all the simulations were performed using the cruder mesh. Finally, Lagrangian points on the computational mesh were used to simulate the gauges.

Figures 15-20 illustrate the experimental traces together with the simulation results for six different impact velocities. The longitudinal stress is illustrated for the gauges and the hydrostatic pressure is illustrated for the simulations.

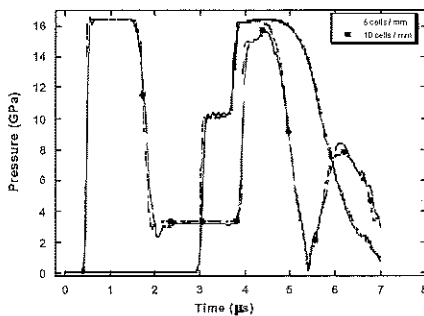


Figure 14: Results for 811 m s^{-1} simulation at different mesh resolution

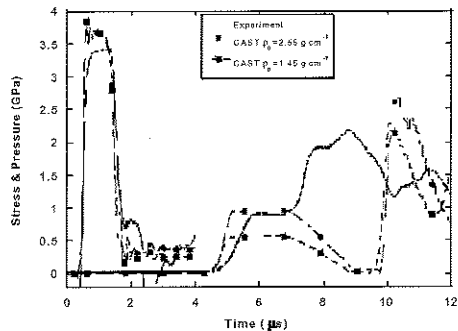


Figure 15: Results for 200 m s^{-1} impact

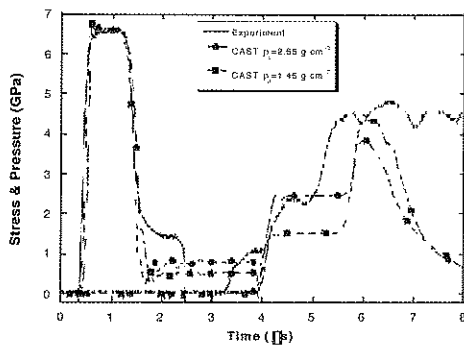


Figure 16: Results for 351 m s⁻¹ impact

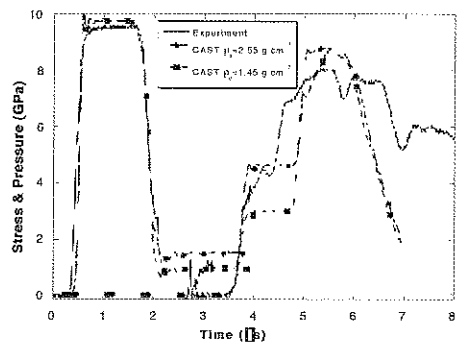


Figure 17: Results for 505 m s⁻¹ impact

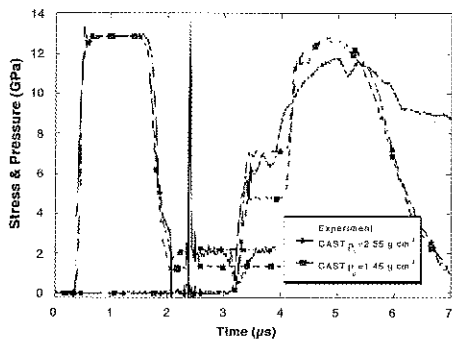


Figure 18: Results for 652 m s⁻¹ impact

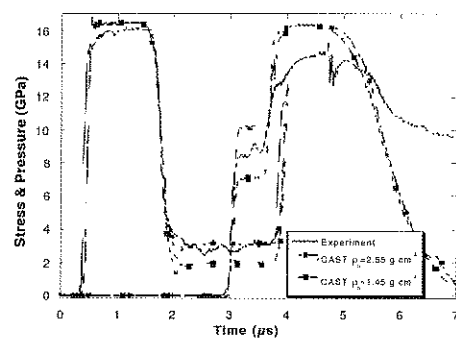


Figure 19: Results for 811 m s⁻¹ impact

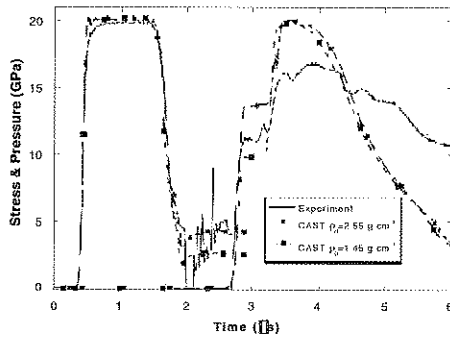


Figure 20: Results for 969 m s⁻¹ impact

From the figures, it can be seen that the simulations predict the first gauge trace with reasonable agreement, which corresponds to a copper-on-copper impact. Therefore, the current model for Cu can adequately describe the copper properties. In addition, the time between the Lagrangian points agrees well with the time difference of the two embedded gauges. There is less agreement for the rear gauge. The sand model with initial density 1450 kg m⁻³ always under predicts the first step of the gauge. However, when the theoretical maximum density is used, the agreement on the height of the first step is better at low impact velocities but is progressively over predicted at higher velocities. Both models

over predict the duration of the first step for low velocities but match closely for impact speeds in excess of 811 m s^{-1} . The main cause for this is that the porosity remains constant in the model but in reality the porosity and by extension the bed thickness decreases significantly during shock compression. Therefore, these discrepancies could well be attributed to the simplified nature of the sand model. The version of CAST used, does not support a porous EoS and therefore the predictions are for an idealized case. A more sophisticated model is required where porosity and strength are considered. Finally, note that when modeling a gauge mounted in epoxy, it is suggested that this be included as a 0.2 mm thick layer of PMMA. However, because of the fine mesh resolution needed, no such layer was introduced in the simulations.

CONCLUSIONS

Several longitudinal shots have been performed on dry sand. The results are reproducible and the sand is well behaved. Two Hugoniot curves were constructed based on initial and theoretical maximum densities and were used to perform simulations using the CAST-EDEN hydrocode. The simulations are in reasonable agreement with experiments. However, it is apparent that the model has a limited use and a more sophisticated model is needed which should include porous collapse.

ACKNOWLEDGEMENTS

L. Taylor and D. Tam of the Naval Surface Warfare Centre (NSWC-USA) and G. Evans of QinetiQ (UK) have sponsored this work. Dr. I.G. Cullis, P.D. Church of QinetiQ and A. Milne Fluid Gravity Ltd. provided the hydrocode. Finally, we thank D.L.A. Cross and R. Flaxman for technical support

REFERENCES

1. K. Tsembeles, J.C.F. Millett, W.G. Proud and J.E. Field, Shock Compression of Condensed Matter-1999, (eds. M.D. Furnish, L.C. Chhabildas and R.S. Hixson), 1267.
2. K. Tsembeles, W.G. Proud and J.E. Field, Shock Compression of Condensed Matter-2001, (eds. M.D. Furnish, N.N. Thadhani and Y. Horie), 1385.
3. H.T. Goldrein, S.G. Grantham, W.G. Proud and J.E. Field, Shock Compression of Condensed Matter-2001, (eds. M.D. Furnish, N.N. Thadhani and Y. Horie), 1105.
4. L. Laine, Ø. Ranestad, A. Sandvik and A. Snekkevik, Shock Compression of Condensed Matter-2001, (eds. M.D. Furnish, N.N. Thadhani and Y. Horie), 431.
5. M.v. Thiel, Compendium of Shock Wave Data. Report UCRL-50108, 1966, University of California, Livermore.
6. N. K. Bourne, Z. Rosenberg, D. J. Johnson, J. E. Field, A. E. Timbs and R. P. Flaxman, *Meas. Sci. Technol.* **6**, 1462 (1995).
7. J.J. Gilman, Shock Compression of Condensed Matter-1991, (eds. S.C. Schmidt, R.D. Dick, J.W. Forbes and D.G. Tasker), 387.

CONTACT

K. Tsembeles can be contacted via e-mail at: kt226@phy.cam.ac.uk

The Physics and Chemistry of Solids Group had a variety of research interests. To learn more about our activities, please visit our main website at: <http://www.pcs.phy.cam.ac.uk/fsp>

Characterisation and Modelling of a Bi-Layered Polymer Material

M. Welle, W. Riedel, S. Hiermaier, K. Thoma

Fraunhofer Institut für Kurzezeitdynamik, Ernst-Mach-Institut (EMI)

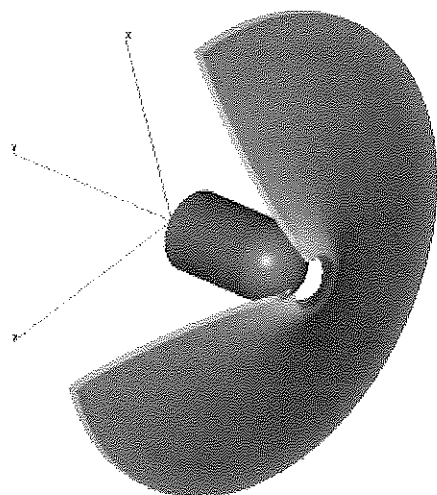
Eckerstr. 4, D-79104 Freiburg, Germany

ABSTRACT

For several decades, polymers have been the standard material type for automobile interior components. In the past, such components were primarily designed with respect to functionality and styling. Nowadays, the integration of airbags and the implementation of severer passenger security standards have classified many components as safety relevant. The present study demonstrates the state of the art in characterizing, modelling and simulating a bi-layered polymeric material under crash relevant conditions. Important is the application of a new optical strain measurement technique within the whole range of temperatures and strain rates. The capability of a state of the art modelling approach in a finite element scheme with explicit time integration [1] to replicate dynamic deformation and failure is demonstrated.

INTRODUCTION

The present study describes the results of a cooperative study between the Fraunhofer Ernst-Mach-Institut (EMI) and an industrial partner.



The investigated material was a bi-layered polymer. It is used for typical automobile interior components consisting of two thermoplastic layers on Polypropylene basis – a base and a cover material. A precise description of the material behaviour, in the present case with respect to typical conditions for crash applications, is an important precondition for reliable vehicle simulations. Therefore, the experimental characterization and the investigation of numerical models are following a specific procedure:

- Separate characterization of both materials in tensile tests
- Derivation of model parameters and simulation of tensile tests
- Validation of the numerical model of the composite material

Figure 1: Simulation of component test

MATERIAL CHARACTERISATION

OPTICAL STRAIN MEASUREMENT

One key aspect of dynamic testing of thermoplastics is the choice of an appropriate measurement technique. Standard strain methods as crosshead displacement, strain gauges or extensometers have only limited applicability for dynamic testing. With these methods, it is not possible to measure the entire plastic hardening curve detail. Failure strains of polymers can reach up to several hundred percent. Furthermore, local strain distributions can cause in uniaxial tensile tests a necking effect and with subsequent cold-drawing. For this reasons, a new measurement technique - an optical strain evaluation procedure - has been developed at EMI [2].

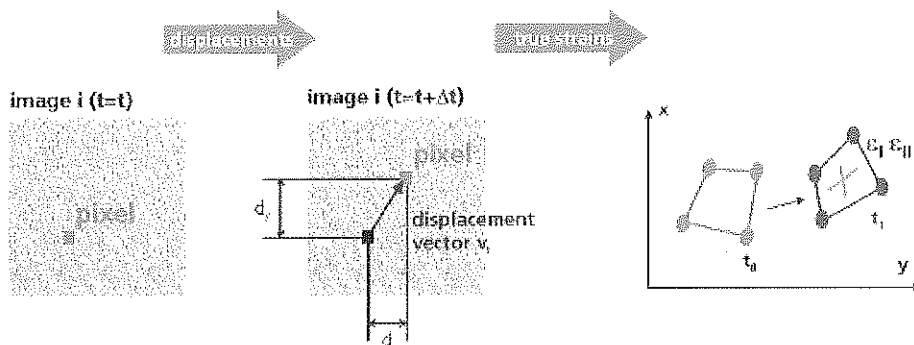


Figure 2: Principle of optical strain measurement

The principle of this optical strain measurement is based on displacement analysis by greyscale correlation of digital picture series. Therefore, a significant natural or artificial surface colour structure is essential. However, irregular grids can be used. A high-speed camera is recording digital images of the surface of the specimen during the test. Based on these images the local displacements are investigated via greyscale correlation. The determination of true strains is following the technique used in commercial numerical codes, allowing direct comparison between experimental and simulation data.

The local displacements are calculated for a reference area that has the size of a typical finite element. Figure 3 shows the significant differences among stress-strain curves obtained for different strain measurements techniques with different reference lengths.

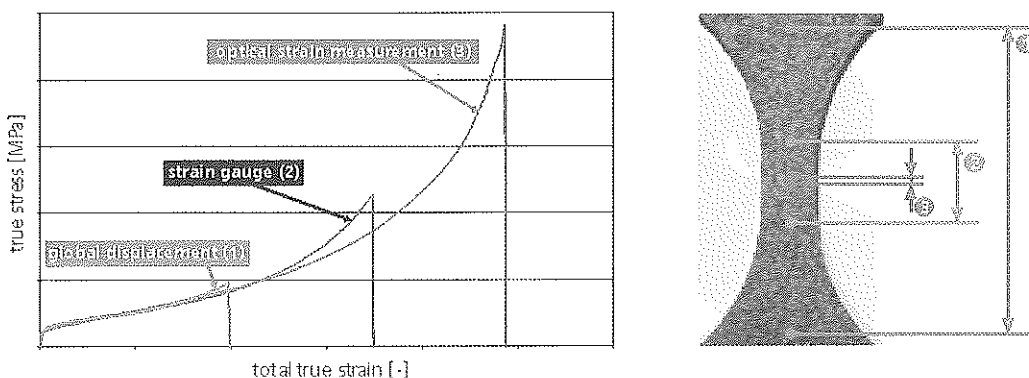


Figure 3: Comparison of stress-strain curves obtained with different reference dimensions

TENSILE TEST

Experimental investigations

Both materials were characterized using uniaxial tensile tests. The loading conditions for the test program were typical for crash applications – three different strain rates (quasi-static, 2/s and 200/s) and 3 different temperatures (-35°C, 23°C, 85°C). Several specimen geometries were used for each material, they were optimized in order to reach specific strains and strain rates. Specimens were taken out in parallel and normal orientation with respect to extrusion direction of the raw material to analyze a possible manufacturing influence.

In all tests up to a strain rate of 2/s a hydraulic testing device was used. The test specimens were fixed with special low-weight grips. Figure 4 shows the system with climate chamber, high-speed camera and illumination (foreground: test chamber, background: supplier chamber).

A special drop weight facility was used to reach a strain rate of 200/s (fig. 4). A specimen was fixed between a load cell and a yaw. An impactor with linear guides hit the yaw and expanded the specimen. For the tempered tests a climate chamber was used.

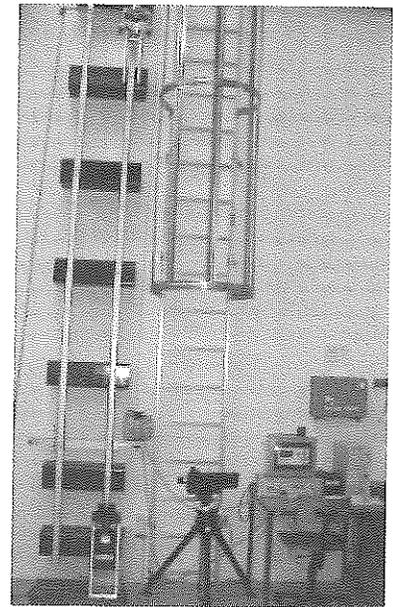
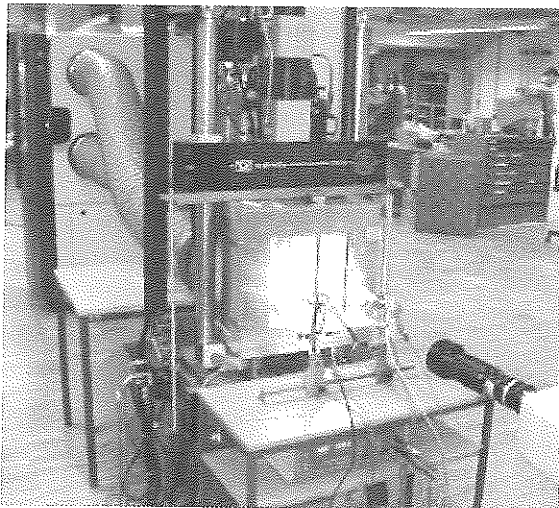


Figure 4: Experimental investigations - hydraulic test device (left), drop weight facility (right)

The samples were loaded uniaxially up to failure. Results of all experiments were the global load and displacement signals. Additionally, the surface texture of the test specimens was recorded by a high-speed camera to get digital images for the optical strain measurement.

Base material

For statistical reasons all test configurations were replicated four times. A choice of exemplary results is shown in the following graphs. Figure 5 shows results of tests which were made at different strain rates and Figure 6 shows results at different temperatures.

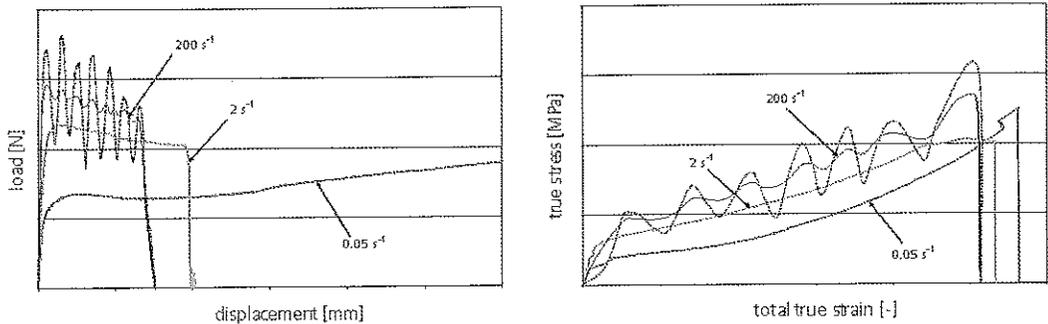


Figure 5: Load-displacement (left) and true stress-strain (right) at different strain rates and $T = 23^{\circ}\text{C}$

The following properties could be noticed:

- The Young's modulus is largely independent of the applied strain rate.
- The plastic material behaviour strongly depends on the strain rate. Load level and load maximum clearly increase for higher strain rates.
- Fracture strain is subject to a variation, which is typical for polymers (fig. 6). Nevertheless, the average fracture strain decreases with increasing strain rate.

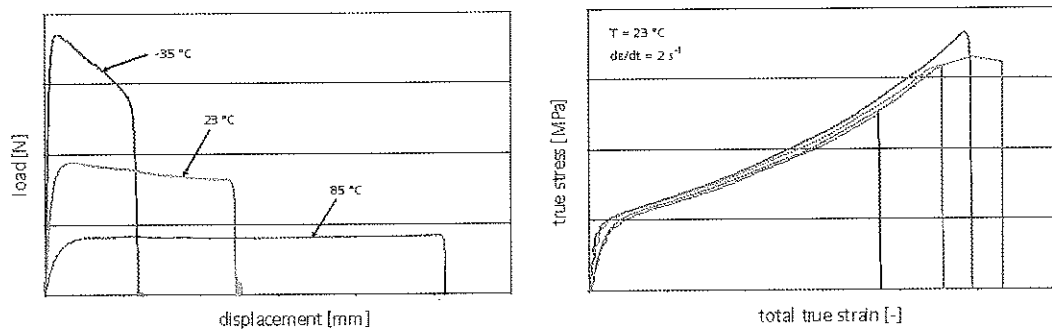


Figure 6: Load-displacement (left) and true stress-strain (right) at a strain rate of 2/s

The following temperature sensitivities could be noticed:

- The Young's modulus decreases with increasing temperature.
- Load level and maximum load decreases significantly with increasing temperatures.
- Average fracture strain increases with higher temperatures.
- Strain rate influence on force level and fracture strains decreases with falling temperatures.

Cover material

The behaviour of the cover material is qualitatively similar to the base material with respect to temperature and strain rate effects. Therefore, only one exemplary result is shown in Figure 7. Compared to the base material, the load level of the cover material is lower, whereas the average fracture strain is higher.

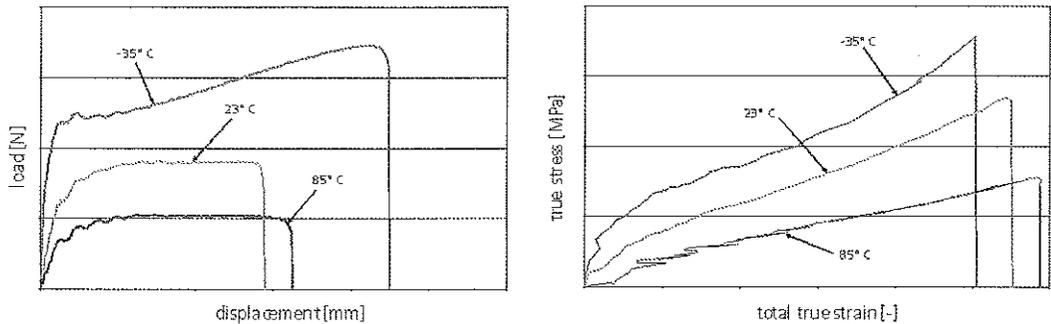


Figure 7: Load-displacement (left) and true stress-strain (right) at different temperatures ($de/dt = 2/s$)

However, differences concerning isotropy can be noticed. In contrast to the isotropic base material, the cover material shows anisotropy. This behaviour is caused by the thin lacquering. Figure 8 compares fracture strains of transverse and longitudinal specimens. It can be seen that the transverse samples have a higher fracture strain as the longitudinal samples. Furthermore, Figure 8 shows that the tests are reproducible.

The images (fig. 8) point out that the lacquering causes the detected anisotropic behaviour as the adhesive strength varies with the loading direction.

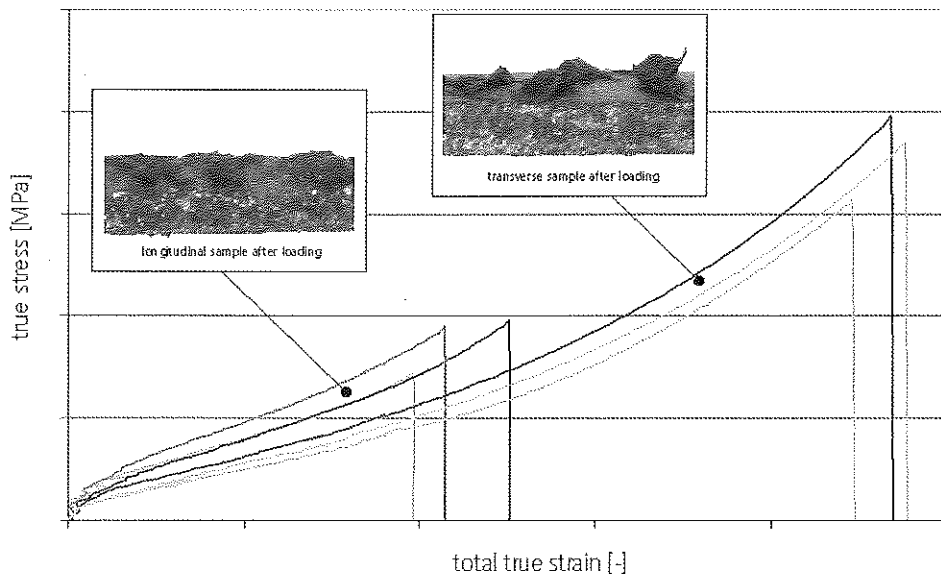


Figure 8: Stress-strain curves and images of samples after loading

SIMULATION

A finite element program with explicit time integration (commercial code PAM -CRASH [1]) was used for the simulation of the dynamic loading. The specimen was discretized by shell elements (4- nodes, single integration point).

An element of the type using the Belotschky-Tsay formulation was employed. To describe the material behaviour, an elastic-plastic material law for shells with elastic stiffening and failure (MAT 143) was used. The measured total stress-strain curves served as input. Different analytical strain rate models can be used to model strain rate effects. In this study the Cowper-Symonds law [3] was used as a closed analytical approach. The input of a basic stress-strain curve $\sigma_0(\varepsilon)$ and of two parameters D and p , describing the experimental dependency (fig. 9), is required for this description [1].

Only the sample section between the grips of the loading device was modeled. All degrees of freedom were fixed at the lower edge, at the upper edge a velocity boundary condition was prescribed for all nodes. In the horizontal direction the grid resolved 10 elements to accurately simulate necking effects.

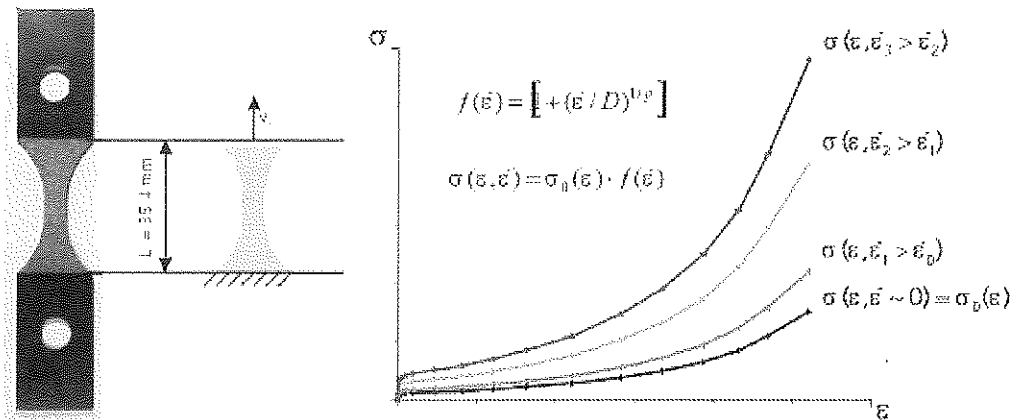


Figure 9: Numerical model (left) and analytical strain rate model (right)

Based on the measured true stress-strain curves derived in the uniaxial tensile tests, parameter sets for the Cowper-Symonds model were derived for both materials at each temperature. The maximum strain of the total true stress-strain curves was used as failure criterion. Figure 9 shows the numerical model and an exemplary input curve. The investigated numerical models were separately validated on the basis of local stress-strain and global load-displacement characteristics in simulations of the tensile tests. Figure 10 shows exemplary experimental and simulation results. Good agreement of the simulation results and the experimental data can be stated. Both load level and fracture strain were reproduced in a good quality.

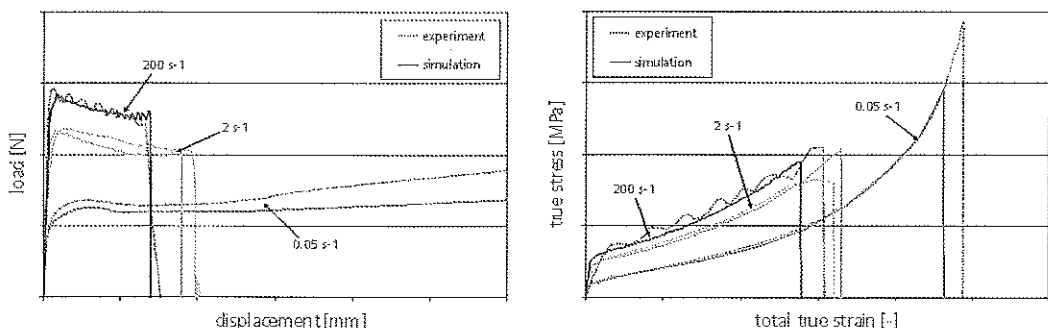


Figure 10: Comparison between experiment and simulation at ambient temperature

In summary, the material law chosen, the input curves and the Cowper-Symonds parameters could be verified as an appropriate description of the material behaviour in the considered strain rate range.

COMPONENT TEST

EXPERIMENTAL SETUP

A component test, based on a future practical application, was performed to validate the simulation of the composite material behaviour. A circular plate of the composite polymer material was impacted at 7 m/s by a circular rod with hemispherical nose. The plate was fixed at the outer edge and had an external diameter of 90 mm. A drilled hole in the middle of the plate defined a predamage. The impactor (mass 3.16 kg) impacted the plate center. The experiments were performed at different temperatures (-35°C, 23°C and 85°C). Load and displacement were recorded. Additionally, a high-speed camera took images of the dynamic deformation and failure behaviour.

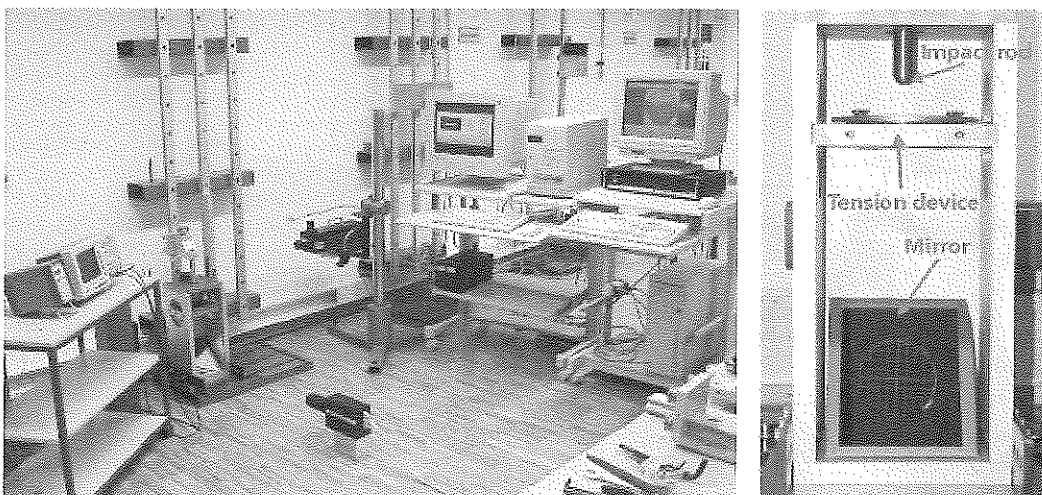


Figure 11: Component test – experimental setup

Good reproducibility of the experimental results was obtained (fig. 13). Exemplary results for different temperatures are shown in Figure 12. The following properties could be observed:

- The load level decreases and maximum displacement increases with higher temperatures.
- The slope of force progression is similar at all temperatures.
- The plateau at the beginning of the load curve gets longer with increasing temperatures.

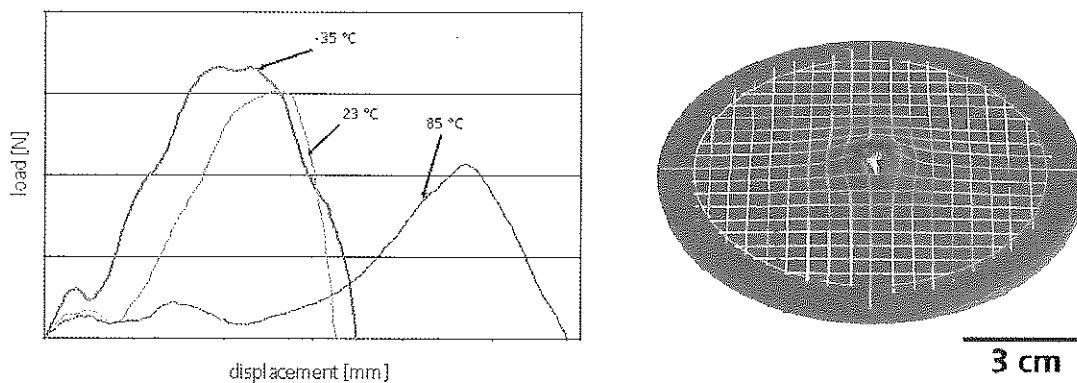


Figure 12: Load-displacement curves for component test (left) and sample after failure (right)

SIMULATION

The numerical simulation of component test was performed using shell elements for the plate. A high grid resolution was used to reproduce details of the failure behaviour. Base and cover material were discretized separately and connected by a tied contact (type 32). At the outer nodes, all degrees of freedom were fixed. The impactor was modeled as a rigid body and had an impact velocity of 6.8 m/s. The contact between impactor and composite material was modeled with a sliding contact (type 34). [1]

The input data was given by the determined input curves and the Cowper-Symonds parameters. The simulation results matched experimentally observed load level as well as the peak load. In order to estimate the influence of the anisotropy of the cover material detected in the uniaxial tensile tests, simulations with different sets of input data were done.

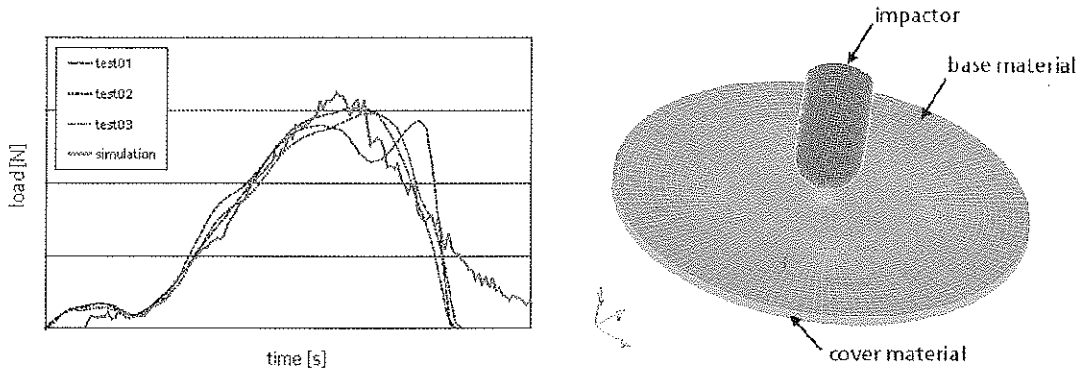


Figure 13: Comparison of experimentally observed and simulated load curves at ambient temperature (left) and numerical model (right)

An exemplary simulation result at a temperature of 23°C is given in Figure 13. The slope of the load curve, the maximum load level and the absorbed energy could be reproduced very well.

However, deficiencies in terms of the failure behaviour were noticed. Simulations with excentric impact gave a better agreement of the load-displacement curve during the fracture process. Another explication could be the fact that friction between composite material and impactor is not incorporated in the model.

The anisotropy had no important effect on the component test, contrary to the uniaxial tensile test. There were no significant deviations of the simulation results using the different input data sets for the cover material.

Due to the position of the camera with a view normal to the plate, the 2D-images taken in the experiments could only be used to qualitatively compare the deformation. Parallel to the impact direction the possibilities for comparison of experimental and simulated deformation and failure behaviour are limited.

CONCLUSION

SUMMARY

This paper has described the state of the art study to characterize, model and simulate a bi-layered polymeric material under crash relevant conditions. The material behaviour was measured by separate uniaxial tensile test campaigns for both material layers. The application of a new optical strain measurement technique within the whole range of temperatures and strain rates was of central importance. Thereby it was possible to investigate true stress-strain curves for extremely high elongations and strong localisation effects which are typical for polymers.

The corresponding numerical simulation with a finite element program with explicit time integration could validate the material model approach, the determined input curves and the parameter set for Cowper-Symonds strain rate dependency.

In order to validate the composite material behaviour, a component test was made, based on a future practical application. The combination of material models adequately described the composite behaviour. Only the failure evolution could not be predicted in all details.

As an overall goal, the capability of a state of the art modelling approach in a commercial crash code to replicate dynamic behaviour crash relevant polymer components was demonstrated.

PERSPECTIVES

In further studies, high-speed cameras with higher pixel and time resolution will be applicable. Thereby improved stress-strain data for measurements with high strains or strain rates can be obtained.

Additionally, a 3D-optical evaluation of the component test is being developed to provide spatially resolved deformations. A detailed comparison of experimentally observed deformations and simulated data in all 3 directions is the goal.

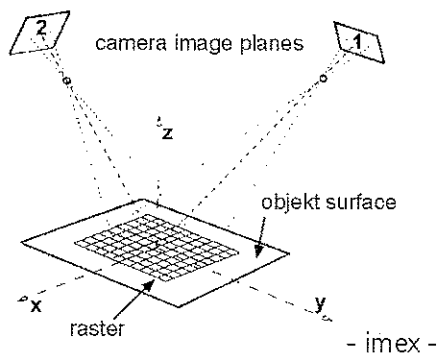


Figure 14: Principle of 3D-correlation

REFERENCES

- [1] N.N., ESI: PAM-CRASH - Version 2000, Theory Notes Manual, March 2000
- [2] Junginger, M., Werner, H., Möller, F., Thoma, K.: Material Testing of Thermoplastics - New Analysis and Application for the Automotive Industry. Materials Week, Munich (2000).
- [3] Cowper, G.R. and Symonds, P.S., Strainhardening and strain-rate effects in the impact loading of cantilever beams, Technical Report, No.28, Brown University (1957)